

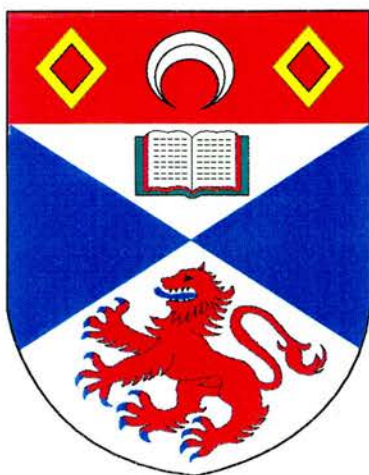
University of St Andrews



Full metadata for this thesis is available in
St Andrews Research Repository
at:

<http://research-repository.st-andrews.ac.uk/>

This thesis is protected by original copyright



**ELECTROCHEMISTRY OF NOVEL LITHIUM
SALT COMPLEXES IN NON-AQUEOUS,
POLYETHER AND GEL MEDIA**

A thesis presented for the degree of

Doctor of Philosophy

in the Faculty of Science of the University of St. Andrews

by Alasdair M'Call Christie, *B.Sc.*

*Centre for Electrochemical
and Material Sciences*

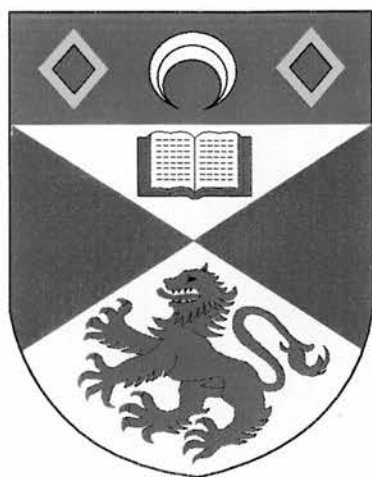
School of Chemistry

St. Andrews

January, 1995



TL
B708



**ELECTROCHEMISTRY OF NOVEL LITHIUM
SALT COMPLEXES IN NON-AQUEOUS,
POLYETHER AND GEL MEDIA**

A thesis presented for the degree of

Doctor of Philosophy

in the Faculty of Science of the University of St. Andrews

by Alasdair M^cCall Christie, *B.Sc.*

Centre for Electrochemical

and Material Sciences

School of Chemistry

St. Andrews

January, 1995



TL
B708

DECLARATION

I, Alasdair M^cCall Christie, certify that this thesis has been composed by myself, that it is a record of my own work, and has not been submitted in any previous application for a higher degree.

Signed:

Date: 5.1.95

I was admitted to the Faculty of Science in the University of St. Andrews under Ordinance General No. 12 on 1 October, 1991 and as a candidate for the degree of Doctor of Philosophy on 1 October, 1992.

Signed:

Date: 5.1.95

CERTIFICATION

I hereby certify that Alasdair M^cCall Christie, B.Sc. has spent twelve terms of research work under my supervision, and that he has fulfilled the conditions of the Resolution and Regulations appropriate to the degree of Doctor of Philosophy.

Signed:

Date: 5.1.95

C.A. Vincent

Director of Research

LIBRARY DECLARATION

In submitting this thesis to the University of St. Andrews, I understand that I am giving permission for it to be made available for use in accordance with regulations of the University Library for the time being in force, subject to any copyright vested in the work not being affected thereby. I also understand that the title and abstract will be published, and that a copy of the work may be made and supplied to any bona fide library or research worker.

Signed:

Date: 5.1.95

For my parents and Lynn

“There may be no ultimate theory, and even if there is, we may not find it.”

Stephen Hawking (1993)

Acknowledgements

Thanks must be given to my supervisor, Professor Colin Vincent, for his guidance and constructive comments throughout my Ph.D years, and for giving encouragement to work with my own ideas. I would like to express my appreciation to Professor Peter Bruce and all the members of *C.E.M.S.*, past and present, for their general good humour and stimulating discussions.

My thanks are also due to the technical staff at St. Andrews, in particular John Smith, Colin Smith and Jim Rennie, who suffered from continuous bombardment of requests. I am indebted to the Associated Octel Company Ltd., in particular to Dr. Barbara Richards, for financial support and provision of the lithium complexes, and to the EPSRC for CASE funding.

Special thanks must go to my family for their support over my many years of study. Finally, I would like to thank Lynn, my wife and colleague, for standing by me through the good times and the bad.

ABSTRACT

Electrochemical studies have been performed on some novel lithium salt complexes in polyether media, propylene carbonate and poly(methyl methacrylate) gels. The electrochemical performances of these electrolytes containing added ligands were assessed with particular attention given to their applicability to modern lithium rechargeable battery systems.

Conductivity data was obtained for complexes of lithium hexafluorophosphate in non-aqueous polyether media and propylene carbonate over a wide range of concentration (10^{-3} M to 1M) and analysed using the Fuoss-Kraus, Fuoss (1978) and Casteel-Amis methods. The electrolyte parameters, namely molar conductivity at infinite dilution, dissociation constants for ion-pairs and triple-ions, and maximum specific conductivities, have been obtained. These parameters, particularly at low salt concentration, have been interpreted in terms of ion-ion interactions.

Kinetics and mechanisms for the electrodeposition of lithium from non-aqueous solvents and gel media were studied using chronoamperometric, cyclic voltammetric and chronopotentiometric methods at a microelectrode. Nucleation and crystal growth models have been proposed for each electrolyte. Exchange current densities, coulombic stripping efficiencies and lithium corrosion rates were evaluated.

TABLE OF CONTENTS

List of Commonly Used Symbols.....	ix
Constants.....	xii
Abbreviations.....	xiii

CHAPTER ONE

Introduction	1
1.1. Electrochemical Power Sources.....	1
1.2. Lithium Batteries: An Overview	2
1.2.1. Introduction	2
1.2.2. Primary Lithium Cells	2
1.2.3. Secondary Lithium Cells.....	3
1.3. Positive Electrode Materials	4
1.4. Negative Electrode Materials	5
1.5. Electrolytes	9
1.6. Solvent Systems.....	10
1.6.1. Non-aqueous.....	10
1.6.2. Polymer.....	11
1.6.3. Gel.....	14
1.7. Aims of the Thesis.....	15

REFERENCES.....	16
-----------------	----

CHAPTER TWO

Electrochemical Theory and Methodologies.....	20
2.1. Electrode Processes	20
2.1.1. Electron Transfer.....	20
2.1.2. Very Low Overpotentials	24
2.1.3. High Overpotentials: The Tafel Equations	25
2.2. Mass Transport	27
2.2.1. Diffusion Control	27
2.2.2. Diffusion to a Planar Electrode	28
2.2.3. Microelectrodes.....	30
2.3. Electrodeposition	32
2.3.1. Nucleation and Growth of Monolayers	34
2.3.2. Nucleation and Growth of Three-Dimensional Centres	35
2.3.2.1. Diffusion Controlled Growth	35
2.3.2.1. Kinetic Controlled Growth.....	42
2.4. Cyclic Voltammetry	43
2.4.1. Reversible Reactions	45
2.4.2. Irreversible Reactions	47
2.4.3. The EC Reaction.....	49
2.4.4. Phase Formation.....	50
2.5. A.C. Impedance Spectroscopy.....	52

2.5.1. Simple Systems	56
2.5.2. Cells with Blocking Electrodes	60
2.6. Electrolytic Conductance and Conductivity	61
2.6.1. Definitions.....	61
2.6.2. Electrolyte Solutions	63
2.6.3. Ion Association	65
2.6.4. Paired Ion Model.....	69
2.6.5. Higher Association	74
2.6.5.1. Triple Ion Formation	74
2.6.5.2. Re-dissociation of the Ion-pair	80
REFERENCES.....	82

CHAPTER THREE

Experimental Procedures.....	85
3.1. Preparation of Salts	85
3.1.1. Lithium Perchlorate	85
3.1.2. Lithium hexafluorophosphate and Lithium tetrafluoroborate	85
3.2. Lithium Complexes	85
3.3. Solvent Preparation.....	87
3.3.1. Diglyme.....	87
3.3.2. Poly(ethylene oxide) 400	87
3.3.3. Tetraglyme and propylene carbonate.....	88

3.4. Preparation of Electrolytes	90
3.4.1. Liquids	90
3.4.2. Amorphous Polymer Electrolytes.....	90
3.4.3. Gels.....	90
3.5. Instrumentation.....	91
3.5.1. Conductivities	91
3.5.2. Cell Calibration	93
3.5.3. Cyclic Voltammetry and Chronoamperometry	94
3.5.4. Microelectrode Construction	96
3.5.5. Differential Scanning Calorimetry	97
3.5.6. Nmr Measurements	97
REFERENCES.....	98

CHAPTER FOUR

Conductivities and Ion Association in Non-aqueous Media	99
4.1. Introduction.....	99
4.2. Determination of Solvent Relative Permittivities.....	100
4.3. Ion Association	102
4.3.1. Low Permittivity Media.....	108
4.4.2. High Permittivity Media	117
4.4. Specific Conductivities.....	122
4.5. Conclusions.....	130

REFERENCES	132
------------------	-----

CHAPTER FIVE

The Li/Li⁺ Couple in Polyether Electrolytes	134
---	------------

5.1. Introduction	134
-------------------------	-----

5.2. Results and Discussion	135
-----------------------------------	-----

5.2.1. Kinetics of the Li/Li ⁺ Couple	135
--	-----

5.2.2. Nucleation and Growth	146
------------------------------------	-----

5.2.3. Lithium Reactivity and Passivation	156
---	-----

5.3. Conclusions	162
------------------------	-----

REFERENCES	164
------------------	-----

CHAPTER SIX

The Li/Li⁺ Couple in Propylene Carbonate Electrolytes and Poly(methyl methacrylate) Gels	166
--	------------

6.1. Introduction	166
-------------------------	-----

6.2. Experimental	167
-------------------------	-----

6.3. Results and Discussion	168
-----------------------------------	-----

6.3.1. Ligand Binding	168
-----------------------------	-----

6.3.2. Solvent Characterisation	171
---------------------------------------	-----

6.3.3. Potentials Positive of Bulk Lithium Deposition	174
---	-----

6.3.4. Kinetics of the Li/Li ⁺ Couple	176
--	-----

6.3.5. Nucleation and Growth of the Lithium Deposit.....	189
6.3.6. Lithium Reactivity and Passivation	195
6.4. Conclusions.....	201
REFERENCES.....	203

CHAPTER SEVEN

Ion Association: A Molecular Modelling Perspective.....	206
7.1. Introduction to Molecular Modelling.....	206
7.2. General Minimisation Strategy	207
7.3. Minimisation Algorithms Used	210
7.3.1. Steepest Descents.....	210
7.3.2. Conjugate Gradients.....	211
7.4. Results and Discussion	213
7.4.1. Properties of the Anion.....	213
7.4.2. Association to Pairs.....	219
7.4.3. Higher Aggregates	221
7.5. Conclusions.....	228
REFERENCES.....	229

CHAPTER EIGHT

Concluding Remarks	231
8.1. Initial Studies	231
8.2. Electrolytic Conduction.....	233
8.3. Lithium Plating and Stripping.....	234
8.4. Electrochemical Stability	235
8.5. General Conclusions.....	236
8.6. Future Work	237
APPENDIX 1 Solvent Stabilities	239

APPENDIX 2

Conductivity of PEO₃Lithium Triflate as a Function of Temperature.....	251
A2.1. Experimental	251
A2.1.1. Lithium trifluoromethanesulphonate (lithium triflate).....	251
A2.1.2. Preparation of PEO ₃ Lithium Triflate	252
A2.1.3. Powder X-Ray Diffraction	252
A2.1.4. Conductivity Measurements.....	256
A2.2. Results	259

APPENDIX 3

Charge Transfer at a Metal/Ion Electrode.....	263
A3.1. Introduction	263
A3.2. Theory	263

List of commonly used symbols

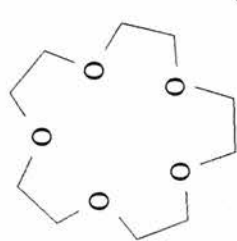
A	Cross sectional area of conductor
a	Radius of a micro-disk
a	Contact pair distance
C	Capacitance
c_i	Concentration of species i
c_O^σ, c_R^σ	Surface concentrations of O and R
c_O^∞, c_R^∞	Bulk concentrations of O and R
c_{max}	Concentration at maximum specific conductivity
D	Diffusion coefficient
D_i	Diffusion coefficient of species i
E	Applied potential
E_e	Equilibrium potential
E_e^\ominus	Standard equilibrium potential
E_p	Peak potential
E_{max}	Potential amplitude
f	Frequency
f	Activity coefficient (fugacity)
I_{max}	Current amplitude
I	Current density
$\vec{I}, \overleftarrow{I}$	Partial current densities for the forward and reverse reactions
I_0	Exchange current density
I_p	Peak current density
I_{appl}	Applied current density
I_{corr}	Corrosion current density
i	Current
J_i	Flux of species i
j	Imaginary number, $\sqrt{-1}$
K_R	Association constant for solvent-separated pairs
K_S	Association constant for contact pairs

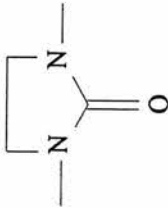
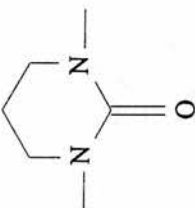
K_A	Total association constant for pairs
K_i	Association constant for free ions
K_t	Association constant for triple ions
$\vec{k}, \overleftarrow{k}$	Rate constants for the anodic or cathodic reactions
k_0	Rate constant at 0V vs. the reference electrode
k^0	Standard apparent rate constant
k_l	Rate of corrosion
L	Length of conductor
M	Relative molar mass
m	Molal concentration
N	Number of nuclei
N_∞	Maximum number of nucleation sites
n	Number of electrons
O	Oxidised species
R	Reduced species
R	Resistance
R	Sum of cation and anion cospheres
r_0	Radius of a micro-sphere
r_{ij}	Distance between ions i and j
S	Onsager slope
T	Temperature (K)
t	Time (seconds)
t_f	Forward deposition time
x	Mole fraction
Y^*	Complex admittance
Z^*	Complex impedance
Z'	Real impedance
Z''	Imaginary impedance
z	Charge valency

α	Fraction of contact pairs
α_c, α_a	Transfer coefficients for the cathodic and anodic processes
α_i	Fraction of free ions
α_t	Fraction of triple-ions
δ	Radius of growing hemispherical diffusion zone
δ	NMR chemical shift
ε	Permittivity
ε_r	Relative permittivity (dielectric constant)
γ	Fraction of free ions
Λ, Λ_c	Molar conductivity
Λ_m	Molal conductivity
Λ_o	Limiting molar conductivity
Λ_o^T	Limiting molar conductivity of triple-ions
λ_o	Limiting molar ionic conductivity
κ	Specific conductivity
κ_{max}	Maximum specific conductivity
η	Overpotential
η	Viscosity
ν	Sweep rate
θ_{ex}	Extended area covered
θ	Actual fraction of area covered
θ	Phase angle
ρ	Density
ρ	Specific resistance
τ_r	Reverse transition time
ω	Angular frequency

Constants

Elementary charge	e	=	$1.602\ 177 \times 10^{-19}$ C
Faraday constant	F	=	96485 C mol ⁻¹
Boltzmann constant	k	=	$1.380\ 66 \times 10^{-23}$ JK ⁻¹
Avagadro constant	N	=	$6.022\ 14 \times 10^{23}$ mol ⁻¹
Gas constant	R	=	8.314 51 JK ⁻¹ mol ⁻¹
Vacuum permittivity	ϵ_0	=	$8.854\ 19 \times 10^{-12}$ J ⁻¹ C ² m ⁻¹

Type	Abbreviation	Name	Formula
Amines	TMEDA	1,1,4,4-Tetramethyl ethylene diamine	$(\text{CH}_3)_2\text{NCH}_2\text{CH}_2\text{N}(\text{CH}_3)_2$
	PMDETA	1,1,4,7,7-Pentamethyl diethylene triamine	$(\text{CH}_3)_2\text{NCH}_2\text{CH}_2\text{N}(\text{CH}_3)\text{NCH}_2\text{CH}_2\text{N}(\text{CH}_3)_2$
	HMTETA	1,1,4,7,10,10-Hexamethyl triethylene tetramine	$(\text{CH}_3)_2\text{NCH}_2\text{CH}_2\text{N}(\text{CH}_3)\text{CH}_2\text{CH}_2)_2\text{N}(\text{CH}_3)_2$
	DME /	1,2-Dimethoxyethane /	$\text{CH}_3\text{OCH}_2\text{CH}_2\text{OCH}_3$
	Monoglyme	Ethylene glycol dimethyl ether	
	DEE	1,2-Diethoxyethane /	$\text{CH}_3\text{CH}_2\text{OCH}_2\text{CH}_2\text{OCH}_2\text{CH}_3$
ETHERS	Diglyme	Ethylene glycol diethyl ether	
	Triglyme	Diethylene glycol dimethyl ether	$\text{CH}_3(\text{OCH}_2\text{CH}_2)_2\text{OCH}_3$
	Tetraglyme	Triethylene glycol dimethyl ether	$\text{CH}_3(\text{OCH}_2\text{CH}_2)_3\text{OCH}_3$
	Hexaglyme	Tetraethylene glycol dimethyl ether	$\text{CH}_3(\text{OCH}_2\text{CH}_2)_4\text{OCH}_3$
		Hexaethylene glycol dimethyl ether	$\text{CH}_3(\text{OCH}_2\text{CH}_2)_6\text{OCH}_3$
	15-Crown-5	1,4,7,10,13-pentaoxy cyclopentadiene	 $\text{C}_{10}\text{H}_{20}\text{O}_5$

Type	Abbreviation	Name	Formula
UREAS	DMI	1,3-Dimethyl-2-imidazolidinone	 $C_3H_{10}N_2O$
	DMPU	N,N'-Dimethyl propylene urea	 $C_6H_{12}N_2O$

CHAPTER ONE

Introduction

1.1. Electrochemical Power Sources

Batteries are electrochemical storage devices which, on application of an external load, can convert the energy produced from a chemical reaction into electricity. A battery generally consists of an outer case, current collectors to transport the current from the electrode material, positive and negative electrodes separated by an electronically insulating material and an ion conducting electrolyte. Every cell reaction involves an oxidation and reduction process. During discharge, oxidation takes place at the negative electrode, and reduction at the positive.

There are essentially three main cell categories from which a power source may be identified [1]. A *primary cell* is one in which the cell reactants are irreversibly consumed during a single discharge, thus ending its useful life. *Fuel cells* [2-5] are essentially batteries where the reactants are stored externally, and supplied on a continuous basis. A fuel, such as methane gas, undergoes oxidation by a series of half reactions resulting in the conversion of chemical energy into electrical energy. Two major markets are seen for fuel cells: vehicle propulsion and power plants for stationary electrical requirements. A *secondary cell* is capable of being recharged after its reactants have been used and may thus be regarded as a device for storing electrical energy. This type of cell is an attractive prospect when considering the fact

that a new primary battery can be >1000 times more expensive than the cost of recharging using the mains electrical supply.

1.2. Lithium Batteries: An Overview

1.2.1. Introduction

The rate of technological advance over the last three decades has necessitated the manufacture of portable lightweight power sources with high energy density [6]. In particular, the miniaturisation of electronic devices in recent years has demanded novel approaches to battery design.

Lithium is an extremely attractive metal for use in electrochemical power sources due to its light weight and highly electropositive nature, providing high power and energy density. Lithium metal is highly reactive with both inorganic and organic materials giving rise to the possibility of decomposition of both the electrolyte and solvent. Reaction products are generally deposited on the Li surface as passivating films [6-12] inhibiting Li corrosion and thus increasing the battery's shelf-life.

1.2.2. Primary Lithium Cells

In the last thirty years, developments of primary lithium power sources [6, 13] have occurred in parallel with those of the electronics industry, following initial research on liquid organic electrolytes for alkali batteries pre-1960. In the late 1960's, commercial

cells based on the Li/copper oxide system were introduced, while research began into the Li/SOCl₂ and Li/SO₂ cells. Devices requiring only low discharge rates for their operation, such as watches and calculators, have been using long life primary Li cells for many years now (among them Li/CuO, Li/MnO₂ and Li/FeS₂).

In a primary cell, the lithium is consumed during discharge, and at the end of its useful discharge life there will be no Li metal remaining, ie. the cell is designed to be *lithium-limited*.

1.2.3. Secondary Lithium Cells

Many modern devices, such as video cameras, portable computers and electric vehicles, require high rate discharge power sources. Although there are well established primary high rate discharge cells (eg. Li/SO₂) [6, 14, 15], it is more economical to use a rechargeable, or secondary, Li battery [16-18]. The success of primary lithium battery systems during the last decade has encouraged the development of the rechargeable lithium battery [6, 13, 20-22] for new applications.

Some applications require high voltage power sources from a number of series-connected cells. A built-in mechanism to prevent overcharge of individual cells and oxidative degradation of the electrolyte is required. One method uses an external electronic circuit which prevents the cell voltage from increasing beyond the anodic oxidative limit of the electrolyte (eg. +4.2V vs. Li/Li⁺). Another involves the use of a *redox shuttle* [23] in which an additive remains inactive until a charge cut-off voltage

is reached, at which point it is oxidised at the positive electrode to products which diffuse to the negative electrode and are then either electrochemically reduced or reacted with lithium to regenerate the starting material. This cycle maintains the cell potential at the oxidation potential of the redox reagent until the charging process is terminated. The redox material would ideally have the following properties: be highly soluble in the electrolyte and have an oxidation potential lower than that of the electrolyte but higher than the usual charge limit of the cell; the ability to reduce its oxidised form at the negative electrode without side reactions, and chemical stability in the cell of both the oxidised and reduced forms of the shuttle reagent.

During overdischarge, the negative electrode is at a potential lower than that of the positive electrode except under voltage reversal conditions, so the redox shuttle method cannot be employed. A small amount of a reversible material with a lower discharge potential than that of the cathode material can be incorporated into the positive electrode, or inclusion of a material which can act as a form of chemical diode, shutting the cell down if the potential drops below a specific value.

1.3. Positive Electrode Materials

The discharge and charge processes of most of the active cathode materials involve the extraction of lithium from a host matrix and insertion of lithium to a host matrix, respectively. Recently, transition metal oxides, such as Cr_3O_7 , CoO_2 and MnO_2 , have proved to be attractive positive electrode materials, allowing efficient lithium

insertion/extraction reversibility with high discharge potentials of ca. 3.0 - 4.0 V versus Li/Li⁺, fulfilling a requirement for high energy density batteries.

A common cathode material among the transition metal oxides is MnO₂ which has previously been used in primary lithium cells. Extraction of lithium from this cathode material for rechargeable batteries requires a modification to the crystal structure of MnO₂ [24, 25]. The crystal structure of this modified MnO₂ has been identified as a mixture of γ -β-MnO₂ and Li₂MnO₃.

Cathode materials possessing higher discharge potentials, in order to manufacture a lithium battery with much higher energy density, have been investigated more recently. The cobalt oxide (CoO₂), for example, has a discharge potential of >4.0V vs. Li/Li⁺. The discharge voltage is higher than those of MnO₂, V₂O₃ and other oxides [26]. The Li_xMn₂O₄ (spinel) has also been investigated by many groups, showing high discharge potentials sufficient for high energy density capabilities. A new preparation by Huang and Bruce [27], has since shown superior cycling properties to that of the conventional spinel.

1.4. Negative Electrode Materials

In a secondary cell, where lithium is used as the negative electrode, Li must be replated during charging, some of which will become passivated and thus electrochemically isolated. Dendritic growth of Li metal, rather than a smooth deposit, often occurs during the plating process [6, 13]: this depends on many factors

and in particular on current density. Figure 1-1 shows a scanning electron micrograph of a lithium electrode surface morphology after charging in a propylene carbonate solution containing $1.0 \text{ mol dm}^{-3} \text{ LiBF}_4$.

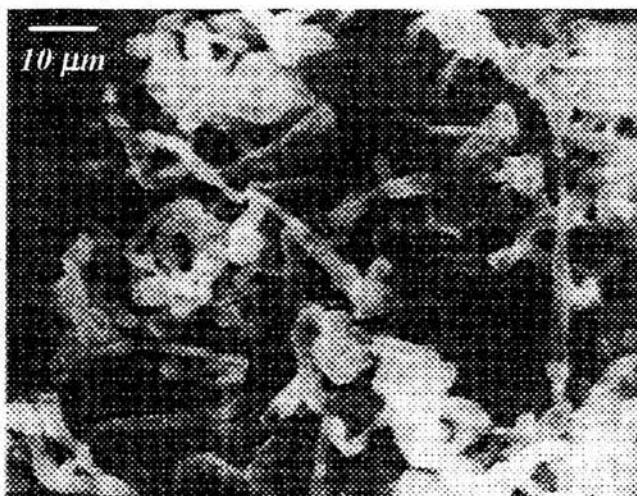


Figure 1-1 Scanning electron micrograph of lithium electrodeposited from propylene carbonate containing $1.0 \text{ mol dm}^{-3} \text{ LiBF}_4$ at 1.0 mAcm^{-2} .

The formation of dendritic deposits may lead to internal short circuits between the electrodes which disappear during discharge. These so-called *soft-shorts* are capable of passing high currents causing significant local heating and eventual melting of the separator and electrolyte decomposition. If the separator melts, catastrophic cell failure may result. Even if the separator does not melt, the heat generated may decompose the electrolyte exothermically [28].

Passivation of the lithium electrode and dendritic Li growth leads to a decrease in the cycling efficiency. The practical rechargeable lithium battery requires a very high cycling efficiency (>99%) if it is to last several hundred cycles. Using a material with

lower Li activity for the negative electrode than Li metal reduces the risk of passivation and inhibits reaction with the electrolyte.

There are generally two classes of alternative materials capable of accepting and exchanging large quantities of lithium ions, comprising Li insertion compounds and Li alloys. They must satisfy the following criteria:

- ◆ low weight;
- ◆ small free energy change upon Li insertion;
- ◆ high rates of diffusion of Li^+ in the solid structure of the anode;
- ◆ high reversibility of Li insertion;
- ◆ good electronic conductivity;
- ◆ thermal and chemical stability with the electrolyte;
- ◆ ease of manufacture and processing.

Some of the materials under study include the Li insertion compounds $\text{Li}_x\text{Fe}_2\text{O}_3$, Li_xWO_2 and graphitic carbon, and alloys such as $\beta\text{-LiAl}$, LiCdPb , LiAlMn [29-32] and composites such as $\text{Li}/\text{Li}_3\text{N}$ and Li_xPb -poly(paraphenylene) [29]. The carbon electrodes insert Li into its layered structure according to eqn. 1-1:



where $0 < y < 1$ depending upon the carbon used. Dahn *et al* [33] showed successful intercalation of two lithiums per six carbons (Li_2C_6) during the first cycle and one reversibly on successive cycles.

Batteries with no metallic lithium are termed *Li-ion* or *rocking-chair batteries*. The Li ions essentially rock between the intercalation compounds during charge/discharge cycles (Figure 1-2), providing a safer approach to the lithium rechargeable battery.

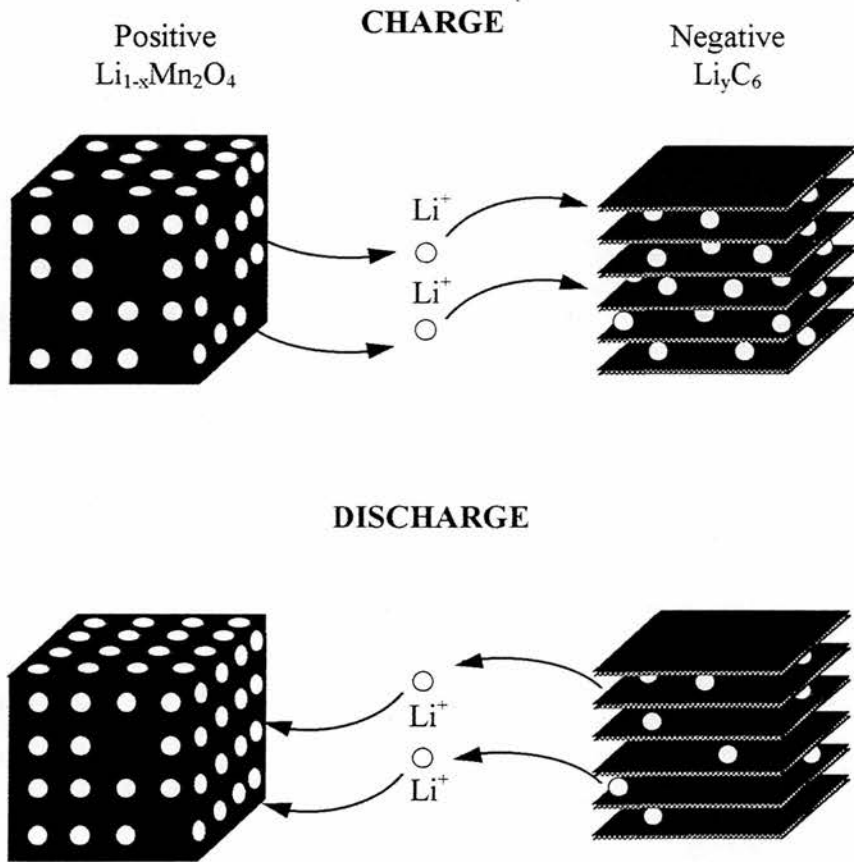


Figure 1-2 The charge and discharge mechanism for a Li-ion battery where both the cathode and anode are intercalation compounds.

The cell voltage is determined by the difference between the electrochemical potential of Li in the two intercalating electrodes.

1.5. Electrolytes

Lithium batteries may be fabricated using a range of lithium salts. The anion is chosen with consideration of the stability toward oxidation at the positive electrode, stability toward reduction at the negative electrode, solubility and dissociation tendency in the solvent. Solubility is an important factor, since high salt concentrations may be required to produce solutions of sufficient conductivity to maintain a cell at low internal cell resistance. The most widely used salts are LiClO_4 , LiPF_6 , LiBF_4 , LiAsF_6 and LiCF_3SO_3 . Ideally, the Li salt would be stable to reductive reaction with lithium, compatible with the chosen solvent and not decompose when heated to 180°C .

Purification of salts for use in lithium batteries is a matter of concern. Water is often present in a salt, and once introduced into the electrolyte solution it can react with the Li anode. LiPF_6 does not have either the toxicity problems of LiAsF_6 or the safety problems associated with LiClO_4 , however, it does suffer from poor thermal stability in its pure form, decomposing to PF_5 and LiF . The decomposition products can cause polymerisation of electrolytes of some commonly used non-aqueous solvents, resulting in cell failure. This is evidenced by the fact that no manufacturer of lithium cells use this highly conducting salt in their batteries.

Novel complexes of LiPF_6 , incorporating ether-oxygen or nitrogen coordinating ligands, have been prepared [34, 35] by the Associated Octel Company Ltd. The object of their preparative process is to provide a LiPF_6 electrolyte with a very low water content which does not use LiPF_6 as a starting material, and thus would not contain the impurities resulting from the decomposition of the unstable salt.

1.6. Solvent Systems

1.6.1. *Non-aqueous*

The solvents of interest in lithium battery systems must be aprotic. That is, there must be no labile or active hydrogen atoms since they will react with lithium to evolve hydrogen gas [6]. The main protic impurity in non-aqueous solvents is water which must be removed, leaving no more than trace levels. During charging the electrode potential can exceed +4V versus Li/Li^+ , a region where most non-aqueous solvents undergo oxidative decomposition [6] (Appendix 1). Organic esters such as ethylene carbonate and propylene carbonate are generally more stable than ether solvents. If gaseous products are formed at any time within a sealed battery, the pressure build-up will result in catastrophic failure.

As mentioned in section 1.5, the conductivity of the electrolyte solution must be sufficiently high. Consequently, the solvent must be capable of dissolving the chosen lithium salt to high concentration ($>0.5 \text{ mol dm}^{-3}$). The conductivity of a salt generally passes through a maximum on increasing salt concentration. This latter decrease in

conductivity has been interpreted [36] as a decrease in the ionic mobility due to increasing solution viscosity and the association of mobile ions to non-conducting ion-pairs. Optimum performance for practical lithium batteries can be obtained by using a mixed solvent system, containing a low viscosity solvent and a high permittivity solvent. Mixed solvent systems recently studied include 1,2-dimethoxyethane (DME) with propylene carbonate (PC) [37, 38] and DME/PC with tetrahydrofuran (THF) [37].

1.6.2. Polymer

Polymer electrolytes are ionically conducting phases formed by the dissolution of salts into suitable coordinating polymers [39]. An example of such a system is a Li salt complex of poly(ethylene oxide), PEO [40]. Figure 1-3 shows the helical structure of PEO where the ether oxygens coordinate to the Li^+ . The anions and hydrogens have been removed for clarity.

Extensive research into the development of rechargeable lithium batteries is ongoing due to the advantages they offer in comparison with conventional liquid systems. For example, polymer electrolytes can be manufactured into thin films with large surface areas giving high power levels ($>100 \text{ W dm}^{-3}$). Construction of all solid-state batteries can proceed in a variety of configurations, and be incorporated into devices such as cellular telephones, and thin smart credit cards.

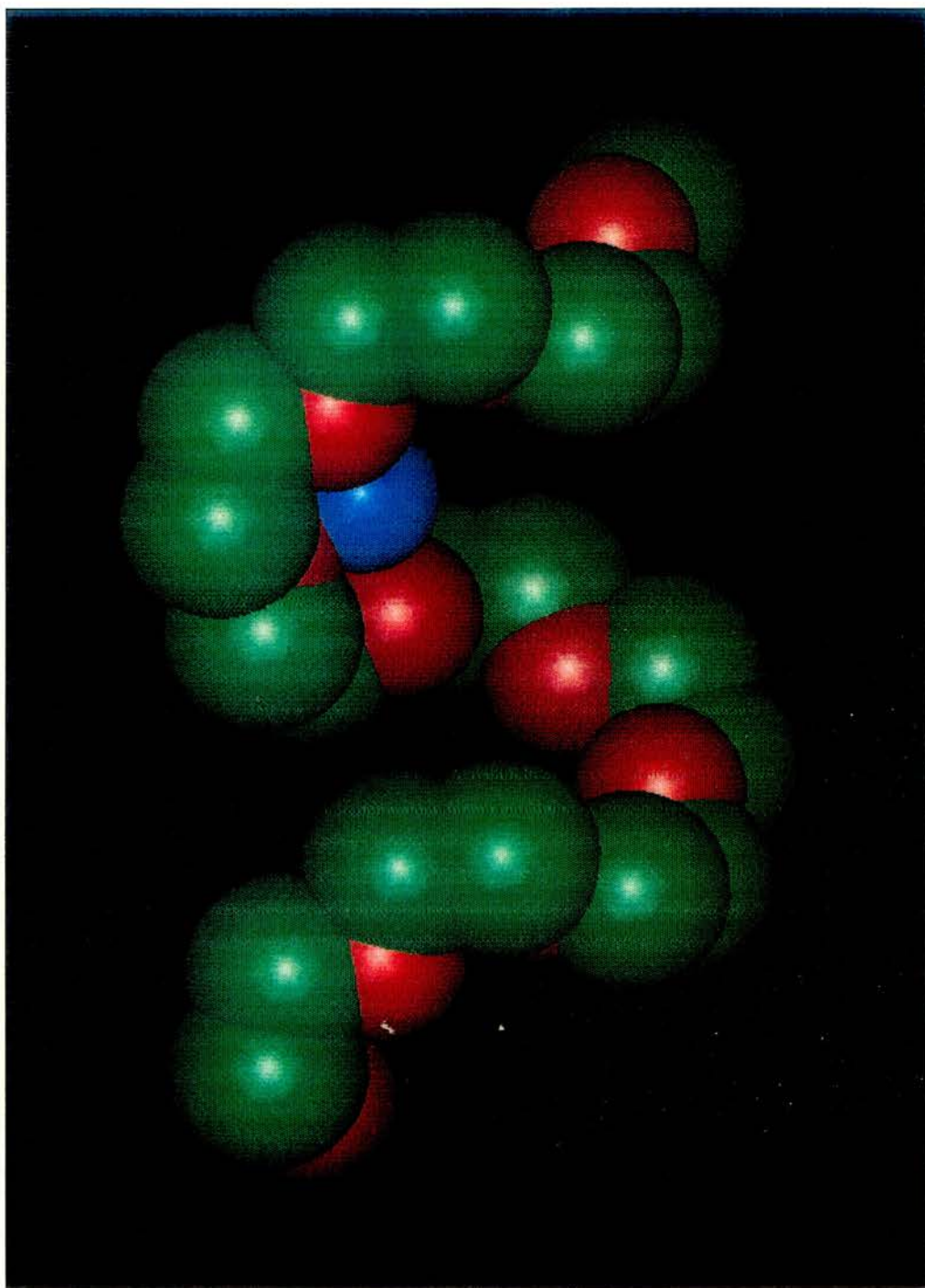


Figure 1-3 A Li^+ coordinated by ether oxygens of a poly(ethylene oxide) chain. The hydrogen atoms and anions have been removed for clarity. Each Li^+ is capable of further coordination by the anions.

Inter-cell leakage and self-discharge, associated with liquid electrolytes, are not encountered and the significant reduction in weight is realised as high energy and power densities.

The process by which net ionic motion takes place in polymer electrolytes is different from that in low molecular weight solvent-based systems, since long-range displacement of the solvent is not observed. Ionic transport occurs via local relaxation processes in the polymer chains which may provide liquid-like degrees of freedom [41]. Intra- and interpolymer transitions between ion coordinating sites, and segmental motion of the chains are believed to play a major role in the ion conduction mechanism. The polymer has similar macroscopic properties as a solid, due to chain entanglements or cross-linking.

High conductivity at ambient temperatures is of prime importance for any electrolyte system, but since the polymer electrolyte also acts as the separator between the cathode and anode, it must also possess good dimensional stability. The low ambient temperature conductivities of polymer electrolytes (ca. 10^{-8} - 10^{-9} Scm^{-1}) is largely the result of the low mobility of ions. Conductivities of the order of 10^{-3} Scm^{-1} , comparable with those of organic liquid electrolytes, are sought. However, it has been estimated that a conductivity of about 10^{-4} Scm^{-1} at room temperature is the limit of conventional polymer electrolytes [42].

1.6.3. Gel

Non-conventional polymer electrolytes with conductivities of $>10^{-3} \text{ Scm}^{-1}$ at room temperature can be obtained by immobilising high dielectric solvents containing lithium salts in a solid polymer matrix [43-47]. Examples of these *gel electrolytes* include a Li salt dissolved in propylene carbonate, incorporated into polyacrylonitrile (PAN) or poly(methyl methacrylate), (PMMA). Conductivities of some gel electrolytes (No. 1-5) are compared with conventional polymer electrolytes (No. 6) in Table 1-1. The PAN based electrolytes have two to six orders of magnitude higher conductivity than the long chain polymers such as PEO.

Table 1-1 Conductivities of PAN based polymer electrolytes compared to conventional PEO based electrolytes at 20°C. *Taken from ref.[21].*

Number	ELECTROLYTES	Ionic Conductivity Scm^{-1}
1	21 m% PAN/ 38 EC/ 33 PC/ 8 m% LiClO_4	1.7×10^{-3}
2	21 m% PAN/ 41 EC/ 35 PC/ 3 m% LiPF_6	1.4×10^{-3}
3	21 m% PAN/ 38 EC/ 33 PC/ 8 m% LiAsF_6	2×10^{-3}
4	21 m% PAN/ 40 EC/ 34 PC/ 5 m% LiCF_3SO_3	2×10^{-3}
5	21 m% PAN/ 41 EC/ 35 PC/ 3 m% $\text{LiN}(\text{SO}_2 \text{CF}_3)_2$	2×10^{-3}
6	PEO / $(\text{LiClO}_4)_{0.13}$	3.9×10^{-9}

m% represents mole percent

1.7. Aims of the Thesis

The novel Li salt complexes, containing either diglyme or pentamethyl diethylene-triamine, aim to show improved electrochemical performance in comparison with the “pure” salt. The work presented here focuses on a few of the aspects mentioned in the previous sections and attempts to assess the applicability of the complexes to real battery systems. The following areas of research have been investigated in polyether, propylene carbonate and poly(methyl methacrylate) gel media:

- ◆ Ionic conductivities, providing information on relative power outputs of each electrolyte and the effects of the ligands on ion association;
- ◆ Kinetics of the Li/Li^+ couple at a Ni electrode/electrolyte interface;
- ◆ Mechanisms for the nucleation and growth of lithium metal centres at a Ni electrode surface during the plating process;
- ◆ Lithium cycling efficiencies by potentiostatic and galvanostatic methods;
- ◆ Electrochemical stabilities of ligands and solvents;
- ◆ Computer modelling of ion association in media of high and low permittivity.

REFERENCES

1. *Modern Batteries*, C.A. Vincent, Edward Arnold (publisher), London (1984).
2. A.F. Sammells, *J. Chem. Ed.*, 60, 320 (1983).
3. M. Hayes, *Chem. Brit.*, 22, 1101 (1986).
4. A.J. Appleby and F.R. Foulkes, *Fuel Cell Handbook*, Kreiger, Malabar (1993).
5. K.B. Prater, *J. Power Sources*, 51, 129-144 (1994).
6. *Lithium Batteries* (Edited by J.P. Gabano), Academic Press, London and New York (1983).
7. Y. Geronov, F. Schwager and R.H. Muller, *J. Electrochem. Soc.*, 129(7), 1422-1429 (1982).
8. G. Nazri and R.H. Muller, *ibid*, 132(9), 2054-2058 (1985).
9. D. Aurbach, M.L. Daroux, P.W. Faguy and E. Yeager, *ibid* 134(7), 1611-1620 (1987).
10. D. Aurbach and H. Gottlier, *Electrochimica Acta*, 34(2), 141-156 (1989).
11. D. Fauteux, *ibid*, 38(9), 1199-1210 (1993).
12. D. Aurbach, Y. Ein-Ely and A. Zabin, *J. Electrochem. Soc.*, 141(1), L1-L3 (1994).
13. J.A.R. Stiles in *Practical Lithium Batteries* (Edited by Y. Matsuda and C.R. Schlaikjer), JEC Press, USA (1988).
14. W.F. Meyers, B. Bell and J.W. Simmons, *US Patent No. 3423242* (1969).
15. D.L. Maricle, J.P. Mohns, *US Patent No. 3567515* (1971).
16. D.W. Murphy and J.N. Carides, *J. Electrochem. Soc.*, 126, 349 (1979).
17. M. Lazzari and B. Scrosati, *ibid*, 127, 773 (1980).

18. M. Armand in *Materials for Advanced Batteries* (Edited by D.W. Murphy, J. Broadhead and B.C.H. Steele), Plenum Press, New York (1980).
19. J.M. Tarascan and D. Guyomard, *Electrochimica Acta*, 38(9), 1221-1231 (1993).
20. Z. Takehara and K. Kanamura, *ibid*, 38(9), 1169-1177 (1993).
21. K.M. Abraham, *ibid*, 38(9), 1233-1248 (1993).
22. D. Fouchard and L. Lechner, *ibid*, 38(9), 1193-1198 (1993).
23. K.M. Abraham, D.M. Pasquariello and E.B. Willstaedt, *J. Electrochem. Soc.*, 137, 1856 (1990);
U.S. Patent No. 4857423;
European Patent No. 0319182.
24. T. Nohua, T. Saito, N. Furukawa and H. Ikeda, *J. Power Sources*, 26, 389 (1989).
25. T. Nohua, T. Saito, I. Nakare and N. Furukawa, *J. Power Sources*, 26, 389 (1989).
26. K. Mizushima, P.C. Jones, P.J. Wiseman and J.B. Goodenough, *Mat. Res. Bull.*, 15, 783 (1980).
27. H. Huang and P.G. Bruce, *J. Electrochem. Soc.*, 141(7), L76 (1994);
H. Huang and P.G. Bruce, *ibid*, 141(9), L106 (1994);
H. Huang and P.G. Bruce, *in-press*.
28. D.M. Pasquariello, K.M. Abraham, E.B. Willstaedt, D.H. Shen and S. Surampudi, *Fall Meeting of the Electrochem. Soc.*, Toronto, Canada, Abstract No.46, October (1992).
29. K.M. Abraham, D.M. Pasquariello and E.B. Willstaedt, *ibid*, 137, 743 (1990).

30. B. Di Pietro, M. Patriarca and B. Scrosati, *J. Power Sources*, 8, 289n (1982).
31. J.J. Auburn and Y.L. Barberio, *J. Electrochem. Soc.*, 134, 638 (1987).
32. J.R. Dahn, U. Von Sacken, M.W. Juzkow and H. Al-Janaby, *ibid*, 138, 2207 (1991).
33. J.R. Dahn, R. Fong and M.J. Spoon, *Phys Rev. B*, 42, 6424 (1990).
34. Duracell Inc., Improved method for preparing non-aqueous electrolytes, *European Patent Application No. 90302078.2* (Sept. 1990).
35. The Associated Octel Company Ltd., Lewis base complexes of alkali metal salts, *European Patent Application No. 88309913.7* (Oct. 1988).
36. *Electrolyte Solutions* (Edited by R.A. Robinson and R.H. Stokes), Butterworths, London, 2nd ed. (1965).
37. D. Yunchang, X. Guanguang and C. Jianguo, *J. Power Sources*, 34, 189 (1991).
38. M. Ishikawa, S. Wen and Y. Matsuda, *ibid*, 45, 229 (1993).
39. C.A. Vincent, *Pro. Solid State Chem.*, 17, 145 (1987).
40. *Polymer Electrolyte Reviews*, vols. 1 & 2 (Edited by C.A. Vincent and J.R. MacCallum), Elsevier Applied Science, London and New York (1987).
41. *Solid Polymer Electrolytes*, F.M. Gray, VCH, New York (1991).
42. K.M. Abraham in *Applications of Electroactive Polymers* (Edited by B. Scrosati), Chapman and Hall, London (1993).
43. O. Bohnke, G. Frand, M. Rezrazi, C. Rousselot and C. Truche, *Solid State Ionics* 66, 97-104 (1993).
44. O. Bohnke, G. Frand, M. Rezrazi, C. Rousselot and C. Truche, *ibid*, 66, 105-112 (1993).

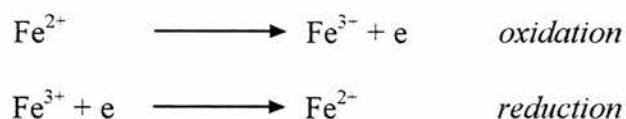
45. K.M. Abraham and M. Alamgir, *J. Power Sources*, 43-44, 195-208 (1993).
46. R. Xue, H. Huang, M. Menetrier and L. Chen, *ibid*, 43-44, 431-438 (1993).
47. G. Dautzenberg, F. Croce, S. Passerini and B. Scrosati, *Chem. Mater.*, 6, 538-542 (1994).

CHAPTER TWO

Electrochemical Theory and Methodologies

2.1. Electrode Processes

An electrode reaction is a heterogeneous process involving transfer of electrons to or from a surface. The electrode reaction may involve oxidation of a species by the loss of electrons to the electrode or reduction of a species by gain of electrons from the electrode. For example,



Electrode reactions are extremely diverse since the electroactive species can be organic or inorganic, neutral or charged, the solvent itself, films formed on the electrode surface, or even the electrode material.

2.1.1. Electron Transfer

Consider the simple electrode reaction which takes place at an inert surface:



where the two species, O and R , are completely stable and soluble in the solvent medium which generally contains an excess of an electroinactive electrolyte. A minimum of three steps occur:



and the rate of reduction, and hence cathodic current, is determined by the rate of the slowest step. The electron transfer may consist of a number of steps, particularly if $n > 1$.

The equilibrium potential of the electrode is given by the *Nernst equation*:

$$E_e = E_e^\ominus + \frac{RT}{nF} \ln \frac{c_O^\sigma}{c_R^\sigma} \quad 2-5$$

where E_e is the equilibrium potential, E_e^\ominus the standard potential of the couple O/R , and c_O^σ and c_R^σ are the surface concentrations of O and R , respectively. From eqn. 2-5, it is seen that the standard potential is equal to the equilibrium potential when the surface concentrations of O and R are equal.

While no net current is flowing and there is no overall chemical change at the electrode, the rate of reduction of O and the oxidation of R in the dynamic equilibrium at the surface of the electrode will be equal. Thus,

$$-\vec{I} = \overleftarrow{I} = I_0 \quad 2-6$$

where I_0 is defined as the exchange current density, \vec{I} and \overleftarrow{I} are the partial current densities for the forward and reverse reactions, respectively. The negative sign reflects the IUPAC convention [1] that a cathodic current is negative and anodic current is positive.

At any non-equilibrium potential, the measured current density is given by

$$I = \vec{I} + \overleftarrow{I} \quad 2-7$$

The partial current densities are dependent on their individual rate constants and the concentration of the electroactive species at the electrode surface, such that

$$\vec{I} = -nF \vec{k} c_O^\sigma \quad \text{and} \quad \overleftarrow{I} = nF \overleftarrow{k} c_R^\sigma \quad 2-8$$

The rate constants are usually found to vary with the applied electrode potential E according to the equations [2]:

$$\vec{k} = \vec{k}_0 \exp\left\{-\frac{\alpha_C nF}{RT} E\right\}$$

and $\overleftarrow{k} = \overleftarrow{k}_0 \exp\left\{\frac{\alpha_A nF}{RT} E\right\}$ 2-9

where α_C and α_A are the electron transfer coefficients for the anodic and cathodic processes, respectively. k_0 is the rate constant for the anodic or cathodic reactions at 0 V versus the reference electrode, where $\vec{k}_0 = -\overleftarrow{k}_0$. For a simple process $\alpha_A + \alpha_C = 1$.

The *overpotential*, η , is defined as the deviation of the potential E at the working electrode (the electrode at which the reaction of interest is occurring) from the equilibrium value E_e such that

$$E = \eta + E_e \tag{2-10}$$

Substituting eqns. 2-8 and 2-9 into eqn. 2-7 gives

$$I = nF \overleftarrow{k}_0 \exp\left(\frac{\alpha_A nF(\eta + E_e)}{RT}\right) c_R^\sigma - nF \vec{k}_0 \exp\left(-\frac{\alpha_C nF(\eta + E_e)}{RT}\right) c_O^\sigma \tag{2-11}$$

Using eqn. 2-6, the exchange current density at equilibrium is:

$$\begin{aligned}
I_0 &= nF k_0^{\leftarrow} \exp\left(\frac{\alpha_A nF E_e}{RT}\right) c_R^{\sigma} \\
&= nF k_0^{\rightarrow} \exp\left(-\frac{\alpha_C nF E_e}{RT}\right) c_O^{\sigma}
\end{aligned}
\tag{2-12}$$

Rearranging eqn. 2-11 using the expression $\exp(x) \exp(y) = \exp(x+y)$, then upon inserting of eqn. 2-12 the empirical *Butler-Volmer* equation [3] is obtained:

$$I = I_0 \left\{ \exp\left(\frac{\alpha_A nF}{RT} \eta\right) - \exp\left(-\frac{\alpha_C nF}{RT} \eta\right) \right\}
\tag{2-13}$$

This shows how the current density varies with exchange current density, overpotential and the transfer coefficients. Although eqn. 2-13 is a general expression, it is more practical to use a limiting form.

2.1.2. Very Low Overpotentials

At very low values of overpotential, where $\left(\frac{RT}{\alpha_A nF} \gg \eta \ll \frac{RT}{\alpha_C nF}\right)$, the exponential terms of eqn. 2-13 can be expanded as a series. The quadratic and higher order terms are negligible so that the Butler-Volmer equation reduces to

$$I = I_0 \left\{ \frac{\alpha_A nF}{RT} \eta + \frac{\alpha_C nF}{RT} \eta \right\}
\tag{2-14}$$

Since $\alpha_A + \alpha_C = 1$, eqn. 2-14 can be reduced further to give

$$I = I_0 \left(\frac{nF}{RT} \eta \right) \quad 2-15$$

2.1.3. High Overpotentials: The Tafel Equations

At high positive overpotentials the rate of the anodic reaction $|\vec{I}|$ is much greater than the rate of the cathodic reaction $|\overleftarrow{I}|$, and the second term in the Butler-Volmer equation may be ignored. The anodic current density can then be given by

$$\ln(I) = \ln(I_0) + \left(\frac{\alpha_A nF}{RT} \eta \right) \quad 2-16$$

Conversely, at high negative overpotentials the rate of the cathodic reaction $|\overleftarrow{I}|$ is much greater than the rate of the anodic reaction $|\vec{I}|$, and the cathodic current density is given by

$$\ln(-I) = \ln(I_0) - \left(\frac{\alpha_C nF}{RT} \eta \right) \quad 2-17$$

These limiting forms of the Butler-Volmer equation at high overpotentials are known as the *Tafel equations* and provide a method for determining the exchange current density and transfer coefficients. A plot of $\ln(I)$ versus η for a simple system is of the general form shown in Figure 2-1. At large overpotentials the Tafel equations are

valid, revealing straight lines. The transfer coefficients may then be obtained from the gradients of the plot in the cathodic and anodic regions. Extrapolation of these linear regions back to the equilibrium potential yields the exchange current density.

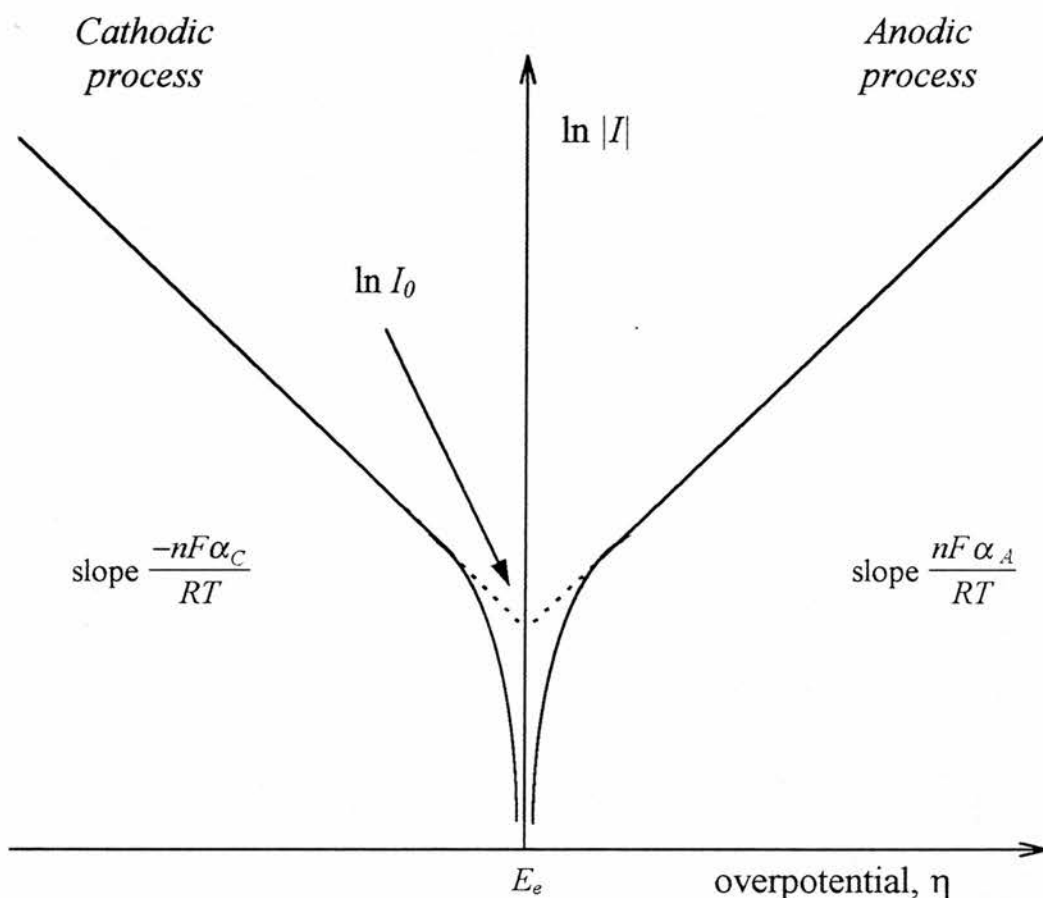


Figure 2-1 Experimental determination of the kinetic constants, I_0 and α , using the Tafel equations.

The exchange current density, however, varies with the concentrations of O and R at the surface of the electrode. Through manipulation of eqns. 2-5 and 2-12, the

standard rate constant for the electron transfer at the standard potential, E^θ , is defined as

$$k^\theta = \frac{I_0}{nF(c_O^\infty)^{\alpha_A}(c_R^\infty)^{\alpha_C}} \quad 2-18$$

which is independent of O and R . The I - E characteristic is now specified completely by k^θ and a transfer coefficient.

2.2. Mass Transport

In electrochemical systems there are essentially three modes of transport to consider [2]. *Diffusion* is the natural movement of species through solution down a concentration (or more correctly, activity) gradient, without the effects of the electric field. Movement of charged species, due to a potential field, is termed *migration* and is the method by which charge passes through an electrolyte. Mechanical forces acting on the solution, such as stirring, are all forms of forced *convection*.

2.2.1. Diffusion Control

Since diffusion is independent of the electric field, the transported species can be charged or neutral. The rate of diffusion depends on the concentration gradients defined by *Fick's first law*. This states that the rate of diffusion, or flux, of a species i through a plane parallel to the electrode surface is given by

$$J_i = -D_i \frac{dc_i}{dx} \quad 2-19$$

where J_i is the flux of the species i , D_i the diffusion coefficient and dc/dx the concentration gradient in direction x towards a planar surface.

2.2.2. Diffusion to a Planar Electrode

Fick's first law can be used to relate the current density to the chemical change at the electrode surface, $x = 0$, by equating the flux of species O and R with the flux of electrons, such that

$$\frac{I}{nF} = -D_O \left(\frac{dc_O}{dx} \right)_{x=0}$$

or

$$\frac{I}{nF} = D_R \left(\frac{dc_R}{dx} \right)_{x=0} \quad 2-20$$

If a system initially containing O but no R is stepped from the equilibrium potential, E_e , to a potential well negative, the surface concentration of O will change from c_O^∞ to a small value as determined by the Nernst equation (eqn. 2-5). Diffusion then takes place to minimise the differences in concentration, resulting in the relaxation of the concentration profiles towards their steady state. Figure 2-2 shows how the concentration profiles for the species O and R develop with time.

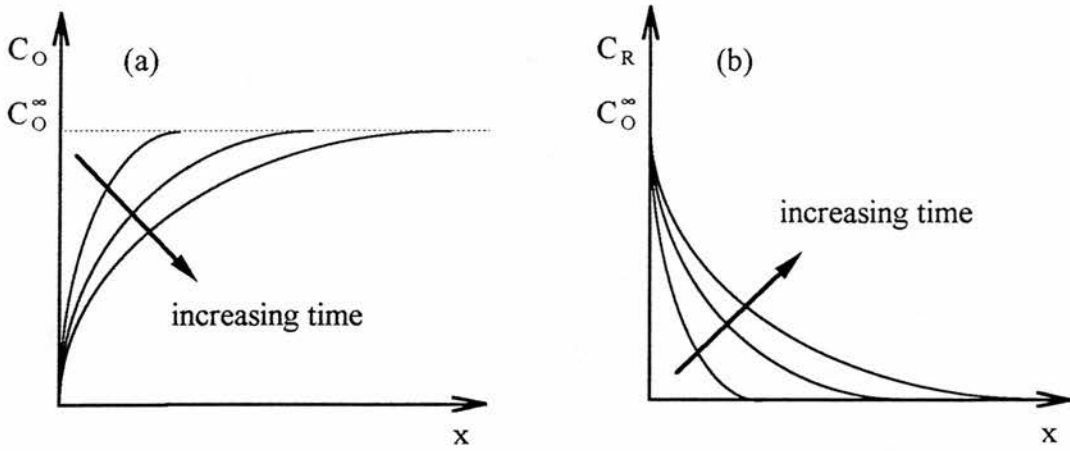


Figure 2-2 Concentration profiles for the potential step experiment initially with O but no R at a potential where the process is diffusion controlled.

The change in concentration with time is given by *Fick's second law*,

$$\frac{\partial c_i}{\partial t} = D_i \frac{\partial^2 c_i}{\partial x^2} \quad 2-21$$

which must be solved to obtain the complete form of the transient using the relevant boundary conditions describing the particular potential step experiment, ie.

at $t = 0$,	$c_O = c_O^\infty$	for all x	(no electrode reaction)
at $t > 0$,	$c_O = c_O^\infty$	at $x = \infty$	(bulk solution)
	$c_O^s = 0$	at $x = 0$	(limiting diffusion current)

Applying the *Laplace transform* [2] to eqn. 2-21, with respect to t , leads to

$$I(t) = \frac{nF D^{1/2} c_0^\infty}{\pi^{1/2} t^{1/2}}$$

2-22

This expression is known as the *Cottrell equation* [4] and is the exact form of the $I-t$ transient, assuming linear diffusion to a planar electrode surface. Figure 2-3 shows the shape of the transient described by eqn. 2-22.

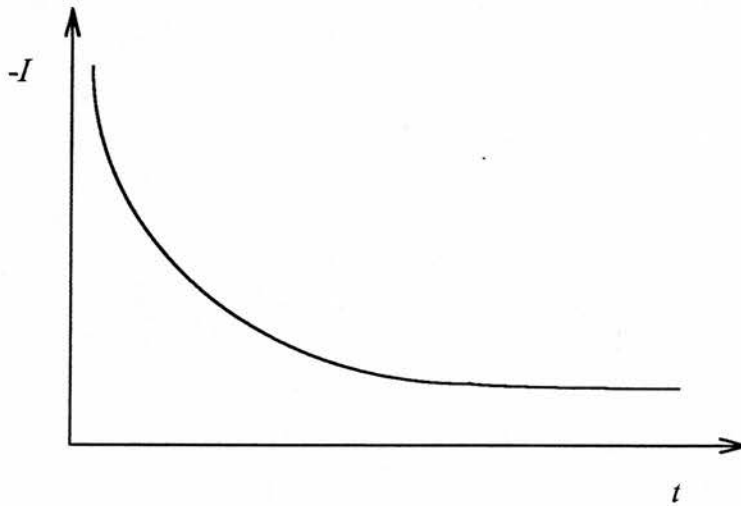


Figure 2-3 Variation of current with time according to the Cottrell equation.

2.2.3. Microelectrodes

At a spherical electrode of radius r_0 , the relevant diffusion equation is

$$\frac{\partial c_i}{\partial t} = D_i \left\{ \frac{\partial^2 c_i}{\partial r^2} + \frac{2\partial c_i}{r\partial r} \right\} \quad 2-23$$

with boundary conditions:

at $t = 0,$	$r \geq r_0$	$c_O = c_O^\infty$	(no electrode reaction)
at $t > 0,$	$r = \infty$	$c_O = c_O^\infty$	(bulk solution)
	$r = r_0$	$c_O^s = 0$	(limiting diffusion current)

Applying the same method of solution as for eqn. 2-22, we obtain

$$I(t) = \frac{nF D^{1/2} c_O^\infty}{(\pi t)^{1/2}} + \frac{nFD c_O^\infty}{r_0} \quad 2-24$$

This is the Cottrell equation plus a spherical correction term. At short times the spherical contribution is negligible (eqn. 2-24 then reduces to eqn. 2-22) and diffusion to a sphere can be treated as linear diffusion. At long times the spherical term becomes dominant leading to a time-independent steady-state current. Due to the effects of natural convection the steady-state is never reached at conventional sized electrodes, but the smaller the electrode radius, the more easily and faster the steady-state is achieved.

The limiting diffusion current for spherical and hemispherical microelectrodes follows directly from eqn. 2-24. Thus, after a certain time depending on the electrode size, a steady-state is reached, and the current density is given by

$$I = \frac{nFD c_O^\infty}{r_0} = 2\pi nF r_0 D c_O^\infty = 2nF d D c_O^\infty \quad 2-25$$

where d is defined as the surface length, equal to $2\pi r_0$. In general for microelectrodes, the current density is sufficiently high, due to the high rate of diffusion, that interference from natural, or even forced, convection is negligible.

For a micro-disc electrode, the effects of radial diffusion must be considered due to the non-uniform accessibility of the surface. The relevant equation is

$$\frac{\partial c_i}{\partial t} = D_i \left\{ \frac{\partial^2 c_i}{\partial r^2} + \frac{\partial c_i}{r \partial r} + \frac{\partial^2 c_i}{\partial x^2} \right\} \quad 2-26$$

which does not have an exact solution. Numerical analysis, however, shows that at long times the current is equal to that of a hemisphere of radius $a = \pi r_0/2$, such that

$$I = 4nFaD c_{\infty}^{\circ} = 2nFdD c_{\infty}^{\circ} \quad 2-27$$

where the d is once again the surface length, equal to $2a$. Here, the current density is the same as that of the hemispherical electrode. This, and the similarity between eqns. 2-23 and 2-26, indicates that the simpler model of the hemisphere can be applied to the more easily manufactured disc, without significant error.

2.3. Electrodeposition

The electrodeposition of a metal involves several steps [2]. The first step involves mass transport, ie. the movement of the ionic species from the bulk solution to the

electrode. This involves movement of the metal ion through the solvent medium and is therefore affected by a number of factors including the solution viscosity, the nature of the solvation sheath surrounding the ion and temperature. Charge transfer from the electrode to the ion then takes place, altering its solvation environment such that there is partial or complete loss of the solvation sheath, forming an *ad-atom*. It is known that small centres with a high surface area to volume ratio are thermodynamically unstable [5] and will tend to dissolve back into solution. An ad-atom must diffuse across the surface to an energetically favourable site, followed by clustering of other atoms of the electrodeposit to form the stable nucleus of a new phase. A schematic of this process is shown in Fig. 2-4. This process is more favourable when a large overpotential is applied which provides a large concentration of adsorbed metal ions.

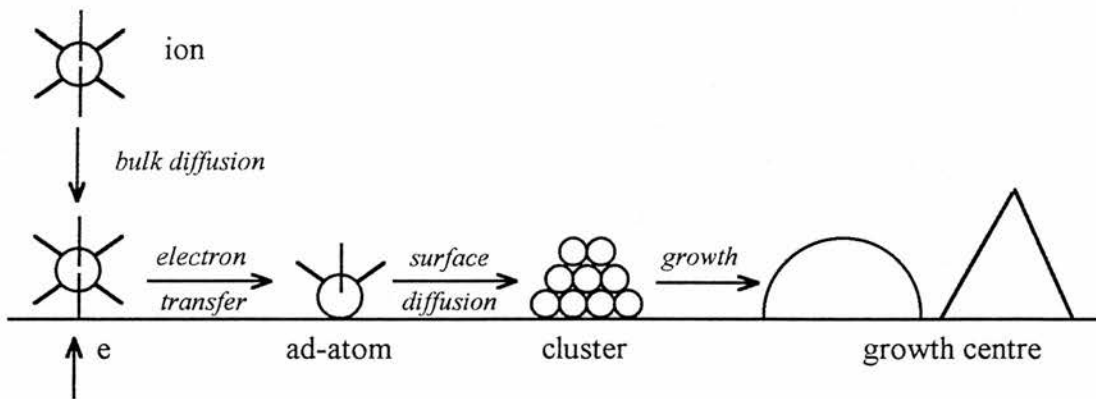


Figure 2-4 Schematic representation of the electrocrystallisation process of a metal on a foreign substrate.

The continued growth of nuclei of electrodepositing metals or electrochemically formed oxides can only take place by a faradaic process and the observed current is

therefore an exact measure of the combined rate of nucleation and growth of the mature nuclei or crystallites. A variety of current-potential-time responses can be explored and any particular experiment can be repeated to give the mean values and statistical variance of the results. Analysis of the current transients over both short and long periods can yield information on the kinetics and the form of the nucleation and growth.

2.3.1. *Nucleation and Growth of Monolayers*

The growth of metals on inert substrates such as carbon and the formation of anodic films, for example during corrosion, involve the formation of a new phase as the initial step. In general, the growth of the deposit involves disc-shaped centres one atom or one molecule thick. These growth centres expand to form a monolayer across the surface of the electrode. Successive monolayer formation can occur by the nucleation of new growth centres on the freshly formed surface.

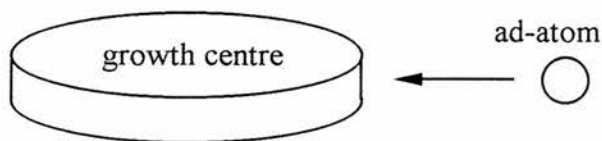


Figure 2-5 Incorporation of ad-atoms at the periphery of the expanding 2-D growth centre.

This process is referred to as two-dimensional electrocrystallisation. A detailed theoretical description of the current transients was given by Fleischmann and Thirsk [5].

2.3.2. *Nucleation and Growth of Three-Dimensional Centres*

The electrocrystallisation of a new phase on a foreign substrate often involves the nucleation and growth of three-dimensional centres which grow not only parallel to the surface, as with monolayer formation, but also perpendicular to the surface. The shapes of such growth centres are more complex, but by assuming them to be based on simple geometries expressions for the current transient may be found.

2.3.2.1. *Diffusion Controlled Growth*

The principal nature of the current transient is the rising section corresponding to the growth of the electroactive area either as each nucleus grows and/or the number of new nuclei increases. When the number of active sites on the surface of the substrate is not large and thereby limits the total number of nuclei, the steady-state rate of nucleation is described by the relation [5, 6]

$$N(t) = N_{\infty} \{1 - \exp(-A N_{\infty} t)\} \quad 2-28$$

where N is the number of nuclei, t is the time and A is the steady-state nucleation rate constant per site, discussed elsewhere [6] and known to be a function of overpotential, solution composition and substrate surface free energy.

At high values of A or t it can be seen that $dN/dt \rightarrow 0$ and that N approaches N_{∞} , the maximum number of nuclei obtainable under the imposed conditions. N_{∞} may be thought of as the total number of available sites at the electrode surface. But, as will be shown, the final number of nuclei is more often controlled by other factors, in particular by the effect of overlapping diffusion zones.

The charge transfer rate for most metal deposition reactions is sufficiently high for the continued growth of established or mature nuclei to be mass transport controlled. Under conditions of mass transport control the current density for a fixed number of nuclei, N , growing by a hemispherical diffusive flux is [7]

$$I(t) = \frac{zF\pi(2Dc)^{3/2} M^{1/2} N t^{1/2}}{\rho^{1/2}} \quad 2-29$$

where zF is molar charge of the depositing species, D is its diffusion coefficient, c its concentration in mol cm^{-3} , M its relative molar mass and ρ its density. Crystallite morphologies other than hemispherical have been observed [5], but because the depletion zones around growing crystallites advance radially more rapidly than the perimeters of the crystallites themselves, the mass transfer flux assumes hemispherical properties. The depletion zones are also referred to as diffusion zones of diffusion

fields. In previous treatments of multiple nucleation, the assumption has been made that nuclei grow independently of each other, and that well before the current maximum, the total current could be identified with the sum of individual currents. However, microscopic observation and current studies [8, 9] of the electrode surface indicate a significant difference between the rate of growth of N crystallites and that predicted by the independent growth model.

The overlap of neighbouring depletion zones is responsible for the current maxima observed in diffusion controlled systems. Scharifker, *et al* [8, 9] considered a set of hemispherical nuclei randomly distributed on the electrode surface and growing under diffusion control. A hemispherical diffusion zone develops from each and grows outwards at a radial velocity such that its radius δ is given by

$$\delta(t) = (kDt)^{1/2} \qquad 2-30$$

where k is a numerical constant determined by the conditions of the experiment. At short times, the current will be given by eqn. 2-29 but as the radii of the diffusion zones grow and begin to overlap, replacement of material in the planes close to the electrode surface becomes restricted and eventually the only source of depositing material is that reaching the electrode perpendicularly, as shown in Figure 2-4. The corresponding diffusive flux and growth current can then be expressed in terms of semi-infinite linear diffusion to that fraction of the electrode within the circular perimeter of the growing diffusion zone. The planar area of a single diffusion zone at time t can be expressed as

$$S(t) = \pi \delta^2(t) = \pi kDt \quad 2-31$$

If immediately following time $t = 0$, N centres were instantaneously nucleated per unit area, then at a later time t

$$\theta_{ex} = N\pi kDt \quad 2-32$$

where θ_{ex} is the fraction of the area covered by diffusion zones assuming that none overlap. However, because the nuclei are randomly distributed on the electrode surface there will be overlap and the actual fraction of area covered, θ , can be related to θ_{ex} by the *Avrami theorem* [10], ie.

$$\theta = 1 - \exp(-\theta_{ex}) \quad 2-33$$

so that from eqn. 2-32

$$\theta = 1 - \exp(-N\pi kDt) \quad 2-34$$

and the radial flux density of electroactive material through the boundaries of the diffusion zones will be given by the equivalent planar diffusive flux to an electrode of fractional area θ .

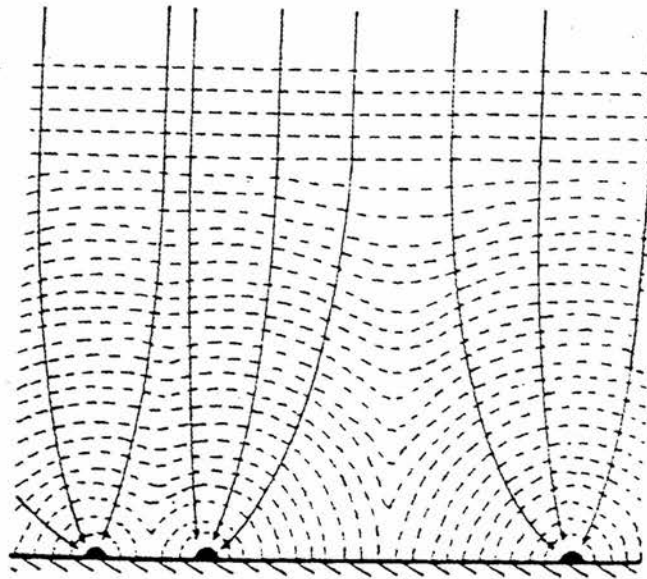


Figure 2-4 Schematic representation of the growth of the diffusion zones and their eventual overlap. The arrows indicate the directions of the diffusional field during the growth of the nuclei.

Conservation of mass requires that the amount of material entering into the diffusion zones is equal to the amount incorporated into the growing nuclei. The current density to the electrode surface is therefore

$$I = \frac{zF D^{1/2} c \theta}{\pi^{1/2} t^{1/2}} = \frac{zF D^{1/2} c}{\pi^{1/2} t^{1/2}} \{1 - \exp(-N\pi kDt)\} \quad 2-35$$

At very short times $N\pi kDt \ll 1$ and $\{1 - \exp(-N\pi kDt)\} \cong N\pi kDt$. Thus, as $Nt \rightarrow 0$ eqn. 2-35 becomes

$$I_{Nt \rightarrow 0} = zF D^{3/2} \pi^{1/2} cNk t^{1/2} \quad 2-36$$

which is identical to the current flowing to N isolated hemispherical nuclei [7]. Comparing eqn. 2-36 with the expression defining the sum of currents flowing to individual nuclei, we see that k is defined as

$$k = \left(\frac{8\pi cM}{\rho} \right)^{1/2} \quad 2-37$$

By a similar working, if nucleation is progressive then $N(t) = AN_{\infty}t$ and

$$I = \frac{zF D^{1/2} c}{\pi^{1/2} t^{1/2}} \left\{ 1 - \exp\left(\frac{-AN_{\infty}\pi k' D t^2}{2} \right) \right\} \quad 2-38$$

and k' is evaluated by taking the limit $AN_{\infty}t \rightarrow 0$ and comparing it again with the independent model, where the current density varies with $t^{3/2}$. For progressive nucleation, k' is then defined as

$$k' = \frac{4}{3} \left(\frac{8\pi cM}{\rho} \right)^{1/2} \quad 2-39$$

The equations 2-35 and 2-38 describe the extended current transient for 3D instantaneous and progressive nucleation followed by diffusional controlled growth, respectively. Simulated current transients are shown in Fig. 2-5 (a) and (b). In each case the current passes through a maximum before approaching the limiting diffusion current to a planar electrode.

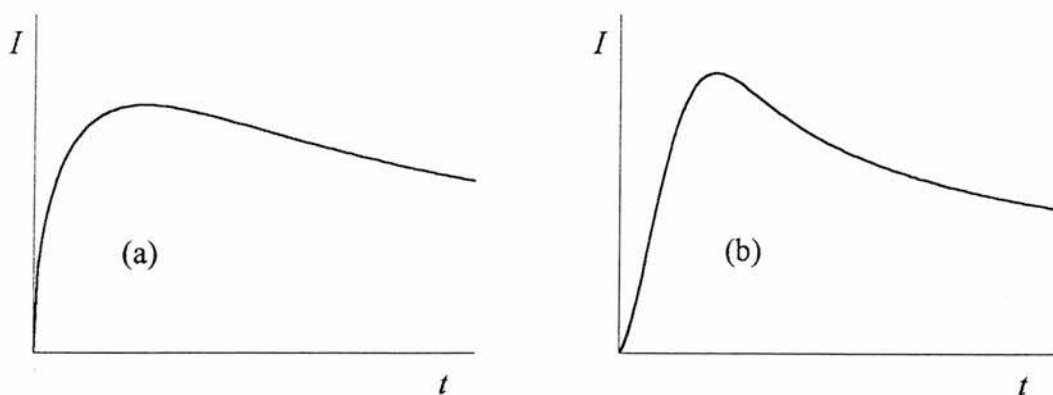


Figure 2-5 3D diffusion controlled growth following (a) instantaneous nucleation and (b) progressive nucleation.

A typical set of experimental current transients is shown in Fig. 2-6, closely resembling the curves predicted by the theoretical expressions of Scharifker.

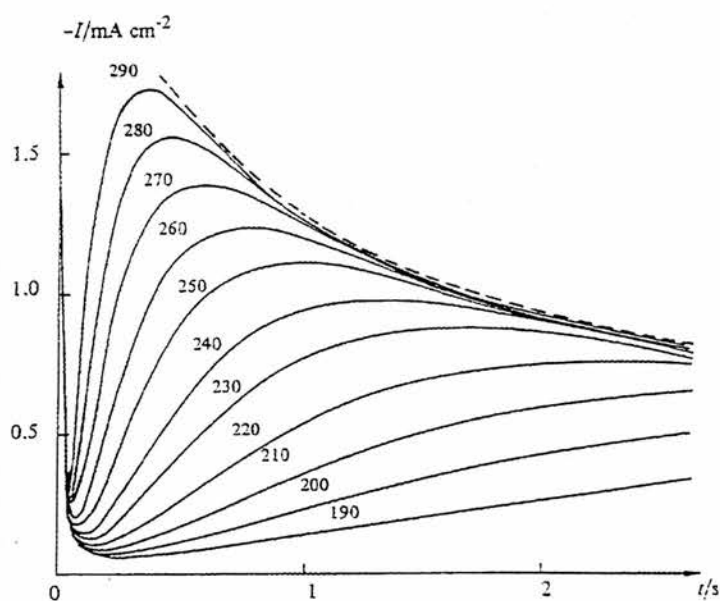


Figure 2-6 $I-t$ response for the electrodeposition of mercury onto vitreous carbon from $\text{Hg}_2(\text{NO}_3)_2$ solution at varying overpotentials indicated in mV. From ref. [9].

2.3.2.1. Kinetic Controlled Growth

If a right-circular cone can be taken as an example of a 3-D centre, then growth parallel to the surface takes place with a rate constant k_3 , and that perpendicular to the surface with rate constant k_3' . The total current into the growing cone is obtained by integration of the individual contributions of a stack of discs which build the cone.

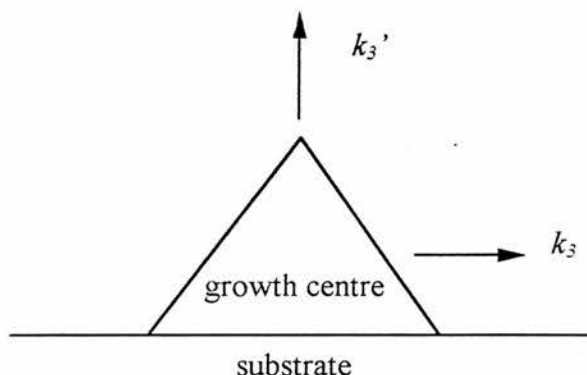


Figure 2-7 Growth of a three-dimensional centre: the right circular cone.

When a number of discrete growing centres interact, their overlap must be taken into account, and the expressions representing the current transient are given as [2, 5]

$$I = nF k_3' \left\{ 1 - \exp\left(\frac{-\pi M^2 k_3^2 N_\infty t^2}{\rho^2}\right) \right\} \quad 2-40$$

for instantaneous nucleation, and

$$I = nF k_3' \left\{ 1 - \exp\left(\frac{-\pi M^2 k_3^2 A t^3}{3\rho^2}\right) \right\} \quad 2-41$$

for progressive nucleation. The general behaviour of the transients can be seen in Fig. 2-8. At short times the exponential terms are small such that the rising current densities vary with t^2 and t^3 , respectively. At long times a plateau approaching nFk_3' is reached in each case, since thickening of the layer is restricted to growth perpendicular to the electrode surface.

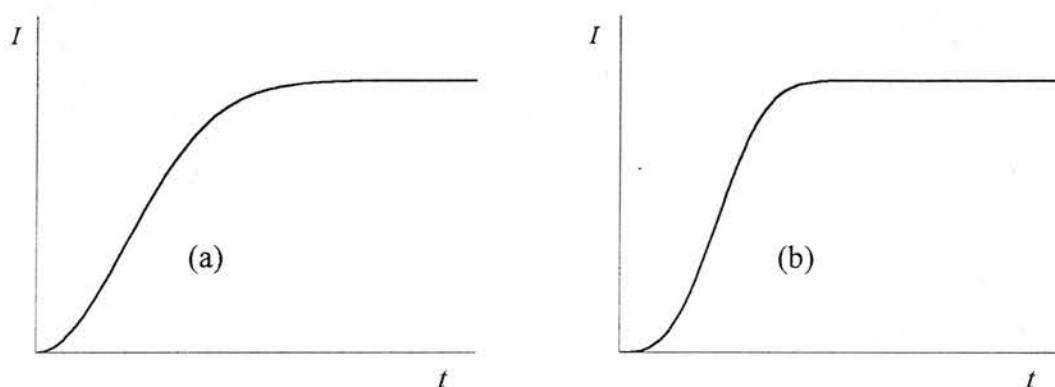


Figure 2-8 3-D kinetic controlled growth following (a) instantaneous nucleation and (b) progressive nucleation.

Other geometries have been considered using a similar approach by Abyaneh [11], Bosco & Rangarajan [12] and Abyaneh & Fleischmann [13].

2.4. Cyclic Voltammetry

Cyclic voltammetry is a very powerful technique for the probing of electroactive species, and is particularly useful in the initial studies of a new system. Many experiments can be carried out within a few minutes, and the results are presented in a form which can rapidly be analysed in a qualitative manner. Quantitative analysis

can also be performed, yielding kinetic parameters. The theory and practice of cyclic voltammetry is described extensively in the literature [2, 14].

The $E-t$ waveform used in cyclic voltammetry is shown in Figure 2-9. The potential of the working electrode, controlled against the reference electrode, is swept from a starting potential E_1 to a second potential at E_2 .

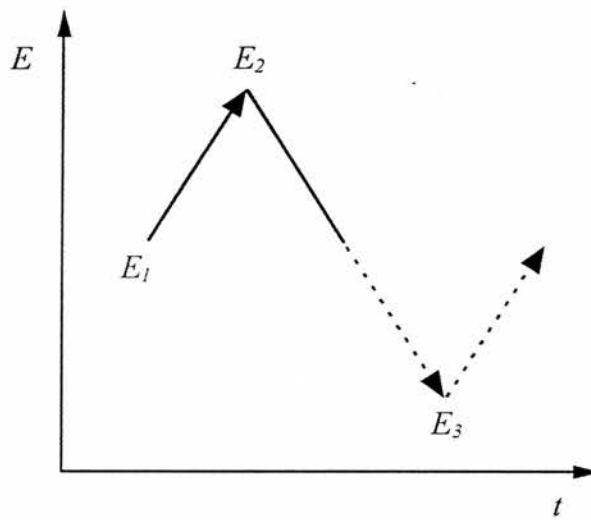


Figure 2-9 A possible potential-time profile used in cyclic voltammetry.

On reaching E_2 the sweep is reversed and the electrochemical characteristics of the products and/or intermediates of the forward sweep are then probed. When the potential returns to E_1 , the sweep may be either terminated, continued on to a potential, E_3 , or reversed again. Single or multiple cycles can be performed at varying scan rates, while the current is monitored as a function of potential

2.4.1. Reversible Reactions

A reversible reaction is one where the rate of charge transfer is fast relative to the rate of mass transport, and both the O and R are stable. A typical cyclic voltammogram (CV) for a reversible process is shown in Fig. 2-10, where O and R are soluble species. The ratio of surface concentrations of O and R is given by the Nernst equation, and hence as the potential is swept cathodically the surface concentration of reactant must decrease, and the concentration gradient then increases. It is expected from eqn. 2-20 (section 2.2.2) that an increase in cathodic current follows. Due to the relaxation effect of diffusion, the concentration gradient now begins to decrease resulting in a corresponding decrease in current.

On reversing the sweep, the product R continues to be formed until the potential reaches the charge transfer equilibrium and begins to reoxidise back to O , with a corresponding anodic current flowing. The magnitude of the current increases, as before, until the surface concentration of R is depleted and the current becomes diffusion controlled. Solution of Fick's second law for species O and R , with the relevant experimental boundary conditions, reveals the exact form of the CV for a reversible process. The *Randles-Sevcik equation* [15-17] shows that under planar diffusion control, the peak current density is

$$|I_p| = 0.4463nF \left(\frac{nF}{RT} \right)^{1/2} c_i^\infty D^{1/2} \nu^{1/2} \quad 2-42$$

where I_p is the peak current for either the cathodic or anodic process and v is the sweep rate. Thus, it is evident that a plot of I_p against $v^{1/2}$ should be linear and pass through the origin for such a reversible process.

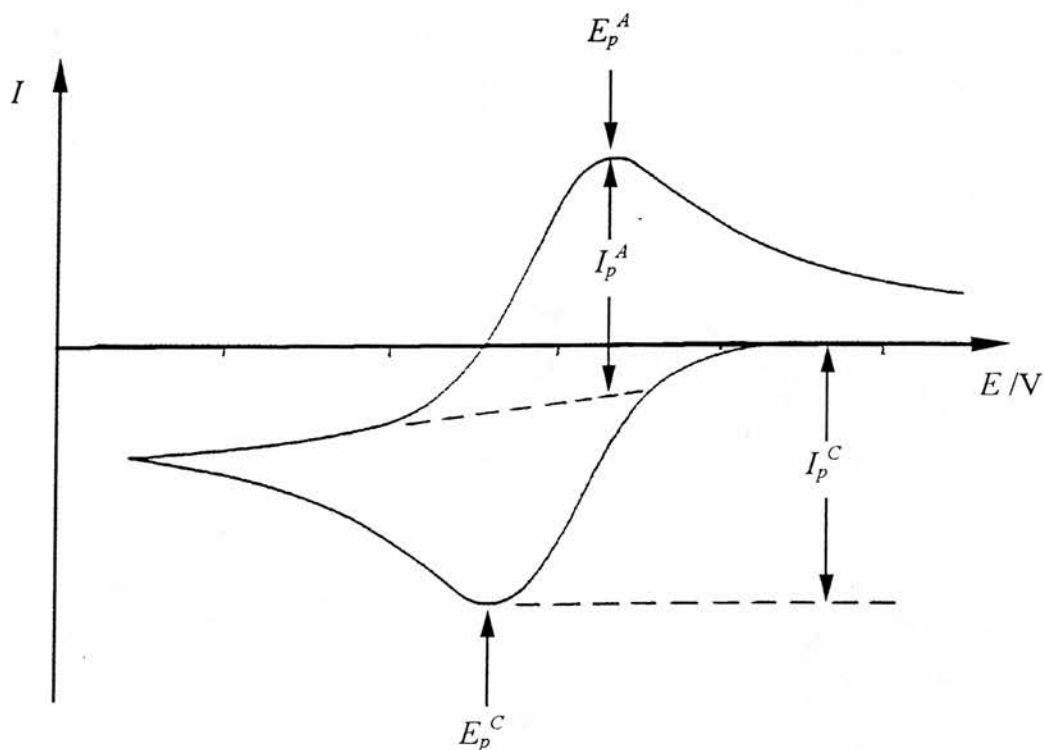


Figure 2-10 Typical cyclic voltammogram for a reversible process, for the reaction $O + e \rightleftharpoons R$. Initially there is only O present in solution before sweeping cathodically

Table 2-1 Diagnostic tests for cyclic voltammograms of reversible processes at 25°C.

1.	$\Delta E_p = E_p^A - E_p^C = 59 / n \text{ mV}$
2.	$ E_p - E_{p/2} = 59 / n \text{ mV}$
3.	$ I_p^A / I_p^C = 1$
4.	$I_p \propto \nu^{1/2}$
5.	E_p is independent of ν
6.	at potentials beyond E_p , $I^{-2} \propto t$

2.4.2. Irreversible Reactions

In the case of an irreversible process, the rate of charge transfer is insufficient to maintain Nernstian equilibrium at the surface. At low potential sweep rates the rate of charge transfer may be fast relative to mass transport and a reversible CV is observed. As the sweep rate is increased, the rate of mass transport increases and becomes comparable with charge transfer rate, resulting in peak separation.

The solution to Fick's second law for the peak current density of a totally irreversible system [17] is given by

$$|I_p| = 0.282 \frac{\pi^{1/2} F^{3/2}}{(RT)^{1/2}} n(\alpha C n \alpha)^{1/2} c_{\infty}^{\circ} D_0^{1/2} \nu^{1/2} \quad 2-43$$

where n_α is the number of electrons transferred up to, and including, the rate determining step. The peak current density is therefore a function of the square root of the sweep rate, as in the reversible case. A reverse peak is absent in such a system, although lack of anodic wave may also be due to a fast following chemical reaction. In the reversible case E_p^C is independent of sweep rate, but for the irreversible case Nicholson & Shain [17] have shown that E_p^C varies with the sweep rate according to:

$$E_p^C = K - \frac{2.3RT}{2\alpha_C n_\alpha} \log v \quad 2-44$$

where

$$K = E_e^\theta - \frac{RT}{\alpha_C n_\alpha F} \left\{ 0.78 - \frac{2.3}{2} \log \left(\frac{\alpha_C n_\alpha F D}{(k^\theta)^2 RT} \right) \right\}$$

Thus, as the sweep rate increases, the cathodic peak shifts to more negative potentials.

Table 2-2 Diagnostic tests for totally irreversible processes at 25°C.

1.	No reverse peak
2.	$I_p^C \propto v^{1/2}$
3.	E_p^C shifts $-30/\alpha_C n$ mV for each decade increase in v
4.	$ E_p - E_{p/2} = 48/\alpha_C n$ mV

2.4.3. The EC Reaction

An ec reaction implies an electron transfer process followed by a chemical step. The electron transfer may be reversible, quasi-reversible or irreversible and the chemical step may be reversible or irreversible and of first or higher order. Such a scheme is described by equations 2-45 and 2-46.



When the electron transfer is totally irreversible the chemical step will have no effect on the shape of the voltammogram. However, when the charge transfer process is reversible, the effect of the chemical reaction will be most noticeable on the reverse sweep where R is oxidised. If the rate of the chemical reaction is fast, R is rapidly removed from near the electrode and at low sweep rates no anodic peak will be observed. As the sweep rate is increased, a reverse peak becomes apparent, until at high enough rates the voltammogram assumes reversible behaviour. The chemical reaction has the effect of shifting the cathodic peak potential positive of the value obtained for the reversible electron transfer reaction.

All other combinations of electrochemical reaction followed by a chemical step have been treated by Nadjo & Saveant [18] and Nicholson & Shain [17].

Table 2-3 Diagnostic tests for ec processes.

1.	$ I_p^A/I_p^C $ is less than one but tends to unity as ν is increased
2.	$I_p^C/\nu^{1/2}$ decreases slightly with increasing ν
3.	E_p^C is positive of the value for the reversible case
4.	E_p^C shifts negatively with increasing ν , and in the pure kinetic region shifts by $30/n$ mV per 10 fold increase in ν (this changes to $19/n$ mV for a second order reaction)

2.4.4. Phase Formation

A characteristic CV for the plating and stripping of a metal M at an electrode is of the form shown in figure 2-11. On sweeping cathodically (a) from the equilibrium potential, E_e , almost zero current flows until a potential has been applied sufficient for nucleation to take place. The formation of these nuclei requires a potential more negative than that required to reduce M^+ cations. Upon reaching this *nucleation overpotential*, the magnitude of the current increases as deposition occurs (b). Deposition continues (c) on the reverse sweep at the surface of freshly deposited M , generally following Butler-Volmer kinetics (Appendix 3), and the magnitude of the current in this region is therefore greater than that of the forward sweep. As the potential is swept positive of E_e , oxidation of M takes place and the current rises rapidly (d) until available deposit is depleted. If the plating and stripping processes are the only reactions occurring at the electrode, then the charge passed on the forward and reverse sweeps must be equal. That is, all the metal ions reduced on the

forward scan to form the deposit are re-oxidised on the reverse scan back into solution. The plating and stripping process at many metal surfaces is often more complex than the ideal system described above, involving underpotential deposition [19, 20] (so-called due to the formation of reduced metal at the electrode surface at positive potentials of E_e), and alloy formation [21].

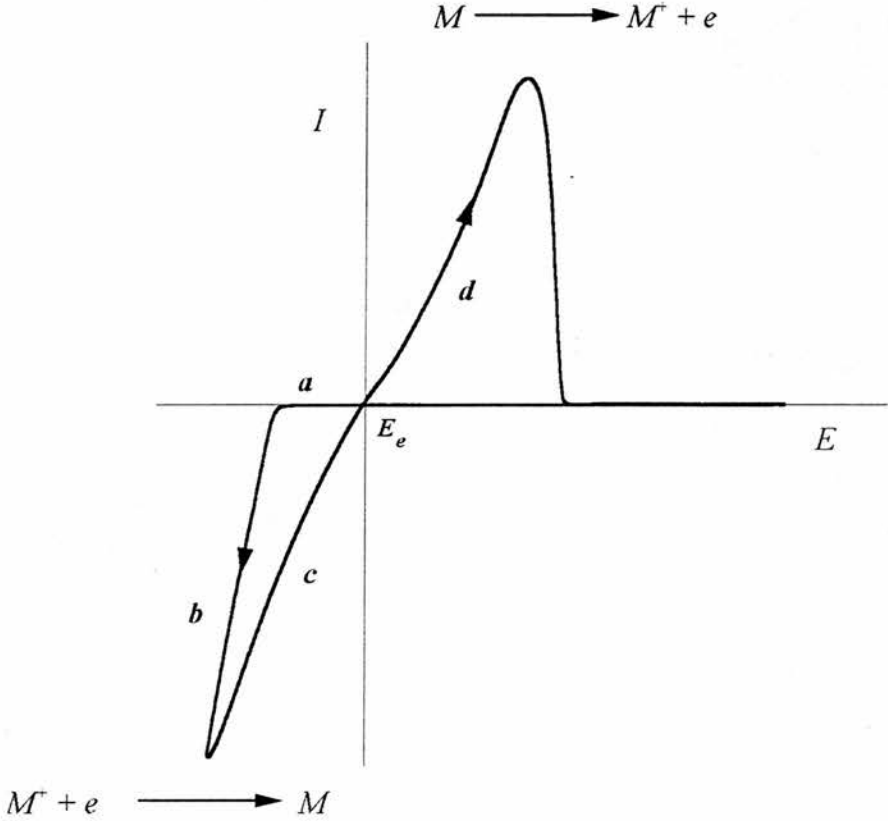


Figure 2-11 Plating and stripping of a metal M at an inert electrode.

Surface films, composed of trace impurities and electrolyte breakdown products [22], can be formed anodically of the equilibrium potential, and evidence suggests that the same film forming reactions also occur under open-circuit conditions. Possible mechanisms include the reaction of M^+ ions with oxygen and water to form

insoluble salts. Underpotential deposition of the metal in non-aqueous media may result from the reduction of an existing surface film rather than the reduction of M^r in solution in the presence of surface films. The films resulting from such electrode reactions are important in that they modify the electrode surface for the metal deposition process.

2.5. A.C. Impedance Spectroscopy

This technique involves the application of a small amplitude, sinusoidal voltage across the cell while monitoring the sinusoidal current passed as a result of the perturbation. There are, in general, two parameters which represent the current response. The first is a measure of the opposition of the flow of charge (E_{max} / I_{max}), where E_{max} and I_{max} are the maximum values of the sinusoidal voltage and current, respectively. The second is the phase angle, θ , between the current and voltage. Combining these two parameters describes the impedance of the system, defined by the vector quantity Z , which can be represented as a point on a vector diagram as in Fig. 2-12.

There are, therefore, three ways to describe the vector, ie. by its magnitude $|Z|$ and phase angle θ , the components along the real and imaginary axes ($|Z| \cos \theta$ and $|Z| \sin \theta$, respectively), or by a complex number, $Z^* = Z' - jZ''$.

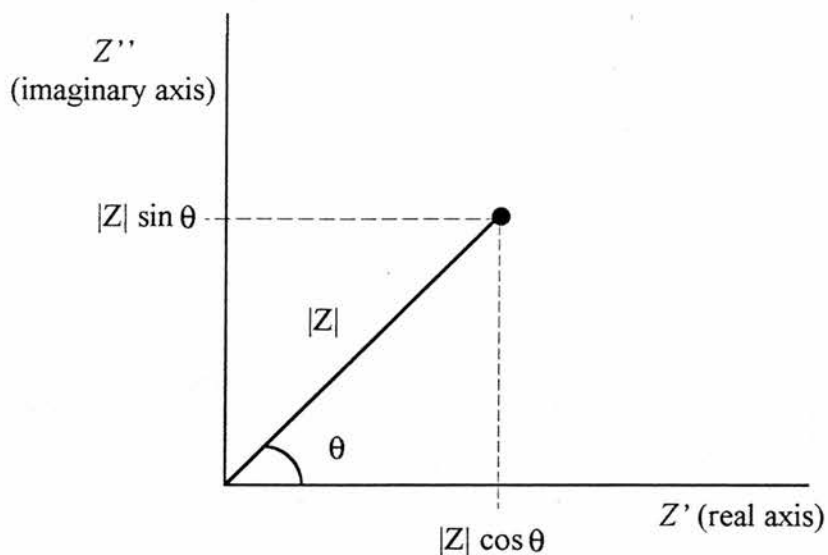


Figure 2-12 Representation of the impedance of a cell on a vector (Argand) diagram.

During an ac experiment, the complex impedance of the system is measured as a function of frequency. Simple systems give characteristic impedance plots in the complex plane which can be modelled by equivalent circuits, generally constructed from resistors and capacitors, designed to reproduce the ac response of the cell under investigation.

The magnitude of the impedance of a resistor is simply given by its resistance and is independent of frequency ($\theta = 0$), such that

$$|Z| = R$$

2-47

The corresponding complex impedance plot for a resistor is therefore a single point displaced along the real axis by a distance R for all frequencies, as shown in Fig. 2-13.

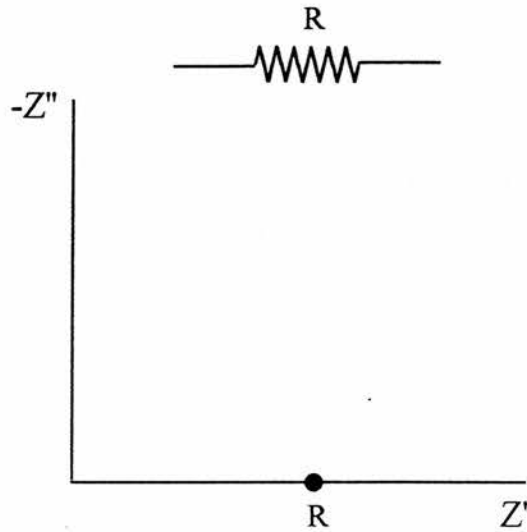


Figure 2-13 The complex impedance plot for a resistor.

The capacitance, C , is defined as the charge, q , stored per unit potential difference, E , between electrode plates, such that

$$C = \frac{q}{E} \quad 2-48$$

The current that passes through a capacitor is then given by

$$I = \frac{dq}{dt} = C \frac{dE}{dt} \quad 2-49$$

A sinusoidal voltage of amplitude E_{max} can be represented as:

$$E = E_{max} \sin(\omega t) \quad 2-50$$

where ω is the angular frequency, defined by $\omega = 2\pi f$, and f is the signal frequency in Hz. Thus,

$$I = E_{max} \omega C \cos(\omega t) \quad 2-51$$

or
$$I = E_{max} \omega C \sin\left(\omega t + \frac{\pi}{2}\right) \quad 2-52$$

It is seen from eqn. 2-52 that the voltage lags behind the current by a phase angle of $\theta = -\pi/2$. The impedance of a capacitor (E/I) is therefore frequency dependent and has a magnitude of $1/\omega C$:

$$Z = \frac{-j}{\omega C} \quad 2-53$$

The complex impedance plot for a capacitor, shown in Fig. 2-14, defines a vertical spike coincident with the imaginary axis, since there is no real displacement for lack of a resistive component.

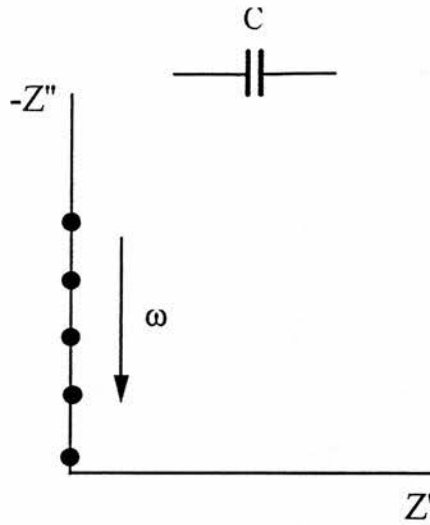


Figure 2-14 The complex impedance plot for a capacitor.

2.5.1. Simple Systems

Having determined the impedance of each of the individual elements of the circuit, the impedance of a network of components can be found. When components are connected together in series the impedances are directly additive

$$Z_{total}^* = Z_1^* + Z_2^* + Z_3^* + \dots \quad 2-54$$

This is illustrated by a resistor and capacitor in series, where

$$Z_{total}^* = R - \frac{j}{\omega C} \quad 2-55$$

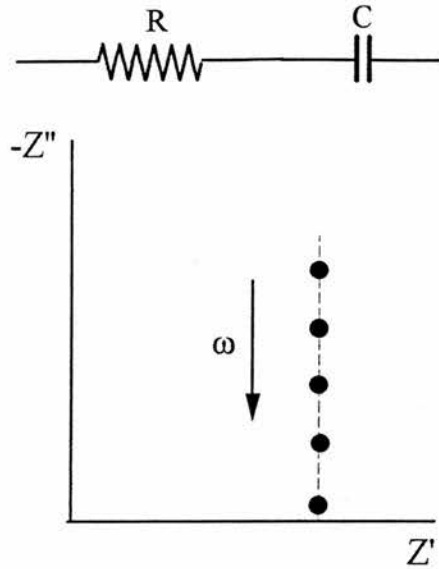


Figure 2-15 The complex impedance plot for a resistor and capacitor in series.

In the complex impedance plane eqn. 2-55 defines a vertical line displaced a distance R along the real axis (Fig. 2-15). As the frequency is increased the impedance of the capacitor is reduced and the contribution of the imaginary component to the impedance reduces correspondingly.

When components are connected together in parallel the impedances are not directly additive, but their inverse complex admittances ($Y^* = 1/Z^*$) are

$$Y_{total}^* = Y_1^* + Y_2^* + Y_3^* + \dots \quad 2-56$$

where $Y^* = Y' + jY'' = \frac{1}{Z' - jZ''}$ 2-57

Thus, the real and imaginary parts are defined as

$$Y' = \frac{Z'}{Z'^2 + jZ''^2} \quad \text{and} \quad Y'' = \frac{Z''}{Z'^2 + jZ''^2} \quad 2-58$$

The admittance of a resistor and capacitor are $1/R$ and $j\omega C$, respectively. The total admittance of the parallel RC circuit is then given by:

$$Y_{total} = \frac{1}{R} + j\omega C \quad 2-59$$

Rearranging eqn. 2-59, the total impedance is found to be

$$\begin{aligned} Z_{total}^* &= \frac{1}{\left(\frac{1}{R} + j\omega C\right)} = \frac{R - j\omega C R^2}{1 + (\omega C R)^2} \\ &= \left[\frac{R}{1 + (\omega C R)^2} \right] - j \left[\frac{\omega C R^2}{1 + (\omega C R)^2} \right] \\ &= Z' - jZ'' \end{aligned} \quad 2-60$$

Providing the Z' and Z'' scales are equal, eqn. 2-60 defines a semicircle in the complex impedance plane, with a diameter R along the real axis (Fig. 2-16).

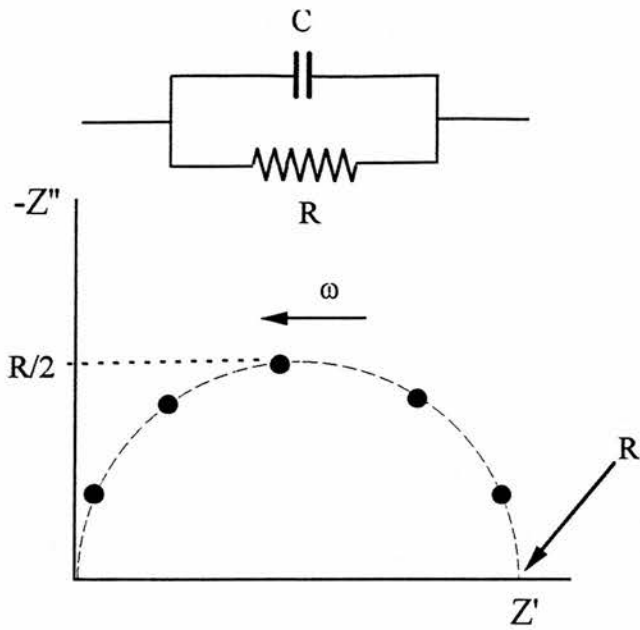


Figure 2-16 The complex impedance plot for a resistor and capacitor in parallel.

At the maximum of the semi-circle,

$$\frac{R}{1+(\omega CR)^2} = \frac{\omega CR^2}{1+(\omega CR)^2} \quad 2-61$$

and solving with respect to R gives

$$R = \frac{1}{\omega_{\max} C} \quad 2-62$$

allowing both R and C to be determined from the complex impedance plot.

2.5.2. Cells with Blocking Electrodes

In a system where there is no finite electrode reaction, the electrode is said to be blocking. A simple case for a real system consists of an electrolyte solution separating two blocking stainless-steel electrodes. When the ac voltage is applied to the cell, the electrodes become alternately positively and negatively charged. The ions of the electrolyte migrate back and forth in phase with the voltage, which can be represented by a *bulk resistance* R_b in the equivalent circuit. As the ions are alternately accumulated and depleted from the region near the surface of the electrode, a layer of equal and opposite charge is formed at each electrode. The electrode/electrolyte interface thus behaves like a parallel plate capacitor, represented by a *double layer capacitance* C_{dl} . The solvent molecules also become polarised in the alternating field and can be represented by a *bulk capacitance* C_b . Since the polarisation of the solvent and the migration of ions are considered to occur in parallel, the equivalent circuit modelling the system will place the elements R_b and C_b in parallel. This parallel combination is in series with the capacitance at the electrode, C_{dl} . In a symmetrical cell, the capacitance from each electrode is usually summed and represented by a single element, such that $1/C_{dl} = 1/C_{dl(1)} + 1/C_{dl(2)}$. The total impedance is then given by [23]

$$Z_{tot} = \frac{R_b}{1 + (\omega C_b R_b)^2} - j \left\{ \frac{\omega C_b R_b^2}{1 + (\omega C_b R_b)^2} + \frac{1}{\omega C_{dl}} \right\} \quad 2-63$$

which represents the full ac impedance plot shown in Fig. 2-17.

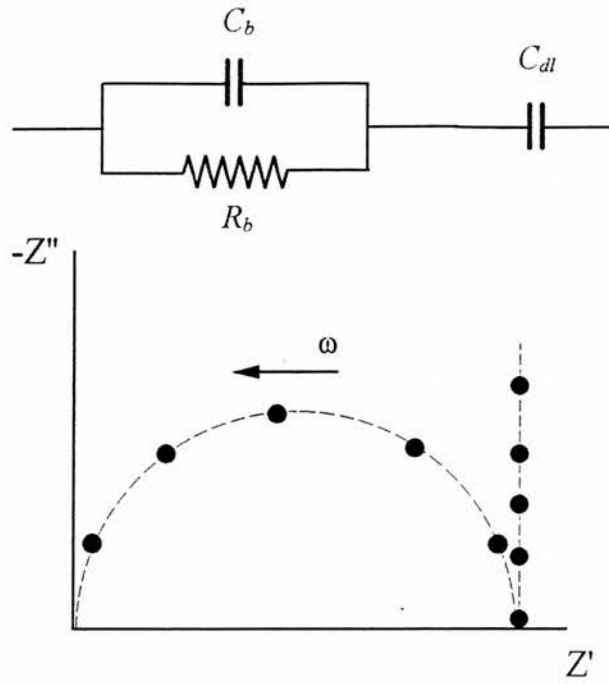


Figure 2-17 The complex impedance plot for a cell with two blocking electrodes.

2.6. Electrolytic Conductance and Conductivity

Conductance measurements of electrolyte solutions have been recorded over the last century in both aqueous and non-aqueous media, and more recently in polymer [24, 25] and gelled [26, 27] electrolyte systems. Such measurements can be taken with a high degree of precision.

2.6.1. Definitions

The electrical resistance, R , of a uniform conductor is defined as

$$R = \rho \left(\frac{L}{A} \right)$$

2-64

measured in absolute ohms, Ω , where L is the length of the conductor and A is the cross-sectional area and the proportionality constant, ρ , is called the *specific resistance*. If we take

$$\kappa = \frac{1}{\rho} \tag{2-65}$$

then on comparison of eqns. 2-64 and 2-65 we obtain

$$\kappa = \left(\frac{L}{A}\right) \frac{1}{R} \tag{2-66}$$

which defines the *specific conductivity*, κ , in units $\Omega^{-1}\text{cm}^{-1}$ (or Scm^{-1}). The reciprocal of resistance ($1/R$) is known as the *specific conductance*. Reducing the conductivity to a unit concentration scale defines

$$\Lambda_c = \frac{1000\kappa}{c} \quad \text{or} \quad \Lambda_m = \frac{\kappa}{m} \tag{2-67}$$

where Λ_c and c are the molar conductivity and the molar concentration, and Λ_m and m are the corresponding molal quantities. The ratio (L/A) , in units of cm^{-1} , is termed the *cell constant* and is an easily determined quantity.

2.6.2. Electrolyte Solutions

Electrolytes are substances which give rise to ion formation. By definition, *strong electrolytes* are completely ionised and mobile upon dissolution into a solvent. *Weak electrolytes*, however, are not fully dissociated in solution, but become more so upon dilution. This effect is described by the *Ostwald dilution law*:

$$K_d = \frac{\alpha^2 c}{1 - \alpha} \qquad 2-68$$

where K_d is the dissociation constant, α the fraction of free ions and c the concentration. Although strong electrolytes are fully dissociated, restrictions on ion mobilities persist. A central ion is, on a time averaged scale, surrounded by an atmosphere of counter-ions with opposite charge, leading to two situations [28] under the influence of an applied field. The first is called the *relaxation effect* caused by the time delay for the restructuring of the ionic atmosphere around the central ion following its movement through the solution. An asymmetrically distributed atmosphere is constructed, resulting in an attraction of the central ion in the opposite direction to that of its motion. The movement of the atmosphere in the opposite direction induces some solvent movement. This viscous hindrance imposed on the central ion is called the *electrophoretic effect*.

If the conductivity of an electrolyte was simply a linear function of the number of charge carriers, then by plotting the molar conductivity against concentration a straight line parallel to the concentration axis would be seen. However, the molar

conductivity deviates from this ideal with increasing concentration, suggesting that the loss of mobility may arise from (i) ionic atmosphere effects noted above and (ii) association of free ions to form neutral species. In the limit of infinite dilution, Kohlrausch suggested that association of ions is negligible and presented an empirical relationship between Λ and $c^{1/2}$ for strong electrolytes:

$$\Lambda = \Lambda_0 - a\sqrt{c} \quad 2-69$$

where a is an arbitrary constant, now known to be related to ionic atmosphere effects as described below, and Λ_0 is the *molar conductivity at infinite dilution* (or limiting molar conductivity). Weak electrolytes do not have such a linear form since their dissociation is considered to increase with increasing dilution, as noted above. The use of the term “dilute” is open to interpretation, but throughout this text it is taken to be in the range where the classical *Debye-Huckel model* [29] is valid. This accounts satisfactorily for the thermodynamic properties of electrolyte solutions by regarding ions as hard spheres separated by a medium with relative permittivity equal to that of the pure solvent.

Based on the Debye-Huckel theory, Onsager developed an expression [30], which dealt with the relaxation and electrophoretic effects:

$$\Lambda = \Lambda_0 - S\sqrt{c} \quad 2-70$$

where S is a combination of constants derived from the physical properties of the solvent. Eqn. 2-70 compares well with the empirical Kohlrausch equation (eqn. 2-69).

2.6.3. Ion Association

In many cases the experimental data obtained deviates from the slope predicted by Onsager, and the mean ionic activity coefficients differ from those of the Debye - Huckel theory. It was suggested by Bjerrum that under certain circumstances a univalent ion may associate with an ion of opposite charge to form a non-conducting ion-pair. A critical distance for ion-pairing, q , was defined as

$$q = \frac{Z_+ Z_- e^2}{8\pi \epsilon_r \epsilon_0 kT} \quad 2-71$$

where Z_i is the valency of the ionic species i , ϵ_r is the relative permittivity of the solvent, ϵ_0 is the vacuum permittivity, k the Boltzmann constant, T the temperature and e the elementary charge. Pairing can take place if the ion separation becomes less than q , otherwise the Debye-Huckel model holds. As the relative permittivity of the solvent decreases, the critical pairing distance increases resulting in a higher degree of association.

By plotting Λ against $c^{1/2}$, the curve generally falls into one of five patterns shown in Figs. 2-18 to 2-22.

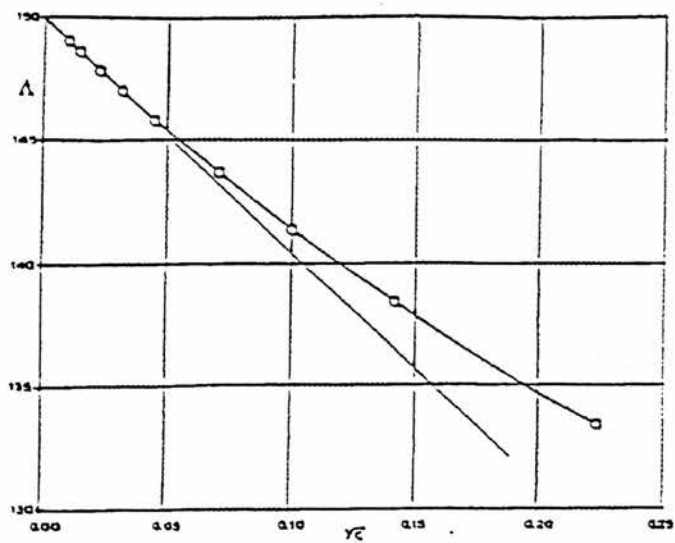


Figure 2-18 *Type I*: Molar conductivity of potassium chloride in water. From ref. [31].

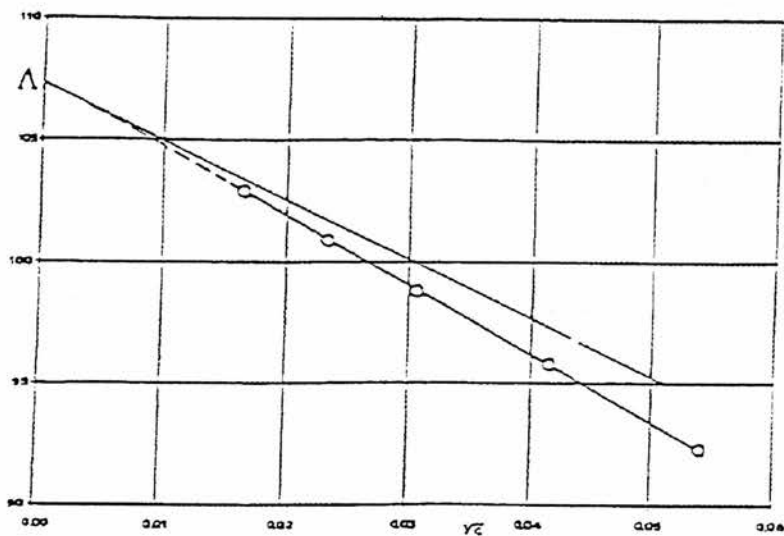


Figure 2-19 *Type II*: Molar conductivity of tetraethylammonium picrate in methanol. From ref. [32].

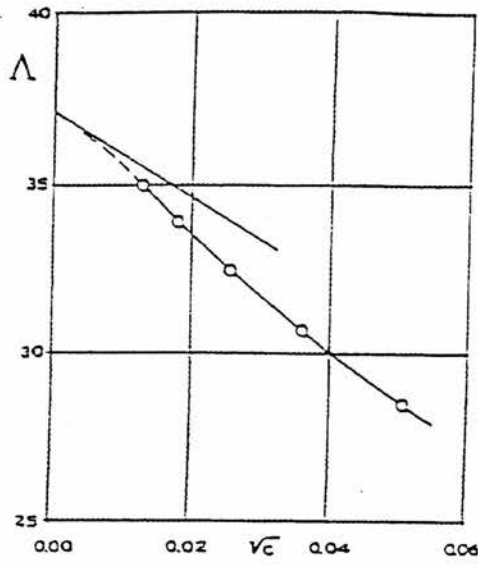


Figure 2-20 *Type III*: Molar conductivity of tetrabutylammonium bromide in 70 dioxane - 30 water. *From ref. [33].*

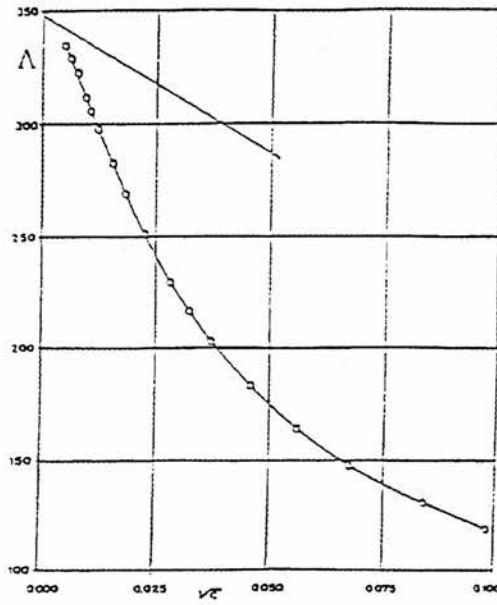


Figure 2-21 *Type IV*: Molar conductivity of potassium chloride in liquid ammonia. *From ref. [34].*

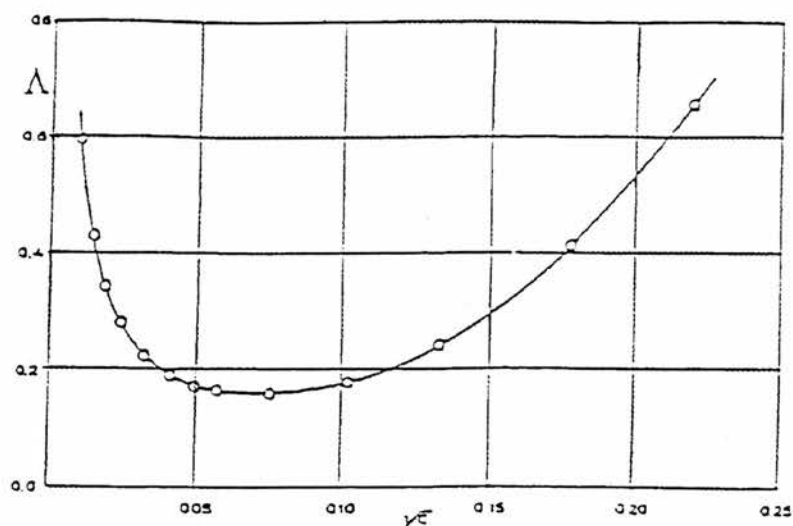


Figure 2-22 *Type V*: Molar conductivity of tetra-iso-amylammonium nitrate in 93.6 dioxane - 6.4 water. *From ref. [35].*

For ionophores (compounds which are ionic lattices as solids) in solvents of high dielectric constant, $\Lambda(c)$ approaches the limiting tangent from above (Type I). Ionogens (compounds which are molecular lattices as solids, and react with some solvents to produce ions) may also show similar behaviour; for example hydrogen chloride in water. Dissolving a specific ionophore in a range of solvents of decreasing relative permittivity, will successively drop the slope of the $\Lambda - c^{1/2}$ curve toward the limiting tangent. Eventually, it will cross over and approach from below as slight association to pairs occurs (Type II). Type III is observed when association to pairs is sufficient to cause an inflexion in the observed concentration range. Association becomes even more pronounced (Type IV) until finally a minimum is observed (Type V) indicating an increase in the number of charge carriers.

2.6.4. Paired Ion Model

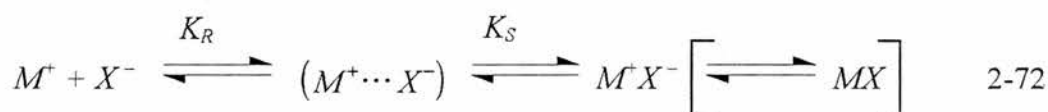
The extended theoretical expressions mentioned earlier were based on rigid charged spheres of diameter, a , in a continuum, and on the postulated equilibrium between free ions and non-conducting ion-pairs. The definitions of the relaxation and electrophoretic effects in these expressions contain a , but since the ion-atmosphere induces long-range effects they should depend only on the charges of the ions and not on their size. The equations also depend on the use of the macroscopic relative permittivity which does not hold at a microscopic level. A new model was thus proposed in 1978 by Fuoss [36], which corrects for these approximations.

In dilute solution, most of the ions will have solvent molecules as nearest neighbours, but it is possible that a given ion will have an ion of opposite charge in its shell of nearest neighbours. Such pairs are defined as *contact pairs*, where the distance separating the centres of ions i and j is $r_{ij} = a$. The nearest neighbours to a contact pair are solvent molecules surrounding the pair to form a cage. Eventually, on a time scale comparable with the time constant for thermal motion, one of the ions will exchange sites with an adjacent solvent molecule, dissociating the contact pair. Meanwhile, another contact pair has formed elsewhere in solution so that the time averaged concentration of contact pairs remains constant.

Ions whose nearest neighbours are solvent molecules, but find an ion of opposite charge in the next nearest shell are called *solvent-separated ion pairs*. For these, $r_{ij} = (a + s)$, where s is the diameter of a sphere corresponding to the average

volume per solvent molecule. Solvent-separated pairs of higher order are also present with $r_{ij} = (a + ms)$, where m is a positive integer greater than 1. Unique partners can, therefore, be defined for cations which find only one anion in the range $a \leq r_{ij} \leq R$, where R is the sum of the radii of the cation and anion solvent cospheres. Thus, ions for which $r_{ij} > R$ are defined as *unpaired*.

When thermal motion and attractive forces bring a cation and anion to a distance $r=R$ apart, they are classed as paired. Further diffusion may reduce the centre-to-centre distance, until eventually a contact pair is formed. If the solute is an ionogen, a rearrangement to form a neutral molecule may occur. Alternatively, ions for which $a \leq r_{ij} \leq R$ may diffuse to distances $r > R$, hence dissociating. The equilibria representing this scheme can be given by



where the symbol $(M^+ \cdots X^-)$ represents a solvent-separated pair, $M^+ X^-$ a contact pair and MX a neutral molecule. The concentration of unpaired ions is $c\gamma$, and paired ions is $c\alpha(1-\gamma)$, where c is the molar concentration, α the fraction of contact pairs and γ the fraction of free ions.

The equilibrium constants for eqn. 2-72 are then:

$$K_R = \frac{(1-\alpha)(1-\gamma)}{c\gamma^2 f^2} \quad 2-73$$

$$K_S = \frac{\alpha}{(1-\alpha)} = \exp\left(\frac{-E_S}{kT}\right) \quad 2-74$$

where K_R describes the formation and separation of solvent-separated pairs by diffusion in and out of spheres of diameter R , and K_S describes the short-range process by which contact pairs form and dissociate; E_S is the difference in energy between a pair in the states ($r = R$) and ($r = a$) and f is the mean activity coefficient.

Rearranging eqn. 2-74 gives

$$(1-\alpha) = \frac{1}{(1+K_S)} \quad 2-75$$

Substituting eqn. 2-75 into 2-73 gives the conductimetric pairing constant

$$K_R = \frac{(1-\gamma)}{(1+K_S)c\gamma^2 f^2} \quad 2-76$$

$$K_A = K_R(1+K_S) = \frac{(1-\gamma)}{c\gamma^2 f^2} \quad 2-77$$

which is used to determine the concentration $c\gamma$ of active ions which produce the long range inter-ionic effects. Conductivity measurements can produce at least three parameters: the limiting molar conductivity Λ_0 , a distance parameter R , and K_S which includes all the short-range effects. By treating the equilibrium of solvent-separated pairs to contact pairs as a “reaction”, all the complex short-range ion-solvent and ion-ion interactions can be included in this one parameter, without needing to consider the details [36].

Having K_A in the form of eqn. 2-77 reveals the failure of the pre-1978 *iso-dielectric* rule, which defines

$$K_A = \left(\frac{4\pi N \alpha^3}{3000} \right) \exp\left(\frac{e^2}{\alpha \epsilon_r kT} \right) \quad 2-78$$

implying that a given electrolyte with fixed distance α should have the same pairing constant in different solvents with the same relative permittivity (dielectric constant); however, experimental deviations from this rule have been observed [36]. In eqn. 2-77, the solvent-separated pair parameter, K_R , contains ϵ_r but the contact-pair parameter, K_S , is defined only by the system under study.

Contact pairs form by a sequence of ion-solvent site interchanges within the spheres of diameter R , until two ions of opposite charges become nearest neighbours. Once a contact pair forms, the electrostatic attraction will hold the pair together for a time longer than the time scale of Brownian motion. The surrounding solvent will also

serve to stabilise the pair through its caging effect. When an external field is applied the pair will experience a torque and begin to rotate, and if the field is removed the pair will return to a random orientation. Thus, it can be seen that the pairs act as electric dipoles, contributing only to charging current. The conductance function is given by

$$\Lambda = [1 - \alpha(1 - \gamma)] \left\{ \Lambda_0 \left(1 + \frac{\Delta X}{X} \right) + \Delta \Lambda_e \right\} \quad 2-79$$

where $\Delta X/X$ and $\Delta \Lambda_e$ represent the relaxation and electrophoretic effects, respectively. For the case of ionogens, where α is very near unity ($-E_s/kT \gg 1$), the conductance equation reduces to

$$\Lambda = \gamma \left\{ \Lambda_0 \left(1 + \frac{\Delta X}{X} \right) + \Delta \Lambda_e \right\} \quad 2-80$$

The equilibrium constant for the effective reaction $M^+ + X^- \rightleftharpoons MX$ is then

$$K_A = \frac{(1 - \gamma)}{c\gamma^2 f^2} \approx K_R K_S \quad 2-81$$

since $K_S \gg 1$. For ionophores in solvents of low dielectric constant, α is also near unity; for $\alpha > 0.98$ $\{1 - \alpha(1 - \gamma)\} \approx \gamma$ and eqn. 2-79 can be approximated by eqn. 2-80.

2.6.5. Higher Association

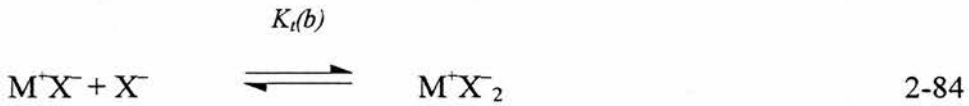
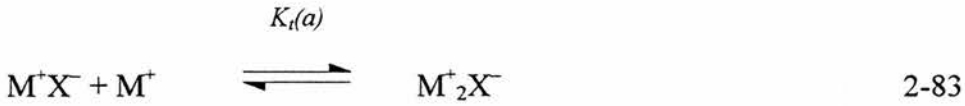
In low dielectric constant solvents, the electrolytic behaviour under very dilute conditions is similar to that of weak electrolytes in high dielectric constant solvents. However, as the concentration of electrolyte increases, a conduction minimum may be observed. This behaviour falls into neither of the two main classes, thus prompting the construction of a new conduction model to describe the increase in molar conductivity after the minimum.

2.6.5.1. Triple Ion Formation

Triple ion formation was first postulated by Fuoss and Kraus [35] in 1933 to account for the conductance behaviour of dioxane-water mixtures. Petrucci, *et al* [37, 38] and Nicolas, *et al* [39] have observed similar behaviour with LiClO_4 in 1,3-dioxolane and in THF.

Although an ion-pair is electrically neutral, a dipole field exists which attracts either a cation or anion to form a triple-ion. In particular, the dipoles of salts with one large ion and one small ion are highly associated. Such triple-ion clusters form in solvents with $\epsilon_r < 20$ since the potential energy for an ion in contact with a counter-ion of the pair becomes sufficient to stabilise the configuration.

The hypothesis is made that the following equilibria exist:



For simplicity, it is generally assumed that the probability of forming $M_2^+X^-$ is equal to that of $M^+X_2^-$, such that

$$K_i(a) = K_i(b) = K_t$$

where α_i and α_t represent the fraction of solute existing as free ions and triple ions, respectively. Similarly, K_i and K_t are the association equilibrium constants for the formation of ion-pairs and ion-triples. From equation 2-82, the mass action equation for the binary equilibrium is given by

$$K_i = \frac{[M^+X^-]}{[M^+][X^-]} = \frac{(1 - \alpha_i - 3\alpha_t)}{c\alpha_i^2} \quad 2-84$$

approximating the activity coefficients by unity. Rearranging eqn. 2-84 to solve for α_i :

$$\alpha_i^2 (c K_i) + \alpha_i - (1 - 3\alpha_i) = 0 \quad 2-85$$

which is in the form of a quadratic with solutions

$$\alpha_i = \frac{-1 \pm \sqrt{1 + 4c K_i (1 - 3\alpha_i)}}{2c K_i} \quad 2-86$$

Here, only the positive root has any physical significance. The mass action equation for triple-ion formation (eqns. 2-83 and 2-84) is given by

$$\begin{aligned} K_t &\approx \frac{[M_2 X^+]}{[M^+ X^-][M^+]} \quad \text{or} \quad \frac{[M X_2^-]}{[M^+ X^-][X^-]} \\ &= \frac{\alpha_i}{c \alpha_i (1 - \alpha_i - 3\alpha_i)} \end{aligned} \quad 2-87$$

again taking activity coefficients equal to unity. Rearranging eqn. 2-87 to solve for α_i

$$c \alpha_i (1 - \alpha_i - 3\alpha_i) K_t - \alpha_i = 0 \quad 2-88$$

$$\alpha_i (3c \alpha_i K_t + 1) = c \alpha_i K_t (1 - \alpha_i) \quad 2-89$$

$$\alpha_i = \frac{c \alpha_i K_t (1 - \alpha_i)}{(3c \alpha_i K_t + 1)} \quad 2-90$$

On comparison of eqn. 2-84 with eqn. 2-87, we find

$$K_t = \alpha_t \sqrt{\frac{K_i}{c(1-\alpha_i-3\alpha_t)^3}} \quad 2-91$$

such that

$$\alpha_t = K_t \sqrt{\frac{c(1-\alpha_i-3\alpha_t)^3}{K_i}} \quad 2-92$$

and on rearrangement of eqn. 2-84,

$$\alpha_i = \sqrt{\frac{(1-\alpha_i-3\alpha_t)}{cK_i}} \quad 2-93$$

If Λ_0 represents the sum of the limiting molar conductivities for the free ions (by Kohlrausch's law of the independent migration of ions), and Λ_0^T the sum of the limiting molar conductivities of the two triple-ion species, then the observed molar conductivity Λ_c can be given by

$$\Lambda_c = \alpha_i \Lambda_0 + \alpha_t \Lambda_0^T \quad 2-94$$

provided the effects of interionic forces upon mobility are neglected, giving

$$\Lambda_c = \Lambda_0 \sqrt{\frac{(1-\alpha_i-3\alpha_t)}{cK_i}} + \Lambda_0^T K_t \sqrt{\frac{c(1-\alpha_i-3\alpha_t)^3}{K_i}} \quad 2-95$$

which is of the form

$$\Lambda_c = A c^{-1/2} + B c^{1/2} \quad 2-96$$

At concentrations lower than where the minimum occurs, $A c^{-1/2}$ dominates and the majority of species are ion-pairs. The fraction of solute present as ion-pairs is given by $(1 - \alpha_i - 3\alpha_t)$, which will be close to unity in this region. As the concentration increases, $B c^{1/2}$ becomes more significant. When Λ_c is dependent on both functions equally, a minimum is reached which is then followed by domination of the $B c^{1/2}$ term with a corresponding increase in molar conductivity.

At low concentrations, where α_i and α_t are small, ion-pair formation is dominant and eqn. 2-96 can be reduced to its limiting form:

$$\Lambda'_m = A' c^{-1/2} + B' c^{1/2} \quad 2-97$$

where

$$A' = \Lambda_0 \sqrt{\frac{1}{K_i}} \quad \text{and} \quad B' = \Lambda_0^T K_t \sqrt{\frac{1}{K_i}} \quad 2-98$$

Rearranging eqn. 2-97 into a more convenient form we have

$$\Lambda'_c c^{1/2} = A' + B' c \quad 2-99$$

and on plotting $\Lambda_c c^{1/2}$ versus c , a straight line will be observed with intercept A' and slope B' . While proving satisfactory for a large region of the data, these simplified equations are often inadequate at very low concentrations, i.e. experimental data has a downward curvature. Combining the Debye - Huckel expression for f_{\pm} with the mass action equations of 2-82, 2-83 and 2-84 the expression for Λ becomes [35]:

$$\Lambda = \left(1 - \frac{S}{\Lambda_0^{3/2}} (c\Lambda)^{1/2}\right) (\alpha_i \Lambda_0 + \alpha_i \Lambda_0^T) \quad 2-100$$

where S is the coefficient of the Onsager tangent given by

$$S = \frac{8.204 \times 10^5}{(\epsilon_r T)^{3/2}} \Lambda_0 + \frac{82.501}{\eta (\epsilon_r T)^{1/2}} \quad 2-101$$

Rearranging eqn. 2-100 to its linear form gives

$$\Lambda g(c) c^{1/2} = \frac{\Lambda_0}{K_i^{1/2}} + \frac{\Lambda_0^T K_i}{K_i^{1/2}} \left(1 - \frac{\Lambda}{\Lambda_0}\right) c \quad 2-102$$

with
$$g(c) = \frac{\exp\left(\frac{-\beta'}{\Lambda_0^{1/2}} (c\Lambda)^{1/2}\right)}{\left(1 - \frac{S}{\Lambda_0^{3/2}} (c\Lambda)^{1/2}\right) \left(1 - \frac{\Lambda}{\Lambda_0}\right)^{1/2}} \quad 2-103$$

where β' is the Debye-Huckel activity coefficient term

$$\beta' = \frac{1.8247 \times 10^6}{(\epsilon_r T)^{3/2}}$$

A plot of $\Lambda g(c)c^{1/2}$ against $(1-\Lambda/\Lambda_0)c$ reveals a straight line with almost no curvature in the more dilute region.

2.6.5.2. *Re-dissociation of the Ion-pair*

Over the years, the presence of a minimum in the $\Lambda(c)-c^{1/2}$ plots has been widely accepted as proof of the existence of triple-ions. However, as far back as 1968, Cavell and Knight proposed [40] that quantitative estimates of triple-ions in media of low dielectric constant are grossly exaggerated unless values of the relative permittivity ϵ_r of the solution at varying salt concentrations were taken into account.

Ac impedance studies [41-43] on high molecular weight polymer electrolytes have shown that ϵ_r increases as a function of concentration. Eqn. 2-71 shows that as the dielectric constant of the solvent increases, the association to pairs decreases and the time averaged fraction of free ions will increase. The functional dependence of the association constant upon permittivity has been represented by

$$K(\epsilon_r) = K_0 \exp\left\{\frac{e^2}{a \epsilon_r kT}\right\} \quad 2-104$$

As the number of ion-pairs increases, the permittivity of the solution will increase, resulting from the larger dipole concentration. The evidence may then suggest that the dominating charge carriers after the conduction minimum is the increasing fraction of free ions. Raman evidence for such a process has been found by Schantz [44] and Stevens *et al* [45].

Petrucci and co-workers have shown [46], however, that the apparent lack of fit of data to the Fuoss-Kraus model (eqns. 2-100 and 2-102) in some regions can be corrected for by the introduction of the solution permittivity and viscosity as variable quantities. This hypothesis is thus a combination of the triple-ion theory and the idea put forward by Cavell and Knight.

REFERENCES

1. Reports on the IUPAC Convention on Electrochemistry, *Electrochimica Acta*, 27, 629 (1982); *Pure and Appl. Chem.* 37, 503 (1974); 51, 1159 (1979).
2. *Instrumental Methods in Electrochemistry*, Southampton Electrochemistry Group, Ellis Harwood, Chichester (1990).
3. J.A.V. Butler, *Trans. Faraday Soc.*, 19, 729 (1924);
T. Erdey-Gruz and M. Volmer, *Z. Physik Chem*, 150A, 203 (1930).
4. F.G. Cottrell, *Z. Physik Chem.*, 42, 385 (1902).
5. M. Fleischmann and H.R. Thirsk in *Advances in Electrochemistry and Electrochemical Engineering* (Edited by P. Delahay and C.W. Tobias), Interscience, New York (1962).
6. *A Guide to the Study of Electrode Kinetics*, H.R. Thirsk and J.A. Harrison, Academic Press, London (1972).
7. G.J. Hills, D.J. Schiffrin and J. Thompson, *Electrochimica Acta*, 19, 657 (1974).
8. G. Gunawardena, G. Hills, I. Montenegro and B. Scharifker, *J. Electroanal. Chem.*, 138, 225-239 (1982).
9. B. Scharifker and G. Hills, *Electrochimica Acta*, 28(7), 879-889 (1983).
10. M. Avrami, *J. Phys. Chem.*, 7, 1103 (1939); 8, 212 (1940); 9, 177 (1941).
11. M.Y. Abyaneh, *Electrochimica Acta*, 36, 727-732 (1991).
12. E. Bosco and S.K. Rangarajan, *J. Electroanal. Chem.*, 134, 213 (1982).
13. M.Y. Abyaneh and M. Fleischmann, *ibid*, 119, 187 (1981).

14. *Electrochemical Methods*, A.J. Bard and L.R. Faulkner, John Wiley and Sons (1980).
15. J.E.B. Randles, *Trans. Faraday Soc.*, 44, 327 (1948).
16. A. Sevcik, *Coll. Czech Chem. Comm.*, 13, 349 (1958).
17. R.S. Nicholson and I. Shain, *Anal. Chem.*, 36, 706 (1964).
18. L. Nadjo and J.M. Saveant, *J. Electroanal. Chem.*, 48, 113 (1973).
19. K. Jütter and W. Lorenz, *Zeitsch. Phys. Chem. (Neue Folge)*, Bd 122, S163-185 (1980).
20. D. Wagner and H. Gerischer, *Electrochimica Acta*, 34(9), 1351-1356 (1989).
21. A.N. Dey, *J. Electrochem. Soc.*, 118(10), 1547 (1971).
22. E. Peled in *Lithium Batteries* (Edited by G.P. Gabano), Academic Press, London and New York (1983).
23. P.G. Bruce in *Polymer Electrolyte Reviews vol.1* (Edited by J.R. MacCallum and C.A. Vincent), Elsevier Applied Science, London and New York (1987).
24. M.A. Ratner and A. Nitzan, *Faraday Discuss. Chem. Soc.*, 88, 19-42 (1989).
25. P.G. Bruce and C.A. Vincent, *J. Chem. Soc. Faraday Trans.*, 89(17), 3187-3203 (1993).
26. K.M. Abraham and M. Alamgir, *J. Electrochem. Soc.*, 137(5), 1657 (1990).
27. O. Bohnke, G. Frand, M. Rezrazi, C. Rousselot and C. Truche, *Solid State Ionics*, 66, 97-104 (1993); 66, 105-112 (1993)
28. *Electrolyte Solutions*, R.A. Robinson and R.H. Stokes, Butterworths, London (1957).
29. P. Debye and E. Huckel, *Phys. Z.*, 24, 185 (1923).
30. L. Onsager, *ibid*, 28, 277 (1927).

31. T. Schedlovsky, *J. Am. Chem. Soc.*, 54, 1411 (1932).
32. F. Accascina, A. D'Aprano and R.M. Fuoss, *ibid*, 81, 1058 (1959).
33. P.L. Mercier and C.A. Kraus, *Proc. Natl. Acad. Sci. U.S.*, 41, 1033 (1957).
34. V.F. Hnizda and C.A. Kraus, *J. Am. Chem. Soc.*, 71, 1565 (1949).
35. R.M. Fuoss and C.A. Kraus, *ibid*, 55, 2387 (1933).
36. R.M. Fuoss, *J. Phys Chem.*, 82, 2427 (1978);
R.M. Fuoss and R.M. Jarret, *J. Phys. Chem.*, 89, 3167 (1985).
37. D. Saar, J. Brauner, H. Farber and S. Petrucci, *J. Phys. Chem.*, 84, 341
(1980)
38. S. Onishi, H. Farber and S. Petrucci, *ibid*, 84, 2922 (1980).
39. M. Nicolas and R. Reich, *ibid*, 83, 749 (1979).
40. E.A.S. Cavell and P.C. Knight, *Zeitsch. Phys. Chem. (Neue Folge)*, 57, 331
(1968).
41. I. Albinsson, B.E. Mellander and J.R. Stevens, *J. Phys. Chem.*, 96(1), 681
(1992).
42. Y. fu, K. Pathmanathan and J.R. Stevens, *ibid*, 94(9), 6323 (1991).
43. I. Albinsson, B.E. Mellander and J.R. Stevens, *Solid State Ionics*, 60, 63-66
(1993).
44. S. Schantz, *J. Phys. Chem.*, 94(9), 6296 (1991).
45. I. Albinsson, B.E. Mellander and J.R. Stevens, *Solid State Ionics*, 1044-1053
(1992).
46. M. Delsignore, H. Farber and S. Petrucci, *J. Phys. Chem.*, 89, 4968 (1985).

CHAPTER THREE

Experimental Procedures

3.1. Preparation of Salts

3.1.1. *Lithium Perchlorate*

Lithium perchlorate (LiClO_4 , m.p. 236°C , Aldrich 99%+) was dried by heating the sample at 160°C for a period of 48 hours under dynamic vacuum. After cooling, the dry sample was transferred to an argon filled glove box for storage.

3.1.2. *Lithium hexafluorophosphate and Lithium tetrafluoroborate*

The LiPF_6 and LiBF_4 salts (Aldrich, 98%) are thermally unstable in their pure form (Figure 3-1), with LiF as the major breakdown product. It was therefore decided that the salts should be used as received.

3.2. Lithium Complexes

Complexes of the form $(M_aX.nL)_b$, where M represents an alkali metal such as lithium, X is a suitable anion and L is a chosen electron donating ligand, were prepared by the Associated Octel Company Ltd [1, 2]. The procedure involves the reaction of an alkali metal M with an anhydrous salt of the anion X in the presence of

the ligand L , and a purified hydrocarbon solvent under an inert atmosphere. For example:



The lithium complex salts used in this work contain ligands of diglyme (DG) or pentamethyldiethylenetriamine (PMDETA). These salt complexes include $\text{LiPF}_6.2\text{DG}$, $\text{LiClO}_4.2\text{DG}$, $\text{LiPF}_6.\text{PMDETA}$, $\text{LiBF}_4.\text{PMDETA}$ and $\text{LiCF}_3\text{SO}_3.\text{PMDETA}$. The main advantage of such complexes, from a preparative point of view, is that high yields may be obtained, they are moisture free and are thermally stable (Figure 3-1). Analysis of the complexes used in this work is shown below in table 3-1 [3].

Table 3-1 Analysis of lithium salt complexes.

	% experimental (theoretical)			
	$\text{LiPF}_6.2\text{DG}^\dagger$		$\text{LiPF}_6.\text{PMDETA}^\ddagger$	
C	34.42	(34.29)	33.72	(33.24)
H	6.13	(6.71)	6.43	(7.13)
N	<0.3	(0)	12.91	(12.92)
Li *	1.7	(1.65)	2.2	(2.1)

[†] Perkin Elmer 2400-CHN Analyser

[‡] LECO-CHNS-932 Analyser

* Inductively coupled plasma emission spectroscopy (ICP) ARL-3410 Minitorch instrument

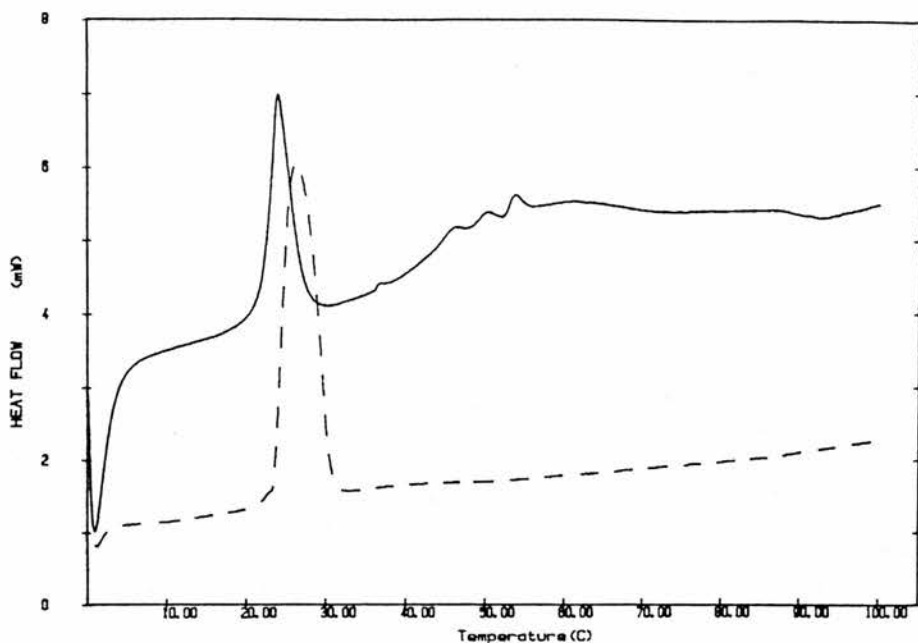


Figure 3-1 DSC heating cycles for (—) LiPF_6 and (---) $\text{LiPF}_6 \cdot 2\text{DG}$.

3.3. Solvent Preparation

3.3.1. Diglyme

Diethyleneglycol - dimethylether (diglyme) (Aldrich, 99%+) was refluxed over fresh lithium under dynamic vacuum. Benzophenone was added as an indicator, changing the colour of the refluxed reaction mixture to a deep blue when the water content was minimised. The middle 60% cut of the solvent was collected and transferred to a glove box for storage.

3.3.2. Poly(ethylene oxide) 400

Low molecular weight poly(ethylene oxide) (PEO400, CH_3 terminated) of average molecular weight 400 (Fluka, 99%+) was dried over 4A molecular sieves for at least one week in a glove box before use.

3.3.3. Tetraglyme and propylene carbonate

Tetraethyleneglycol - dimethylether (tetraglyme) and propylene carbonate (PC) (Aldrich, 99%+) were purified using a 90 plate column Fischer HMS 500C distillation apparatus under dynamic vacuum (10^{-3} mbar) (Fig. 3-2). The relevant temperature settings for each solvent are listed in Table 3-2.

Table 3-2 Temperature settings for the Fischer HMS 500C when distilling tetraglyme and propylene carbonate.

Solvent	Bath temp. °C	(Δt)	Mantle temp. °C	(Δt)
Tetraglyme	147	(8)	90	(3)
Propylene carbonate	120	(14)	57	(3)

After refluxing for at least 1 hour, the first 20% cut was collected at a rate of ca. $25\text{cm}^3\text{hr}^{-1}$. Only the middle 60% cut was kept for use and transferred to a glove box. All solvents were analysed by microelectrode cyclic voltammetry to verify their purity.

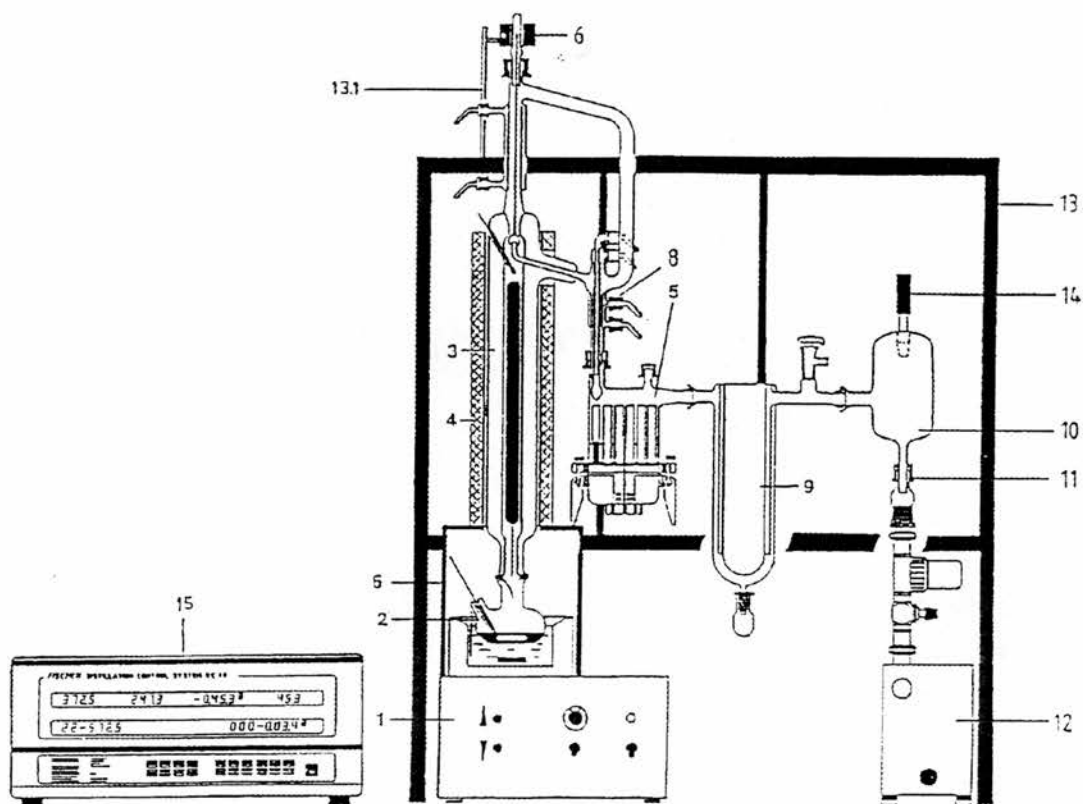


Figure 3-2 General view of the Fischer distillation apparatus HMS 500C.

Legend for Figure 3-2:

- | | | | |
|---|--------------------|------|-----------------------------|
| 1 | Oil bath | 10 | Buffer vessel |
| 2 | Distillation flask | 11 | Vacuum line |
| 3 | SPALTROHR™ column | 12 | Vacuum pump |
| 4 | Heating mantle | 13 | Mounting frame |
| 5 | Fraction collector | 13.1 | Support rod |
| 6 | Solenoid coil | 14 | Vacuum sensor |
| 8 | Distillate cooler | 15 | Distillation control device |
| 9 | Cold trap | | |

3.4. Preparation of Electrolytes

Unless otherwise stated, all operations were performed in an argon filled glove box (mBraun type) where levels of O₂ and H₂O were maintained below 1ppm.

3.4.1. Liquids

All solutions were prepared by directly dissolving known masses of the salt or complex into the desired solvent, followed by stirring to ensure homogeneous mixing.

3.4.2. Amorphous Polymer Electrolytes

Poly(methylene ethylene oxide) (PMEO) of average molecular weight 96000 was prepared according to Booth *et al* [4]. Known masses of PMEO and salt were dissolved in a known quantity of tetraglyme. The solutions were stirred to ensure homogeneity. The casting solvent was then removed on applying a vacuum for 48 hours. Residual tetraglyme was <5wt%.

3.4.3. Gels

Poly(methylmethacrylate) (PMMA) of average molecular weight 120000 (99%+, Aldrich Chemical Co.) was dehydrated at 80°C under vacuum for 12 hours. Known amounts of PMMA was dissolved into the appropriate propylene carbonate solutions and heated to ca. 90-100°C to assist gellification. The final products were highly transparent gels. The macroscopic viscosity of the gel may be altered by varying the

amount of PMMA added. Details of specific gel preparations are described in the appropriate results chapter.

3.5. Instrumentation

3.5.1. Conductivities

All conductance measurements were made by the ac impedance method. Ac experiments were performed using a Solartron 1255 frequency response analyser (FRA) coupled to a Solartron 1286 potentiostat, driven by an IBM compatible PC under software control.

The cells were removed from the glove box and immersed in a water bath at 25°C, or an oil bath at 50°C, and left for at least 1 hour allowing thermal equilibrium to be reached before measurements were made. The frequency response was monitored over the range 1MHz-1Hz.

Low electrolyte concentrations require a cell which can accurately detect small changes in conductance. The cell constant (L/A) of such a cell should therefore be small enough to reflect the small deviations. Similarly, high concentrations require a relatively large cell constant.

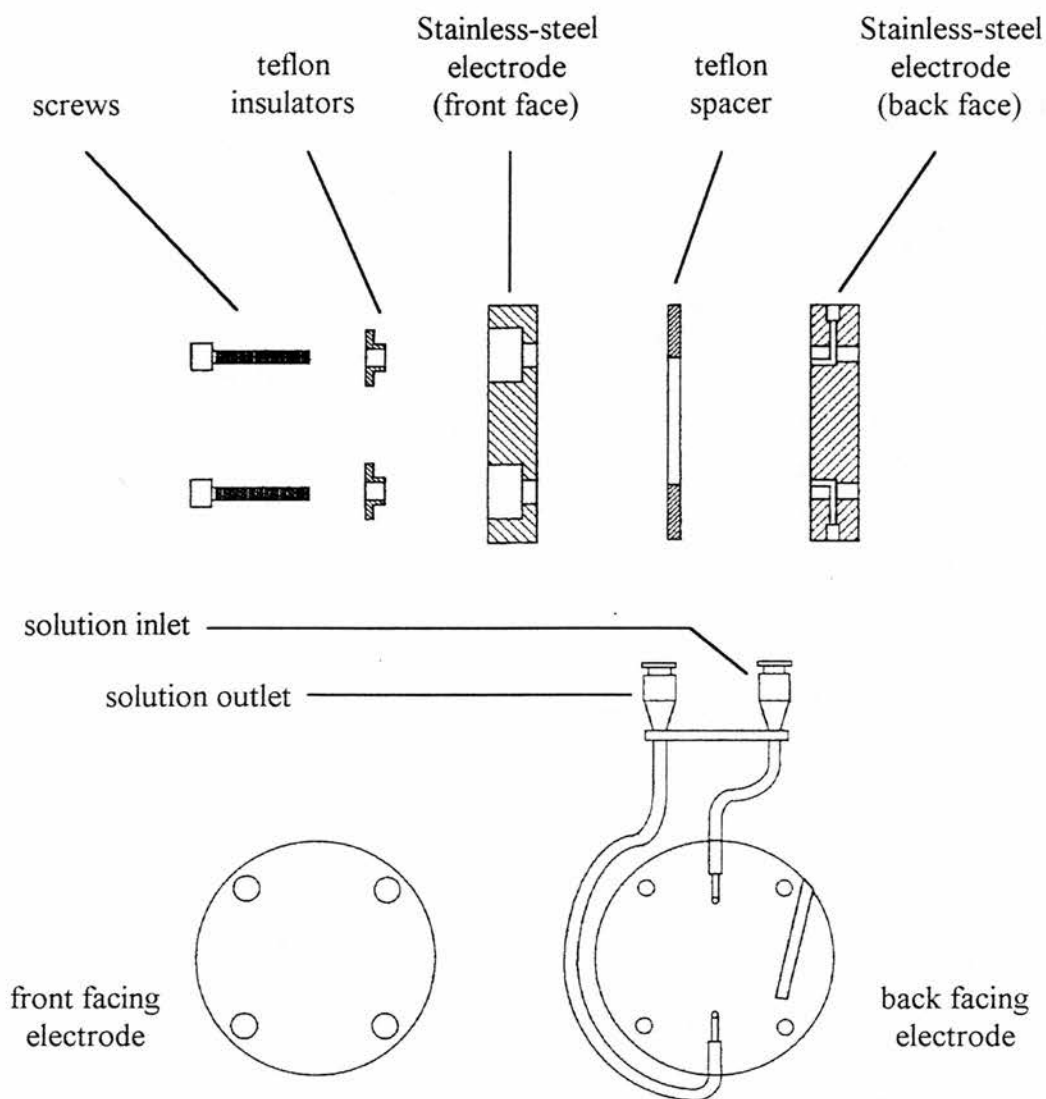


Figure 3-3 Schematic of liquid conductivity cell with low cell constant.

Three cell designs were used throughout the measurements. The first was for the study of electrolytes in low dielectric solvents, such as diglyme and tetraglyme. Fig. 3-3 shows a schematic for the cell design. This cell was constructed of stainless - steel electrodes separated by a teflon spacer. The electrolyte solution was held in a compartment within the spacer, in contact with each electrode. The cell constant was 0.078 cm^{-1} . A syringe was attached to the outlet, and the solution was sucked through

via a teflon inlet tube into the compartment. The teflon taps attached to the cell were then closed within the glove box to seal the solution under argon.

For propylene carbonate solutions, a glass dip-type cell design was used. This cell schematic is shown in Fig. 3-4. The platinum electrodes were sealed into glass such that only one face of each electrode was in contact with the solution. The cell compartment was also made from glass, into which the connecting cap with electrodes was attached. Each of these cells had cell constants of ca. 1.0 cm^{-1} .

3.5.2. Cell Calibration

The cell constant can be calculated by simply measuring the dimensions of the cell. However, this fails to take into account the residual resistance of the connecting leads and roughness of the electrode surfaces. The method chosen here, for liquid work, involved measuring the conductance ($1/R$) of a standard 0.01 molal KCl/water solution. Jones and Bradshaw [5] found the conductivity, κ , at this concentration to be $111.342 \text{ mScm}^{-1}$, which was taken to be the standard. After measuring the background conductance of the distilled water, the cell constant was then found using the expression:

$$\left(\frac{L}{A}\right) = \kappa(R_{\text{solution}} - R_{\text{water}}) \quad 3-4$$

where R_{solution} and R_{water} are the resistances of the KCl solution and the background water, respectively.

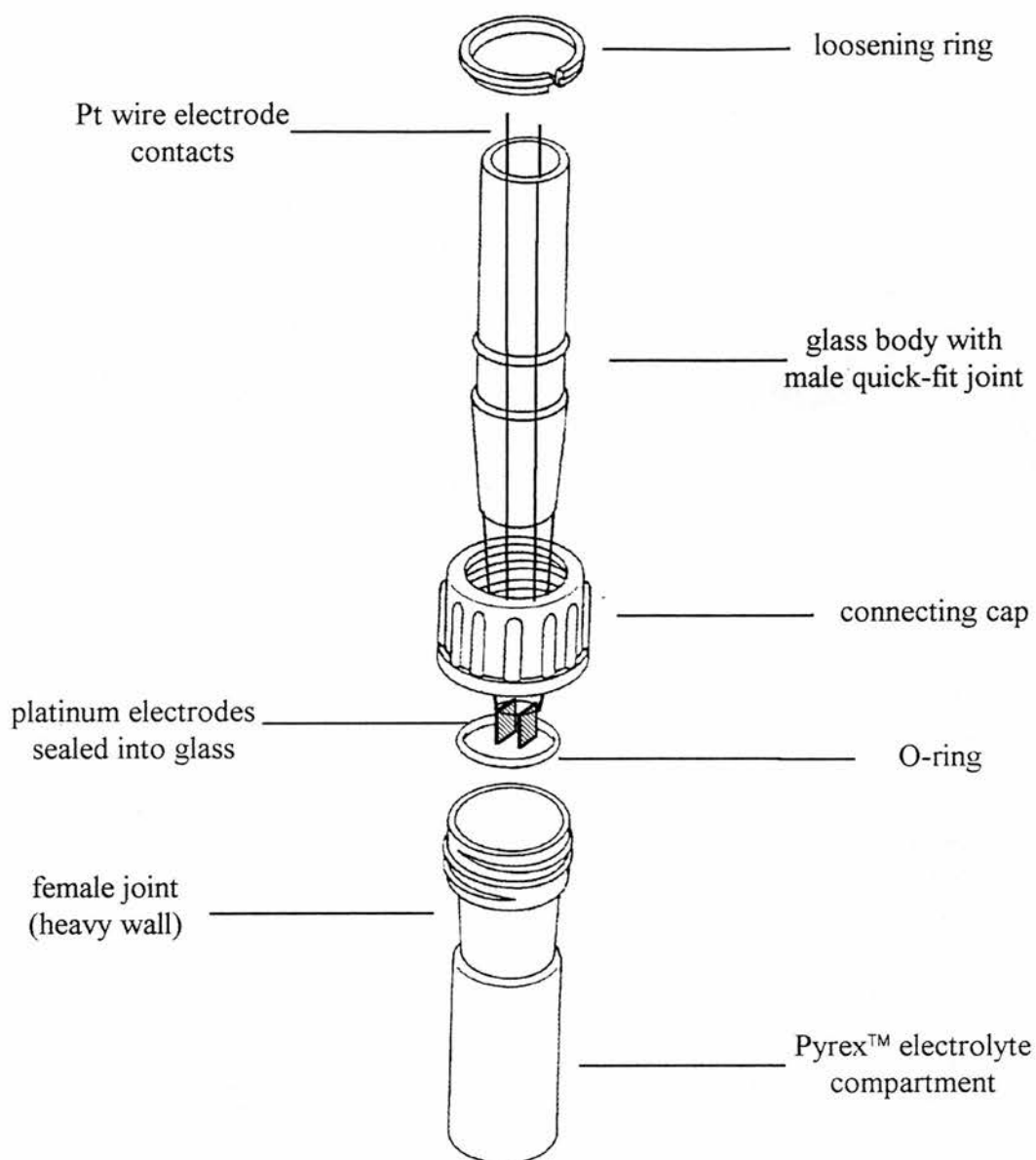


Figure 3-4 Schematic of glass conductivity cell with low cell constant.

3.5.3. Cyclic Voltammetry and Chronoamperometry

Stability window studies on pure solvents, using voltammetry, required a Solartron 1286 potentiostat with a wide potential window capability. The counter-reference electrode for pure solvent work consisted of a glass tube containing a solution of 1M

LiClO₄/propylene carbonate. Into this, a lithium wire (Aldrich Chemical Co.) was dipped, and the end of the tube was closed with a Vicor glass frit attached with heat shrinking teflon. The glass frit allowed electrical continuity to persist without cross-contamination of the different species. Two forms of data collection was used: the potential was applied to the counter electrode while the working micro-electrode was held at virtual ground and the current passing out of the cell was amplified, using an in-house built current amplifier, before being outputted to a Yokogawa x-y recorder; data were collected by an IBM compatible PC under software control (Corrware).

An EG&G PARC potentiostat (model 273A), controlled by an IBM compatible PC under software control (EG&G PARC electrochemical software), were used to collect voltammetry and chronoamperometry data of lithium deposition at a microelectrode. A low-pass filter was applied at all times. Chronopotentiometry experiments were performed using a Solartron 1286 potentiostat driven by an IBM compatible PC under software control (Corrware).

The cell constructions for liquids and solids (including gels) are shown in Fig. 3-5 (a) and (b), respectively. A lithium metal wire was used as a counter-reference in the liquid systems (placed directly into solution) and a lithium disk pressed onto a stainless steel contact was used with the solid samples.

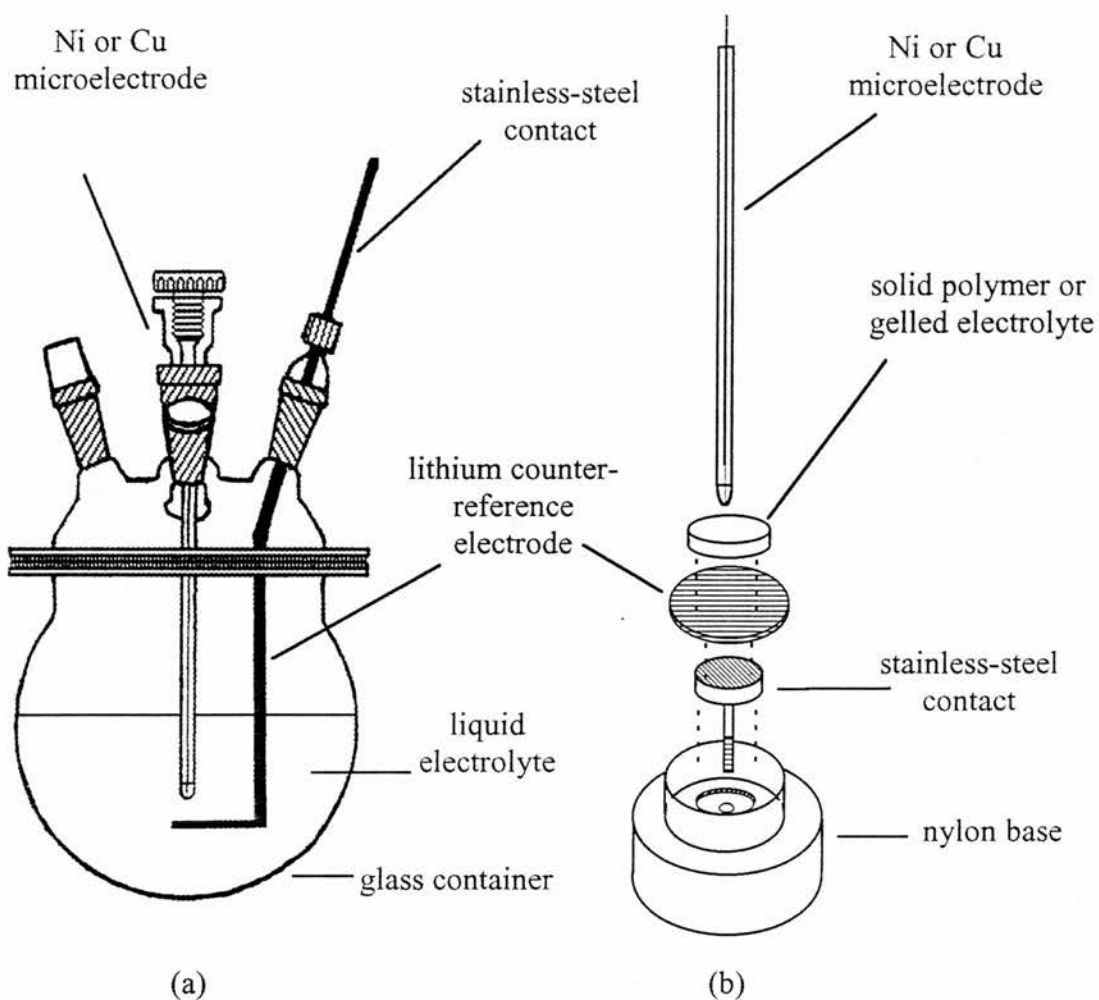


Figure 3-5 Schematics of microelectrode cells for (a) liquids and (b) solid polymers and gels.

3.5.4. Microelectrode Construction

The micro-working electrodes were prepared by rapidly collapsing glass onto nickel or copper wire of appropriate diameter (usually $25\mu\text{m}$), followed by cutting to reveal the micro-disk. Electrical contact was made by connecting a 0.5mm copper wire to

the microwire via solder or a lead plug. The glass seal was checked for selected samples by SEM analysis.

The electrodes were polished first with alumina of decreasing sizes (1 μm , 0.3 μm and 0.05 μm) suspended in water. Polishing was repeated in the argon filled dry box using 0.05 μm alumina suspended in the appropriate polyether or non-aqueous solvent on chemically resistant polishing cloth (Beuhler), followed by rinsing.

3.5.5. *Differential Scanning Calorimetry*

DSC scans were performed on a Perkin Elmer DSC7 differential scanning calorimeter, an IBM compatible PC and TAC 7/3 instrument controller. A liquid nitrogen cooler was used. A sample of the hot pressed polymer electrolyte film was sealed into an aluminium sample pan inside the glove box. Heating and cooling cycles over an appropriate temperature range were applied (10 $^{\circ}\text{C}/\text{min}$), using a sealed argon filled pan as reference.

3.5.6. *Nmr Measurements*

Lithium-7 spectra were obtained using a Bruker AM-300 series spectrometer operating at a frequency of 116.638 MHz. Lithium salt solutions were contained in 5mm nmr tubes and chemical shifts were measured with respect to an external saturated LiCl/D₂O reference at zero. Corrections for magnetic susceptibility were not made.

REFERENCES

1. Duracell Inc., Improved method for preparing non-aqueous electrolytes, *European Patent Application N^o. 90302078.2* (Sept. 1990).
2. The Associated Octel Company Ltd., Lewis base complexes of alkali metal salts, *European Patent Application N^o. 88309913.7* (Oct. 1988).
3. The Associated Octel Company Ltd., *personal communication*.
4. J.R. Craven, R.H. Mobbis, C. Booth and J.R.M. Giles, *Macromol. Chem. Rapid Comm.*, 7, 81 (1986).
5. G. Jones and B.C. Bradshaw, *J. Am. Chem. Soc.*, 55, 1780 (1933).

CHAPTER FOUR

Conductivities and Ion Association in Non-aqueous Media

4.1. Introduction

In practical lithium battery systems the choice of electrolyte solution, optimisation of its salt concentration and purification control are important factors. An electrolyte possessing high specific conductivity with minimal ion-ion interactions is required to maintain the cell at low internal resistance. Since very concentrated solutions ($>0.5\text{M}$) are generally used in practical battery systems, an understanding of the properties of these solutions is required before an electrolyte solution with optimum performance can be selected.

Conductance studies have been performed as a function of lithium salt complex [1, 2] concentration in low molecular weight polyether solvents and in propylene carbonate. The parameters characteristic of solution structure, such as molar conductivity at infinite dilution and association constants, have been extracted and the observed differences in the parameter values are discussed in terms of ion-ion and ion-solvent interactions.

4.2. Determination of Solvent Relative Permittivities

Interpretation of the conductivity results reported in the following sections require the knowledge of the relative permittivity, or dielectric constant ϵ_r , of the solvent media under investigation. Although values of the dielectric constant for PC are well documented in the literature as 64.92 [3] at 298K, there is a lack of such data for some low permittivity solvents, including diglyme and tetraglyme.

The relative permittivity is given by C_b/C_0 in a cell of unit dimensions, where C_b is the bulk capacitance of the pure solvent and C_0 is the vacuum capacitance. As the first step, an ac-impedance measurement of propylene carbonate was performed as an indicator of the accuracy of the technique. The complex impedance plot obtained is shown in figure 4-1. At the angular frequency corresponding to the maximum of the semicircle, $\omega_{max} = 2\pi f$, the magnitude of the impedance of the resistor and capacitor are equal:

$$R_b = \frac{1}{\omega_{max} C_b}$$

thus $\omega_{max} R_b C_b = 1$

4-1

In general, the high frequency response yields information about the properties of the medium between the electrodes. The high frequency semicircle in figure 4-1 yields the bulk resistance of propylene carbonate due to residual impurities in the cell as $R_b =$

52k Ω , and given ω_{max} the bulk capacitance was determined as $C_b = 8 \times 10^{-10}$ F using eqn. 4-1.

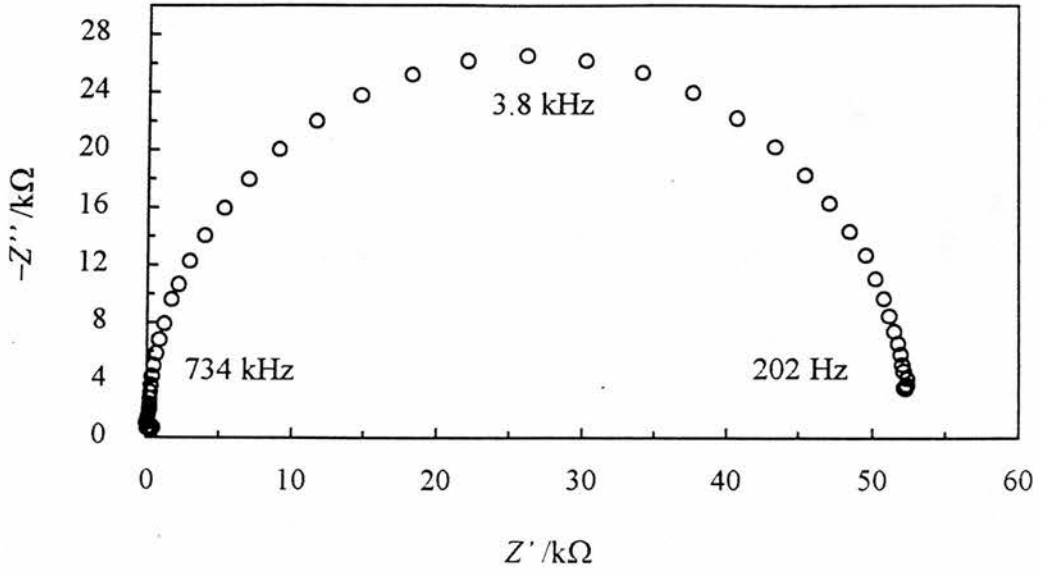


Figure 4-1 Ac-impedance plot of propylene carbonate over the frequency range 202 Hz to 734 kHz.

For a cell with electrode separation L and electrode area A , C_b is related to the dielectric constant of the solvent by

$$C_b = \epsilon_r \epsilon_0 \left(\frac{L}{A} \right)^{-1}$$

leading to
$$\epsilon_r = \frac{C_b \left(\frac{L}{A} \right)}{\epsilon_0} \tag{4-2}$$

The results are summarised in table 4-1.

Table 4-1 Calculated dielectric constants for some non-aqueous solvents.

Solvent	Dielectric Constant		
	<i>this work</i>	<i>literature</i>	
propylene carbonate	64.9	64.92	[3]
diglyme	7.02	-	
tetraglyme	7.28	-	
PEO 400	-	7.83	[4]

4.3. Ion Association

Tables 4-2 to 4-13 list the specific conductivity and molar conductivity data as a function of concentration for LiPF_6 , $\text{LiPF}_6 \cdot 2\text{DG}$, $\text{LiPF}_6 \cdot \text{PMDETA}$, LiClO_4 and $\text{LiClO}_4 \cdot 2\text{DG}$ in some non-aqueous solvents including diglyme, tetraglyme, poly(ethylene oxide) 400 and propylene carbonate.

Table 4-2 Molar conductivities of LiClO_4 in diglyme at 25°C.

$c / 10^3 \text{ mol dm}^{-3}$	$\kappa / \text{mScm}^{-1}$	$\Lambda / \text{Scm}^2 \text{mol}^{-1}$
0.20192	0.001918	9.500
0.40628	0.003304	8.131
0.77218	0.004408	5.709
1.5442	0.005936	3.844
3.0940	0.01066	3.446
6.2189	0.01837	2.954
12.650	0.03432	2.713
26.030	0.07212	2.771

Table 4-3 Molar conductivities of LiClO₄.2DG in diglyme at 25°C.

$c / 10^3 \text{ mol dm}^{-3}$	$\kappa / \text{mS cm}^{-1}$	$\Lambda / \text{S cm}^2 \text{ mol}^{-1}$
0.17222	0.001720	9.989
0.36440	0.002573	7.062
0.71231	0.003933	5.521
1.4823	0.005966	4.025
3.0303	0.01020	3.365
6.0493	0.01704	2.818
11.975	0.03483	2.908
24.446	0.07070	2.892
30.527	0.08731	2.860
39.823	0.1140	2.862
49.980	0.1475	2.951

Table 4-4 Molar conductivities of LiPF₆.2DG in diglyme at 25°C.

$c / 10^3 \text{ mol dm}^{-3}$	$\kappa / \text{mS cm}^{-1}$	$\Lambda / \text{S cm}^2 \text{ mol}^{-1}$
0.21907	0.003201	14.61
0.43936	0.005120	11.65
0.87478	0.008089	9.247
1.7409	0.01297	7.451
3.4697	0.02135	6.153
6.9778	0.03743	5.364
13.905	0.06991	5.028
21.354	0.1099	5.147
27.707	0.1421	5.127
44.770	0.2337	5.221

Table 4-5 Conductivity data of LiPF₆ in TG at 25°C.

$c / 10^3 \text{ mol dm}^{-3}$	$\kappa / \text{mScm}^{-1}$	$\Lambda / \text{Scm}^2 \text{mol}^{-1}$
5.5722	0.01817	3.261
8.5046	0.02473	2.908
14.580	0.04064	2.787
21.862	0.06121	2.800
31.589	0.08984	2.844
44.784	0.1344	3.001
68.612	0.2205	3.214
99.349	0.3397	3.419
148.92	0.5450	3.659
240.97	0.9268	3.846
357.39	1.319	3.691
478.27	1.698	3.550
819.14	2.262	2.761
1263.1	2.203	1.744

Table 4-6 Conductivity data of LiPF₆.2DG in TG at 25°C.

$c / 10^3 \text{ mol dm}^{-3}$	$\kappa / \text{mScm}^{-1}$	$\Lambda / \text{Scm}^2 \text{mol}^{-1}$
3.0784	0.01078	3.500
4.9710	0.01522	3.063
8.1521	0.02291	2.811
12.603	0.03405	2.701
17.809	0.04796	2.693
27.294	0.07433	2.723
38.030	0.1077	2.833
57.366	0.1725	3.006
95.091	0.3110	3.271
147.14	0.5148	3.498
222.30	0.8374	3.767
338.21	1.254	3.708
571.06	1.985	3.476
1002.1	2.860	2.854

Table 4-7 Conductivity data of LiPF₆.PMDETA in tetraglyme at 25°C.

$c / 10^3 \text{ mol dm}^{-3}$	$\kappa / \text{mScm}^{-1}$	$\Lambda / \text{Scm}^2 \text{mol}^{-1}$
9.5027	0.02627	2.7650
12.213	0.03322	2.720
16.002	0.04268	2.667
24.028	0.06389	2.659
30.170	0.08164	2.706
42.952	0.1189	2.768
59.733	0.1705	2.854
92.422	0.2770	2.997
141.91	0.4397	3.098
220.46	0.6771	3.071
359.31	1.063	2.959
482.63	1.290	2.673
637.63	1.496	2.346
1019.1	1.768	1.735

Table 4-8 Conductivity data of LiPF₆ in PEO 400 at 25°C.

$c / 10^3 \text{ mol dm}^{-3}$	$\kappa / \text{mScm}^{-1}$	$\Lambda / \text{Scm}^2 \text{mol}^{-1}$
8.5035	0.00802	0.9427
13.095	0.01262	0.9637
18.417	0.01749	0.9495
26.923	0.02603	0.9669
40.274	0.04001	0.9935
58.319	0.05983	1.026
85.603	0.09280	1.084
121.82	0.1416	1.163
182.90	0.2193	1.199
262.66	0.3172	1.207
383.51	0.4445	1.159
530.94	0.5579	1.051
866.90	0.6616	0.7631
1208.2	0.6192	0.5125

Table 4-9 Conductivity data of LiPF₆.2DG in PEO 400 at 25°C.

$c / 10^3 \text{ mol dm}^{-3}$	$\kappa / \text{mScm}^{-1}$	$\Lambda / \text{Scm}^2 \text{mol}^{-1}$
7.2717	0.007530	1.036
11.510	0.01130	0.9816
16.067	0.01553	0.9667
28.370	0.02776	0.9784
37.806	0.03822	1.011
52.966	0.05625	1.062
66.476	0.07360	1.107
93.163	0.1081	1.160
132.39	0.1652	1.248
198.77	0.2599	1.308
295.77	0.4034	1.364
399.58	0.5514	1.380
659.87	0.8681	1.316
998.79	1.196	1.197

Table 4-10 Conductivity data of LiPF₆.PMDETA in PEO 400 at 25°C.

$c / 10^3 \text{ mol dm}^{-3}$	$\kappa / \text{mScm}^{-1}$	$\Lambda / \text{Scm}^2 \text{mol}^{-1}$
9.8445	0.007530	0.7649
15.310	0.01130	0.7380
23.948	0.01553	0.6486
37.009	0.02776	0.7500
57.001	0.03822	0.6705
86.478	0.05625	0.6504
122.26	0.07360	0.6020
179.92	0.1081	0.6009
260.11	0.1652	0.6353
354.17	0.2599	0.7338
544.44	0.4034	0.7409

Table 4-11 Conductivity data of LiPF₆ in PC at 25°C.

$c / 10^3 \text{ mol dm}^{-3}$	$\kappa / \text{mScm}^{-1}$	$\Lambda / \text{Scm}^2 \text{mol}^{-1}$
13.004	0.2804	21.56
17.162	0.3606	21.01
26.315	0.5396	20.51
34.321	0.6769	19.72
45.535	0.8816	19.36
67.611	1.227	18.15
91.156	1.634	17.92
117.18	1.997	17.05
249.23	4.125	16.55
498.50	5.625	11.28
744.60	6.125	8.226
998.50	6.000	6.009

Table 4-12 Conductivity data of LiPF₆·2DG in PC at 25°C.

$c / 10^3 \text{ mol dm}^{-3}$	$\kappa / \text{mScm}^{-1}$	$\Lambda / \text{Scm}^2 \text{mol}^{-1}$
7.5544	0.1533	20.29
11.286	0.2222	19.69
17.154	0.3341	19.48
28.890	0.5403	18.70
43.099	0.7876	18.27
60.684	1.070	17.63
75.625	1.302	17.22
94.784	1.566	17.05
113.65	2.141	16.87
140.63	2.320	16.50
171.55	2.988	17.42
273.19	4.243	15.53
401.00	5.426	13.53
498.46	7.000	14.04
604.59	6.818	11.28
750.77	8.250	10.99
996.92	8.563	8.589
1150.6	8.550	7.431

Table 4-13 Conductivity data of LiPF₆.PMDETA in PC at 25°C.

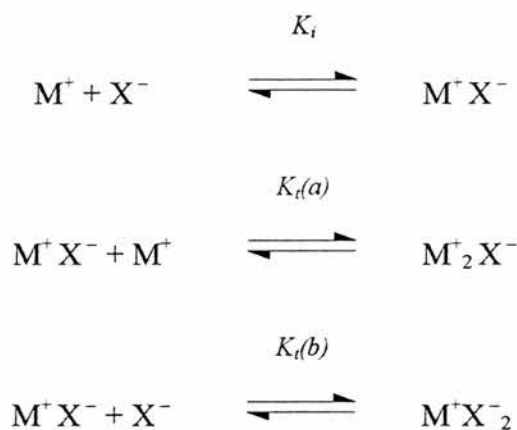
$c / 10^3 \text{ mol dm}^{-3}$	$\kappa / \text{mScm}^{-1}$	$\Lambda / \text{Scm}^2 \text{mol}^{-1}$
7.2902	0.1919	26.33
13.732	0.3406	24.80
25.681	0.5951	23.17
42.188	0.9335	22.13
65.862	1.382	20.98
96.676	2.044	20.33
106.44	2.149	20.19
146.82	2.860	19.48
237.45	4.104	17.28
365.01	5.428	14.87
498.46	6.625	13.29
588.99	7.035	11.94
747.69	7.688	10.28
996.92	8.125	8.150
1130.1	8.239	7.290

4.3.1. Low Permittivity Media

When the solvent permittivity is relatively high and the solution has a moderate salt concentration, the only significant associated species present is ion-pairs [5]. If the solvent permittivity is relatively low, ion-ion interactions dominate and contact ion-pairs, triple ions and even larger aggregates may be stable [6].

The conductance behaviour of LiPF₆, LiPF₆.2DG and LiPF₆.PMDETA in tetraglyme and PEO400 are shown in Figures 4-2 and 4-3. The profiles of these curves are representative of most electrolyte systems in solvents of low dielectric constant, with a sharp decrease in the molar conductivity on increasing concentration from high

dilution, a conduction minimum followed by an increase in the molar conductivity once again. Assuming the charge carriers in the most dilute region of each solution are free ions, the observed fall in the molar conductivity at low concentration is due to the formation of neutral ion-pairs. The rise in molar conductivity from 0.02 to 0.2 mol dm⁻³ has been attributed to the formation of charged triple-ions [6] such as [Li₂PF₆]⁺, since in this concentration range redissociation [7] of the ion-pair due to an increase in the solution permittivity seems unlikely [8]. The hypothesis that the following equilibria exist (Chapter 2) is made:



where K_i , $K_i(a)$ and $K_i(b)$ are the association constants for ion-pairs and the two triple ion configurations, respectively. At low concentrations, where α_i and α_t are small, and assuming that $K_i(a) = K_i(b) = K_i$, ion-pair formation is dominant and the electrolyte conductance (eqn. 2-96) can be reduced to its limiting form:

$$\Lambda'_m = A' c^{-1/2} + B' c^{1/2} \quad 4-7$$

$$\text{where } A' = \Lambda_0 \sqrt{\frac{1}{K_i}} \quad \text{and} \quad B' = \Lambda_0^2 K_i \sqrt{\frac{1}{K_i}} \quad 4-8$$

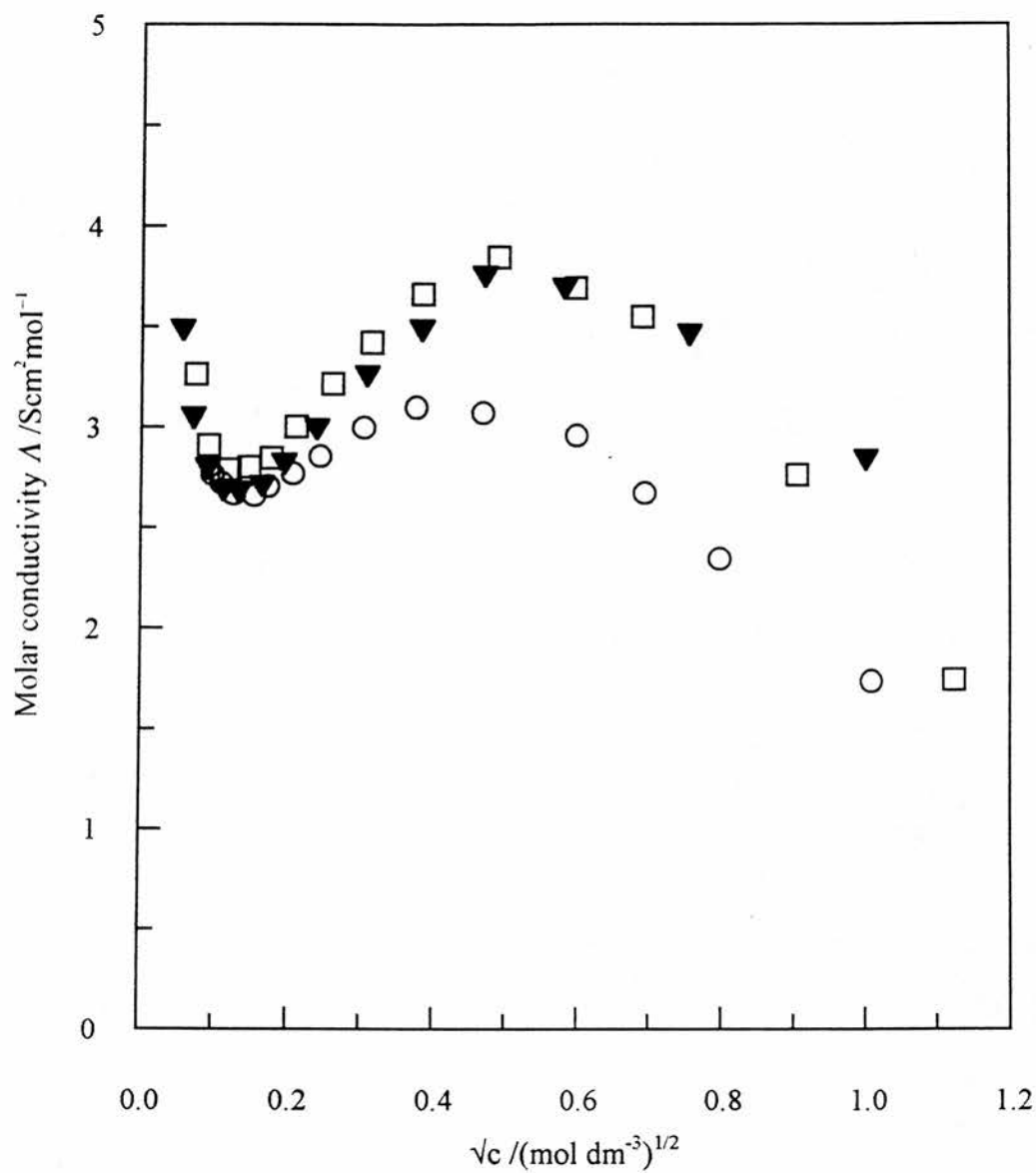


Figure 4-2 Molar conductivity of tetraglyme at 25°C containing (□) LiPF₆, (▼) LiPF₆·2DG and (○) LiPF₆·PMDETA.

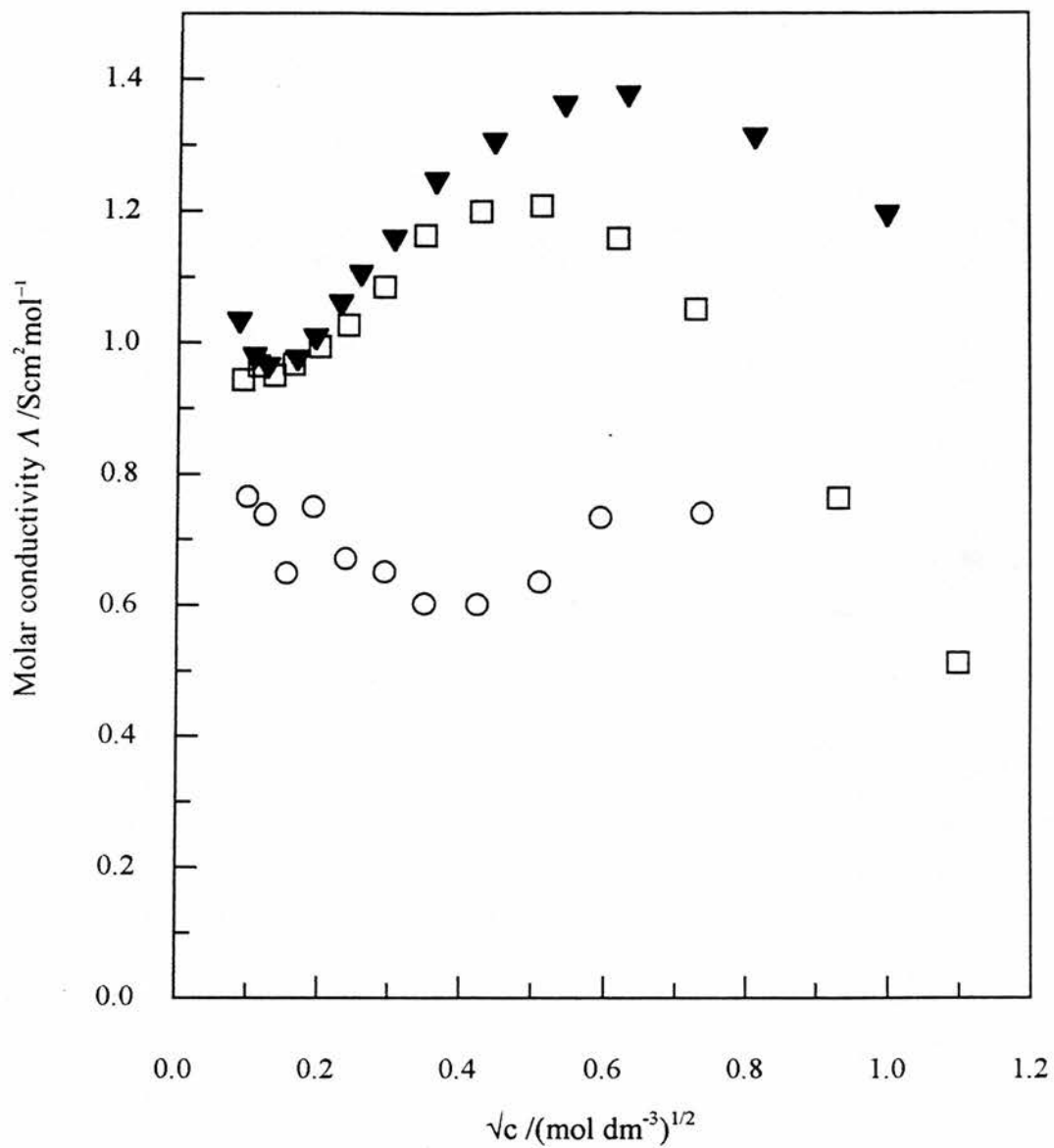


Figure 4-3 Molar conductivity of PEO400 at 25°C containing (□) LiPF₆, (▼) LiPF₆·2DG and (○) LiPF₆·PMDETA.

To apply eqn. 4-7, it is necessary to have estimates of the limiting molar conductivities of the free ions, Λ_0 and the triple ions, Λ_0^T . In many conductometric studies it is possible to obtain Λ_0 by summing the limiting ionic molar conductivities of electrolytes which do not associate [9]. An approximation may also be made by applying Walden's rule [9] which states that for a particular salt the product of its limiting molar conductivity and the viscosity of the solvent in which it is dissolved is approximately constant in different solvent media. That is

$$(\Lambda_0\eta)_{\text{solvent 1}} = (\Lambda_0\eta)_{\text{solvent 2}} \quad 4-9$$

where η is the viscosity of the pure solvent. The data set [10] in table 4-14 was used to calculate a mean Walden product for LiClO_4 as $(\Lambda_0\eta)_{\text{mean}} = 0.614 \text{ Scm}^2\text{Pmol}^{-1}$. The viscosity of diglyme at 25°C is $\eta = 9.81 \times 10^{-3} \text{ P}$ and by applying eqn. 4-9 the limiting molar conductivity in diglyme was estimated as $\Lambda_0(\text{LiClO}_4/\text{DG}) = 62.6 \text{ Scm}^2\text{mol}^{-1}$. The $\text{LiClO}_4 \cdot 2\text{DG}$ complex was assumed to be an identical system to that of the pure salt in diglyme, and therefore the Λ_0 values were taken to be the same. The ratio Λ_0^T/Λ_0 was required for the determination of the triple-ion association constant, K_t .

Fuoss predicted that Λ_0^T/Λ_0 could be found from the temperature coefficient of conductance over a wide range of temperature. Initially, Fuoss and Kraus assumed [6] that the ratio $\Lambda_0^T/\Lambda_0 = 1/3$ but Boileau and Hemery [11] have since recognised that

this is likely to be an underestimate and prefer to take a ratio of 2/3 giving Λ_0^T (LiClO₄/DG) = 41.7 Scm²mol⁻¹.

Table 4-14 Walden products of LiClO₄ in a range of low dielectric constant solvents at 25°C; 1,2-DME: 1,2 - dimethoxyethane; 1,3-DXL: 1,3-dioxolane; N,N-DMF: N,N - dimethylformamide.

Solvent	Λ /Scm ² mol ⁻¹	η /10 ³ P	$\Lambda_0\eta$ /Scm ² P mol ⁻¹
1,2 - DME	149	4.13	0.615
1,3 - DXL	104	5.89	0.612
N,N - DMF	77.4	7.96	0.616

Similarly, the LiPF₆.2DG complex in DG was assumed to be structurally identical to the solvated pure salt, allowing Λ_0 to be estimated as before. Very little literature data is available for LiPF₆, however. Yoshio *et al* [12] proposed that the limiting equivalent triple-ion conductivity in DME ($\eta = 4.5 \times 10^{-3}$ P) was Λ_0^T (LiPF₆/DME) = 96.8 ± 1 Scm²mol⁻¹, taking $\Lambda_0^T/\Lambda_0 = 2/3$. Hence, Λ_0 (LiPF₆/DME) = 144.5 ± 0.8 Scm²mol⁻¹. After obtaining the Walden product for LiPF₆/DME as $\Lambda_0\eta = 0.650$ Scm²Pmol⁻¹ and applying eqn. 4-9, we have Λ_0 (LiPF₆/DG) = 66.3 Scm²mol⁻¹. Using this value for LiPF₆, Λ_0^T was found to be 44.2 Scm²mol⁻¹. A similar calculation was performed to obtain the limiting molar conductivities of LiPF₆ in tetraglyme and PEO400, taking η (tetraglyme) = 3.30×10^{-2} P and η (PEO 400) = 0.1453 P [4].

In propylene carbonate (Table 4-17) the radii of the solvated complexed cations are $R(\text{Li}^+\cdots 2\text{DG}) = 3.87\text{\AA}$ and $R(\text{Li}^+\cdots \text{PMDETA}) = 4.32\text{\AA}$. Assuming that the ligands are the only species present in the first solvation sphere, the R values obtained may be used as an estimate of the Stokes radii, r , in tetraglyme. For a univalent ion, Stokes law [9] reduces to $\lambda_0 = 0.820/\eta r$ \AA , where λ_0 is the limiting molar ionic conductivity. The limiting molar cationic conductivities in TG were calculated as $\lambda_0(\text{Li}^+\cdots 2\text{DG}) = 6.421$ and $\lambda_0(\text{Li}^+\cdots \text{PMDETA}) = 5.752 \text{ Scm}^2\text{mol}^{-1}$. In PC, $\lambda_0(\text{PF}_6^-) = 16.13 \text{ Scm}^2\text{mol}^{-1}$ (section 4.4.2), and on application of the Walden product rule, $\lambda_0(\text{PF}_6^-) = 12.3 \text{ Scm}^2\text{mol}^{-1}$ in TG. Summing the molar ionic conductivities gives $\Lambda_0(\text{LiPF}_6.2\text{DG}/\text{TG}) = 18.7$ and $\Lambda_0(\text{LiPF}_6.\text{PMDETA}/\text{TG}) = 18.0 \text{ Scm}^2\text{mol}^{-1}$. Eqn. 4-9 was then applied to determine Λ_0 for each complex in PEO400.

Table 4-15 Limiting molar conductivities for free ions and triple ions at 25°C.

Solution	Λ_0 $\text{Scm}^2\text{mol}^{-1}$	Λ_0^T $\text{Scm}^2\text{mol}^{-1}$
LiClO ₄ /DG	62.6	41.7
LiPF ₆ /DG	66.3	44.2
LiPF ₆ /TG	18.2	12.1
LiPF ₆ .2DG/TG	18.7	12.5
LiPF ₆ .PMDETA/TG	18.0	12.0
LiPF ₆ /PEO400	4.13	2.75
LiPF ₆ .2DG/PEO400	4.25	2.83
LiPF ₆ .PMDETA/PEO400	4.10	2.73

Rearranging eqn. 4-7 to its linear form

$$\Lambda_c c^{1/2} = A' + B' c$$

4-10

and plotting $\Lambda_c \sqrt{c}$ vs. c , a straight line will be observed with intercept A' and slope B' . Representative plots for LiPF_6 in tetraglyme and $\text{LiPF}_6 \cdot 2\text{DG}$ in PEO400 are shown in Figure 4-4, from which the intercept A' and slope B' were obtained. Curvature was seen in the very dilute region of the diglyme solutions, most likely due to the neglect of interionic effects on mobility.

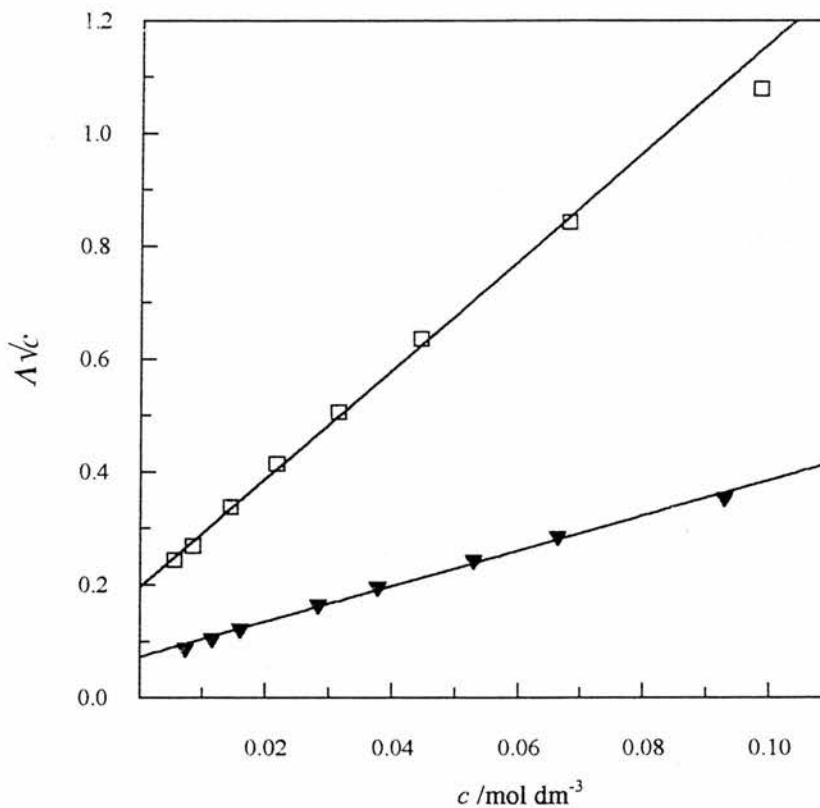


Figure 4-4 Plot of $\Lambda_c \sqrt{c}$ vs. c for (□) LiPF_6 in tetraglyme and (▼) $\text{LiPF}_6 \cdot 2\text{DG}$ in PEO400 at 25°C.

The fitted A' and B' parameters for each electrolyte are given in table 4-16 with both K_i and K_r determined using eqn. 4-8. The rise in molar conductivity observed with the tetraglyme solutions containing hexafluorophosphate salts measured here was more significant than those containing LiClO_4 seen by Gray [13]. All minima occurred at ca. 0.02 mol dm^{-3} in each of the tetraglyme solutions, after which the fraction of charged species increased until ionic mobility became restricted due to higher association and significant solution viscosity. The maximum occurred at ca. 0.25 mol dm^{-3} for tetraglyme containing LiPF_6 or $\text{LiPF}_6 \cdot 2\text{DG}$, and somewhat lower at ca. 0.16 mol dm^{-3} for the $\text{LiPF}_6 \cdot \text{PMDETA}$ solution. Again, the minima for both LiPF_6 and $\text{LiPF}_6 \cdot 2\text{DG}$ in PEO400 occur at ca. 0.02 mol dm^{-3} , as in tetraglyme, however in the presence of the PMDETA ligand the ion mobility not only appears lower, but the point at which charged species becomes significant does not come until a salt concentration of 0.15 mol dm^{-3} .

The similarities between the uncomplexed lithium salt and the DG complex in tetraglyme suggest that either the tetraglyme molecules preferentially coordinate to the Li^+ ion or the TG solvated cation and DG complexed cation are almost identical. The structural difference, however, became apparent as the molecular weight of the solvent was increased to PEO400, in which it appears that the DG ligand successfully shields the cation from further association until a salt concentration greater than 0.35 mol dm^{-3} is reached.

Table 4-16 Fitted A' and B' parameters at 25°C and calculated association constants.

Solution	A' Scm ⁻¹ (cm ³ mol ⁻¹) ^{1/2}	B' Scm ⁻¹ (cm ³ mol ⁻¹) ^{3/2}	K_i dm ³ mol ⁻¹	K_t dm ³ mol ⁻¹
LiClO ₄ /DG	0.1319	15.45	225247	175.84
LiPF ₆ /DG	0.3143	18.55	44498	88.530
LiPF ₆ /TG	0.1962	9.572	8604.9	73.382
LiPF ₆ .2DG/TG	0.1894	8.899	9748.2	70.290
LiPF ₆ .PMDETA/TG	0.2184	7.752	6792.7	53.242
LiPF ₆ /PEO400	0.09361	2.585	1946.5	41.472
LiPF ₆ .2DG /PEO400	0.07277	3.123	3410.9	64.450
LiPF ₆ .PMDETA /PEO400	0.1162	0.7978	1245.0	10.311

4.4.2. High Permittivity Media

Propylene carbonate (PC) has received much attention in recent years as a solvent medium for electrochemical studies with regard to high-energy batteries [14]. It is a stable solvent of moderately high relative permittivity (64.92 at 25°C) [3], a wide liquid range (mp. -42.2°C; bp. 241.7°C) and is inert towards reducing materials such as lithium metal.

The data from all propylene carbonate electrolyte solutions at low salt concentrations, (tables 4-11, 4-12 and 4-13) were analysed with the Fuoss (1978) conductance equation [5, 15] (Chapter 2), expressed as

$$\Lambda = p\{\Lambda_0(1 + RX) + EL\} \quad 4-11$$

$$p = [1 - \alpha(1 - \gamma)] \quad 4-12$$

$$\gamma = 1 - K_\Lambda c \gamma^2 f^2 \quad 4-13$$

$$-\ln f = \frac{\beta k}{2(1 + kR)} \quad 4-14$$

$$\beta = \frac{e^2}{\epsilon kT} \quad 4-15$$

$$K_\Lambda = K_R(1 + K_S) \quad 4-16$$

where RX and EL represent the relaxation and electrophoretic terms, respectively, γ is the fraction of unpaired ions, and α is the fraction of contact pairs. K_Λ is the overall pairing constant evaluated from the association constants of contact-pairs, K_S , and solvent-separated pairs, K_R . All other parameters have their usual meanings [5]. The distance parameter R is defined as the sum of the radii of the cation and anion solvent cospheres. If the centre-centre distance r_{ij} between ions i and j becomes less than R , they are considered to be paired.

The parameters Λ_0 , K_Λ and R were obtained by solving the above equations using the program *SCAN* [16] based on the algorithm developed by Fuoss, where the starting

values of Λ_0 were obtained by a Schedlovsky extrapolation [17]. In practice, the calculations were made by finding the values of Λ_0 and α which minimise

$$\sigma^2 = \frac{\sum_j \{\Lambda_j(\text{calc.}) - \Lambda_j(\text{obs.})\}^2}{(n-2)} \quad 4-17$$

for a sequence of R values, where n is the number of data points. The best-fit value of R corresponds to the minimum in the $\sigma\% = 100\sigma / \Lambda_0$ against R curve. First, a rough scan over a fairly wide range of R values was made, to locate the approximate minimum. A fine scan around this minimum followed and then a final calculation of Λ_0 and α was made using the minimised R value.

Plots of molar conductivity, Λ vs. \sqrt{c} are shown in Fig. 4-5 for LiPF_6 , $\text{LiPF}_6 \cdot 2\text{DG}$ and $\text{LiPF}_6 \cdot \text{PMDETA}$ in propylene carbonate at 25°C. Values of Λ_0 , K_A and R obtained in this way are listed in Table 4-17. Table 4-17 shows that LiPF_6 in the presence of DG can be thought of as relatively unassociated, while the LiPF_6 and $\text{LiPF}_6 \cdot \text{PMDETA}$ appear to form a larger fraction of ion-pairs. Although the molar conductivity for the diglyme complex appears lower than the other salts at high dilution, Λ remains relatively constant to beyond $c = 0.5 \text{ mol dm}^{-3}$. The association constant is related to the distance R , such that as R increases the likelihood of solvent-separated ion-pair formation increases.

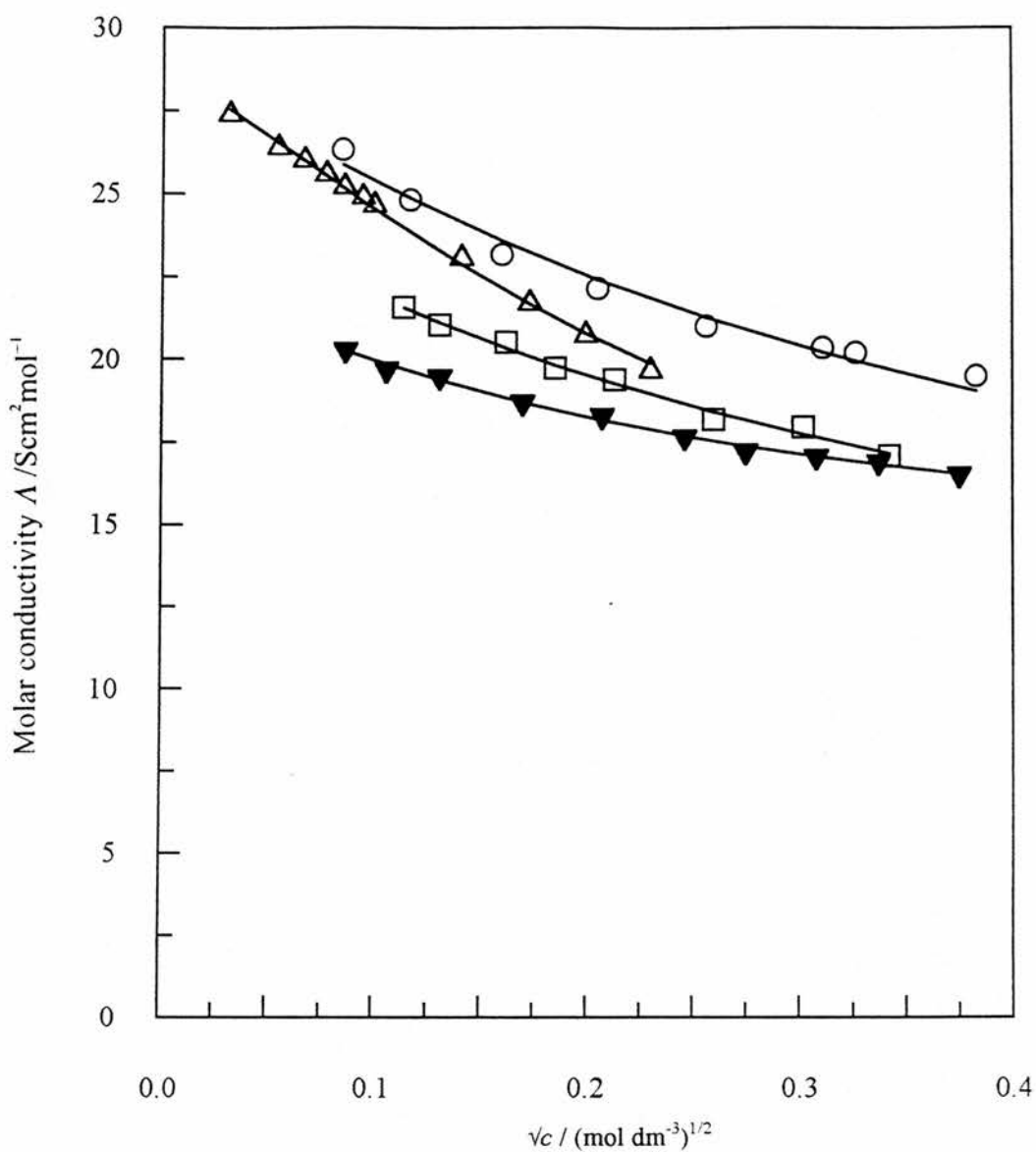


Figure 4-5 Molar conductivity of propylene carbonate at 25°C containing (□) LiPF₆, (▼) LiPF₆·2DG, (○) LiPF₆·PMDETA and (Δ) *LiBF₄. The solid lines represent the fitted conductivity curves according to eqn. 4-11. * Data taken from ref. [18].

Table 4-17 Conductance parameters of LiPF₆ salts in PC at 25°C.

Salt	Λ_0 Scm ² mol ⁻¹	K_A dm ³ mol ⁻¹	K_S	K_R	R Å	Walden Product
LiPF ₆	25.02 ± 0.17	5.69	2.50	1.63	4.66	0.629
LiPF ₆ .2DG	22.58 ± 0.07	2.33	0.72	1.36	3.87	0.567
LiPF ₆ .PMDETA	28.11 ± 0.31	6.20	3.13	1.50	4.32	0.725
LiBF ₄ *	28.48 ± 0.02	10.1	-	-	13.2	0.704

* Taken from ref. [18].

An anion at a distance R from a cation may diffuse further away or toward the cation, eventually forming a contact pair after displacing solvent molecules from within its cosphere. It may be thought that the addition of a ligand about the lithium cation should decrease its mobility.

The data presented here suggests an effect similar to that of conductivity enhancement by addition of crown ethers to non-aqueous solutions [19]. When ligand molecules wrap around the Li⁺ cation a cage, structurally very similar to a crown ether, is formed. While an interior cavity is provided for the cation, the non-polar exterior of the ligands allows passage of the Li⁺-cage through the organic solvent. In the case of the DG this cage also protects the cation from anion association, avoiding the formation of uncharged species and therefore maintaining the fraction of free ions at a level which would otherwise decrease. The pairing distance R for LiPF₆ was found to be 4.66 Å, almost the same as the Stokes radius for Li⁺ in PC (4.8 Å) [20] and much higher than its crystallographic radius [20], indicating substantial solvation

in this medium. If it is assumed that both DG and PMDETA preferentially coordinate to the lithium ion (Chapter 6), then the R values obtained may suggest that the complexed Li^+ may be smaller than the Li^+ cosphere formed from solvation by PC. Since two DG ligands can wrap around the cation the shielding from anion association will be more effective than coordination to a single PMDETA ligand. The limiting molar ionic conductivity for the PF_6^- anion was calculated as $\lambda_0^- = 16.13 \text{ Scm}^2\text{mol}^{-1}$ assuming the independent migration of ions rule holds and that $\lambda_0^+ = 8.89 \text{ Scm}^2\text{mol}^{-1}$ [20]. The higher limiting molar conductivity of Li^+ ---PMDETA suggests that it may in fact be smaller than the Li^+ ---2DG, assuming ion size is the dominating factor upon mobility.

Table 4-18 Limiting ionic conductivities in PC at 25°C.

Cation in PC	$\lambda_0^+ / \text{Scm}^2\text{mol}^{-1}$
Li^+	8.89
Li^+ --- 2DG	6.45
Li^+ --- PMDETA	11.98

4.4. Specific Conductivities

The specific conductivity κ generally passes through a maximum at a salt concentration characteristic of the solvent and solute [21]. In recent years, interest in κ_{max} values for a range of solution mixtures has proved its importance in the development of high energy density lithium rechargeable battery systems [14].

The specific conductivity values κ (mS cm^{-1}) for hexafluorophosphate salts in TG, PEO400 and PC with the corresponding solution concentrations c (mol dm^{-3}) are presented in tables 4-5 to 4-10. The data were analysed using the semi-empirical Casteel-Amis equation [22]

$$\kappa = \kappa_{\max} \left(\frac{c}{c_{\max}} \right)^a \exp \left\{ b(c - c_{\max})^2 - \frac{a}{c_{\max}}(c - c_{\max}) \right\} \quad 4-18$$

where c is the concentration, c_{\max} is the concentration corresponding to the maximum specific conductivity. The constants a and b are arbitrarily chosen and are adjusted during the non-linear least-squares (NLLS) fit along with κ_{\max} and c_{\max} . The Casteel-Amis equation was formulated to fit the specific conductivity κ as a function of the molality (mol kg^{-1}). However, Werblan and Balkowska [23] showed that this equation fits the specific conductivity equally well for molar concentration (mol dm^{-3}) as for molality.

The fitted Casteel-Amis parameters are listed in table 4-19 for each of the electrolyte systems at 25°C. Data for LiAsF_6 , LiClO_4 and LiBF_4 were included [23] for comparison. Experimental points of LiPF_6 , $\text{LiPF}_6 \cdot 2\text{DG}$ and $\text{LiPF}_6 \cdot \text{PMDETA}$ in TG, PEO400 and PC are presented in figures 4-6, 4-7 and 4-8, respectively, with Casteel-Amis fits shown as solid lines. The conductivities of concentrated propylene carbonate solutions of the LiPF_6 complexes were both significantly higher than the pure LiPF_6 salt.

Table 4-19 Casteel-Amis parameters at 25°C for concentrated non-aqueous solutions of LiPF₆, LiPF₆.2DG, LiPF₆.PMDETA, LiAsF₆, LiClO₄ and LiBF₄, where σ is the maximum error.

Solution	κ_{max} mScm ⁻¹	c_{max} mol dm ⁻³	a	b (mol dm ⁻³) ²	σ mScm ⁻¹
LiPF ₆ /TG	2.326	0.9924	1.239	-0.2119	0.014
LiPF ₆ .2DG/TG	3.389	1.961	1.242	0.06138	0.016
LiPF ₆ .PMDETA/TG	1.838	1.705	1.236	0.2149	0.014
LiPF ₆ /PEO400	0.6644	0.9087	1.257	-0.1705	0.0029
LiPF ₆ .2DG/PEO400	1.780	3.220	1.232	0.03928	0.003
LiPF ₆ /PC	6.118	0.7873	1.120	0.3253	0.177
LiPF ₆ .2DG/PC	8.602	1.063	0.9729	-0.1693	0.473
LiPF ₆ .PMDETA/PC	8.225	1.166	0.9625	0.08393	0.087
† LiAsF ₆ /PC	6.262	0.709	0.920	-0.177	0.004
		‡ 0.850			
† LiClO ₄ /PC	5.421	0.662	0.855	0.08	0.019
		‡ 0.794			
† LiBF ₄ /PC	3.715	0.561	0.816	0.177	0.010
		‡ 0.673			

† Taken from reference [23] as a function of molality (mol kg⁻¹).

‡ Converted to a function of molarity.

These results were in direct correlation with the fitted maximum conductivity values κ_{max} for each of the PC systems, decreasing in the order $\text{LiPF}_6\cdot 2\text{DG}$ (8.60 mS/cm) > $\text{LiPF}_6\cdot \text{PMDETA}$ (8.23 mS/cm) > LiAsF_6 (6.26 mS/cm) > LiPF_6 (6.12 mS/cm) > LiClO_4 (5.42 mS/cm) > LiBF_4 (3.72 mS/cm). While behaving in a similar manner to the DG ligand in PC, the PMDETA ligand appears to hinder the mobility of the Li^+ in the liquid polyether media at medium to high concentrations, where the fitted κ_{max} values for each of the polyether systems decreased in the order $\text{LiPF}_6\cdot 2\text{DG}$ > LiPF_6 > $\text{LiPF}_6\cdot \text{PMDETA}$. According to Jasinski [24], the position of the conductivity maximum may be explained by the variation in shielding of the ions by solvent molecules or added ligands.

The existence of a conductance maximum may be thought of as the decrease in conductivity due to restrictions on ion mobility being compensated for by an increase in conductivity due to the higher charge density. Calculation of the coefficient b depends on data at concentrations higher than c_{max} and therefore in a concentration range not sufficiently wide, adjustment of b may be impossible. The value of b tends to be small in all systems [22, 25] and has been shown to become more negative in solvents of decreasing dielectric constant. The coefficient a is mainly controlled by the lower concentration data and appears to be influenced by the solution viscosity. There seems to be several reasons for high values of c_{max} , including weak ion-solvent interactions, small ionic radii or low solvent viscosity. At concentrations up to ca. 0.1 mol dm^{-3} , specific conductivity is governed by almost the same factors that have been considered in highly dilute solutions.

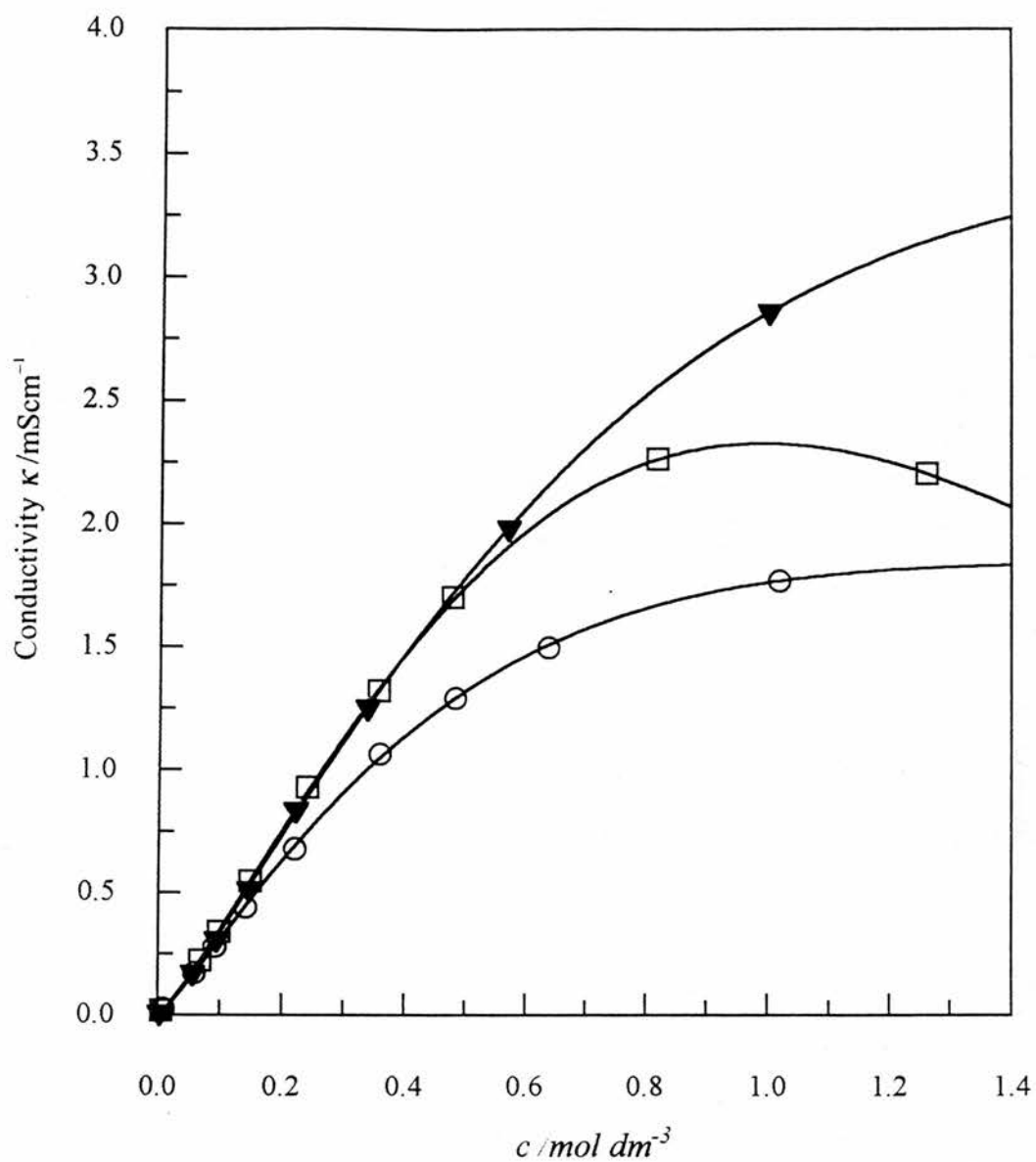


Figure 4-6 Specific conductivity of tetraglyme at 25°C containing (□) LiPF₆, (▼) LiPF₆·2DG and (○) LiPF₆·PMDETA. The fits according to the Casteel-Amis equation are shown as solid lines.

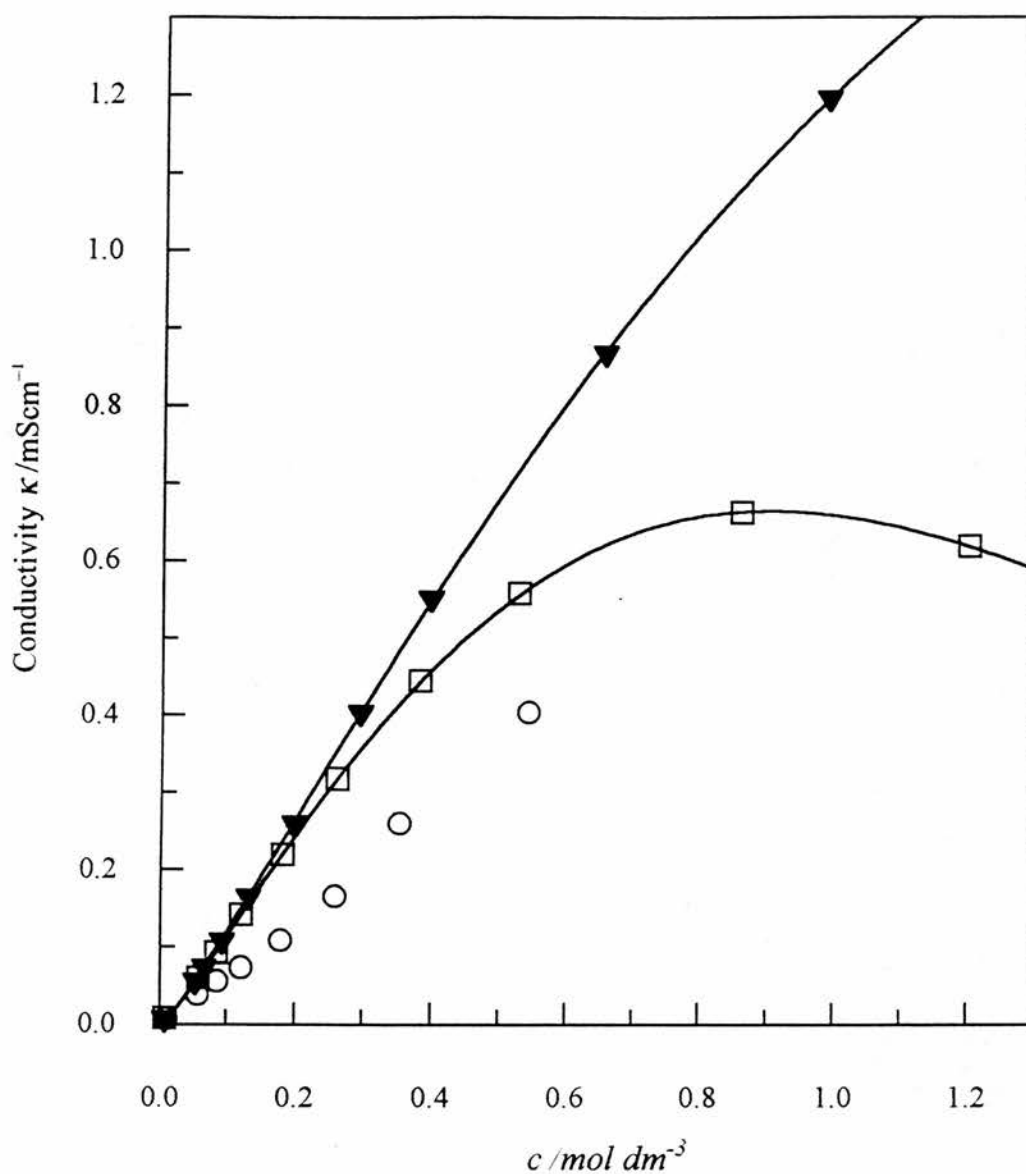


Figure 4-7 Specific conductivity of PEO400 at 25°C containing (□) LiPF₆, (▼) LiPF₆·2DG and (○) LiPF₆·PMDETA. The fits according to the Casteel-Amis equation are shown as solid lines.

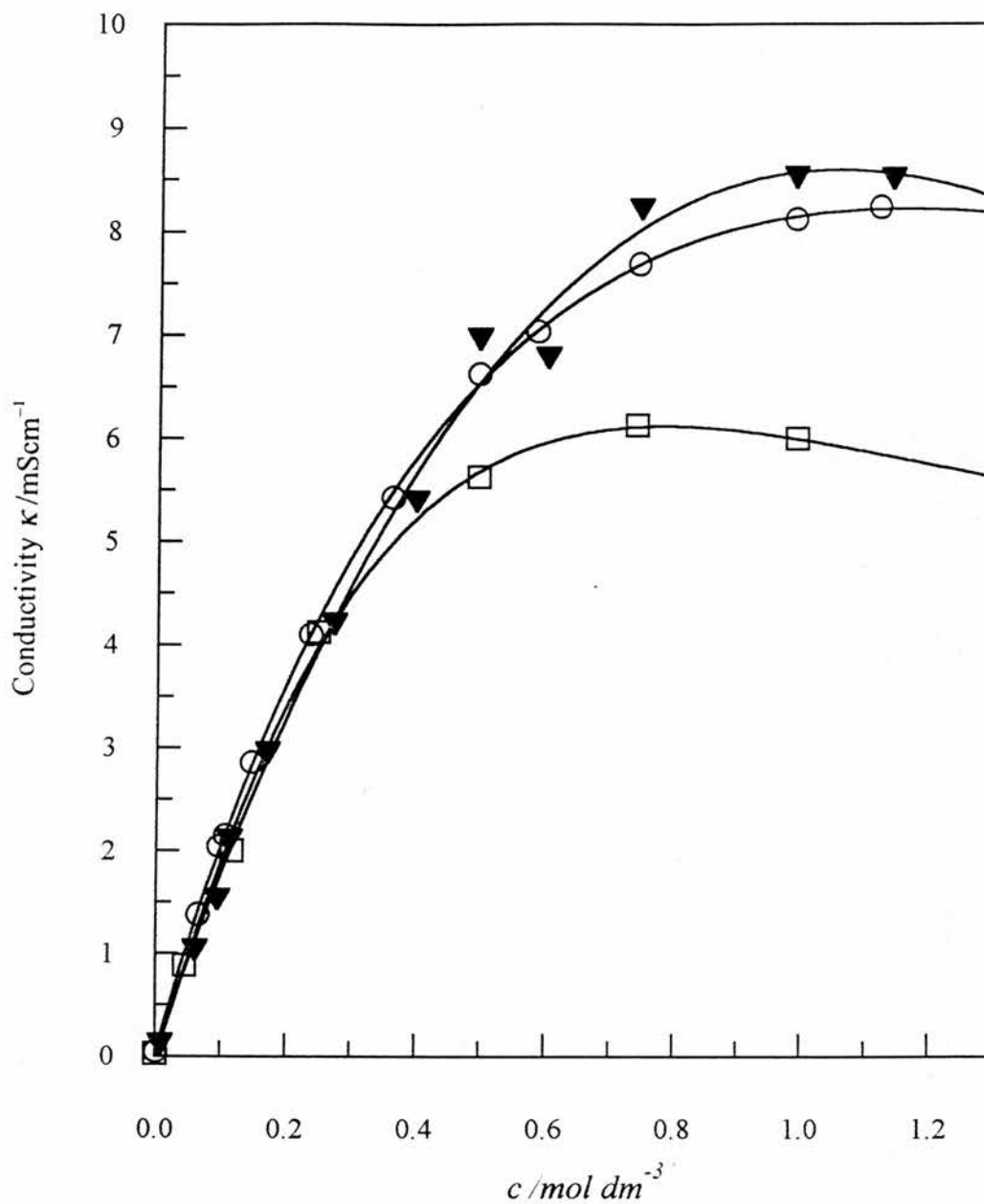


Figure 4-8 Specific conductivity of propylene carbonate at 25°C containing (\square) LiPF_6 , (\blacktriangledown) $\text{LiPF}_6 \cdot 2\text{DG}$ and (\circ) $\text{LiPF}_6 \cdot \text{PMDETA}$. The fits according to the Casteel-Amis equation are shown as solid lines.

At higher concentrations the mobility of ions are governed by factors which are not necessarily accounted for by referring to dilute systems.

Figure 4-9 shows a plot of κ/κ_{max} vs. c/c_{max} for LiPF_6 , $\text{LiPF}_6\cdot 2\text{DG}$ and $\text{LiPF}_6\cdot \text{PMDETA}$ in the polyether solvents and propylene carbonate. A similar plot was also shown by Casteel and Amis [22] for different solutions at varying temperatures.

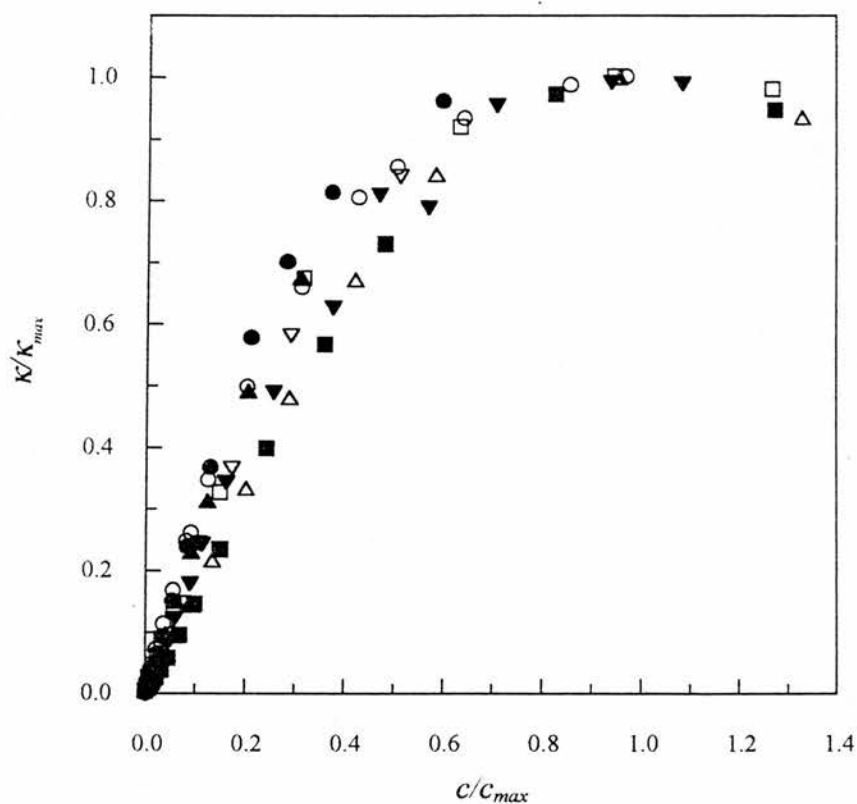


Figure 4-9 Plot of κ/κ_{max} vs. c/c_{max} for all electrolytes from this work listed in table 4-19.

These authors suggested that the opposing forces acting on the electrolyte at the point on the conductivity curve where $c = c_{max}$ and $\kappa = \kappa_{max}$ are virtually the same for any electrolyte solution, regardless of temperature and composition. The results presented here agree well with that idea.

4.5. Conclusions

In low permittivity media, the sharp decrease in molar conductivity at low salt concentrations suggests that association of free ions to non-conducting ion-pairs is dominant. A maximum in the molar conductivity in the moderate to high concentration range gives an indication of the efficiency of the ligand when protecting the Li cation from association. Evidently, the diglyme (DG) ligand was capable of shielding the Li^+ in a similar way as the tetraglyme solvent molecules, while PMDETA was not. As the molecular weight of the polyether was increased, the performance of the DG complex improved, relative to the simple salt, suggesting that the ligand coordination was different from that of the solvent.

In contrast, the association of ions in high permittivity media for the majority of electrolytes is limited to ion-pairs up to moderate salt concentrations. The overall association constants decrease in the order $\text{LiPF}_6 \cdot \text{PMDETA} > \text{LiPF}_6 > \text{LiPF}_6 \cdot 2\text{DG}$ in propylene carbonate (PC), suggesting that the PMDETA “cage” is not able to protect the Li cation in a PC environment at low salt concentration.

The specific conductivity κ generally passes through a maximum characteristic of the salt and solvent. The maximum κ values of the Li salts and complexes in polyether systems decrease in the order $\text{LiPF}_6 \cdot 2\text{DG} > \text{LiPF}_6 > \text{LiPF}_6 \cdot \text{PMDETA}$, while in propylene carbonate κ_{max} decreases in the order $\text{LiPF}_6 \cdot 2\text{DG} > \text{LiPF}_6 \cdot \text{PMDETA} > \text{LiPF}_6$.

REFERENCES

1. Duracell Inc., Improved method for preparing non-aqueous electrolytes, *European Patent Application N^o. 90302078.2* (Sept. 1990).
2. The Associated Octel Company Ltd., Lewis base complexes of alkali metal salts, *European Patent Application N^o. 88309913.7* (Oct. 1988).
3. M.L. Jansen and H.L. Yeager, *J. Phys. Chem.* 77, 3809 (1973).
4. M. Salamon, *personal communication*.
5. R.M. Fuoss, *J. Phys. Chem.*, 82, 2427 (1978).
6. R.M. Fuoss and C.A. Kraus, *J. Amer. Chem. Soc.* 55, 2387 (1933).
7. E.A.S. Cavell and P.C. Knight, *Z. Phys. Chem. (Munich)* 57, 3, (1968).
8. P.G. Bruce and C.A. Vincent, *J. Chem. Soc. Faraday Trans.*, 89(17), 3187-3203 (1993).
9. *Electrolyte Solutions* (Edited by R.A. Robinson and R.H. Stokes), Butterworths, London (1965).
10. J.R. MacCallum, A.S. Tomlin and C.A. Vincent, *Europ. Polymer J.* 20, 787 (1986).
11. S. Boileau and P. Hemery, *Electrochimica Acta*, 21, 647 (1976).
12. M. Yoshio, M. Hyakutake and S. Nishikawa, *Denki Kagaku*, 58(10), 963 (1990).
13. F.M. Gray, *Solid State Ionics* 40/41, 637-640 (1990).
14. *Lithium Batteries* (Edited by J.P. Gabano), Academic Press, London and New York (1983).
15. R.M. Fuoss and R.M. Jarret, *J. Phys. Chem.* 89, 3167-3173 (1985).
16. A.M. Christie, St. Andrews, Scotland (1995).

17. R.M. Fuoss and T. Schedlovsky, *J. Am. Chem. Soc.*, 71, 1496 (1949).
18. P.K. Muhuri and D.K. Hazra, *J. Chem. Soc. Faraday Trans.* 87(21), 3511-3513 (1991).
19. M.L. Kaplan, E.A. Rietman, R.J. Cava, L.K. Holt and E.A. Chandross, *Solid State Ionics* 25, 37-40 (1987).
20. Y. Matsuda, H. Nakashima, M. Morita and Y. Takasu, *J. Electrochem. Soc.*, 128(12), 2552 (1981).
21. J. Barthel, H.J. Gores, P. Carlier, F. Feuerlein and M. Utz, *Ber. Bunsenges Phys. Chem.*, 87, 436 (1983).
22. J.F. Casteel and E.S. Amis, *J. Chem. Eng. Data*, 17(1), 55-59 (1972).
23. L. Werblan and A. Balkowska, *J. Electroanal. Chem.*, 354, 25-38 (1993).
24. R. Jasinski in *Advances of Electrochemistry and Electrical Engineering* vol.8 (Edited by P. Delahay and C.W. Tobias), Wiley, New York (1971).
25. J. Barthel, R. Wachter and H.J. Gores in *Modern Aspects of Electrochemistry*.

CHAPTER FIVE

The Li/Li⁺ Couple in Polyether Electrolytes

5.1. Introduction

The electrochemical process of lithium deposition and dissolution has an important place in studies devoted to the development of rechargeable batteries [1]. Much work has already been done on this subject, mainly in liquid aprotic solvents [2-7]; measurements have also been made at liquid and solid mercury electrodes [8, 9].

Lithium deposition from poly(ethylene oxide)-based electrolytes has been mainly studied at conventional-sized macroelectrodes [10, 11], but since the introduction of microelectrode techniques, experimental problems in highly resistive media are routinely overcome allowing much more detailed information on the kinetics and mechanisms of lithium deposition to be obtained [12]. Electrochemical measurements of lithium deposition at microelectrodes have recently been reported by Farrington *et al* [13] from PEG(400) and by Baril *et al* [14] from solid electrolytes.

In the work described in this chapter, the aim was to determine the kinetics of and mechanisms for lithium deposition from liquid and solid polyether electrolytes containing lithium hexafluorophosphate (LiPF₆) and novel lithium complexes based on this salt. It is known that the thermal stability of LiPF₆ is low, prompting the preparation of thermally stable complexes possessing electrochemical properties

similar to that of the pure salt. The complexes used here are lithium-bis(diglyme)-hexafluorophosphate ($\text{LiPF}_6 \cdot 2\text{DG}$) [15] and lithium-pentamethyl-diethylene triamine-hexafluorophosphate ($\text{LiPF}_6 \cdot \text{PMDETA}$) [16], both found to be thermally stable (Chapter 3) and to enhance conductivity in non-aqueous media (Chapter 4). Tetraglyme and PEO400 are low molecular weight liquid analogues ($-\text{CH}_3$ terminated) of the high molecular weight solid poly(ethylene oxide) (PEO). Poly(methylene ethylene oxide) (PMEO) is a solid polymer of high molar mass which is amorphous at room temperature. Since ion mobility in the high molar mass polymers occurs in the amorphous region, which can be thought of as having a liquid-like structure at the microscopic level, the results from the systems studied here may be extrapolated to the high molar mass PEO systems.

5.2. Results and Discussion

5.2.1. Kinetics of the Li/Li^+ Couple

Figs. 5-1 and 5-2 show voltammograms run at a sweep rate of 10 mV/s at a 25 μm diameter Ni microelectrode vs. Li/Li^+ in tetraglyme containing LiPF_6 and $\text{LiPF}_6 \cdot \text{PMDETA}$ (0.5 mol/kg), respectively. The shapes of the curves for LiPF_6 and $\text{LiPF}_6 \cdot 2\text{DG}$ are typical for a simple plating and stripping process [17]. That is, on the forward sweep the current density is very low until a potential is reached where nucleation of lithium on the nickel surface can take place. The current density then increases rapidly and continues to increase after the scan is reversed since lithium reduction now takes place at lithium centres with increasing surface area. The

deposition process continues until the equilibrium potential of the Li/Li^+ couple at 0V is reached and this is followed by oxidation of the lithium metal at positive potentials with a corresponding anodic stripping peak.

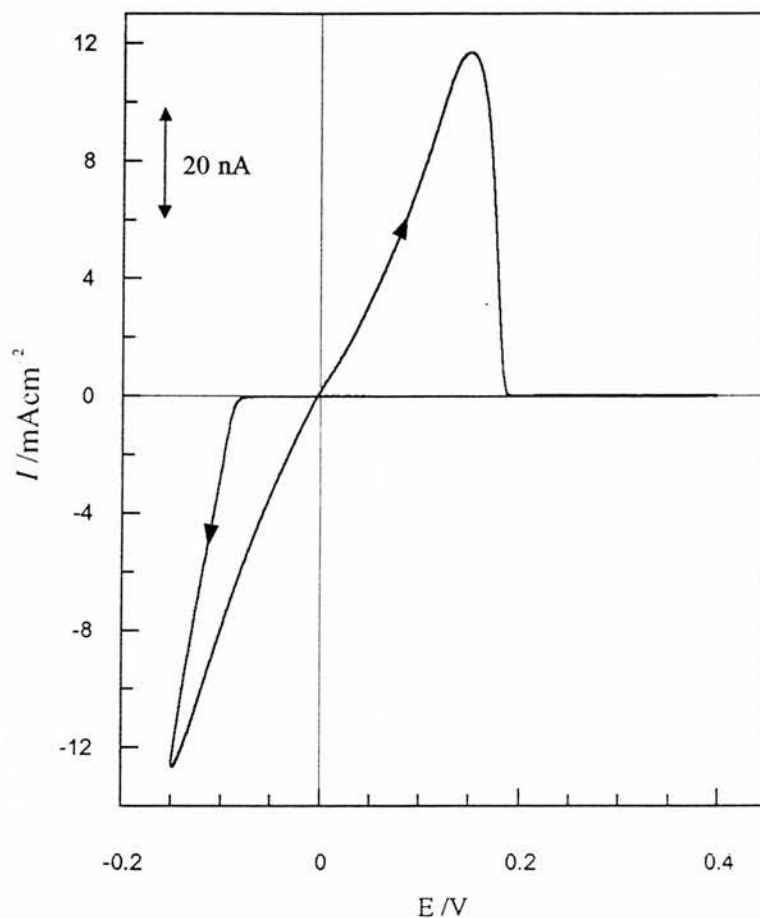


Figure 5-1 Cyclic voltammogram of lithium plating and stripping at a $25\mu\text{m}$ diameter nickel microelectrode vs. Li/Li^+ from LiPF_6 (0.5 mol/kg) in tetraglyme. Sweep rate $\nu = 10\text{mV/s}$.

The voltammogram of the $\text{LiPF}_6\text{.PMDETA}$, however, has a clearly pronounced cathodic plateau and the position of the zero cross-over potential on the reverse scan is cathodic of zero volts, indicating that lithium deposition is accompanied by another

cathodic process. There is no evidence of any other anodic reaction in the potential range applied. On moving the cathodic sweep limit more positive, the plateau decreases in size and the zero cross-over point moves towards the 0V, indicating that the accompanying cathodic process occurs negative of -120mV. Voltammetry experiments were also carried out on PEO400 and PMEO containing the three salts, all with characteristic plating and stripping voltammograms, shown in Figs. 5-3 and 5-4, respectively.

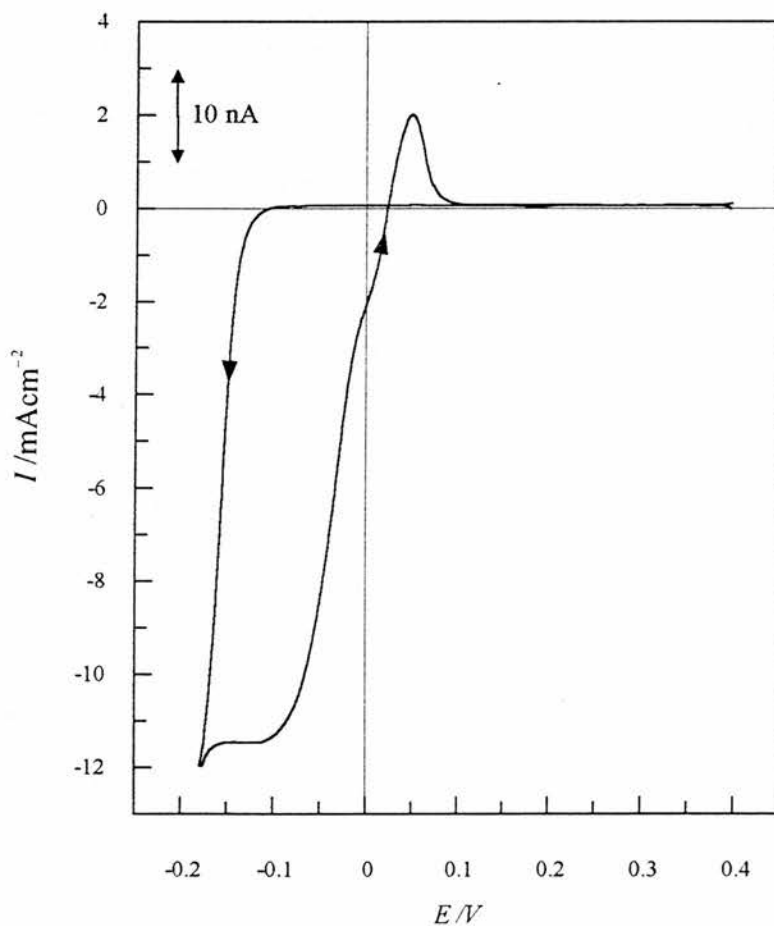


Figure 5-2 Cyclic voltammogram of lithium plating and stripping at a 25 μm diameter nickel microelectrode vs. Li/Li^+ from LiPF_6 .PMDETA (0.5 mol/kg) in tetraglyme. Sweep rate $\nu = 10\text{mV/s}$.

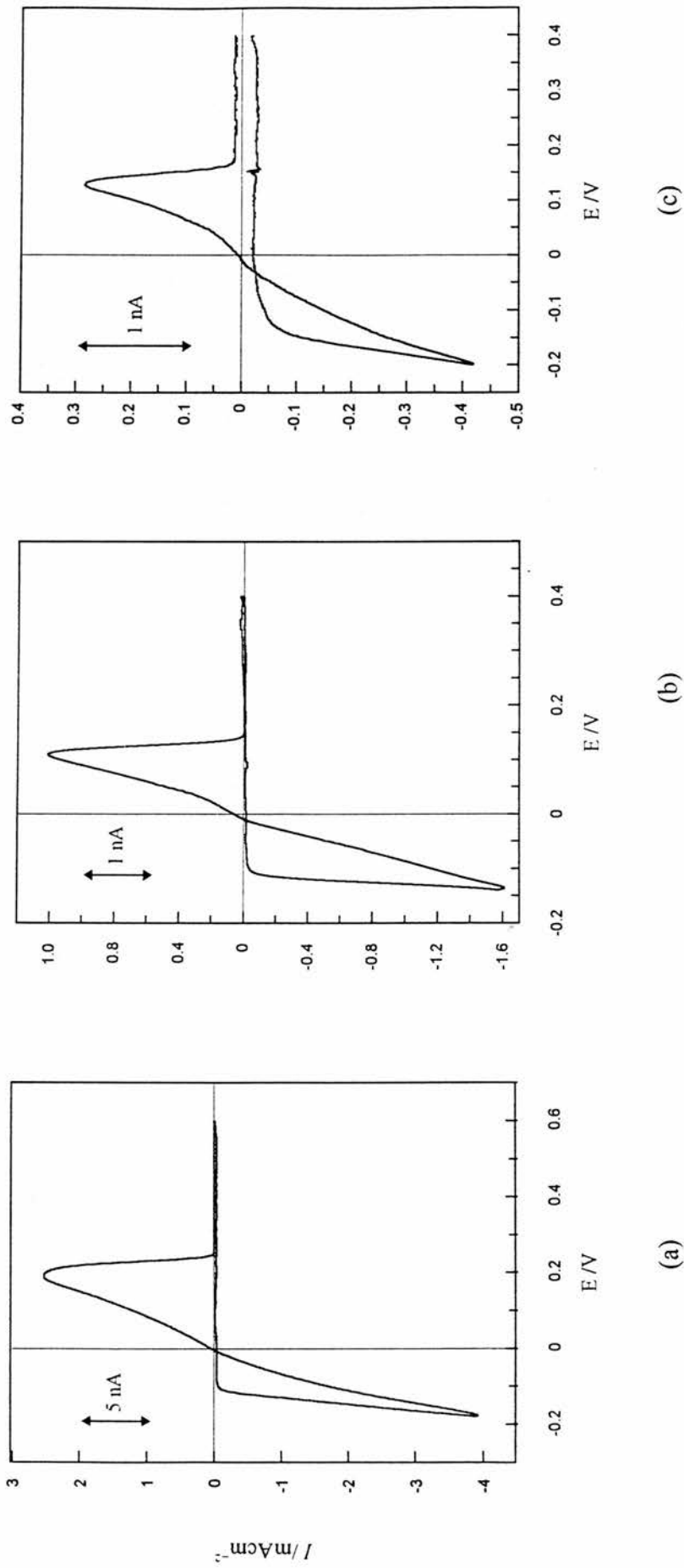


Figure 5-3 Cyclic voltammograms of lithium plating and stripping at a 25 μm diameter nickel microelectrode vs. Li^+/Li from (a) LiPF_6 , (b) $\text{LiPF}_6\text{-2DG}$ and (c) $\text{LiPF}_6\text{-PMDETA}$ (0.5 mol/kg) in PEO(400). Sweep rate $\nu = 10\text{mV/s}$.

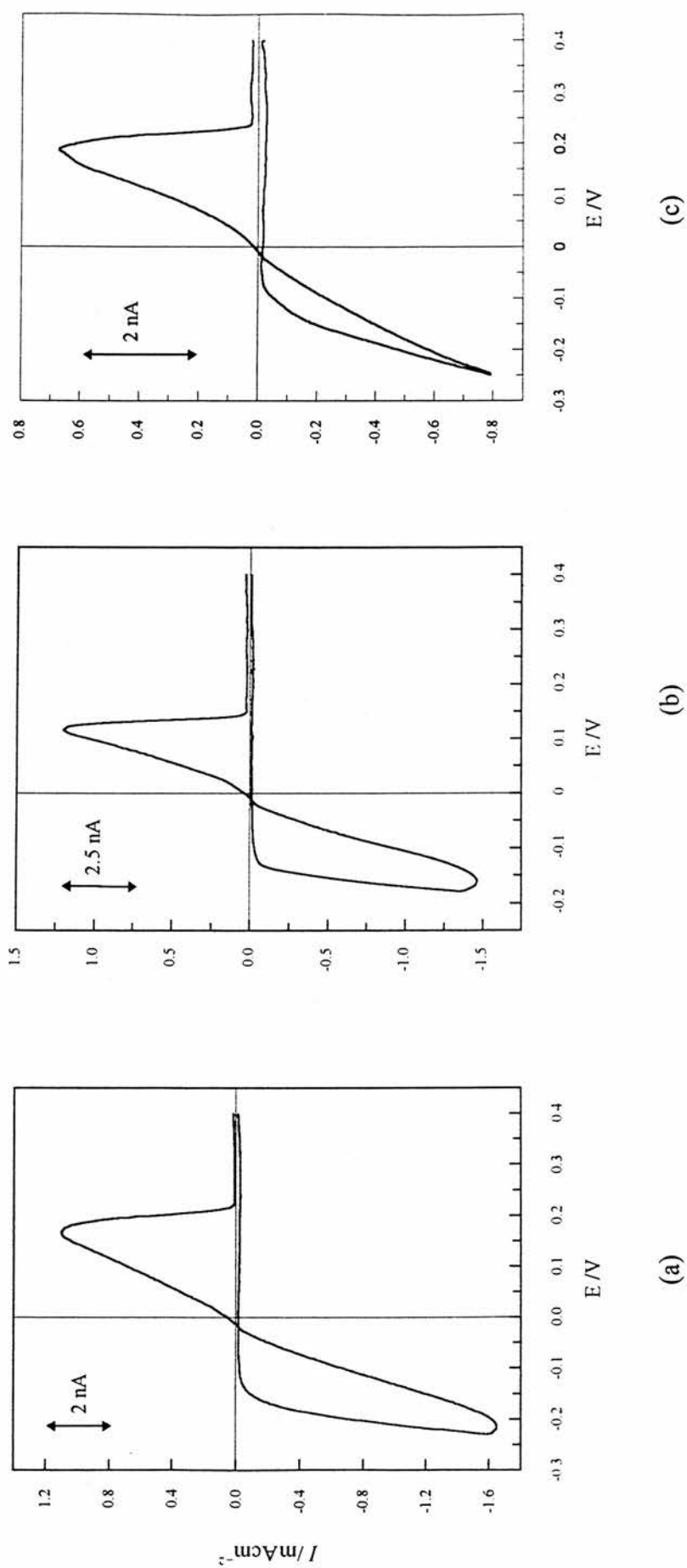


Figure 5-4 Cyclic voltammograms of lithium plating and stripping at a 25- μm diameter nickel microelectrode vs. Li/Li^+ from (a) LiPF_6 , (b) $\text{LiPF}_6\text{-2DG}$ and (c) $\text{LiPF}_6\text{-PMDETA}$ (10 EO:1 Li) in solid PMEO. Sweep rate $\nu = 10\text{mV/s}$.

The characteristic parameters are shown in Table 5-1. As can be seen, the stripping efficiencies obtained in polyether electrolytes, especially in the presence of the ligands, were lower than those found by Pletcher [6] in THF+DEE electrolytes, indicating that the deposition/dissolution reaction is more complex. Nucleation overpotentials decrease in the order $\text{LiPF}_6\text{.PMDETA} > \text{LiPF}_6\text{.2DG} > \text{LiPF}_6$ in tetraglyme, $\text{LiPF}_6\text{.PMDETA} > \text{LiPF}_6, \text{LiPF}_6\text{.2DG}$ in PEO400 and $\text{LiPF}_6 > \text{LiPF}_6\text{.2DG} > \text{LiPF}_6\text{.PMDETA}$ in PMEO. Exchange current values were calculated from the reverse sweep of the CV curve. Fig. 5-5 shows a typical analysis of the reverse sweep by non-linear least-squares (NLLS) fitting to the Butler-Volmer equation. To avoid any possible influence from changes in the surface, the values obtained in this way were compared with the exchange current densities calculated from a linear approximation of the Butler-Volmer equation at very low overpotentials, given by

$$I_0 = \frac{RT}{nF} \left(\frac{\partial I}{\partial \eta} \right)_{\eta \rightarrow 0} \quad 5-1$$

where I_0 is the exchange current density, R is the gas constant, T is the temperature, n is the number of electrons, F is the Faraday constant, I is the current density and η is the overpotential. The I_0 values can be ordered in the same way as the overpotentials suggesting the ligands remain coordinated to the Li^+ in the liquid systems, requiring additional energy to form the intermediate for charge transfer.

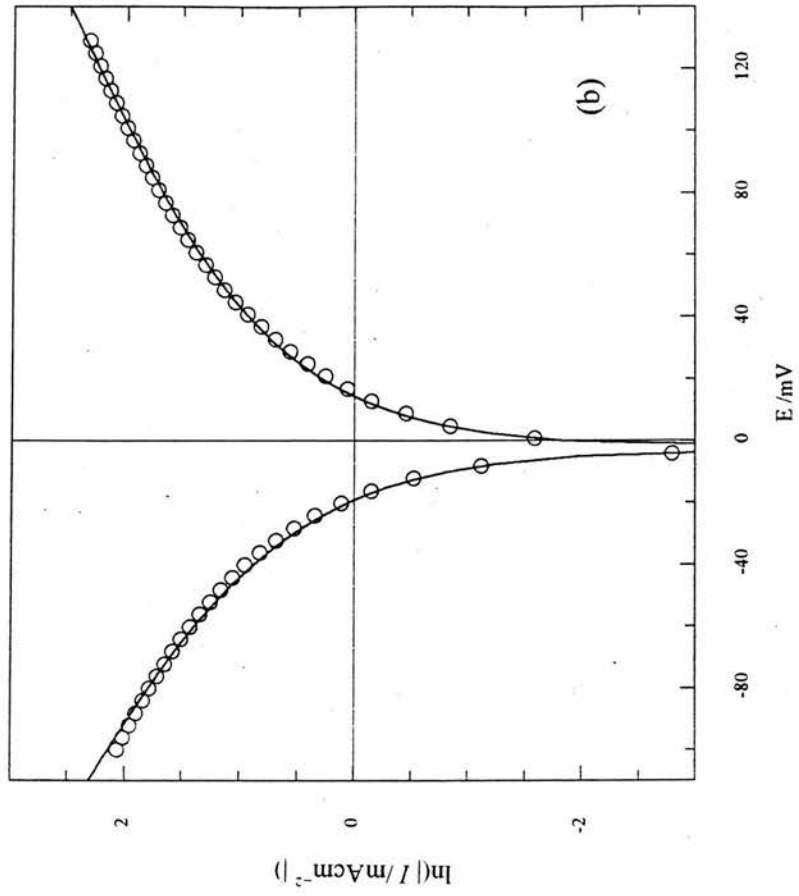
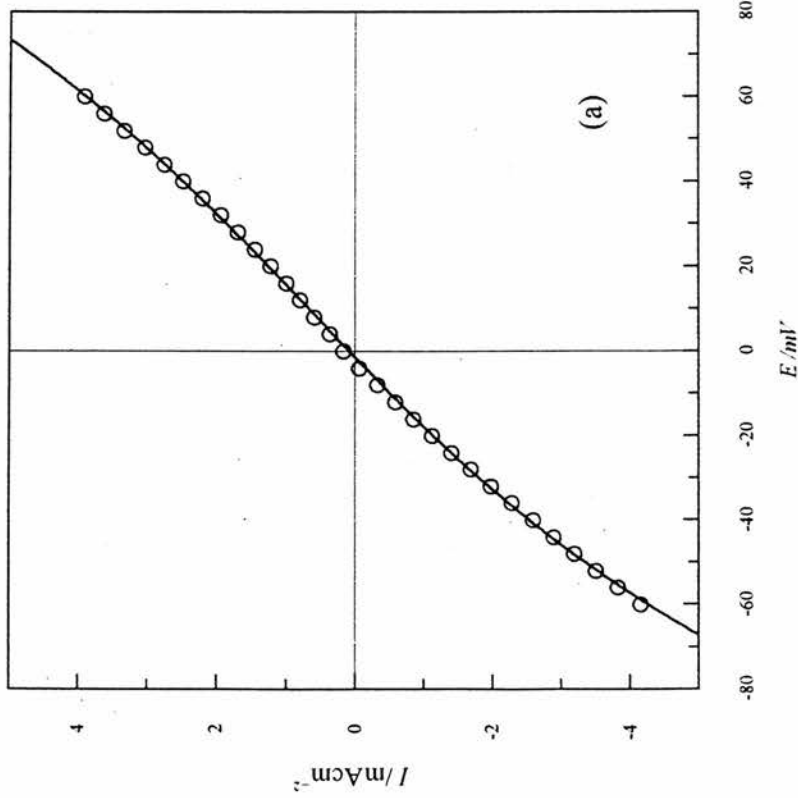


Figure 5-5 (a) Reverse sweep and (b) Tafel slopes of the voltammogram for $\text{LiPF}_6 / \text{tetraglyme}$ at 10mV/s . The solid line represents the NLLS fit to the Butler-Volmer equation. $I_0 = 1.4 \text{ mAcm}^{-2}$.

Table 5-1 Some electrochemical parameters obtained at a 25 μ m Ni microelectrode vs. Li/Li⁺ by cyclic voltammetry; sweep rate $\nu = 10$ mVs⁻¹, T = 298 K.

ELECTROLYTE		Nucleation overpotential	Cathodic current density at $\eta = 0.140$ V.	Exchange current density	Transfer coefficients	Anodic peak potential	Stripping efficiency (1 st cycle)
Solvent	Salt	η /mV	I /mAcm ⁻²	I_0 /mAcm ⁻²	(α) _A	E_p^A /mV	%
tetraglyme	LiPF ₆ (0.53 mol/kg)	-85.0	10.26	1.4 ^{BV} 1.4 ^L	0.47	153	90
	LiPF ₆ .2DG (0.50 mol/kg)	-121	0.100	0.034 ^{BV} 0.033 ^L	0.42	147	68.4
	LiPF ₆ .PMDETA (0.46 mol/kg)	-135	1.44	-	-	50.0	>30
PEO 400	LiPF ₆ (0.51 mol/kg)	-110	1.91	0.27 ^{BV} 0.26 ^L	0.40	200	71.8
	LiPF ₆ .2DG (0.50 mol/kg)	-110	1.6	0.22 ^{BV} 0.16 ^L	0.43	95.0	63.4
	LiPF ₆ .PMDETA (0.49 mol/kg)	-140	-	0.033 ^{BV} 0.025 ^L	0.50	130	46.6
PMEO	LiPF ₆ (1.4 mol/kg)	-175	-	0.12 ^{BV} 0.12 ^L	0.43	166	57.8
	LiPF ₆ .2DG (1.4 mol/kg)	-135	0.25	0.16 ^{BV} 0.12 ^L	0.52	155	42.9
	LiPF ₆ .PMDETA (1.7 mol/kg)	-116	0.15	0.032 ^{BV} 0.040 ^L	0.47	170	64.1

^{BV} Values calculated from NLLS fit of Butler-Volmer curve. ^L Linear part of CV at low overpotentials used with Eqn. 5-1.

The kinetics were studied further by application of a series of double-potential step experiments. A layer of lithium metal was deposited by applying a cathodic overpotential for a specific time, so that the deposition charge passed was ca. 0.5 C/cm². The potential was then stepped back to a value in the anodic range +50mV to +300mV. A set of transients for the anodic polarisation of the lithium layer deposited from LiPF₆.2DG/PEO400 is shown in Fig. 5-6.

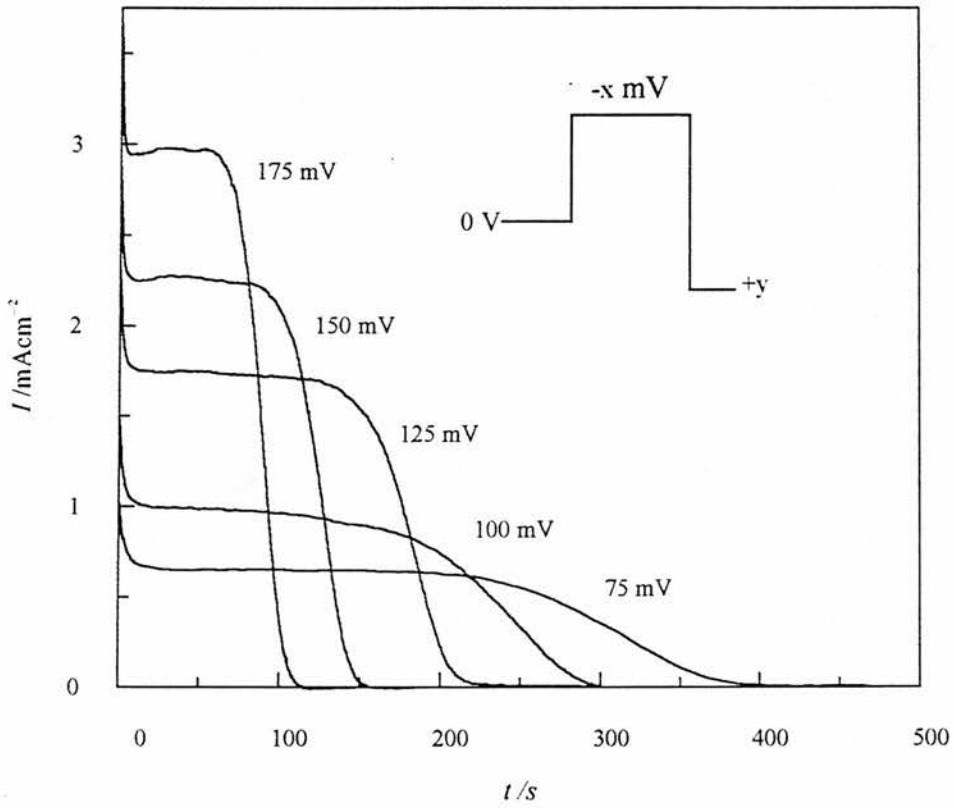


Figure 5-6 Anodic polarisation of freshly deposited lithium from LiPF₆.2DG/PEO 400 at a 25µm diameter Ni microelectrode vs. Li/Li⁺.

At each potential, the lithium oxidises at an approximately uniform rate until the layer is depleted. At more positive overpotentials, the current passes through a peak, caused by reactivation of the deposit, which increases with overpotential. By plotting the steady-state polarisation current against overpotential, the anodic Tafel plots are obtained, shown in Fig. 5-7.

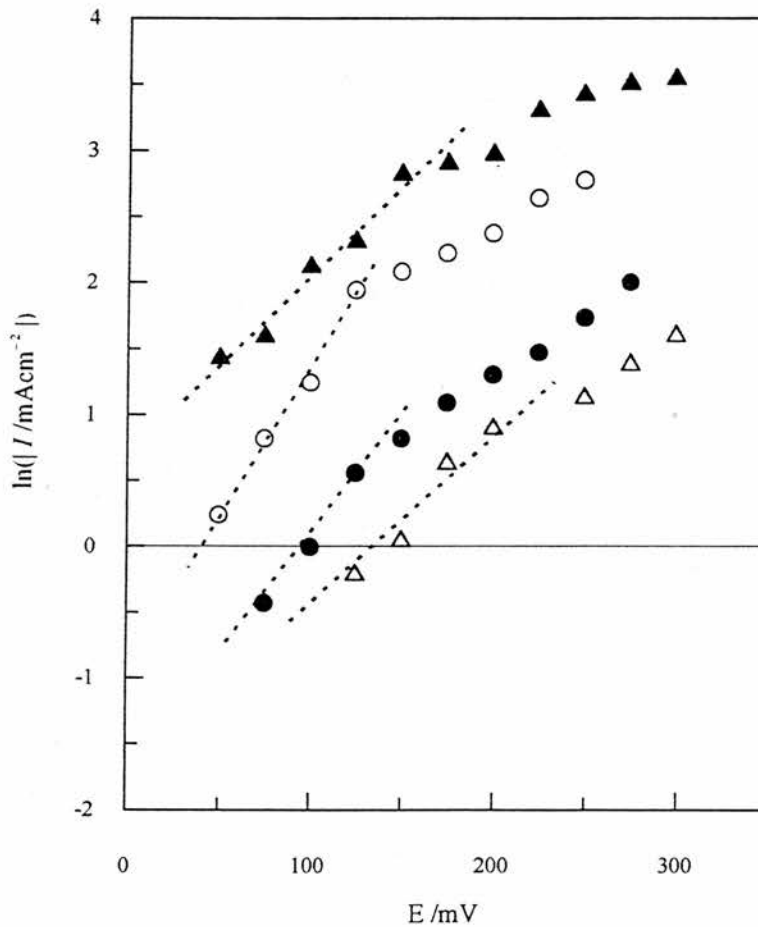


Figure 5-7 Tafel slopes obtained by the anodic polarisation of freshly deposited lithium at a $25\mu\text{m}$ diameter Ni microelectrode vs. Li/Li^+ from (▲) $\text{LiPF}_6/\text{tetraglyme}$, (○) $\text{LiPF}_6 \cdot 2\text{DG}/\text{tetraglyme}$, (●) $\text{LiPF}_6 \cdot 2\text{DG}/\text{PEO}(400)$ and (Δ) $\text{LiPF}_6/\text{PEO}(400)$.

The polarisation currents were taken from the plateau values early in the transients of experiments of the type illustrated in Fig. 5-6. A Tafel straight line is observed in each case up to about 250mV. At higher overpotentials, mass transport control dominates and the currents deviate from the charge-transfer control of the Tafel line. The anodic charge-transfer coefficients and exchange current densities were determined from the Tafel slopes and by extrapolating the lines back to the equilibrium potential (0.0V vs. Li/Li⁺). The results of this analysis are given in Table 5-2.

Table 5-2 The exchange current density and anodic transfer coefficient for some polyether lithium electrolytes, obtained from Tafel plots.

ELECTROLYTE	I_0 / mAcm^{-2}	$(n\alpha)_A$
LiPF ₆ / tetraglyme (0.53 mol/kg)	1.8	0.33
LiPF ₆ .2DG/tetraglyme (0.50 mol/kg)	0.42	0.57
LiPF ₆ /PEO(400) (0.51 mol/kg)	0.24	0.28
LiPF ₆ .2DG/PEO(400) (0.50 mol/kg)	0.18	0.44

The values obtained generally compare well with those extracted from the voltammograms (Table 5-1), considering the difference in the methods used.

5.2.2. *Nucleation and Growth*

The initial stages of electrochemical phase formations are usually associated with two- or three-dimensional nucleation processes [18-20] (as described in Chapter 2), the rate of which and the number of nuclei formed being strongly dependent on the overpotential applied. Chronoamperometric measurements were found to be particularly useful in providing an insight into the morphology of the growing deposit at the electrode surface. Fig. 5-6 represents a set of typical current-transients obtained for liquid PEO400 containing LiPF_6 . The double layer charging current effects only the initial part of the transient. As the electroactive area of the deposit increases, the current rises and approaches a steady-state value where continuous thickening of the layer takes place. When the applied potential step is increased, the rise time decreases and the steady-state current increases. Overall, the transients have the expected features for a nucleation and growth process. At much longer times (several hundred seconds) the current again increases with time. A similar transient was observed by Pletcher [6] in THF, who attributed the feature to the growth of the deposit over the glass surrounds of the electrode. The increase in surface area may also arise from dendritic growth of the deposit into the solution. At potentials lower than the nucleation overpotential (Table 5-1), rising transients were not observed in the time-scale of the experiments

In table 5-3, nucleation and growth models are listed for the initial rising transients as functions of t^n , where n depends on the type of nucleation involved, the geometry of the new phase and the rate determining step (Chapter 2).

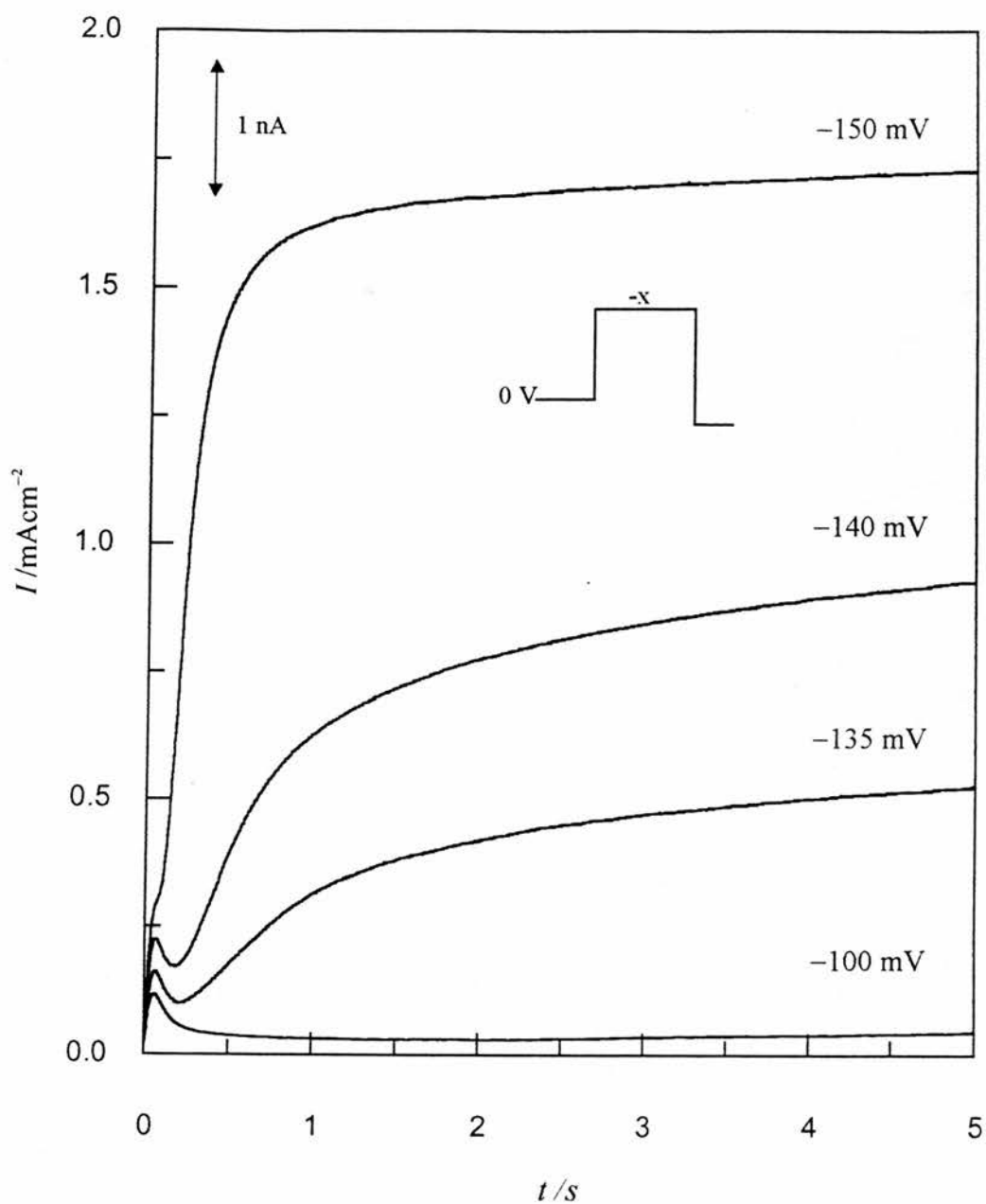


Figure 5-8 Current transients for the nucleation and growth of lithium from $\text{LiPF}_6/\text{PEO}(400)$ at a $25\mu\text{m}$ diameter Ni microelectrode vs. Li/Li^+ . Overpotentials applied are indicated in the figure.

Table 5-3 Types of nucleation and growth processes observed for *initial* current transients where I varies with t^n .

n	Nucleation type	Geometry	Rate determining step
1	instantaneous	2-D cones	kinetic
2	progressive	2-D cones	kinetic
2	instantaneous	3-D cones	kinetic
2	instantaneous	3-D hemispheres	kinetic
3	progressive	3-D cones	kinetic
3	progressive	3-D hemispheres	kinetic
1/2	instantaneous	3-D hemispheres	diffusion
3/2	progressive	3-D hemispheres	diffusion

Linear I vs. t^2 relationships, shown in Fig. 5-9, for the initial transients of LiPF₆/PEO400 (Fig. 5-6) indicate instantaneous nucleation followed by kinetic controlled growth of hemispheres or cones. Such plots are useful and relatively easy to prepare, but in some instances they may be interpreted incorrectly. For example, rising transients that vary with $t^{3/2}$ and t^2 contain a region of overlap where they follow the same path. Under these conditions a straight line will be seen for each model. It was decided that a non-linear least-squares (NLLS) fit was preferable to straight line plots at short times, since the theoretical models for prolonged transients could be matched with the experimental curves up to the current plateaux, or maxima, without the ambiguities associated with the I vs. t^n plots of two closely related rising transients.

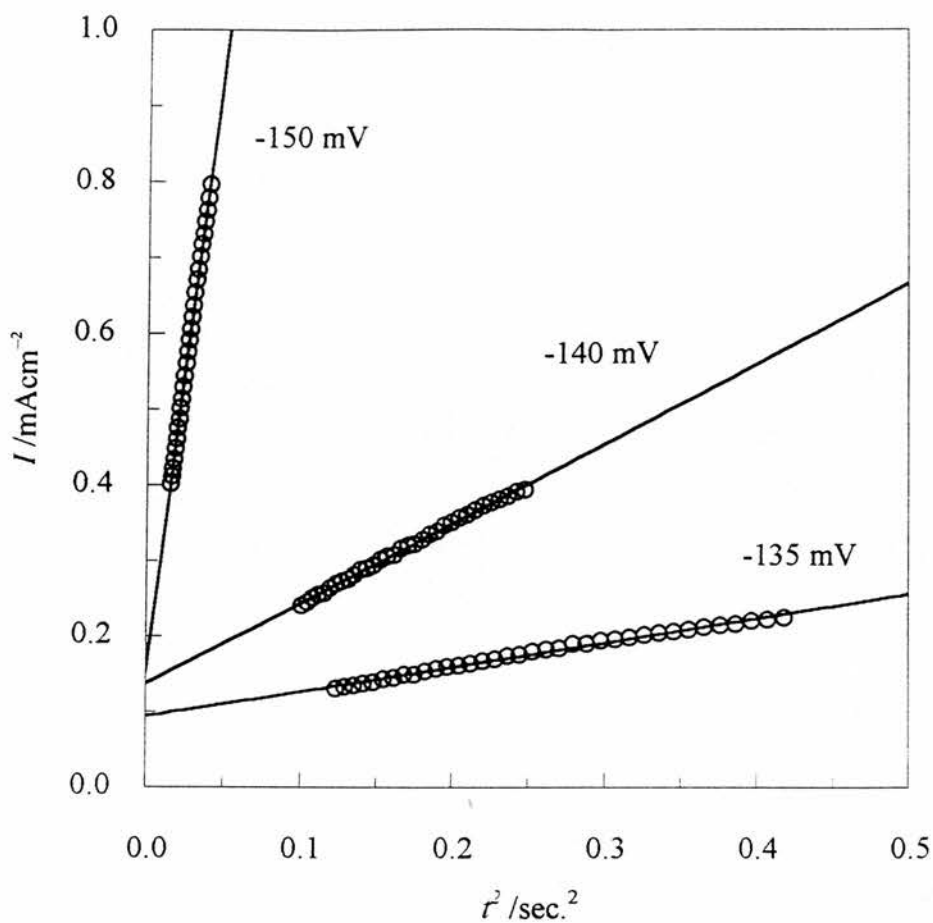


Figure 5-9 $I-t^2$ plots for the data taken from the initial rising transients of $\text{LiPF}_6/\text{PEO400}$ (0.5 mol/kg).

The equations described in Chapter 2 are reduced to their simplest forms and defined for use in the NLLS fitting of the data presented here as:

$$I = a\{1 - \exp(bt^2)\} \quad 5-2$$

$$I = a\{1 - \exp(ct^3)\} \quad 5-3$$

for kinetic controlled growth of cones or hemispheres following three-dimensional instantaneous and progressive nucleation, respectively, where I is the current density and t is the time; and

$$I = \frac{d}{\sqrt{t}} \{1 - \exp(-et)\} \quad 5-4$$

$$I = \frac{d}{\sqrt{t}} \{1 - \exp(-ft^2)\} \quad 5-5$$

for diffusion controlled growth of hemispheres following three dimensional instantaneous and progressive nucleation, respectively. The parameters a-f are arbitrary variables that are calculated during the fit.

Fig. 5-10 shows the current transient for $\text{LiPF}_6/\text{PEO400}$ after stepping the potential from 0V to -150mV. The solid fitted line represents the model for instantaneous 3-D nucleation followed by kinetic controlled growth of hemispheres, or cones. The data obscured by charging current have been removed from the plot. A simulated progressive nucleation curve is represented by the broken line, clearly showing the difference between the two models. The set of current-transients for $\text{LiPF}_6.2\text{DG}/\text{PMEO}$ is shown in Fig. 5-11. Again, the current increases with the electroactive area, but as the diffusion zones of the growing nuclei overlap, maxima are observed.

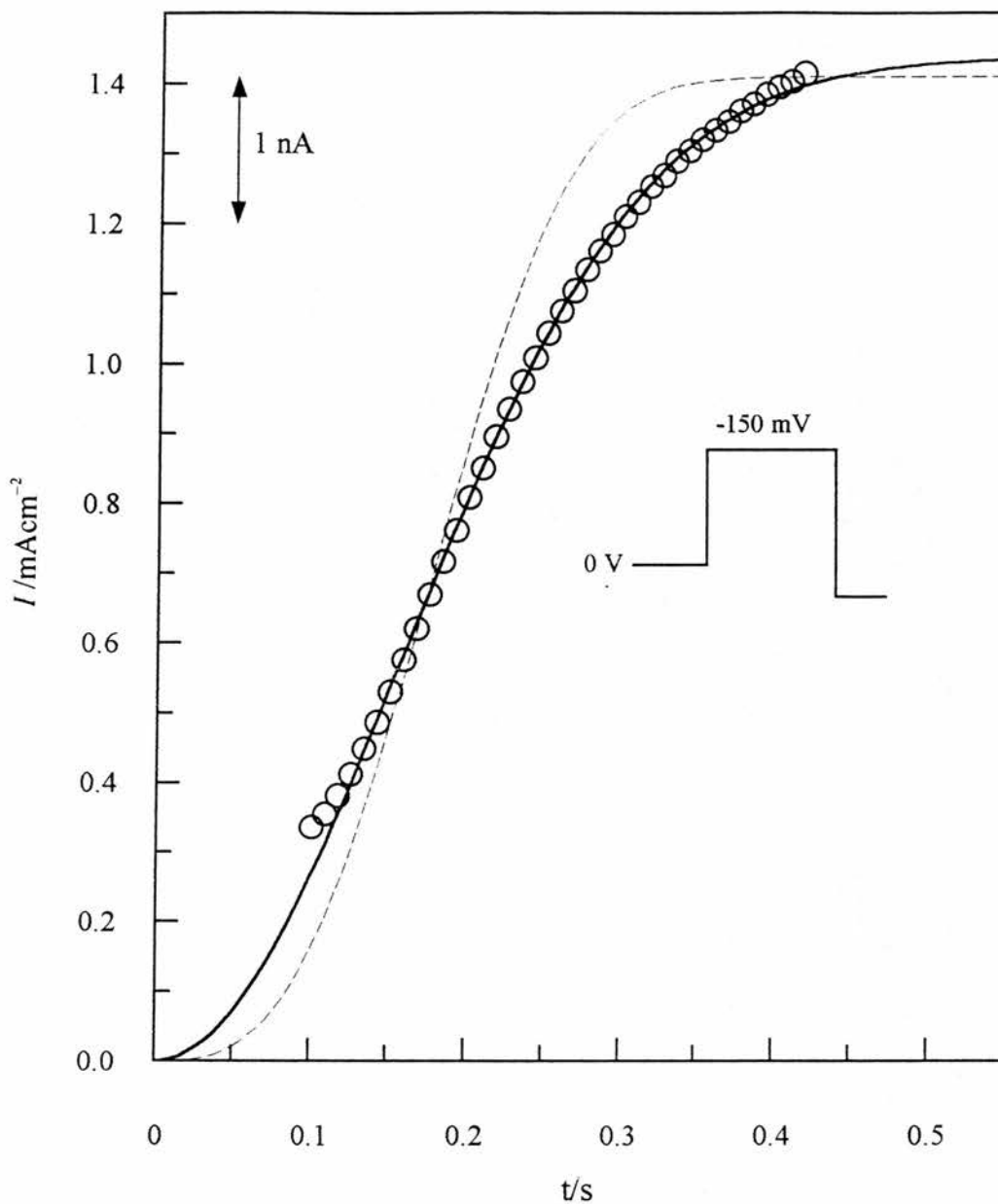


Figure 5-10 Current transient at -150mV for $\text{LiPF}_6/\text{PEO}(400)$ at a $25\mu\text{m}$ diameter Ni microelectrode vs. Li/Li^+ . The solid line is the NLLS fit for instantaneous nucleation followed by kinetic controlled growth of hemispheres or cones. (The broken line shows progressive nucleation.)

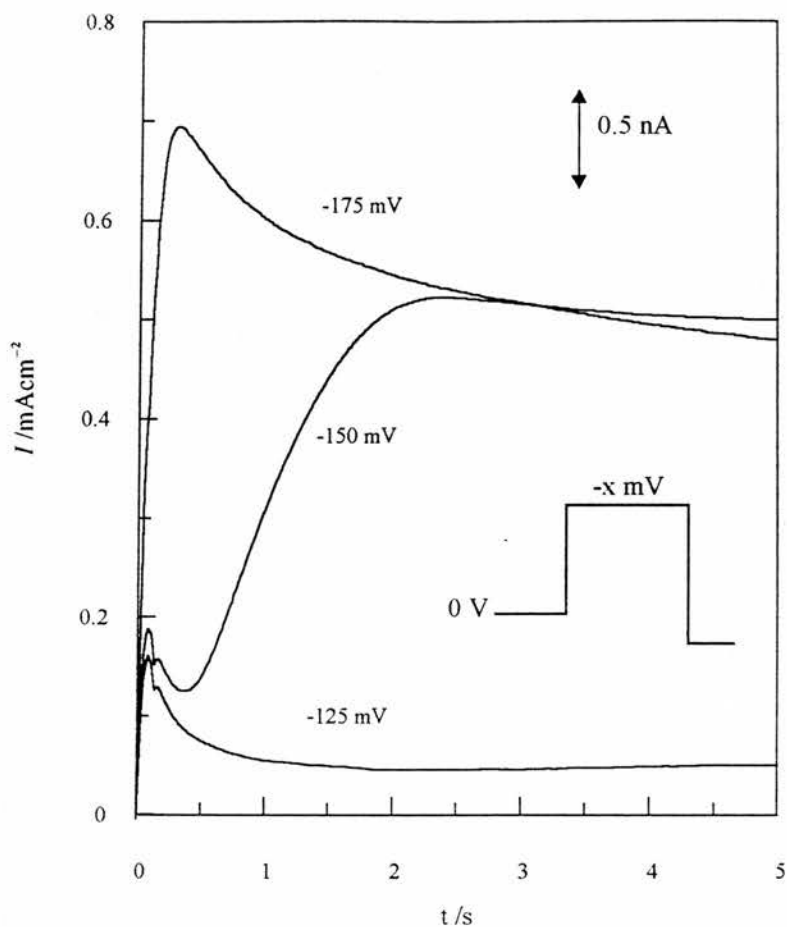


Figure 5-11 Current transients for the nucleation and growth of lithium from $\text{LiPF}_6 \cdot 2\text{DG}/\text{PMEO}$ at a $25\mu\text{m}$ diameter Ni microelectrode vs. Li/Li^+ .

Increasing the overpotential further results in the transient approaching the limiting current to a planar electrode with the additional flux of the spherical contribution to the microelectrode (Eqn. 2-24, Chapter 2). The NLLS fit to the $I-t$ transient for $\text{LiPF}_6 \cdot 2\text{DG}/\text{PMEO}$ at -150mV is shown in Fig. 5-10. The solid line indicates that 3-D progressive nucleation occurs followed by diffusion controlled growth of hemispheres.

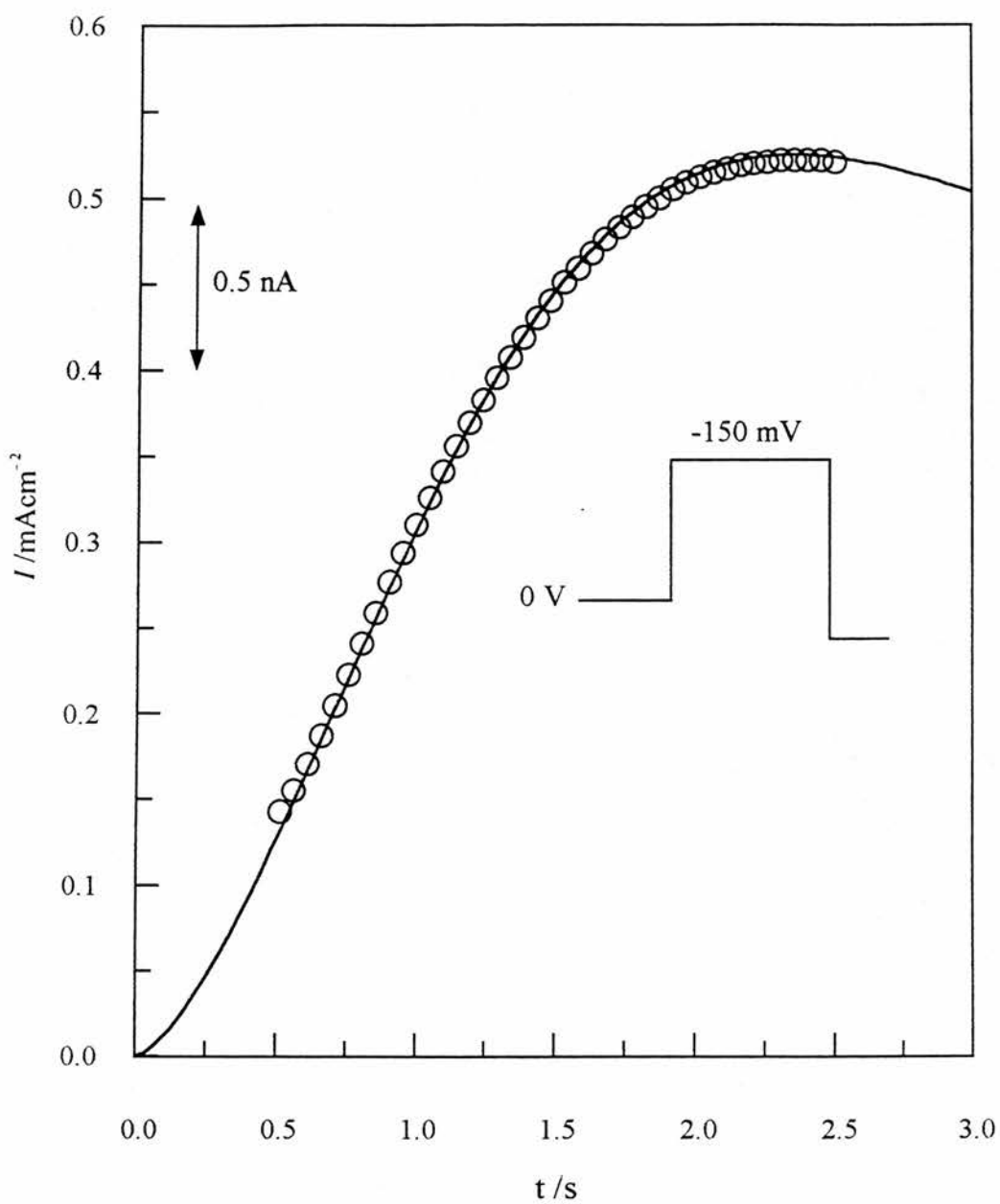


Figure 5-12 Current transient at -150mV for $\text{LiPF}_6 \cdot 2\text{DG}/\text{PMEO}$ at a $25\mu\text{m}$ diameter Ni microelectrode vs. Li/Li^+ . The solid line is the NLLS fit for progressive nucleation followed by diffusion controlled growth of hemispheres.

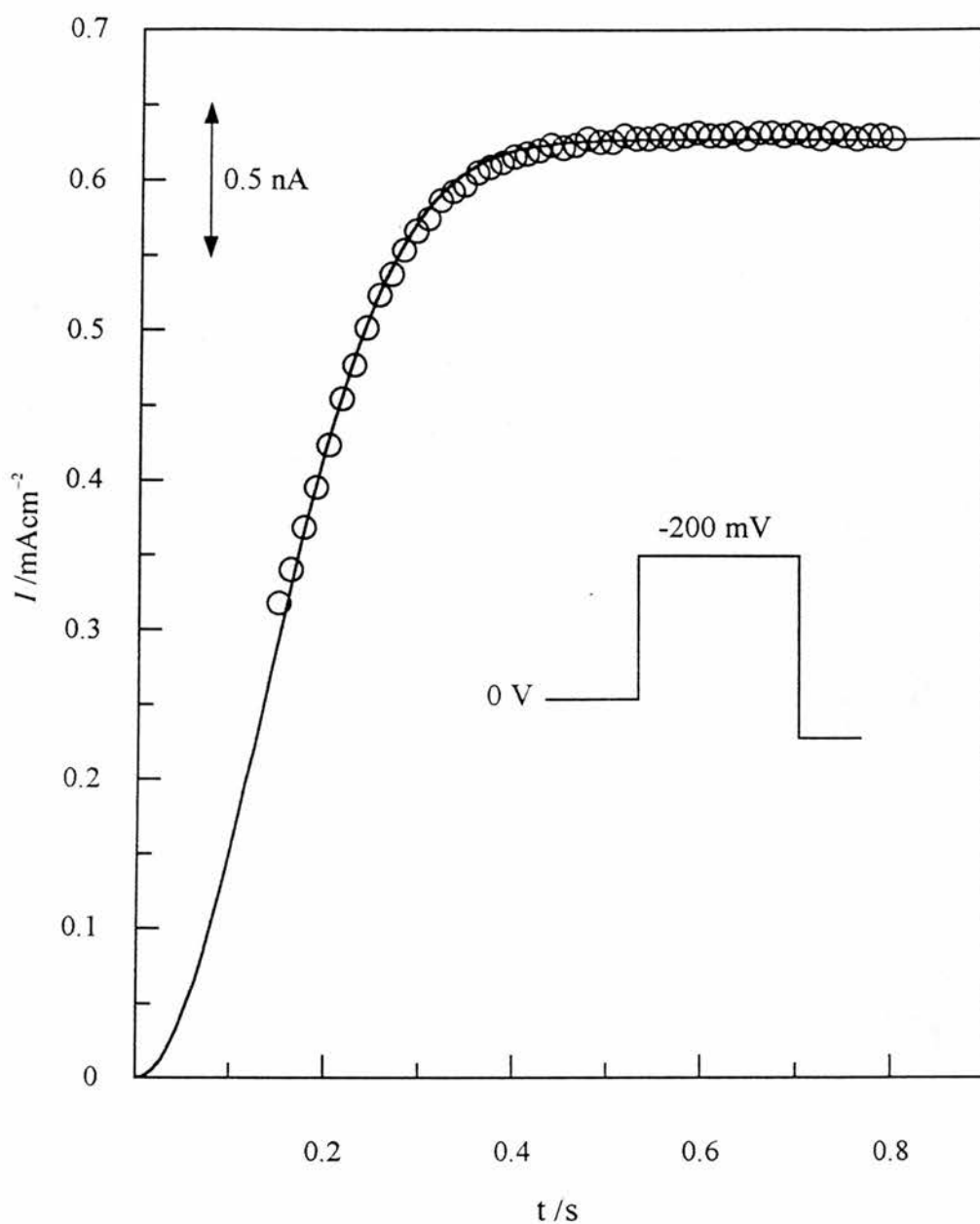


Figure 5-13 Current transient at -200mV for $\text{LiPF}_6\text{.PMDETA/PMEO}$ at a $25\mu\text{m}$ diameter Ni microelectrode vs. Li/Li^+ . The solid line is the NLLS fit for instantaneous nucleation followed by kinetic controlled growth of hemispheres, or cones.

The $I-t$ transient of LiPF_6 .PMDETA /PMEO at -200mV (Fig. 5-13) suggests that nucleation and growth occurs under kinetic controlled growth in a similar way to that of LiPF_6 in each solvent, as described earlier. The models fitted for the salts and complexes in each solvent are listed in Table 5-4.

Table 5-4 Type of nucleation and crystal growth obtained at a $25\mu\text{m}$ diameter nickel microelectrode vs. Li/Li^+ .

ELECTROLYTE		Type of crystal growth	Nucleation type	Goodness-of-fit reduced χ^2
Solvent	Salt			
tetraglyme	LiPF_6 (0.53 mol/kg)	3D cones or hemispheres, kinetic control	instantaneous	1.3×10^{-3}
	LiPF_6 .2DG (0.50 mol/kg)	3D hemispheres, diffusion control	progressive	1.4×10^{-4}
	LiPF_6 .PMDETA (0.46 mol/kg)	3D hemispheres, diffusion control	progressive	3.4×10^{-2}
PEO 400	LiPF_6 (0.51 mol/kg)	3D cones or hemispheres, kinetic control	instantaneous	7.7×10^{-4}
	LiPF_6 .2DG (0.50 mol/kg)	3D hemispheres, diffusion control	progressive	4.9×10^{-4}
	LiPF_6 .PMDETA (0.49 mol/kg)	3D hemispheres, diffusion control	progressive	-
PMEO	LiPF_6 (1.4 mol/kg)	3D cones or hemispheres, kinetic control	instantaneous	7.6×10^{-5}
	LiPF_6 .2DG (1.4 mol/kg)	3D hemispheres, diffusion control	progressive	5.2×10^{-6}
	LiPF_6 .PMDETA (1.7 mol/kg)	3D cones or hemispheres, kinetic control	instantaneous	2.5×10^{-5}

5.2.3. Lithium Reactivity and Passivation

Fig. 5-14 shows a typical current reversal chronopotentiogram obtained for tetraglyme containing LiPF_6 (0.5 mol/kg) at a Ni microelectrode, where the cathodic (forward) and anodic (reverse) currents were both 4nA (0.81 mAcm^{-2}).

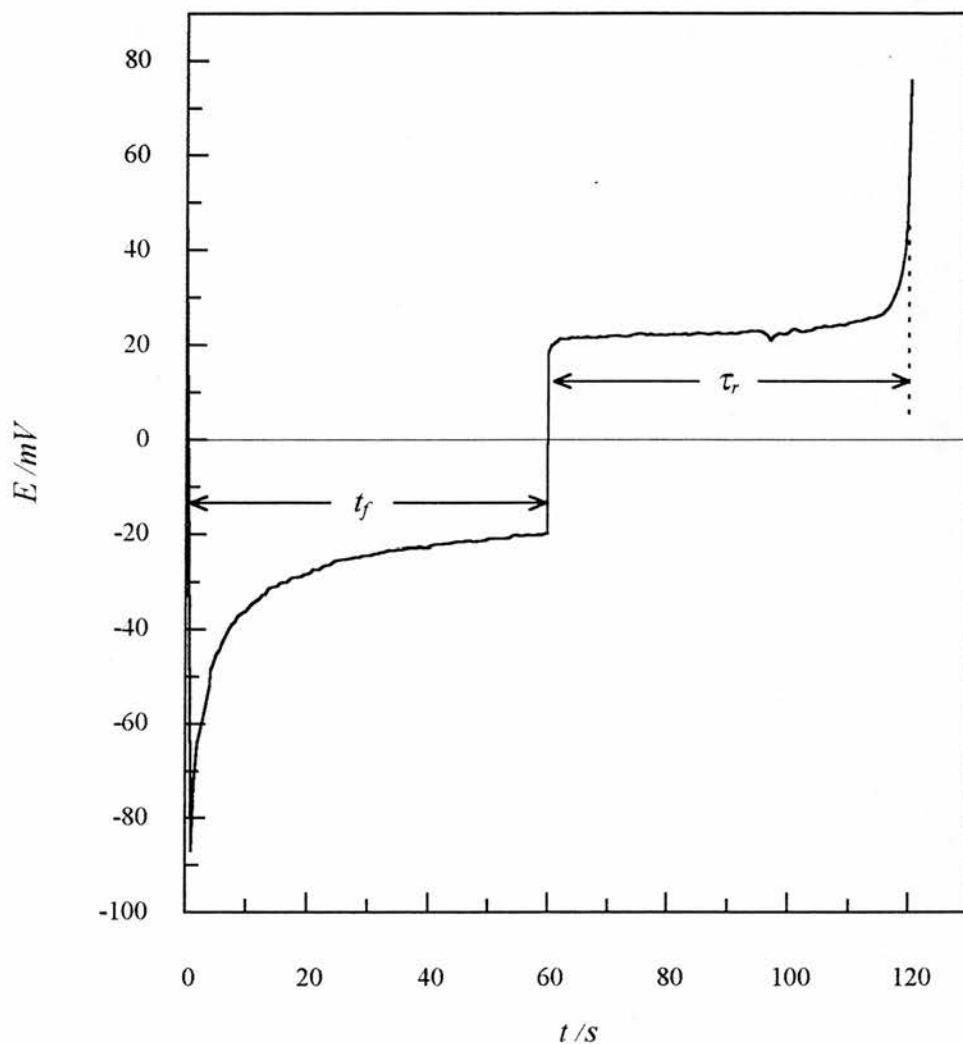


Figure 5-14 Reverse chronopotentiogram for LiPF_6 / tetraglyme at a $25\mu\text{m}$ diameter nickel microelectrode vs. Li/Li^+ , where $I_f = I_r = 4\text{nA}$ (0.81 mAcm^{-2}). Rate of lithium loss $k_l = 4.57 \times 10^{-11} \text{ mol cm}^{-2} \text{ s}^{-1}$.

After depositing a layer of lithium under galvanostatic conditions, an anodic pulse was applied. At the transition time τ_r , the concentration of the reduced lithium metal is equal to zero, and the potential rapidly moves toward more anodic values until another anodic process occurs. The reverse transition time in current reversal chronopotentiometry (CRC) is therefore characterised by a sudden variation in potential. If the ratio of the forward time t_f to that of the reverse transient τ_r is close to unity under these conditions, it is clear that an insoluble product is formed [21, 22] which is stable in the solvent medium. Any decrease in the ratio τ_r/t_f was taken as an indication of a following chemical reaction of the lithium deposit, it being assumed that there is no significant diffusion away from the electrode surface. The charge density unaccounted for by anodic dissolution, assuming corrosion occurs continuously from $t = 0$, is given by

$$I_{appl} \cdot (t_f - \tau_r) = I_{corr} \cdot (t_f + \tau_r) \quad 5-7$$

where I_{appl} is the applied cathodic / anodic current density and I_{corr} is defined as the corrosion current density. Eqn. 5-7 can be rearranged to

$$I_{corr} = I_{appl} \cdot \left\{ \frac{t_f - \tau_r}{t_f + \tau_r} \right\} = I_{appl} \cdot \left\{ \frac{\left(1 - \frac{\tau_r}{t_f} \right)}{\left(1 + \frac{\tau_r}{t_f} \right)} \right\} \quad 5-8$$

when the ratio τ_r/t_f remains constant at different t_f , leading to the rate of lithium corrosion, given by

$$k_l = \frac{I_{corr}}{F} \quad \text{mol cm}^{-2} \text{ s}^{-1}$$

5-9

Table 5-5 shows the calculated values of the rate of lithium loss k_l . It was found that the rate of lithium loss was generally higher in the presence of the ligands in each of the liquid solvents in the order $\text{LiPF}_6 < \text{LiPF}_6\cdot 2\text{DG} < \text{LiPF}_6\cdot \text{PMDETA}$. The PMDETA complex appears to be more promising in the solid PMEO.

Table 5-5 Rate of lithium corrosion, k_l obtained from CRC.

ELECTROLYTE		Rate of lithium loss,	I_{appl}
Solvent	Salt	$k_l / \text{mol s}^{-1} \text{cm}^{-2}$	mAcm^{-2}
	LiPF_6 (0.53 mol/kg)	4.57×10^{-11}	0.81
tetraglyme	$\text{LiPF}_6\cdot 2\text{DG}$ (0.50 mol/kg)	3.03×10^{-9}	0.81
	$\text{LiPF}_6\cdot \text{PMDETA}$ (0.46 mol/kg)	4.83×10^{-9}	0.81
	LiPF_6 (0.51 mol/kg)	3.54×10^{-10}	0.81
PEO 400	$\text{LiPF}_6\cdot 2\text{DG}$ (0.50 mol/kg)	1.97×10^{-10}	0.81
	$\text{LiPF}_6\cdot \text{PMDETA}$ (0.49 mol/kg)	2.03×10^{-9}	0.81
	LiPF_6 (1.4 mol/kg)	5.55×10^{-9}	0.81
PMEO	$\text{LiPF}_6\cdot 2\text{DG}$ (1.4 mol/kg)	1.06×10^{-8}	1.42
	$\text{LiPF}_6\cdot \text{PMDETA}$ (1.7 mol/kg)	7.03×10^{-9}	0.81

The chronopotentiometric measurements indicated a second anodic transient at $E_{\tau/4} = +1.1\text{V}$ vs. Li/Li^+ . At the same potential, an anodic wave was observed on the CV curves, as also found by Armand *et al* [23] with $\text{LiN}(\text{SO}_2\text{CF}_3)_2$ / poly(ethylene oxide) at a stainless-steel electrode. While these authors attributed the peak to impurities, voltammetry studies on the pure solvents in this work did not reveal such a peak, indicating that this is a feature of the electrolyte solution containing added lithium salt. At potentials anodic of 0V, a small cathodic peak was observed in the electrolyte solutions at +0.4V. Pletcher *et al* [24] also observed this peak in propylene carbonate containing lithium salts and suggested that the peak resulted from the underpotential deposition of lithium with a coupled anodic peak at +1V. This underpotential deposition is thought to result from the reduction of an existing surface film, such as LiOH, rather than reduction of Li^+ in solution. A surface film composed of LiOH may be formed by the reduction of trace water in the presence of the lithium cations.

One of the most important parameters characterising lithium behaviour is the coulombic stripping efficiency following periods during which newly deposited metal is held at open-circuit voltage. Fig. 5-15 shows the $I-t$ transients obtained for such an experiment from $\text{LiPF}_6 \cdot 2\text{DG}/\text{PEO}400$. A double-potential step was applied for ca. 200 sec at -135mV, depositing a lithium layer (deposition charge passed was ca. 0.5 C cm^{-2}). A controlled delay between the cathodic and anodic potentiostatic pulses left the cell on open-circuit before stripping the metal off at +100mV. Fig. 5-16 shows the coulombic stripping efficiencies vs. time on open-circuit for those electrolyte solutions examined where stripping under galvanostatic conditions was successful.

After a period of only 60 s. on open-circuit, the rate of lithium dissolution decreased in each case, with an associated decrease in stripping efficiency. In Fig. 5-15, the extent of dissolution remains relatively constant after 240 s., which corresponds to the invariant stripping efficiency in Fig. 5-16 after this time. In all cases examined the lithium became protected from further reaction due to passivation by an ionically conducting layer after a period of time, dependent on electrolyte composition.

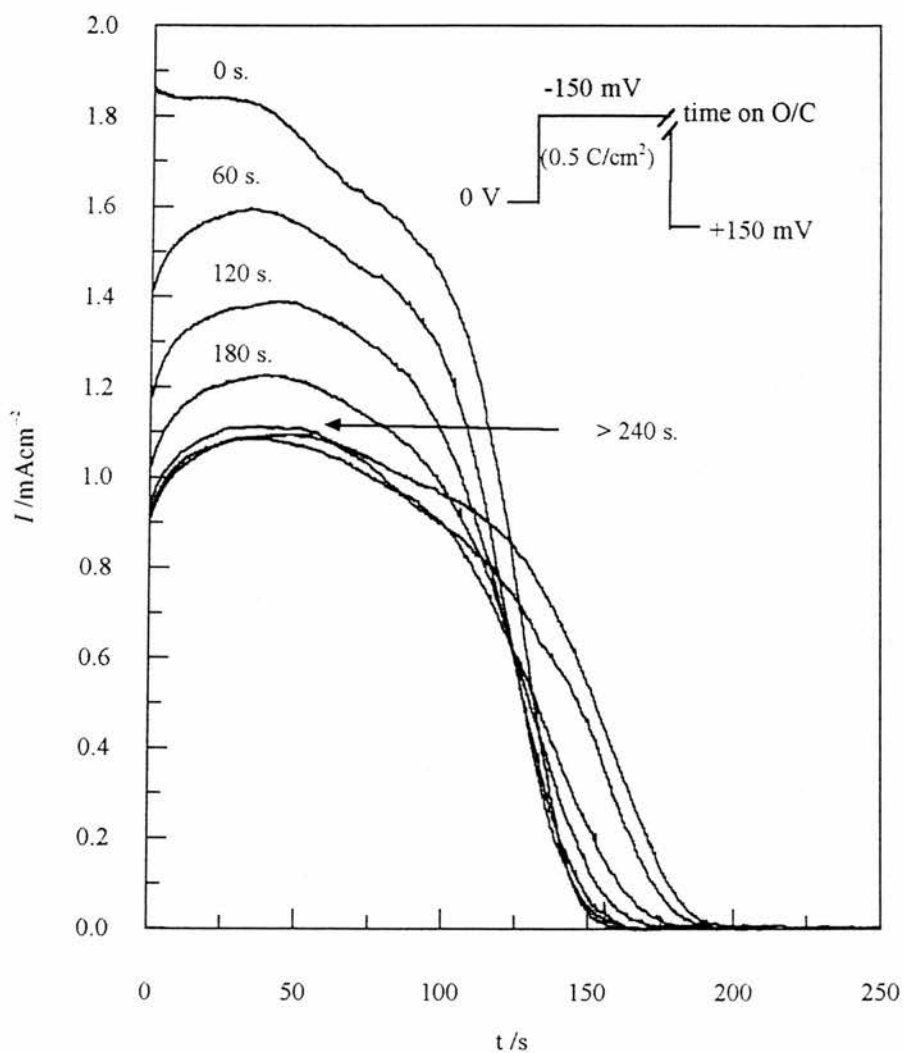


Figure 5-15 Plot of anodic stripping of lithium after time on open-circuit for $\text{LiPF}_6 \cdot 2\text{DG}/\text{PEO}(400)$.

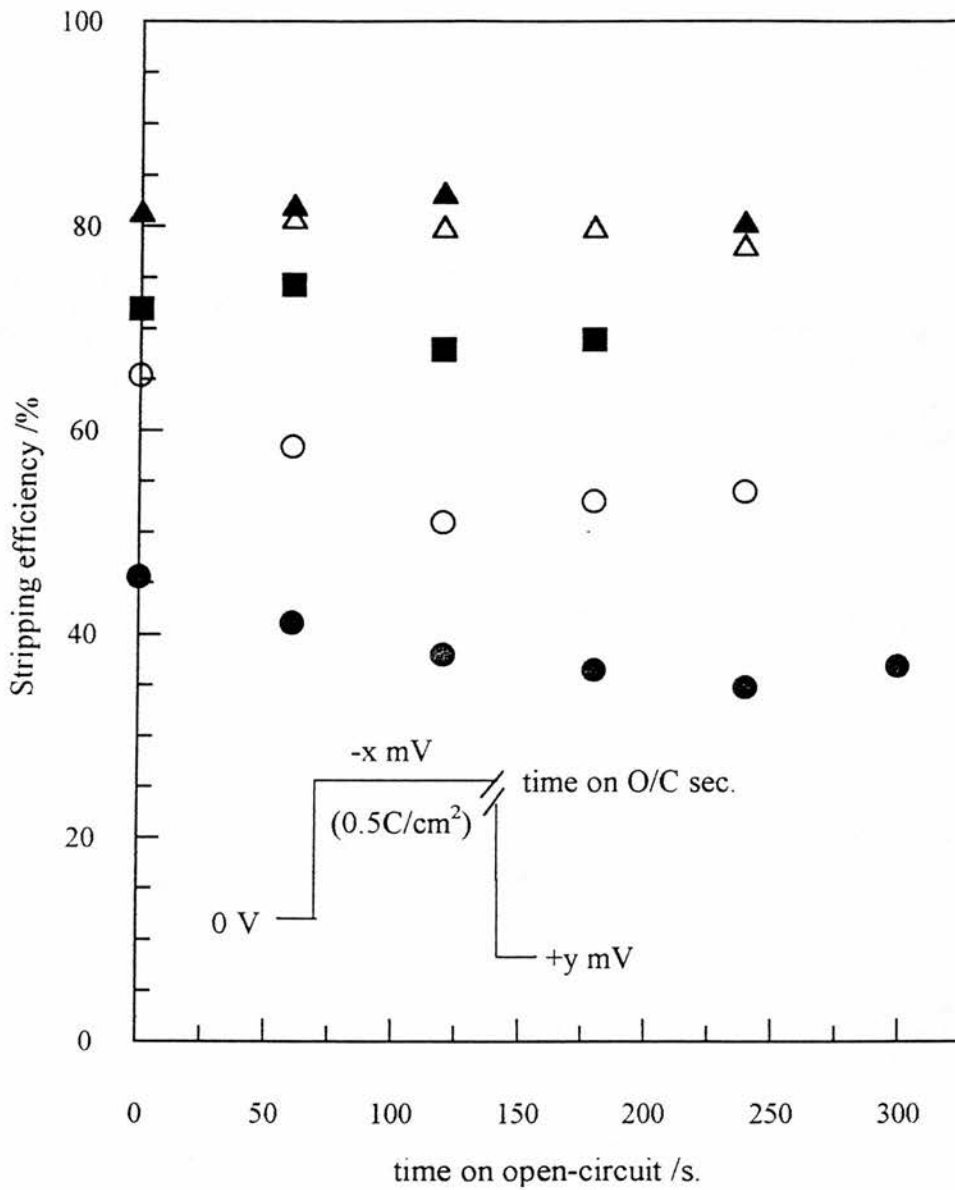


Figure 5-16 Plot of coulombic stripping efficiency versus time on open-circuit of freshly deposited lithium from (▲) LiPF₆/tetraglyme, (Δ) LiPF₆.2DG/ tetraglyme, (■) LiPF₆/ PEO(400), (●) LiPF₆.2DG/ PEO(400) and (○) LiPF₆.PMDETA/ PEO(400).

The stripping efficiency was ca. 80% in all LiPF_6 solutions without a loss of efficiency with time, suggesting that a passivating layer is rapidly formed. The deposit plated from LiPF_6 -2DG solutions was relatively unstable, dropping below 50% stripping efficiency.

5.3. Conclusions

The objective of this study was to assess the electrochemical performance of some novel complexes of lithium hexafluorophosphate dissolved in polyether media of increasing molecular weight. The experiments have shown that the use of microelectrodes in such highly resistive media can produce reliable, undistorted data.

The cyclic voltammetry and potential-step experiments show the kinetics of the Li/Li^+ couple to be relatively fast, and that the ligands play an important role in the charge transfer process and subsequent deposition and dissolution of the metal. Evidently, as the molecular weight of the polyether increases, the nucleation overpotential required for deposition of lithium from the PMDETA complex decreases, while from the simple salt it increases. The Tafel plots in Fig. 5-7 show that in the presence of the ligands, mass-transport control begins to dominate at lower potentials than with the simple salt. The voltammograms show that a crystallisation process occurs in each of the electrolytes, but with varying rates of nucleation resulting in the differences seen in the lithium stripping efficiencies. Although the efficiency is high for LiPF_6 in tetraglyme, this decreases to values well below 70% in most cases. The performance of the PMDETA complex shows improvement on moving from liquid PEO400 to

solid PMEO, while the diglyme complex and simple salt show decreasing efficiencies. The current-transients following a cathodic potential-step show the obvious differences in the growth mechanisms and rate determining step for the electrodeposition process. In particular, diffusion to the electrode surface is certainly an important factor with the complexed lithium ion. The stripping efficiencies obtained from double potential-step experiments indicate that the lithium becomes passivated after only a few minutes and protected from further corrosion. Differences between the stripping efficiencies obtained between the potential-step and CV experiments may be attributed to the differences in the type of deposit formed. The poor dissolution behaviour observed may be due to dendritic or needle-like deposits which are unavailable for anodic dissolution. In a real battery design, however, construction is such that growth of the deposit is restricted, hence reducing the likelihood of dendrite formation, which may result in improved charge/discharge cycling behaviour.

REFERENCES

1. E. Peled in *Lithium Batteries* (Edited by J.P. Gabano). Academic Press, London and New York (1983).
2. V.R. Koch, J.L. Goldman, C.J. Mattos and M. Mulvaney, *J. Electrochem. Soc.* 129, 1 (1982).
3. H. Gerisher and D. Wagner, *Phys. Chem.* 92(11), 1325 (1988).
4. K. Weisemer, U. Ecoltd and D. Rahner, *Electrochimica Acta* 34(8), 1277 (1989).
5. P. Radmall, C.R. Jarvin, J.N. Williamson, P.M. Cook and D.J. Whittaker, Process for electrodeposition of lithium, *Patent Application WO 91-GB370* (Mar. 1991).
6. D.J. Genders, W.M. Hedges and D. Pletcher, *J. Chem. Soc. Faraday Trans.1* 80, 3399 (1984).
7. W.M. Hedges and D. Pletcher, *ibid* 82(1), 179 (1986).
8. W. Lu and A.S. Baranski, *J. Electroanal. Chem.* 335(1-2), 105 (1992).
9. A.S. Baranski, M.A. Drogowska and W.R. Fawcett, *ibid* 215(1-2), 105 (1992).
10. F. Bonino, B. Scrosati, A. Selvaggi, J. Evans and C.A. Vincent, *J. Power Sources* 18, 75 (1985).
11. F. Bonino, B. Scrosati and A. Selvaggi, *Solid State Ionics* 28-30, 853 (1988).
12. D. Pletcher, NATO ASI Ser., Ser E, 197 (Microelectrodes) (1991).
13. J. Xu and G.C. Farrington, *Solid State Ionics* 74, 125-132 (1993);
H.S. Chue and G.C. Farrington, *Solid State Ionics* 57, 35 (1992).
14. D. Baril, M. Gauthier and A. Lasia, *J. Electroanal. Chem.*, in press.

15. Duracell Inc., Improved method for preparing non-aqueous electrolytes, *European Patent Application N^o 90302078.2* (Sept. 1990).
16. The Associated Octel Company Ltd., Lewis base complexes of alkali metal salts, *European Patent Application N^o 88309913.7* (Oct. 1988);
D.S. Wright, PhD thesis, Cambridge, England 1989.
17. S. Fletcher, C.S. Halliday, D. Gates, M. Wescott, T. Liwin and G. Nelson, *J. Electroanal. Chem.* 159, 267 (1983).
18. G. Gunawardena, G. Hills, I. Montenegro and B. Scharifker, *ibid* 138, 225 (1982).
19. P.J. Sonnenveld, W. Visscher and E. Barendrecht, *Electrochimica Acta* 37, 1199 (1992).
20. M. Fleischmann and H.R. Thirsk in *Advances in Electrochemistry and Chemical Engineering*, Vol.3 (Edited by P. Delahay and C.W. Tobias) p.123. Interscience, New York (1962).
21. R.K. Jain, H.C. Gaur and B.J. Welch, *J. Electroanal. Chem.* 79, 211 (1977).
22. T. Berzins and P. Delahay, *J. Amer. Chem. Soc.* 75, 4205 (1953).
23. S. Sylla, J.Y. Sanchez and M. Armand, *Electrochimica Acta* 37, 1699 (1992).
24. D. Pletcher, J.F. Rohan and A.G. Ritchie, *ibid* 39, 1369 (1994).

CHAPTER SIX

The Li/Li⁺ Couple in Propylene Carbonate

Electrolytes and Poly(methyl methacrylate) Gels

6.1. Introduction

Development of a polymer electrolyte rechargeable lithium battery has remained a challenge since the discovery of conducting films of lithium salts in poly(ethylene oxide) in the 1970's [1, 2]. Such lithium polymer electrolytes have poor ambient temperature conductivities, generally in the range 10^{-7} - 10^{-8} Scm⁻¹ [3]. The gelled electrolyte alternative consists of a solid phase where a liquid electrolyte is immobilised by a polymer matrix offering liquid-like conductivity. By varying the amount of added polymer, the viscosity of the gel may be altered to provide mechanical properties similar to that of the solid polymers, while maintaining liquid-like electrical behaviour [4-7]. However, high conductivity alone is not sufficient for an electrolyte to be accepted for rechargeable battery applications, but the electrode/electrolyte interface and kinetic factors must also be considered.

Propylene carbonate (PC) has been used for many years as a component for liquid rechargeable lithium batteries [8]. Recently, gelling agents such as poly(acrylonitrile) (PAN) and poly(methyl methacrylate) (PMMA) have been added to lithium electrolyte solutions containing PC as a main component [4-7, 9-14]. While many electrochemical studies have been made on propylene carbonate electrolytes at

conventional sized electrodes [15, 16] and microelectrodes [17, 18], very little work, other than on transport properties, has been performed on gels [13, 14]. Work presented here will attempt to provide an insight into the electrochemical kinetics and mechanisms for lithium deposition at a microelectrode of some novel lithium complexes dissolved in propylene carbonate and gelled with PMMA. Lithium hexafluorophosphate (LiPF_6) is compared with the complexes lithium-bis(diglyme) hexafluorophosphate ($\text{LiPF}_6 \cdot 2\text{DG}$) [19] and lithium-(pentamethyl-diethylene-triamine) hexafluorophosphate ($\text{LiPF}_6 \cdot \text{PMDETA}$) [20, 21]. Both complexes have been proposed as possible alternatives for LiPF_6 as useful electrolytes which have improved thermal stability (Chapter 3) and higher conductivities in non-aqueous solution (Chapter 4). Similar studies on these systems have been performed at a microelectrode in liquid and solid polyether media (Chapter 5) [22].

6.2. Experimental

Propylene carbonate was purified, poly(methyl methacrylate) dried and the electrolyte solutions prepared using the procedures described in Chapter 3. The molal lithium concentrations for PC solutions were 0.53 mol/kg for LiPF_6 and 0.50 mol/kg for $\text{LiPF}_6 \cdot 2\text{DG}$ and $\text{LiPF}_6 \cdot \text{PMDETA}$. PMMA gels were then prepared by dissolving approximately 30wt% PMMA into the PC solutions and heating to 80-90°C, while stirring, until dissolved. The resulting gelled compositions were LiPF_6 (5.23)/PC (64.77)/PMMA (30.00), $\text{LiPF}_6 \cdot 2\text{DG}$ (13.46)/PC (56.54)/PMMA (30.00) and $\text{LiPF}_6 \cdot \text{PMDETA}$ (11.42)/PC (58.58)/PMMA (30.00). A two-electrode micro-

electrode configuration was used during all experiments with a low-pass filter applied at all times. All electrochemical micro-cells were used as described in Chapter three.

6.3. Results and Discussion

6.3.1. Ligand Binding

The binding of the ligands to the lithium ion once the complex has been dissolved in propylene carbonate may be identical to a solution prepared from the pure salt with ligand added separately. The latter is considered to be a binary mixture. The two components of the binary solvent mixture compete for solvation of the Li^+ cation. If diglyme is added to a propylene carbonate solution containing lithium ions, a change in ^7Li NMR chemical shift may indicate preferential coordination by the ether-oxygens of diglyme. The observed chemical shift may be defined as [23, 24]

$$\begin{aligned}
 \delta_{obs} &= x_{\text{Li-PC}} \delta_{\text{Li-PC}} + x_{\text{Li-DG}} \delta_{\text{Li-DG}} \\
 &= (1-x_{\text{Li-DG}}) \delta_{\text{Li-PC}} + x_{\text{Li-DG}} \delta_{\text{Li-DG}} \\
 &= \delta_{\text{Li-PC}} + x_{\text{Li-DG}} (\delta_{\text{Li-DG}} - \delta_{\text{Li-PC}})
 \end{aligned}
 \tag{6-1}$$

Where $x_{\text{Li-DG}}$ is the mole fraction of $^7\text{Li}^+$ coordinated by diglyme, δ_{obs} is the observed chemical shift, $\delta_{\text{Li-PC}}$ and $\delta_{\text{Li-DG}}$ are the shifts attributed to $^7\text{Li}^+$ solvated by PC and diglyme, respectively. This treatment assumes that the observed chemical shift is simply the fast exchange weighted average of the species involved: an initial state characterised by a chemical shift δ_a , a final state with chemical shift δ_b and an

intermediate whose chemical shift is assumed to be simply the mean $\delta_{obs} = 1/2(\delta_a + \delta_b)$ rather than the combination of all intermediates involved in the interconversion.

Table 6-1 lists the ^7Li chemical shifts of PC solutions containing LiClO_4 upon successive additions of diglyme, while maintaining the concentration of Li^+ at ca. 0.2 mol kg^{-1} in each solution. Rearranging Eqn. 6-1 gives

$$x_{\text{Li-DG}} = \left\{ \frac{\delta_{obs} - \delta_{\text{Li-PC}}}{\delta_{\text{Li-DG}} - \delta_{\text{Li-PC}}} \right\} \quad 6-2$$

Table 6-1 Variation of ^7Li NMR chemical shift on increasing mole fraction of added diglyme.

Mole fraction of diglyme added, $x(\text{DG})$	^7Li chemical shift /ppm
0	-0.396
5.40×10^{-3}	-0.591
3.67×10^{-2}	-0.737
7.23×10^{-2}	-0.806
1.29×10^{-1}	-0.846
2.43×10^{-1}	-0.886
2.50×10^{-1}	-0.883

The mole fractions of $^7\text{Li}^+$ bound by diglyme ligands were calculated according to Eqn. 6-2. Figure 6-1 shows a plot of $x_{\text{Li-DG}}$ against mole fraction of diglyme added. As expected, even at very low concentrations the ether oxygens coordinated rapidly to the lithium ions. After occupying the primary solvation sphere the rate of lithium

binding decreases as higher order shells are filled. This result suggests that addition of a ligand such as diglyme preferentially coordinates to Li^+ in a PC solution. Upon dissolution of the complexes, Li^+ -ligand coordination appears to remain intact on a time-averaged scale. It has been shown [25] that addition of LiClO_4 to PC caused a change in PC carbonyl bond stretch from $\nu_{\text{CO}} = 1793\text{cm}^{-1}$ to $\nu_{\text{CO}} = 1774\text{cm}^{-1}$, and on addition of tetraglyme ($\text{TG}:\text{LiClO}_4 = 50:50 \text{ wt}\%$), ν_{CO} returned to 1791cm^{-1} , implying few PC molecules were complexed to the Li^+ . This would indicate that the effect of the ligands in the PC/complex solution can be duplicated by adding the ligand to a solution of the simple salt. However, for salts such as LiPF_6 and LiBF_4 the thermal stability and purity of the isolated electrolyte can only be controlled by synthesising the stoichiometric complex.

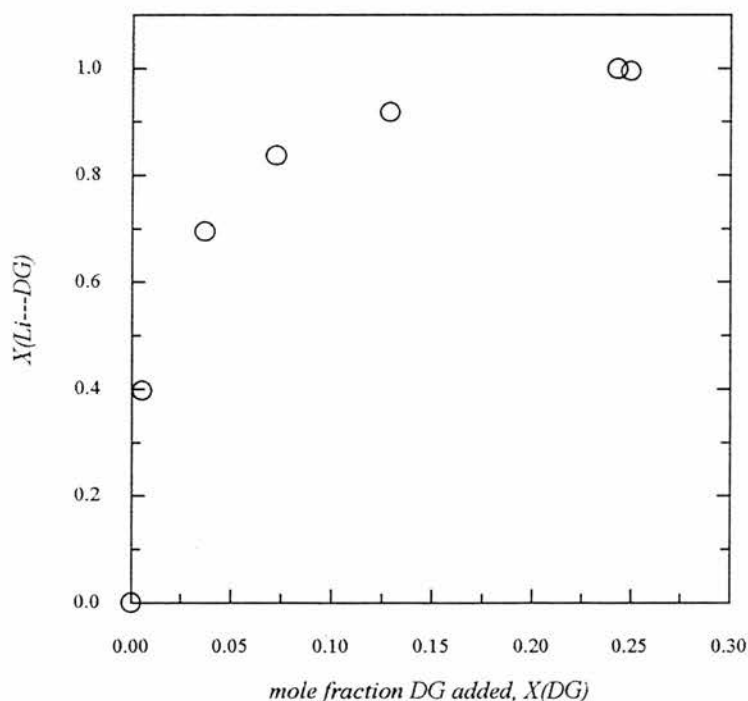


Figure 6-1 Variation of ${}^7\text{Li}^+$ bound by ether-oxygens upon successive additions of diglyme.

6.3.2. Solvent Characterisation

Pure solvents without added electrolyte may be characterised using microelectrodes undistorted by iR drop effects. Several workers have previously studied the propylene carbonate system, suggesting that solvent reduction occurs cathodic of +1V vs. Li/Li^+ [26-28]. Figure 6-2 shows voltammograms at a 25 μm diameter Ni microelectrode (sweep rate = 200 mV/s), with different starting directions of PC distilled in our laboratory. On sweeping cathodically initially (a), no cathodic process was evident and at -5V the current density was less than 1mAcm^{-2} . Similar results were obtained at 10 μm and 25 μm diameter Pt microelectrodes. This confirms the idea suggested by Pletcher *et al* [17] that the cathodic peak seen by others at +1V is attributed to reduction of trace water or some reaction product of the water with PC. Campbell *et al* [27] have shown that with a water content of <15 ppm a cathodic wave still exists. It may be assumed that the water content of our PC is well below the detectable range. A small anodic peak is observed commencing at +2V due to nickel oxide formation. Anodic breakdown of PC started at +4.5V at Ni, more than 1V lower than at Pt, agreeing well with previous literature values [17].

Sweeping anodic to +6V initially (b), resulted in a cathodic wave in the return sweep commencing at +2V, which did not exist when the anodic limit was lowered to +3V. This can be attributed to the reduction of the oxidation products formed during anodic breakdown. Again, at the cathodic limit the current density was very low. Figure 6-3 shows voltammograms recorded for a Ni microelectrode in pure PC gelled with PMMA (30 wt%).

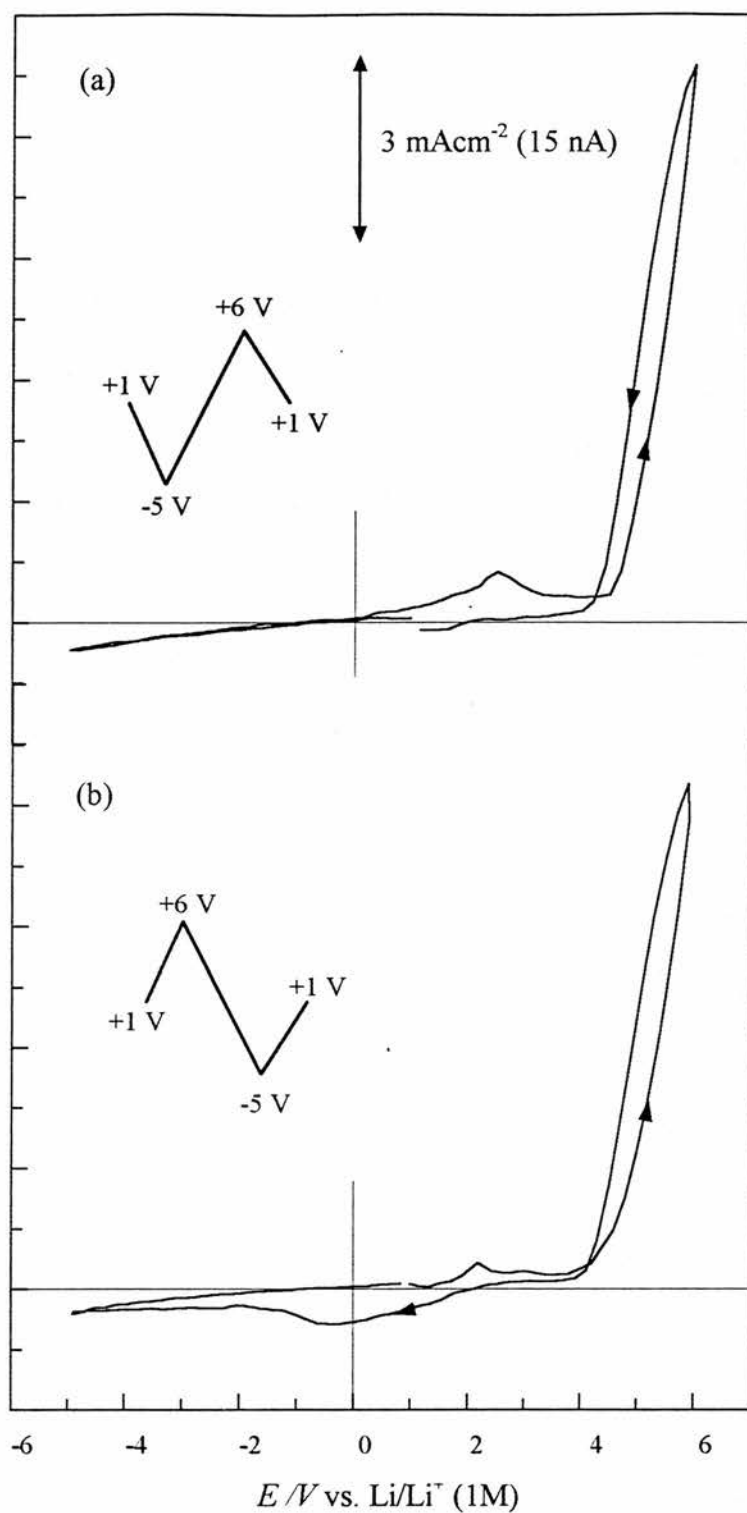


Figure 6-2 Cyclic voltammograms for distilled PC at a $25 \mu\text{m}$ diameter Ni microelectrode vs. Li/Li^+ . Initial sweep direction is (a) cathodic and (b) anodic. Sweep rate = 200 mV/s .

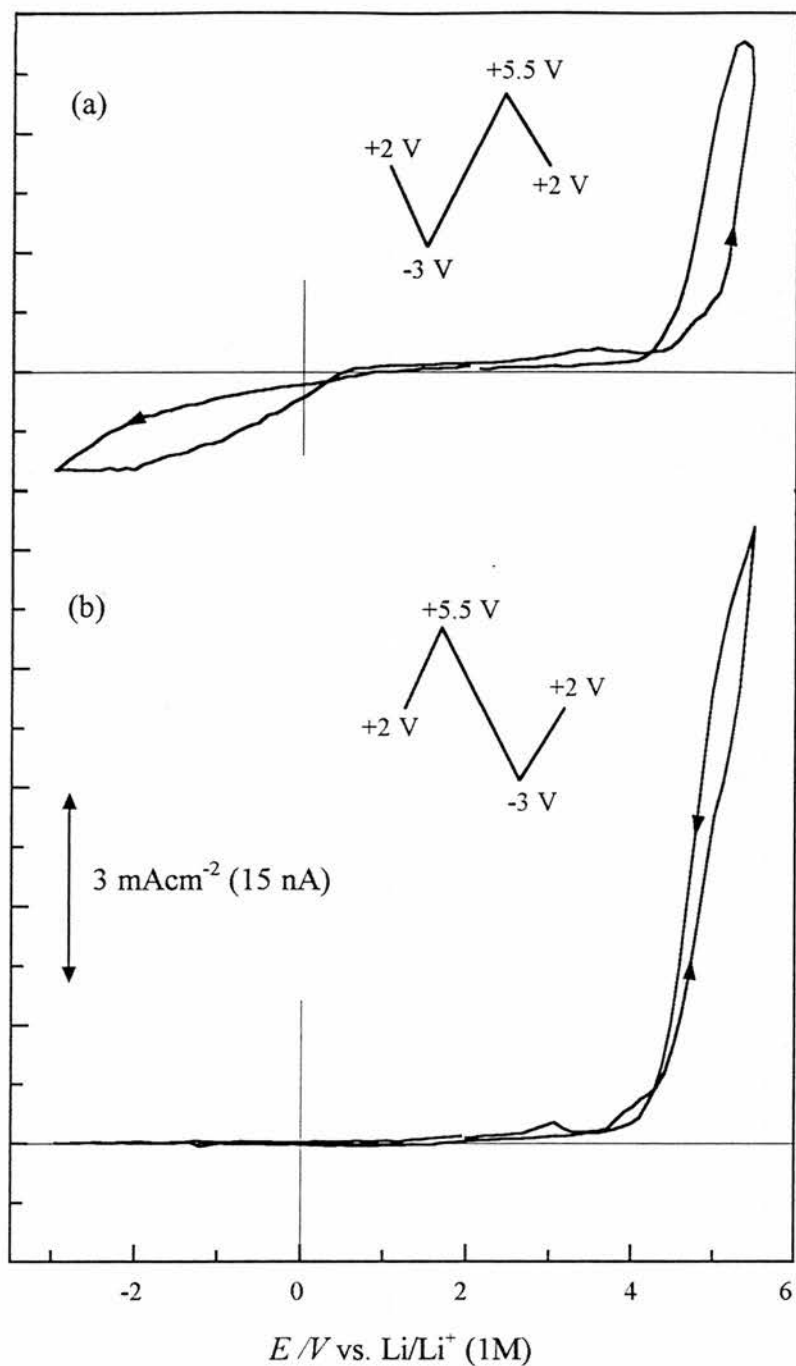


Figure 6-3 Cyclic voltammograms for PC/PMMA(30wt%) at a $25\mu\text{m}$ diameter Ni microelectrode vs. Li/Li^+ . Initial sweep direction is (a) cathodic and (b) anodic. Sweep rate = 200 mV/s.

On sweeping cathodic initially (a), a cathodic current flowed possibly as a result of PMMA reduction or that of trace water from the polymer. As in pure PC, a peak corresponding to nickel oxide formation was observed above +2V followed by anodic breakdown of the solvent. A difference occurred on sweeping anodically first (b). The reduction wave observed in curve (a) was not seen in curve (b), suggesting that if trace water was the cause of the breakdown then all of it was used in the formation of the oxide film and/or was involved with the electrochemical process during anodic breakdown of the solvent. The higher currents at the anodic limit of curve (b) may provide further evidence for this.

6.3.3. Potentials Positive of Bulk Lithium Deposition

On adding a lithium electrolyte to the solvents a quite different *I-E* response was observed at potentials positive of 0V vs. Li/Li^+ . Figure 6-4 shows three cycles of a typical voltammetric response for the lithium/PC and gelled electrolytes over a potential range of +2.5V to 0V at Ni. In the first cycle several peaks were observed during the cathodic sweep at (a) +1.44V, (b) +1.39V, (c) +0.59V and (d) +0.33V. The anodic scan reveals two peaks at (e) +0.92V and (f) +2.07V. Peak (a) has been shown by others [13, 17] to be due to trace water reduction, evidently introduced by the added electrolyte. Koch *et al* [28] showed that the reduction of the AsF_6^- anion occurred ca. +1V suggesting the possibility of the PF_6^- anion breakdown corresponding to peak (b). Peaks (c) and (d) have been attributed to the underpotential deposition (UPD) of lithium from an insoluble lithium hydroxide layer formed at the surface of the electrode [17, 29]. Peak (e) seems likely to correspond to

the stripping of lithium from such an UPD layer, or from a lithium-nickel alloy also formed during the cathodic sweep. Reversing the sweep direction at +0.8V, before the onset of UPD and alloy formation, results in the absence of peak (e) confirming the correlation between the two processes. Cathodic peaks in the range +0.6V - +0.3V with a coupled anodic peak have also been observed in polyether systems [22].

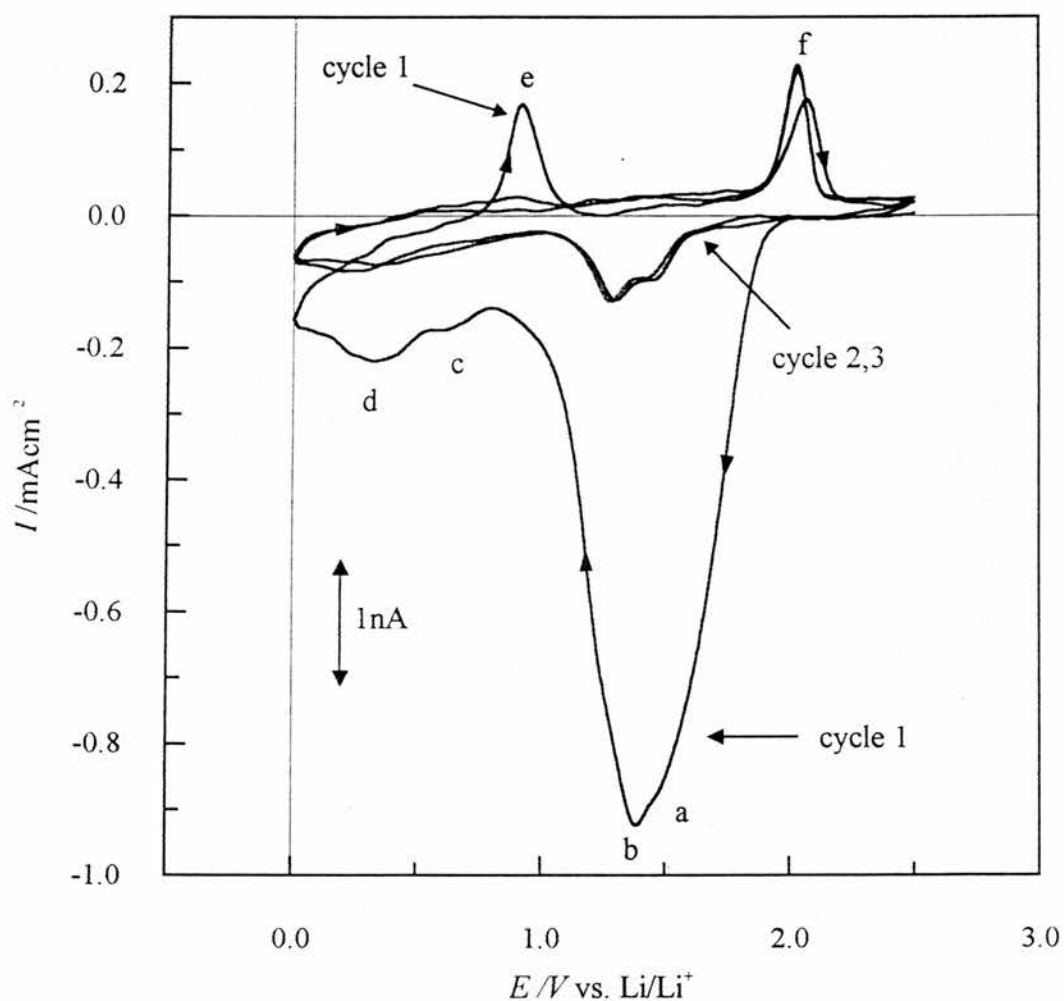


Figure 6-4 Cyclic voltammogram of LiPF_6 .PMDETA/PC/PMMA(30 wt%) at a $25\mu\text{m}$ diameter Ni microelectrode vs. Li/Li^+ . Sweep rate = 10 mV/s.

Nickel-oxide formation results in peak (f), as seen in the pure solvent systems. Further cycles indicate that the water content has greatly diminished with a corresponding decrease in peaks (c), (d) and (e) as the LiOH layer becomes thinner. It appears that as the water content of the electrolyte increases, the amount of lithium available for UPD from a surface layer also increases and the corresponding voltammetry peaks become more pronounced.

6.3.4. Kinetics of the Li/Li⁺ Couple

Figs. 6-5 shows voltammograms of (a) LiPF₆ (0.5 mol/kg) and (b) LiPF₆.2DG in PC at a 25μm diameter Ni microelectrode vs. Li/Li⁺, recorded between +0.5V and -0.2V at 10mV/s. In each case the current density is very low until a sufficient overpotential has been reached for lithium nucleation to take place. The current then increases rapidly as growth of the lithium deposit occurs. This deposition process continues until the equilibrium potential at 0V has been reached, after which point oxidation of the freshly deposited lithium layer proceeds with a corresponding anodic stripping peak. The current densities obtained are comparable with those obtained by Pletcher and co-workers [18] for LiAsF₆ in propylene carbonate. The LiPF₆.PMDETA complex in PC seems to produce much lower current densities - in the same order of magnitude as in solid polyethers (Chapter 5). Fig. 6-6 shows multi-cycle voltammograms for LiPF₆.PMDETA/PC (0.5 mol/kg). The first cycle suffers from the reduction of water and subsequent hydroxide layer formation. As UPD occurred the electrode surface became prepared for successive cycles and the stripping efficiency increased from 29.9% in the first cycle to 97.3% in the third.

Lithium plating and stripping was also performed on 30wt% PMMA gels containing the three electrolytes. The I - E response for each system is shown in Fig. 6-7 (a-c) swept between +0.5V and -0.3V at 10mV/s. The characteristic parameters of each electrolyte in both PC and PMMA gels are listed in Table 6-2.

The stripping efficiencies decreased in the order LiPF_6 (77%) > $\text{LiPF}_6\cdot 2\text{DG}$ (65%) > $\text{LiPF}_6\cdot \text{PMDETA}$ (30%) for the first cycle in propylene carbonate, while the gels decreased in the order $\text{LiPF}_6\cdot 2\text{DG}$ (75%) > LiPF_6 (61%) > $\text{LiPF}_6\cdot \text{PMDETA}$ (26%). These values in PC are comparable with those obtained in other lithium systems [18]. On moving the cathodic limit to -0.5V (Fig. 6-8), the ratio of lithium stripped to plated increased in each case to $\text{LiPF}_6\cdot 2\text{DG}$ (81%) > LiPF_6 (80%) > $\text{LiPF}_6\cdot \text{PMDETA}$ (40%). This would suggest that a passivating layer formed by corrosion of freshly deposited lithium is of finite thickness. As the lithium layer becomes thicker the quantity of lithium used to form this layer becomes less significant relative to the quantity deposited.

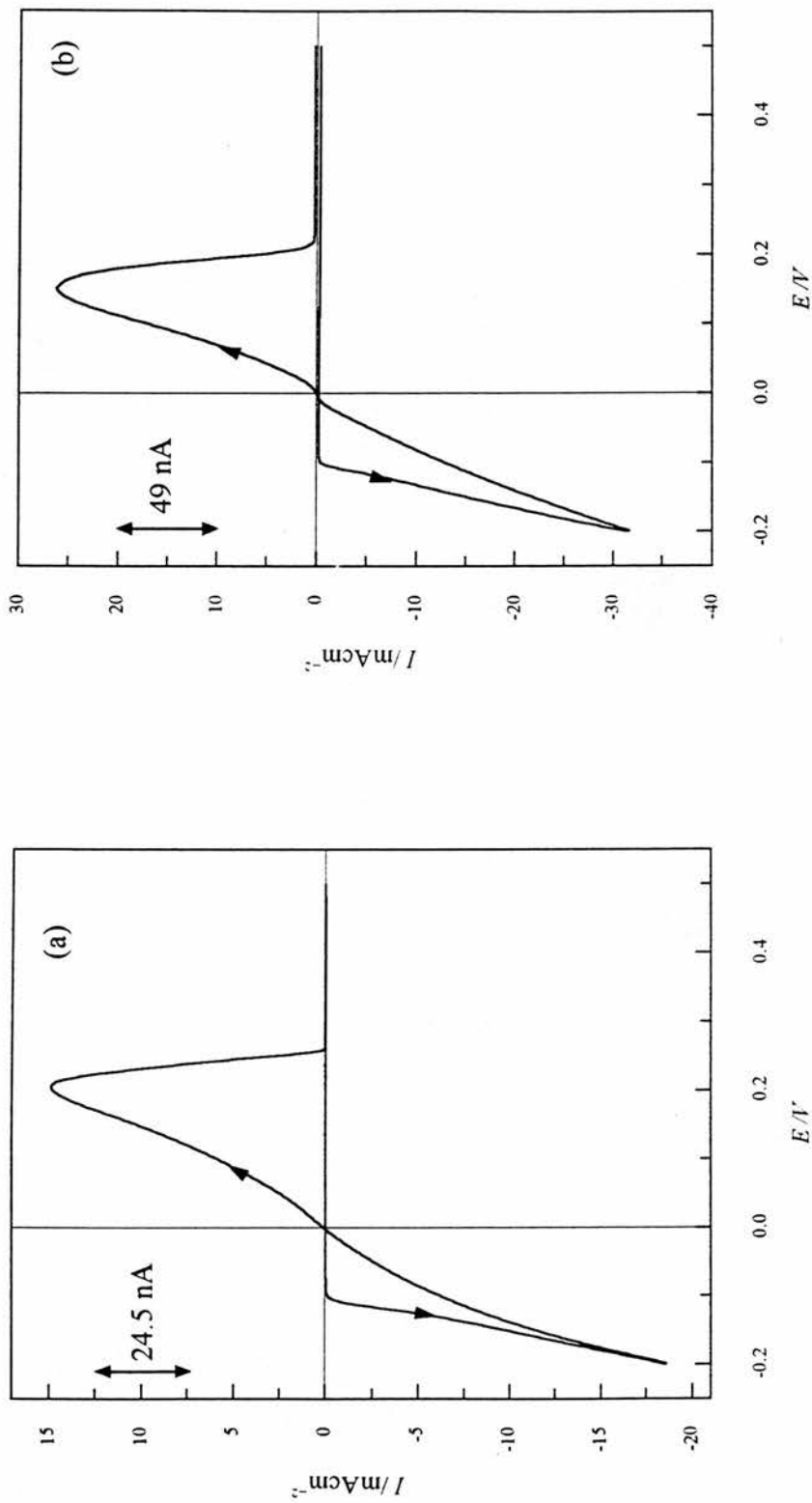


Figure 6-5 Cyclic voltammogram of the lithium plating and stripping at a $25\text{-}\mu\text{m}$ diameter Ni microelectrode vs. Li/Li^+ from (a) LiPF_6 (0.5 mol/kg) and (b) $\text{LiPF}_6 \cdot 2\text{DG}$ in PC. Sweep rate = 10 mV/s .

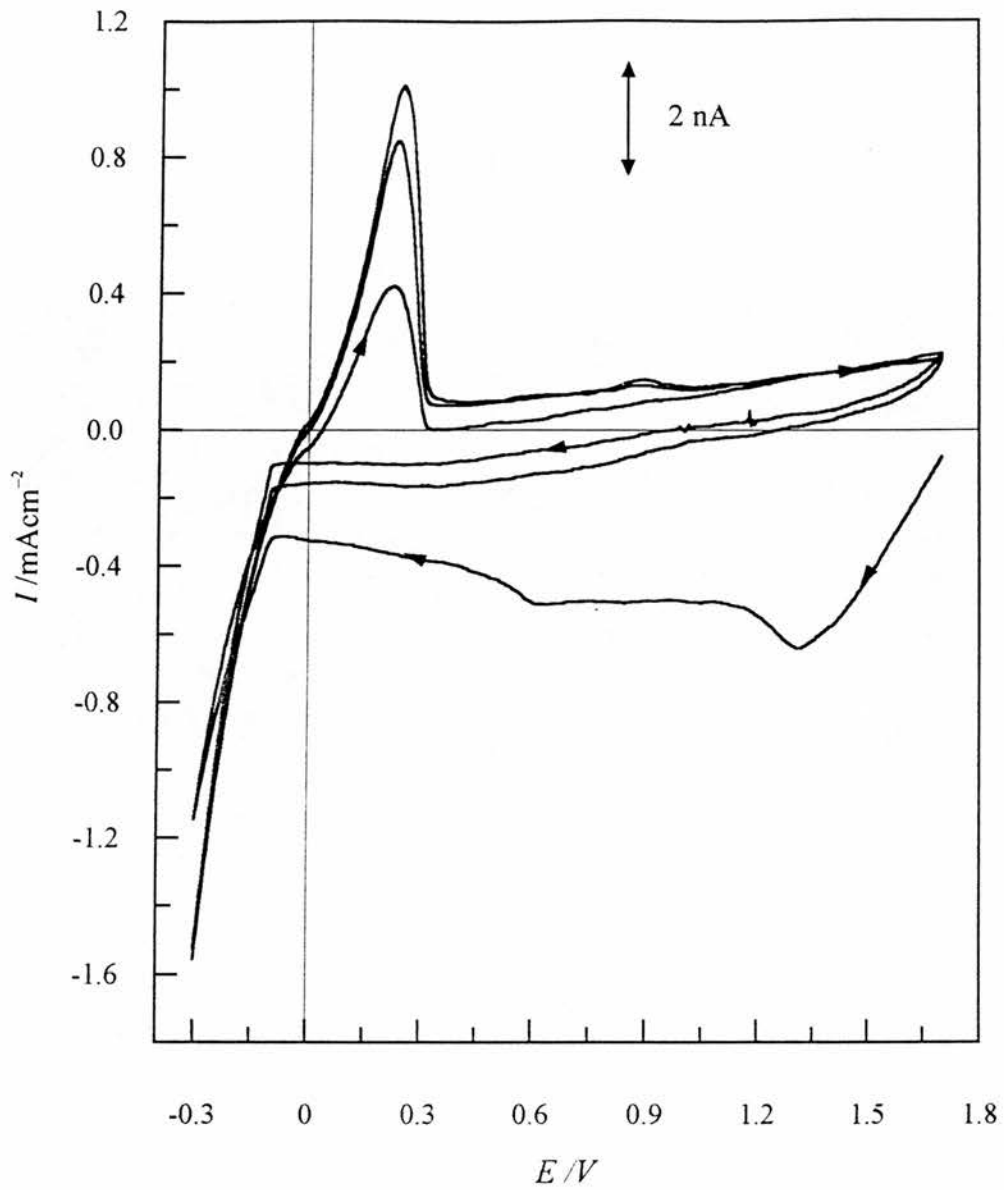


Figure 6-6 Multi-cycle voltammogram of lithium plating and stripping from LiPF_6 .PMDETA / PC (0.5 mol/kg) at a 25 μm diameter Ni microelectrode vs. Li/Li^+ .

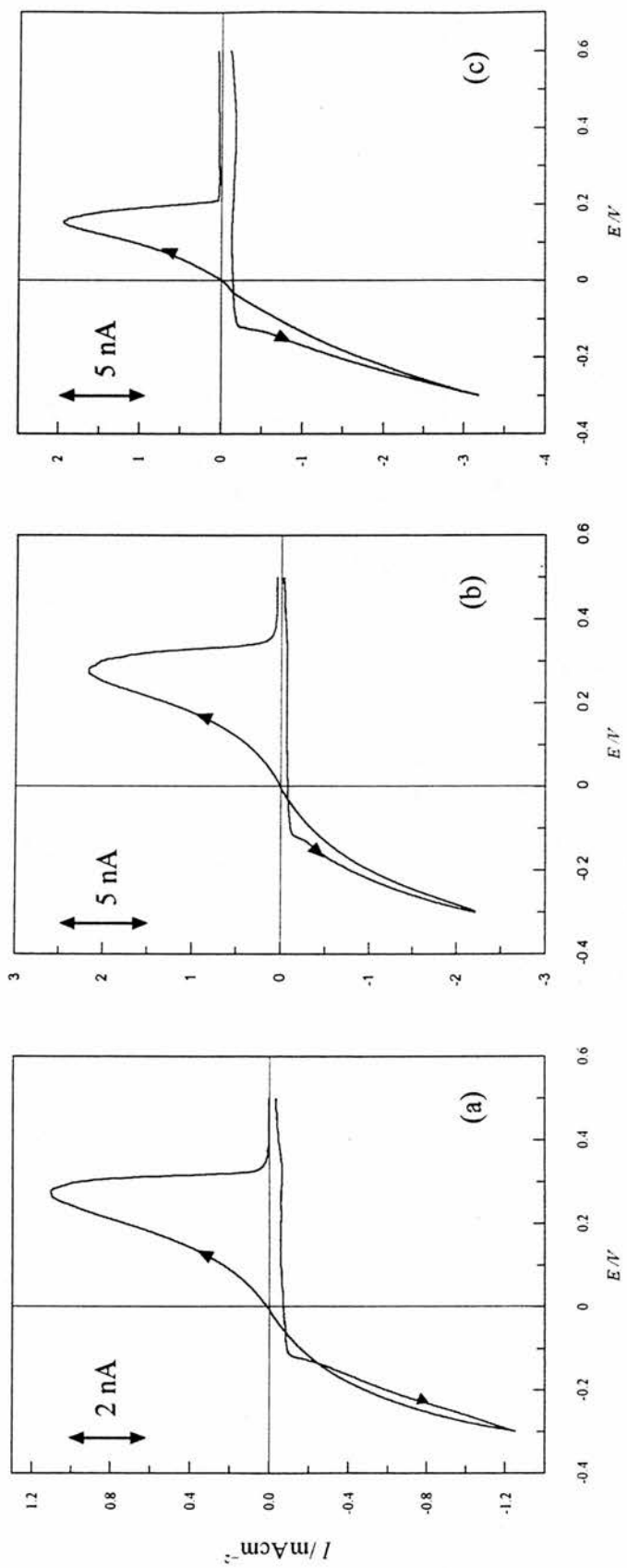


Figure 6-7 Cyclic voltammogram of the lithium plating and stripping at a 25 μ m diameter Ni microelectrode vs. Li/Li⁺ from (a) LiPF₆, (b) LiPF₆.2DG and (c) LiPF₆.PMDETA in PC/30wt% PMMA. Sweep rate = 10mV/s. Cathodic limit = -0.3V.

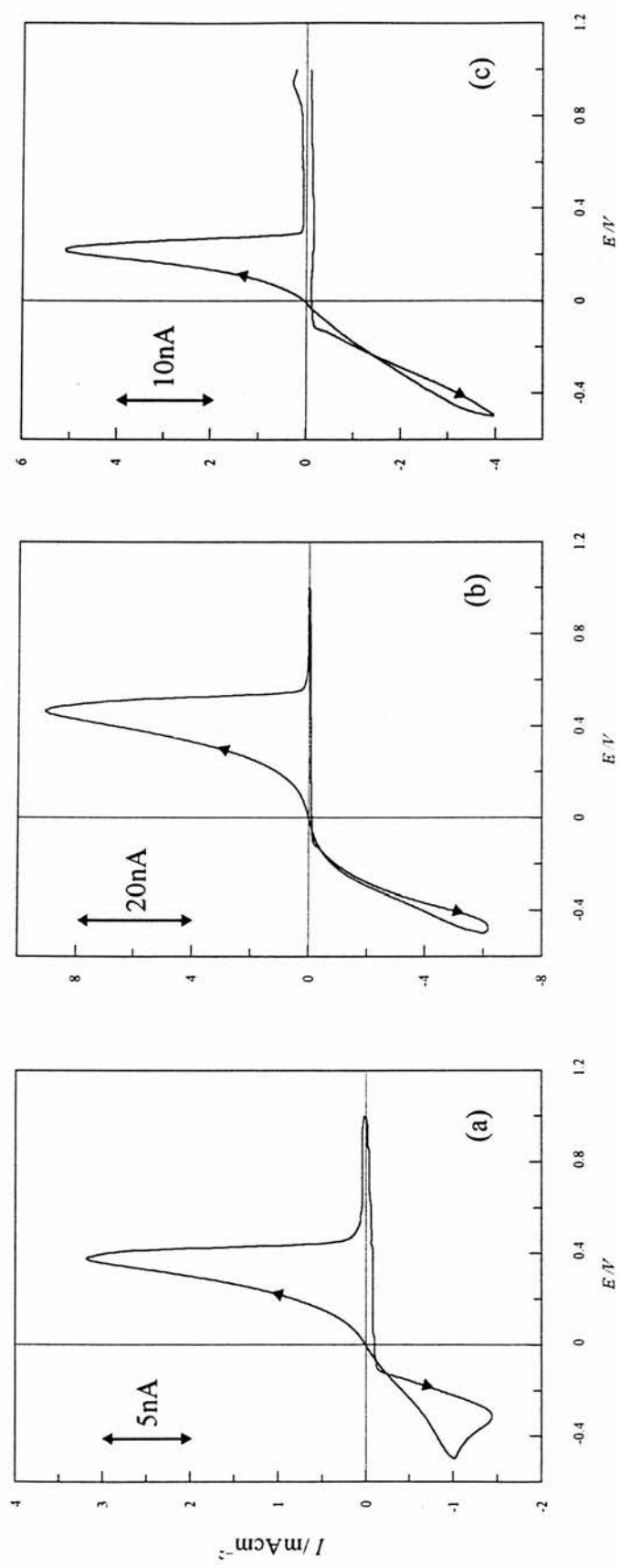


Figure 6-8 Cyclic voltammogram of the lithium plating and stripping at a 25 μ m diameter Ni microelectrode vs. Li/Li⁺ from (a) LiPF₆, (b) LiPF₆:2DG and (c) LiPF₆:PMDETA in PC/30wt% PMMA. Sweep rate = 10mV/s. Cathodic limit = -0.5V.

Table 6-2 Some electrochemical parameters obtained at a 25 μ m Ni microelectrode vs. Li/Li⁺ by cyclic voltammetry; sweep rate $\nu = 10$ mVs⁻¹, T = 298 K.

ELECTROLYTE		Nucleation overpotential	Cathodic current density at $\eta = 0.2$ V.	Exchange current density	Transfer coefficients	Peak potentials	Stripping efficiency (1 st cycle)
Solvent	Salt	η /mV	I /mAcm ⁻²	I_0 /mAcm ⁻²	$(n\alpha)_A$	E_p^A /mV	%
	LiPF ₆ (0.5 mol/kg)	103	18.5	1.06 ^{BV}	0.48	203	77.0
	LiPF ₆ .2DG (0.5 mol/kg)	103	31.5	2.34 ^{BV} 0.901 ^L	0.53	151	65.0
	LiPF ₆ .PMDETA (0.5 mol/kg)	91.0	0.654	0.042 ^{BV} 0.041 ^L	0.45	224	29.9
-----		-----	-----	-----	-----	-----	-----
	LiPF ₆ (0.5 mol/kg PC)	107	0.593	0.0290 ^{BV}	0.53	274	60.6
	LiPF ₆ .2DG (0.5 mol/kg PC)	115	0.782	0.0377 ^L 0.0579 ^{BV}	0.50	274	75.3
	LiPF ₆ .PMDETA (0.5 mol/kg PC)	120	1.43	0.0622 ^L 0.150 ^{BV} 0.138 ^L	0.59	155	26.4

^{BV} Values calculated from a N.L.S. fit to Butler-Volmer curve.

^L Linear part of CV at low overpotentials.

The efficiencies observed in these gels are higher than those seen by Scrosati *et al* [13] in PC/EC/PAN gels at a large nickel electrode. Nucleation overpotentials decrease in the order LiPF_6 , $\text{LiPF}_6\cdot 2\text{DG} > \text{LiPF}_6\cdot \text{PMDETA}$ in PC and $\text{LiPF}_6\cdot \text{PMDETA} > \text{LiPF}_6\cdot 2\text{DG} > \text{LiPF}_6$ in the PMMA gels. This reversal of order from PC to gel suggests that the polymer interacts with the cation and more significantly with the complexed cation. However once the appropriate overpotential has been reached the rate of deposition was more rapid with each of the complexes than with the simple salt. Exchange current densities were calculated from non-linear least-squares (NLLS) fitting of the reverse sweep of the voltammograms to the Butler-Volmer equation. Figs. 6-9 and 6-10 show typical NLLS fits to (a) the reverse sweep and (b) the Tafel slopes of the voltammograms for LiPF_6/PC and $\text{LiPF}_6/\text{PC}/\text{PMMA}$, respectively. The exchange current densities determined in this way were compared with those obtained from a linear approximation to the Butler-Volmer equation at very low overpotentials, defined previously in Chapter 5 (eqn. 5-1) [22].

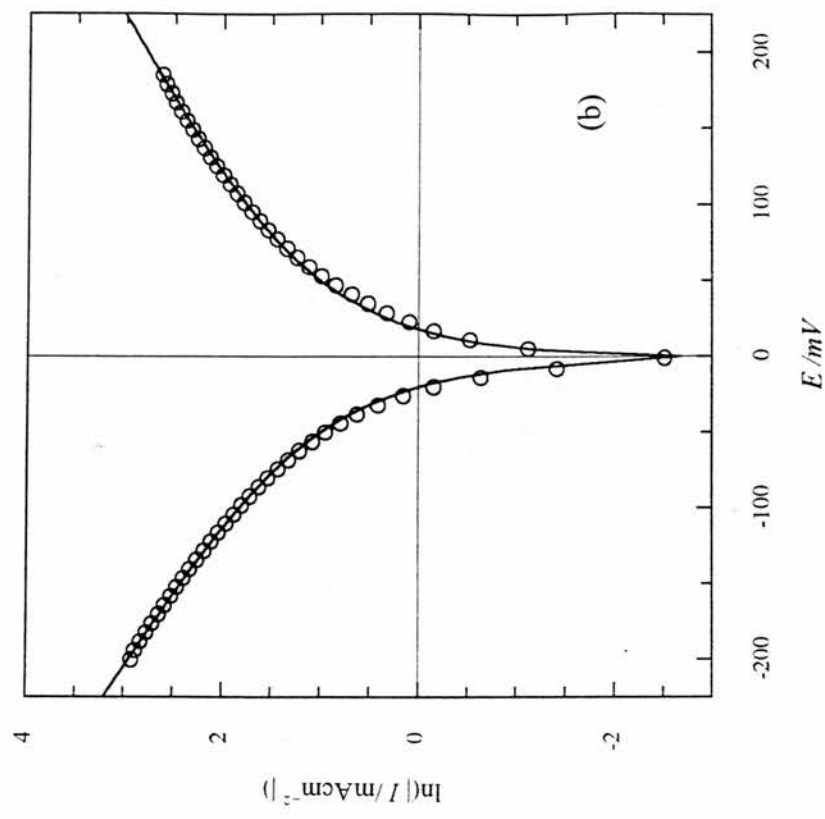
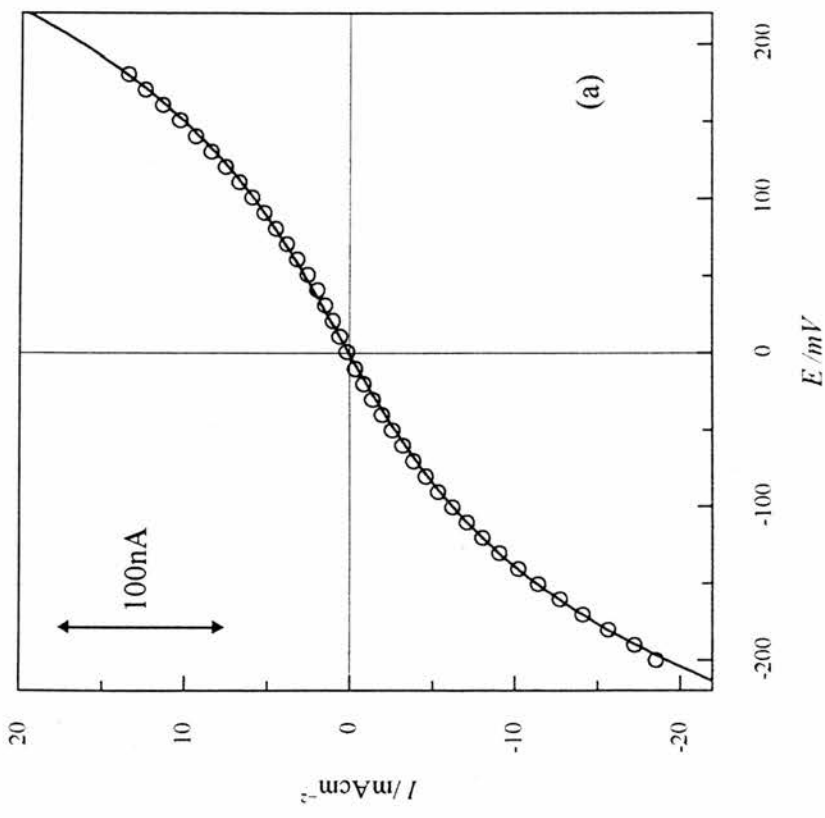


Figure 6-9 (a) Reverse sweep and (b) Tafel slopes of the voltammogram for LiPF₆/PC at 10mV/s. The solid lines represent the NLLS fit to the Butler-Volmer equation.

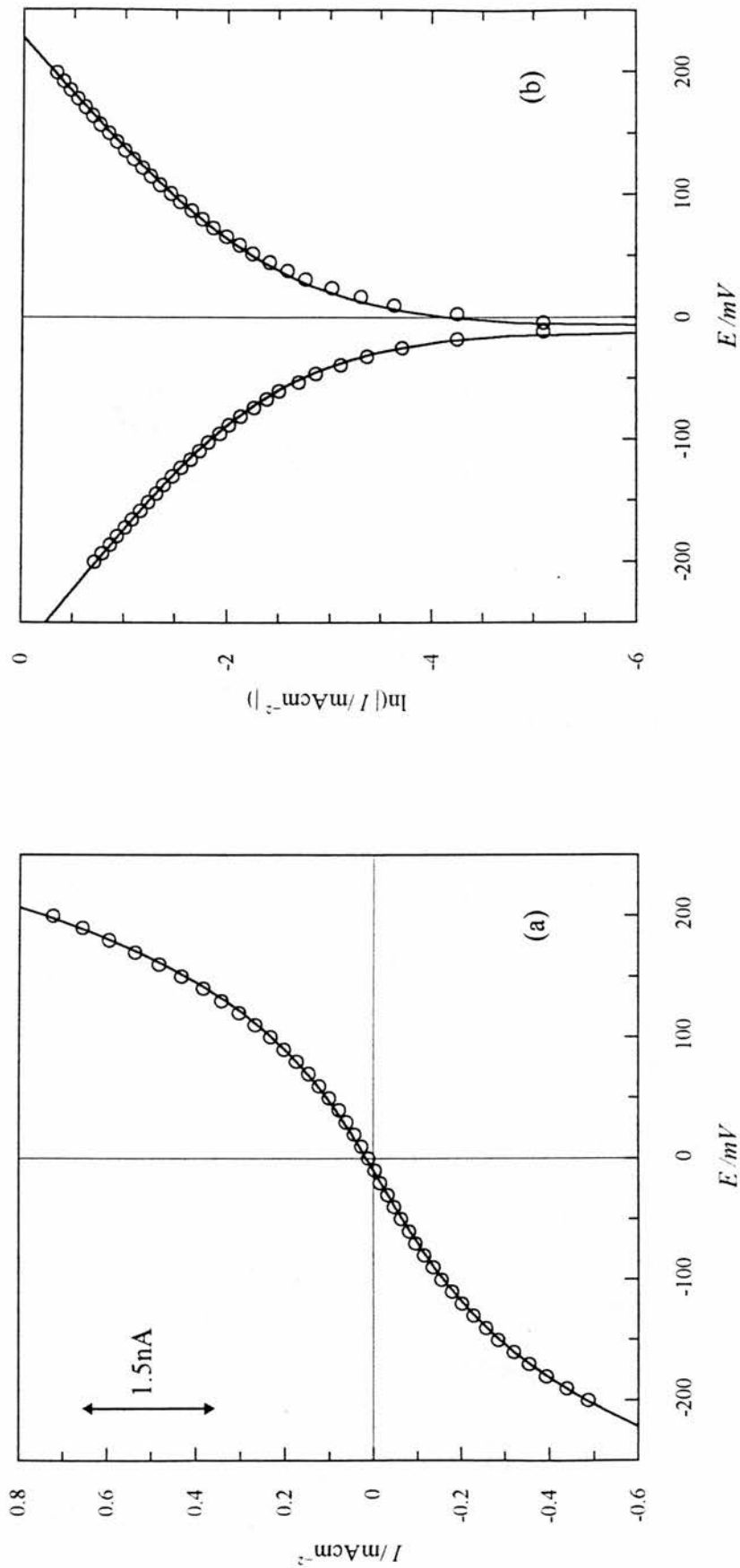


Figure 6-10 (a) Reverse sweep and (b) Tafel slopes of the voltammogram for LiPF₆/PC/PMMA at 10mV/s. The solid lines represent the NLLS fit to the Butler-Volmer equation.

The kinetics of the Li/Li^+ couple were studied further by applying a series of potential-step experiments. A cathodic potential step was applied, passing ca. 0.5 C/cm^2 of charge, to deposit a layer of lithium. The potential was then stepped to an anodic potential in the range $+75\text{mV}$ to $+300\text{mV}$. A set of transients for the anodic polarisation of a freshly deposited lithium layer from LiPF_6/PC is shown in Fig. 6-11.

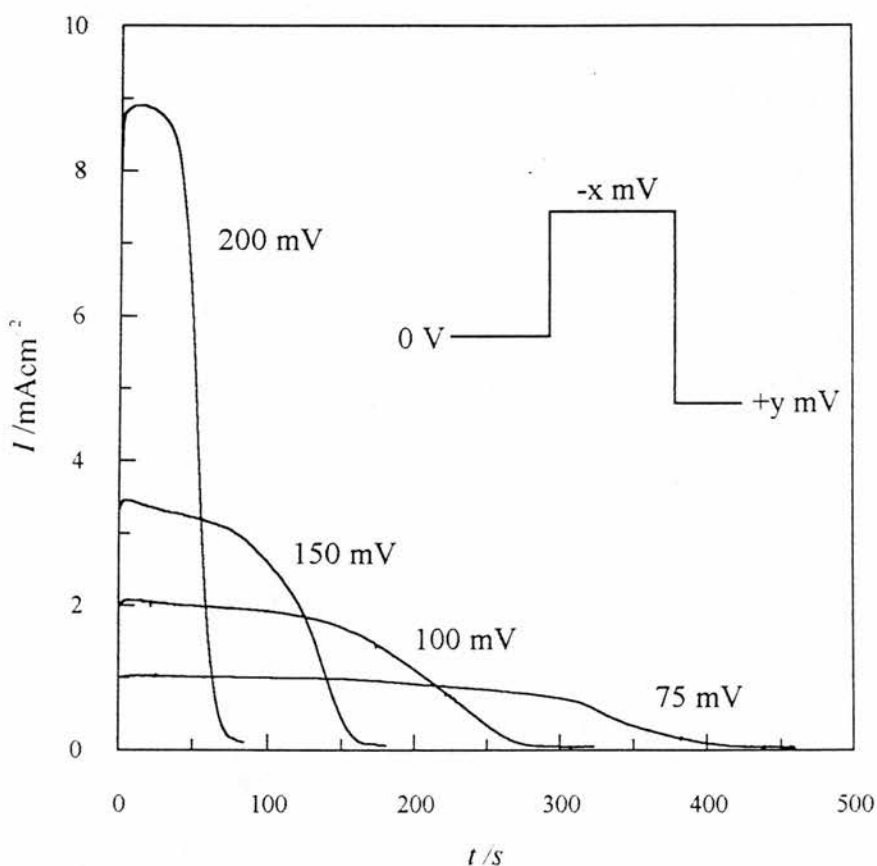


Figure 6-11 Anodic polarisation of deposited lithium from LiPF_6/PC at a $25\mu\text{m}$ diameter microelectrode vs. Li/Li^+ .

After application of the anodic step the lithium oxidises at an approximately uniform rate until the layer is depleted. Reactivation, or pitting, of the deposit at higher overpotentials results in the current transient passing through a peak. By varying the

cathodic deposition potential over the range -75mV to -400mV and applying for 5 secs., the current transients reach steady state plateaux corresponding to thickening of the lithium layer. The steady-state current plateau from each of the polarisation curves can be used to construct the Tafel plot. The Tafel plots for the PC solutions and PMMA gels are shown Figs. 6-12 (a) and (b), respectively. Straight lines are observed in each case corresponding to charge-transfer control. Deviations from the Tafel slopes at very low overpotentials indicate the lower limit to which the limiting form of the Butler-Volmer expression can be used. Where mass transport control dominates the currents deviate from the Tafel line at very high overpotentials. The transfer coefficients and exchange current densities were determined from the slopes and intercept of the lines extrapolated to the equilibrium potential.

Table 6-3 The exchange current densities and transfer coefficients for PC and PMMA gelled electrolytes, obtained from Tafel plots.

ELECTROLYTE		I_0 / mAcm^{-2}	$(n\alpha)_C$	$(n\alpha)_A$
Solvent	Salt			
	LiPF ₆	1.08	0.14	0.24
PC	LiPF ₆ .2DG	2.82	0.29	0.36
	LiPF ₆ .PMDETA	0.146	0.19	0.29
	LiPF ₆	0.134	0.22	0.24
PC/PMMA	LiPF ₆ .2DG	0.0700	0.26	0.37
	LiPF ₆ .PMDETA	0.483	0.13	0.39

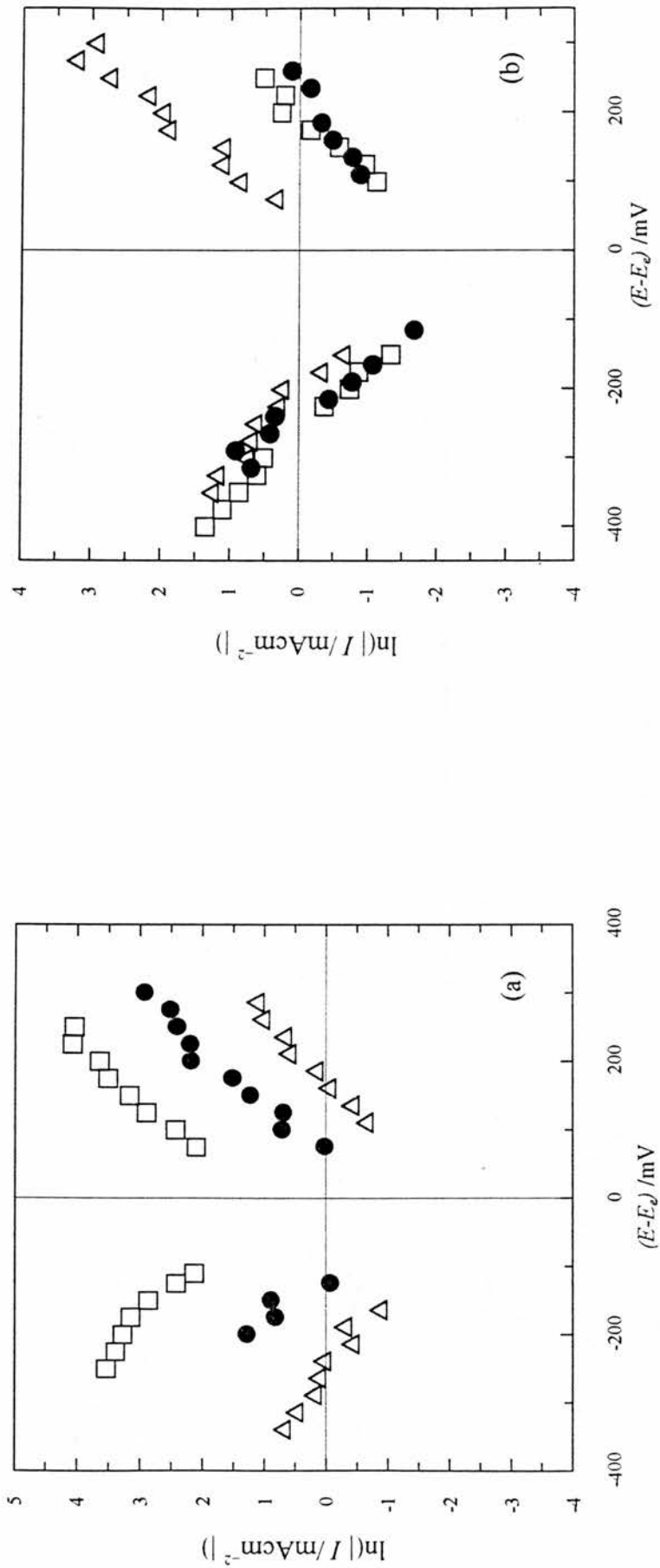


Figure 6-12 Tafel slopes obtained from steady-state current transients of freshly deposited lithium at a 25 μm diameter Ni microelectrode vs.

Li/Li^+ . Data points represent (●) $LiPF_6$, (□) $LiPF_6 \cdot 2DG$ and (Δ) $LiPF_6 \cdot PMDETA$ each in (a) PC and (b) PC / 30wt% PMMA.

Table 6-3 lists the results of this analysis. Taking into consideration the different method for lithium deposition, the values obtained compare well with those determined from voltammetry data.

6.3.5. *Nucleation and Growth of the Lithium Deposit*

Any electrochemical phase transformation generally involves either two- or three-dimensional nucleation processes during the early stages [29, 30] (as described in Chapter 2). The number of nuclei and rate of formation is strongly dependent on the overpotential applied. Chronoamperometry involves the application of a potential-step while recording the current transient, which can provide an insight into the morphology of the deposit growing at the electrode surface. Fig. 6-13 shows a set of experimental current transients for propylene carbonate containing $\text{LiPF}_6 \cdot 2\text{DG}$ (0.5 mol/kg). As the electroactive area of the deposit grows, the current rises and approaches a steady state value where continuous thickening of the layer takes place. On increasing the potential-step the lithium is deposited at a higher rate and the rise time to the steady-state plateau decreases. The general appearance of the $I-t$ transients have the features of a three-dimensional nucleation and growth process. At longer time scales the current rises once more indicating a further increase in the surface area, likely to be due to growth of the deposit over the glass surrounds of the microelectrode [32]. At potential-steps lower than the nucleation overpotentials listed in table 6-2 rising transients were not observed on the experimental time-scale. The initial rising transient follows a function of t^n , where n depends on the type of

nucleation, the geometry of the nuclei and the rate determining step of nuclei incorporation into a growing cluster.

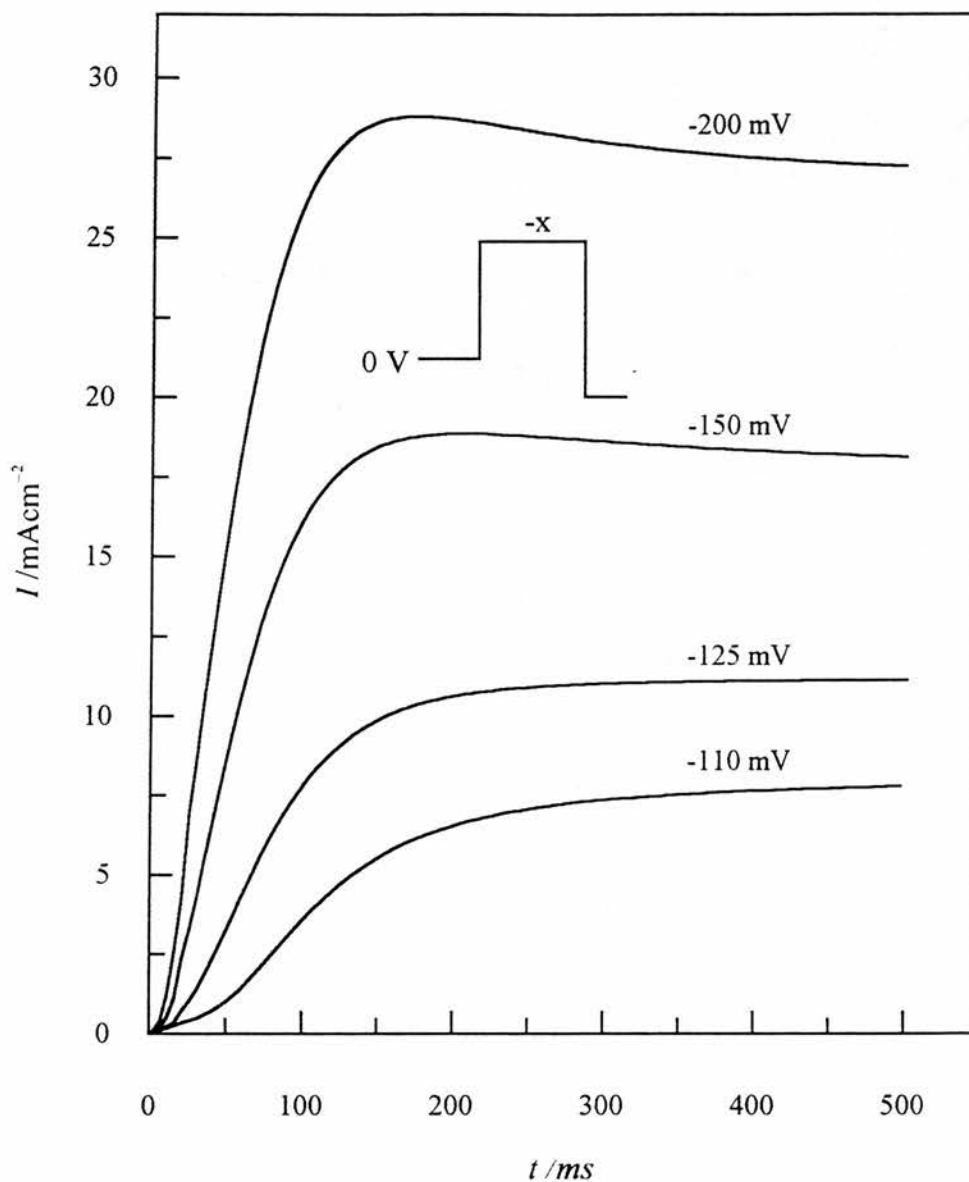


Figure 6-13 Current transients for the nucleation and growth of lithium from $\text{LiPF}_6 \cdot 2\text{DG}/\text{PC}$ (0.5 mol/kg) at a $25\mu\text{m}$ diameter microelectrode vs. Li/Li^+ . The overpotentials applied are indicated in the figure.

It has been shown previously (Chapter 5) that non-linear least-squares fits to prolonged current-transient expressions were preferable over a simple linear fit of the rising section to the appropriate function of t . The equations describing three-dimensional nucleation can be simplified, as shown before (Chapter 5), to

$$I = a\{1 - \exp(bt^2)\} \quad 6-3$$

$$I = a\{1 - \exp(ct^3)\} \quad 6-4$$

for kinetic controlled growth of cones or hemispheres following three-dimensional instantaneous and progressive nucleation, respectively, where I is the current density and t is the time; and

$$I = \frac{d}{\sqrt{t}}\{1 - \exp(et)\} \quad 6-5$$

$$I = \frac{d}{\sqrt{t}}\{1 - \exp(ft^2)\} \quad 6-6$$

for diffusion controlled growth of hemispheres following three dimensional instantaneous and progressive nucleation, respectively. The parameters a-f are arbitrary variables that are calculated during each fit. Fig. 6-14 shows the NLLS fit at each potential as solid lines, clearly indicating the close correlation between the experimental data and the model for instantaneous nucleation followed by kinetic controlled growth of cones or hemispheres.

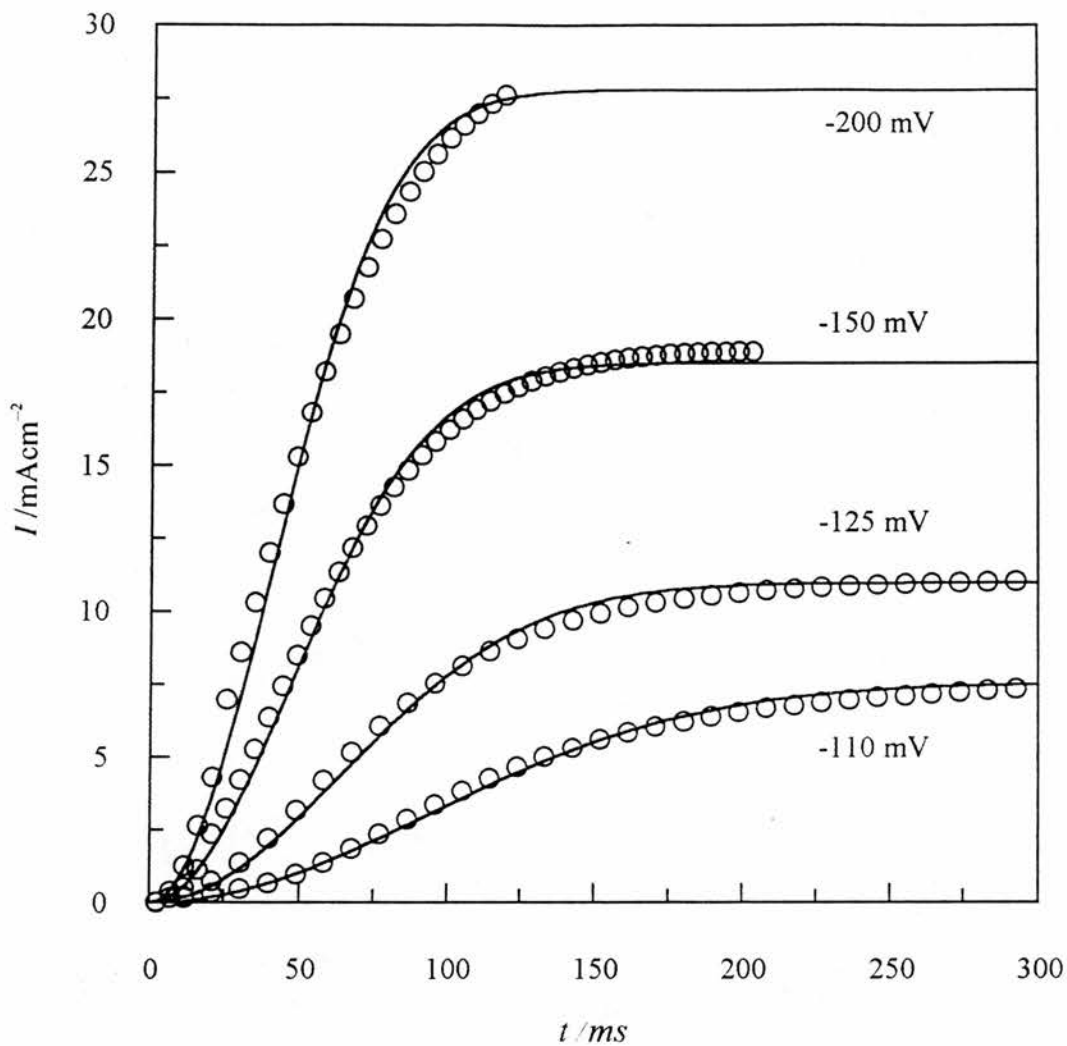


Figure 6-14 Current transients at various overpotentials for $\text{LiPF}_6 \cdot 2\text{DG}/\text{PC}$ at a $25\mu\text{m}$ diameter microelectrode vs. Li/Li^+ . The solid lines indicate NLLS fits for instantaneous nucleation followed by kinetic controlled growth of cones or hemispheres.

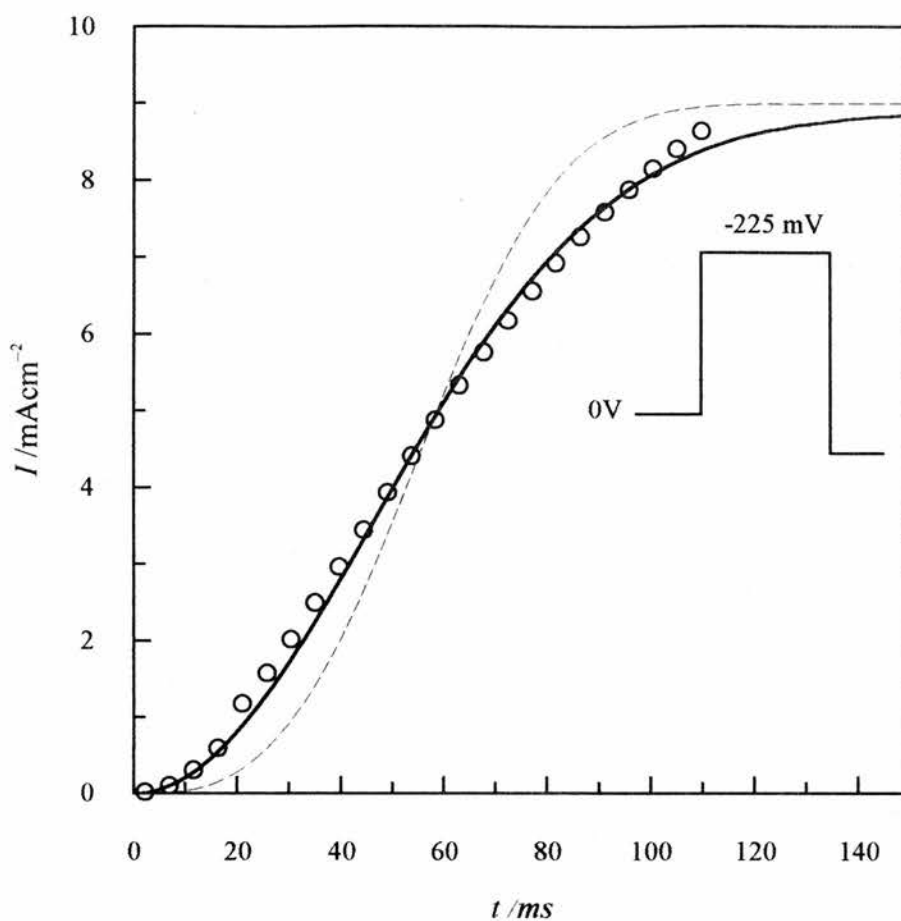


Figure 6-15 Current transient at -225mV for LiPF_6/PC at a $25\mu\text{m}$ diameter microelectrode vs. Li/Li^+ . The solid lines indicates the NLLS fit for instantaneous nucleation followed by kinetic controlled growth of cones or hemispheres. The broken line represents progressive nucleation.

The clear difference between the instantaneous and progressive nucleation models is seen in Fig. 6-15 for LiPF_6 in PC at a potential step of -225mV. A simulation of progressive nucleation followed by kinetic controlled growth is indicated by the broken line.

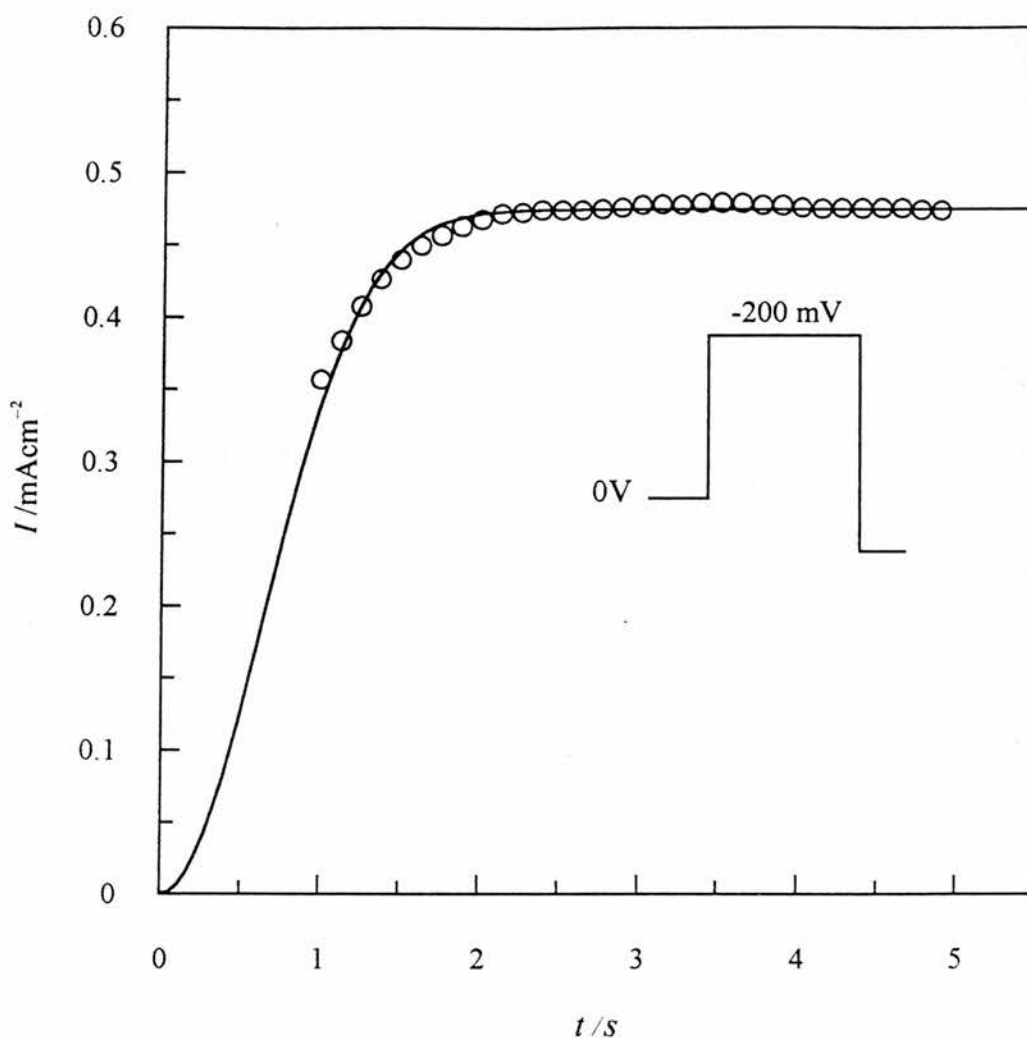


Figure 6-16 Current transient at -200mV for $\text{LiPF}_6\cdot 2\text{DG}/\text{PC}/\text{PMMA}$ at a $25\mu\text{m}$ diameter microelectrode vs. Li/Li^+ . The solid lines indicates the NLLS fit for instantaneous nucleation followed by kinetic controlled growth of cones or hemispheres.

The current transients for the gels suffer from large charging currents which distort the $I-t$ curves during the early stages. This results in a difficult analysis and relies on well formed transients after decay of the charging current. A typical curve is shown in

Fig. 6-16 for the deposition of lithium from $\text{LiPF}_6\cdot 2\text{DG}/\text{PC}/\text{PMMA}$ with the corresponding NLLS fit.

All the electrolytes, in both PC and PC/PMMA gels, appear to undergo instantaneous 3-D nucleation followed by kinetic controlled growth. In some cases, at very high overpotentials, the transients pass through a peak before reaching their steady-state values. This is most likely due to a contribution of linear diffusion, similar to that seen at a conventional sized electrode, since a pure hemispherical diffusion zone does not exist on the time-scale of the experiments at a $12.5\mu\text{m}$ radius micro-disk.

6.3.6. *Lithium Reactivity and Passivation*

A typical current reversal chronopotentiogram is shown in Fig. 6-17 obtained from $\text{LiPF}_6\cdot 2\text{DG}/\text{PC}/\text{PMMA}$ at a Ni microelectrode, where the applied cathodic (forward) and anodic (reverse) currents were both 4nA (0.81 mAcm^{-2}). Current reversal chronopotentiometry (CRC) involves the application of a galvanostatic cathodic pulse for a time t_f to deposit a layer of lithium at the nickel surface before reversing the pulse. On application of the anodic pulse the lithium is uniformly stripped until the surface concentration becomes zero, and the potential moves rapidly positive until reaching an other anodic process. The time taken to reach completion of lithium oxidation is termed the reverse transition time τ_r . The ratio τ_r/t_f provides a useful means of determining galvanostatic stripping efficiencies, and any departure of this ratio from unity indicates a following chemical reaction of the lithium [33, 34], assuming there is no significant diffusion away from the electrode surface.

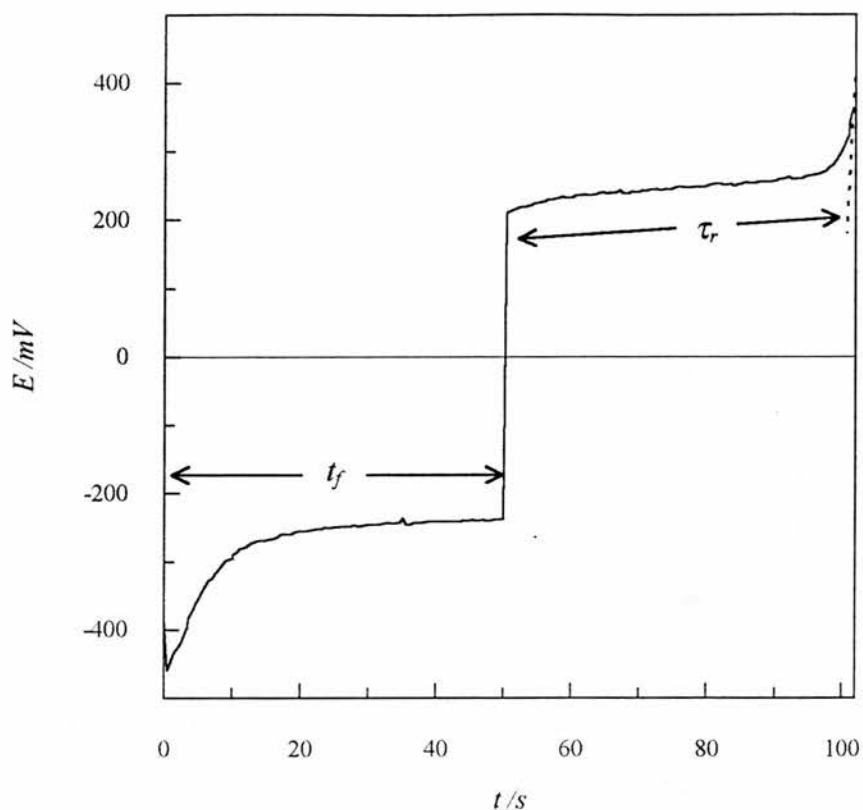


Figure 6-17 Current reversal chronopotentiogram for $\text{LiPF}_6 \cdot 2\text{DG}/\text{PC}/\text{PMMA}$ at a $25\mu\text{m}$ diameter microelectrode. $i_f = i_r = 4\text{nA}$ (0.81 mAcm^{-2}).

The effect of electrode passivation may be established by applying a series of CRC's without repolishing the electrode between cycles. Fig. 6-18 shows (a) a multi-cycling $E-t$ transient for LiPF_6/PC , and (b) a plot of the calculated current efficiencies against cycle number for the propylene carbonate solutions. In each case the efficiency increases after the first cycle, suggesting that a significant quantity of lithium is used to prepare the nickel surface via anodic film and lithium-nickel alloy formation.

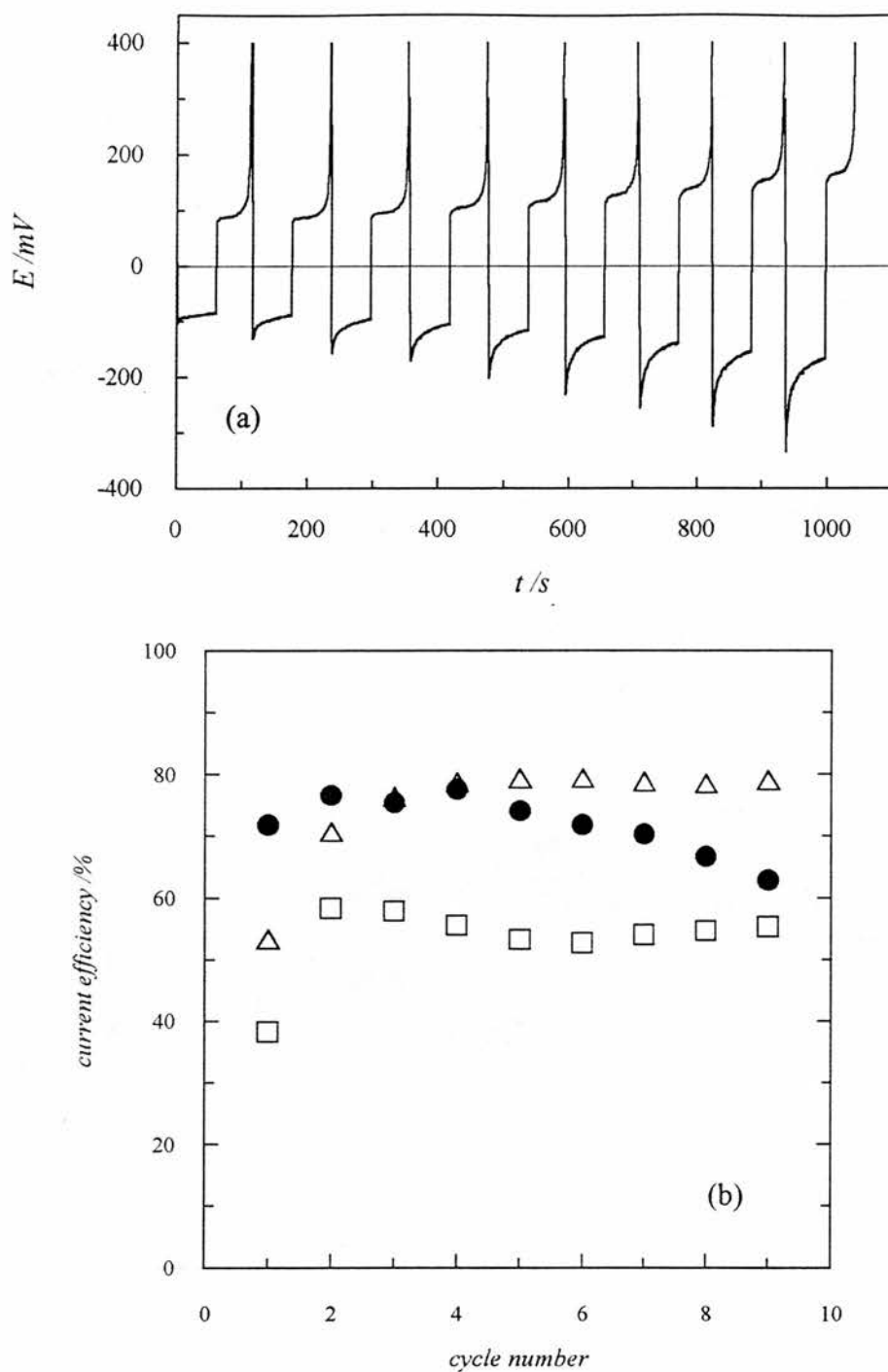


Figure 6-18

(a) multicycling chronopotentiogram for $LiPF_6/PC$ at a Ni microelectrode. (b) Current efficiencies vs. cycle number for PC containing (●) $LiPF_6$, (□) $LiPF_6.2DG$ and (△) $LiPF_6.PMDETA$.

$t_f = 60$ secs., $i_f = i_r = 4nA$ (0.81 mAcm^{-2}).

Successive cycles for LiPF_6 show that after reaching ca. 76% stripping efficiency, the quantity stripped begins to decrease steadily after the 4th cycle to 63% in the 9th, indicating passivation or loss of lithium. The LiPF_6 .PMDETA efficiency increases rapidly to over 78% in the 4th cycle, remaining approximately constant thereafter. After increasing to 58% after the 1st cycle, the efficiency of stripping from LiPF_6 .2DG decreased to a steady value of ca. 55% after cycle 5. When gelled, the performances of LiPF_6 and LiPF_6 .2DG improved significantly to above 90% stripping efficiency, while the LiPF_6 .PMDETA complex remained below 70%.

The corrosion current I_{corr} was determined as before (Chapter 5) using

$$I_{corr} = I_{appl} \cdot \left\{ \frac{t_f - \tau_r}{t_f + \tau_r} \right\} = I_{appl} \cdot \left\{ \frac{\left(1 - \frac{\tau_r}{t_f} \right)}{\left(1 + \frac{\tau_r}{t_f} \right)} \right\} \quad 6-7$$

where I_{appl} is the applied cathodic / anodic current density, when the ratio τ_r/t_f remains constant at different t_f , leading to the rate of lithium corrosion, given by

$$k_l = \frac{I_{corr}}{F} \quad \text{mol cm}^{-2} \text{ s}^{-1} \quad 6-8$$

Table 6-4 shows the calculated values of the rate of lithium loss k_l . In general, the rate of lithium loss was significantly lower with the gels than with the liquid PC.

Table 6-4 Rate of lithium corrosion, k_l , obtained from CRC.

ELECTROLYTE		Rate of lithium loss,	I_{appl}
Solvent	Salt	$k_l / \text{mol s}^{-1} \text{cm}^{-2}$	mAcm^{-2}
	LiPF_6	1.06×10^{-9}	0.81
PC	$\text{LiPF}_6 \cdot 2\text{DG}$	2.21×10^{-9}	0.81
	$\text{LiPF}_6 \cdot \text{PMDETA}$	9.93×10^{-10}	0.81

	LiPF_6	3.50×10^{-10}	0.81
PC/PMMA	$\text{LiPF}_6 \cdot 2\text{DG}$	4.35×10^{-10}	0.81
	$\text{LiPF}_6 \cdot \text{PMDETA}$	1.73×10^{-9}	0.81

It has been generally accepted that lithium is unstable in the presence of propylene carbonate solutions, forming insoluble films at the surface of the lithium, the composition of which can be electrolyte dependent [35, 36]. This passivation behaviour of the freshly deposited lithium was investigated by the measurement of the coulombic stripping efficiencies following periods on open-circuit. A double potential-step was applied in each case to deposit a lithium layer (charge passed was ca. 0.5 C/cm^2). A controlled delay between the cathodic and anodic pulses allowed the cell to rest at open-circuit before stripping the lithium off the electrode at +150 mV. Fig. 5-19 shows a plot of the coulombic stripping efficiencies vs. time on open-circuit for all prepared electrolytes. The efficiencies of LiPF_6/PC and $\text{LiPF}_6 \cdot \text{PMDETA} / \text{PC}$ remained steady at ca. 80% and 35-40%, respectively, indicating that any surface films formed were done so rapidly.

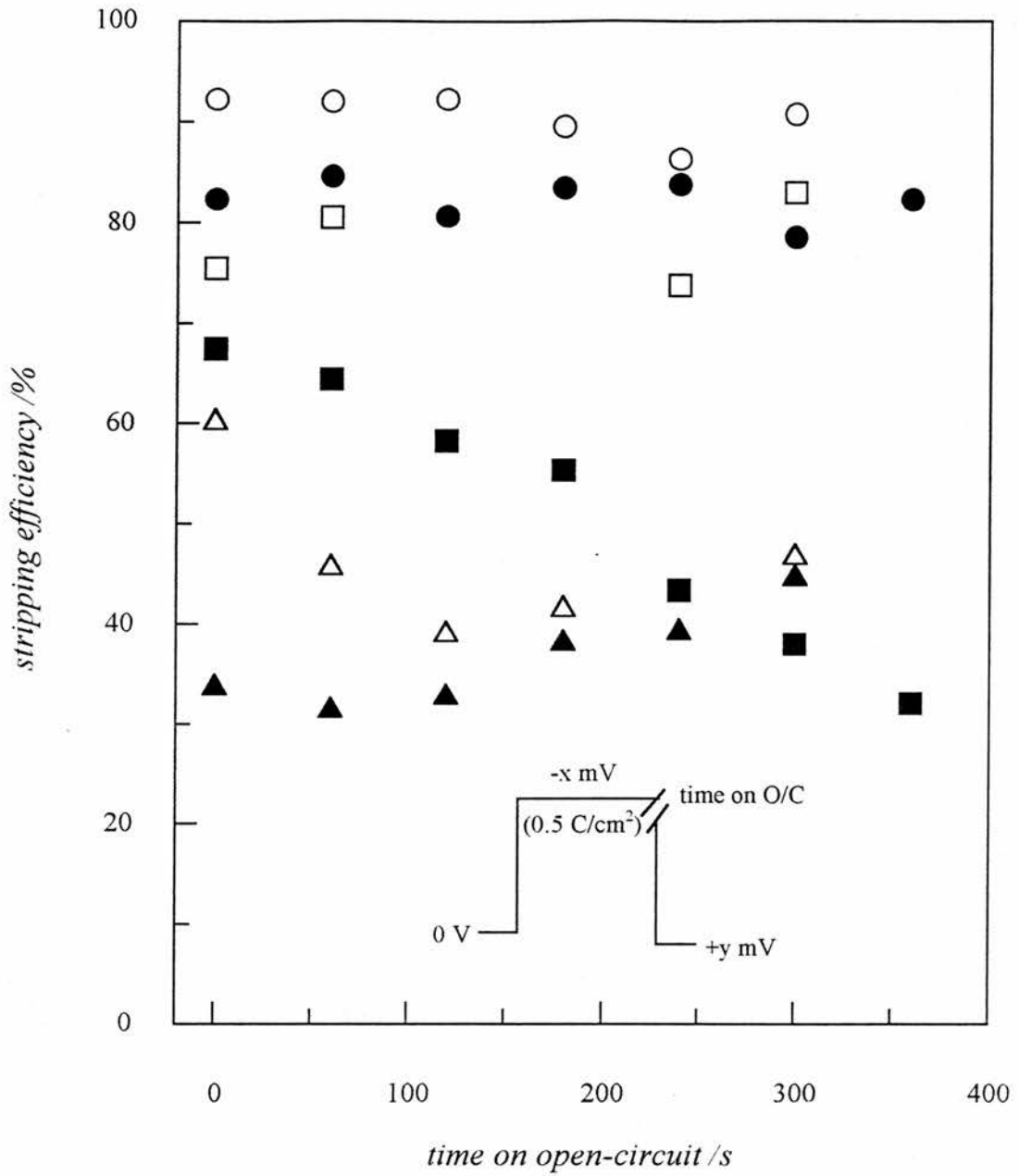


Figure 6-19 Plot of coulombic stripping efficiency vs. time on open-circuit of freshly deposited lithium from (●) LiPF₆ / PC, (■) LiPF₆.2DG / PC, (▲) LiPF₆.PMDETA / PC / PMMA, (○) LiPF₆ / PC / PMMA, (□) LiPF₆.2DG / PC / PMMA and (Δ) LiPF₆.PMDETA / PC / PMMA.

The profile of the $\text{LiPF}_6\text{-2DG/PC}$ plot, however, indicates continuing reaction of the deposited lithium using the majority of the available deposit suggesting that the film was either soluble in the solvent medium or extremely thick. The passivating nature in the $\text{LiPF}_6\text{/PC/PMMA}$ gel was found to be similar to that in PC, but here the stripping efficiency increased to ca. 92%. The diglyme complex appeared to be more stable in the gel, with stripping efficiencies around 80% and stable over a longer period. This highlights the considerable differences between the passivating films formed in both solvent media. Although the efficiency of the PMDETA complex in the PC/PMMA gel was initially ca. 60%, growth of the passivating film reduces this value to about 40%, similar to its performance in PC. This may be simply showing the difference in the rates of growth of essentially similar films.

6.4. Conclusions

Although trace impurities such as water will be a common feature in the manufacture of real battery electrolytes, it is important to identify the role played by such contaminants. Evidence given here for the cathodic stability of ultra-pure propylene carbonate at a nickel microelectrode, without added electrolyte, confirms the suspicions of Pletcher [17] that the cathodic wave or peak observed by others [25-27] is more than likely due to the presence of water and/or oxygen. Voltammetry studies at potentials anodic of bulk lithium deposition revealed several peaks thought to be due to the underpotential deposition of lithium by reduction of an existing lithium hydroxide layer.

The cyclic voltammetry and potential-step experiments show the kinetics of the Li/Li^+ couple to be fast in both propylene carbonate and propylene carbonate gelled with poly(methyl methacrylate). The ligands evidently play an important role by increasing the currents observed in both PC and the gels. The CV's clearly show that a crystallisation process occurs in each case at the nickel microelectrode surface with varying deposition rates, resulting in different stripping efficiencies, all well below 80%. Chronoamperometry measurements showed that all the systems essentially follow the same three-dimensional nucleation and growth models, although the gels not surprisingly appear to suffer from large charging currents during the early stages of the transients due to their high viscosity. Galvanostatic and double potential-step experiments indicate that the $\text{LiPF}_6 / \text{PC} / (30\text{wt}\%) \text{PMMA}$ and $\text{LiPF}_6.2\text{DG} / \text{PC} / (30\text{wt}\%) \text{PMMA}$ gels have high stripping efficiencies above 90%. The high viscosity of these gels may be sufficient to hinder dendritic growth, normally present in the liquid cell where growth of the deposit has more freedom, thus making more lithium available for electrochemical oxidation. The differences between the stripping efficiencies obtained by cyclic voltammetry, chronopotentiometry and potential-step experiments may be attributed to the morphology of the deposit caused by variations in deposition rate. In cases where stripping was inefficient, the deposit may consist largely of dendrites or needles which are unavailable for anodic dissolution.

REFERENCES

1. P.V. Wright, *Br. Polymer J.*, 7, 319 (1975).
2. M.B. Armand, J.M. Chabagno and M. Duclot, *2nd International Meeting on Solid Electrolytes*, Scotland (1978).
3. M. Armand, *Solid State Ionics*, 9/10, 745 (1983).
4. K.M. Abraham and M. Alomgir, *J. Power Sources*, 43-44, 195-208 (1993)
5. O. Bohnke, G. Frand, M. Rezrazi, C. Rousselot and C. Truche, *Solid State Ionics*, 66, 97-104 (1993).
6. O. Bohnke, G. Frand, M. Rezrazi, C. Rousselot and C. Truche, *ibid*, 66, 105-112 (1993).
7. M. Ue, M.Kaitoh, E. Yasukawa and S. Mori, *Electrochimica Acta*, 38(9), 1301 (1993).
8. *Lithium Batteries* (Edited by J.P. Gabono), Academic Press, London (1983).
9. H. Huang, L. Chen, X. Huang, R. Xue, C. Liquor, H. Xuejie and X. Rangjian, *Electrochimica Acta*, 37(9), 1671-1673 (1992).
10. R. Xue, H. Huang, L. Chen and K. Wang, *Solid State Ionics*, 59, 1-4 (1993).
11. F. Croce, S.D. Brown, S.G. Greenbaum, S. Slone and M. Soloman, *Chem. Mater.*, 5, 1268-1272 (1993).
12. R. Xue, H. Huang, M. Menetier and L. Chen, *J. Power Sources*, 43-44, 431-438 (1993).
13. G. Dautzenberg, F. Croce, S. Passerini and B. Scrosati, *Chem. Mater.*, 6, 538-542 (1994).
14. G. Nagasubramanian, A.I. Attia and G. Halpert, *J. Appl. Electrochemistry*, 24, 298-302 (1994).

15. R.D. Rauh and S.B. Brummer, *Electrochimica Acta*, 22, 75-83 (1977).
16. G. Nazri and R.H. Muller, *J. Electrochem. Soc.*, 132(9), 2054-2058 (1985).
17. D. Pletcher, J.F. Rohan and A.G. Ritchie, *Electrochimica Acta*, 39(10), 1369-1376 (1994).
18. D. Pletcher, J.F. Rohan and A.G. Ritchie, *ibid*, 39, 2015-2023 (1994).
19. Duracell Inc., Improved method for preparing non-aqueous electrolytes, *European Patent application N^o. 90302078.2* (Sept. 1990).
20. The Associated Octel Company Ltd., Lewis base complexes of alkali metal salts, *European patent application no. 88309912.7* (Oct. 1988).
21. D.S. Wright, PhD. Thesis, Cambridge, England (1989).
22. A.M. Christie, A. Lisowska-Oleksiak and C.A. Vincent, submitted to *Electrochimica Acta*, (1994).
23. C. Detellier and P. Laszlo, *Helvetica Chimica Acta*, 59(Fasc.4), 1333-1345, (1976).
24. A. Delville, C. Detellier, A. Gerstmans and P. Laszlo, *ibid*, 664 (Fasc. 2), (1981).
25. D. Fish and J. Smid, *Electrochimica Acta*, 37, 2043-2049 (1992).
26. D. Aurbach and H. Gottlieb, *ibid*, 34, 141-156 (1989).
27. S.A. Campbell, C. Bowes and R.S. McMillan, *J. Electroanal. Chem.*, 284, 195-204 (1990).
28. C. Nanyundiah, J.L. Goldman, L.A. Dominey and V.R. Koch, *J. Electrochem. Soc.*, 135, 2914 (1988).
29. D. Wagner and H. Gerischer, *Electrochimica Acta*, 34, 1351-1356 (1989).

30. G. Gunuwardena, G. Hills, I. Montenegro and B. Scharifker, *J. Electroanal. Chem.*, 159, 264 (1983).
31. M. Fleischmann and H.R. Thirsk in *Advances in Electrochemistry and Chemical Engineering*, Vol.3 (Edited by P. Delahay and C.W. Tobias), p.123, Interscience, New York (1962).
32. J.D. Genders, W.M. Hedges and D. Pletcher, *J. Chem. Soc. Faraday Trans. I*, 80, 3399-3408 (1984).
33. T. Berzins and P. Delahay, *J. Amer. Chem. Soc.*, 75, 4205 (1953).
34. R.K. Jain, H.C. Gaur and B.J. Welch, *J. Electroanal. Chem.*, 79, 211 (1977).
35. D. Aurbach, M.L. Daroux, P.W. Faguy and E. Yeager, *J. Electrochem. Soc.*, 134 (7), 1611-1620 (1987).
36. D. Aurbach, Y. Ein-Ely and A. Zaban, *ibid*, 141(1), L1-L3 (1994).

CHAPTER SEVEN

Ion Association: A Molecular Modelling Perspective

7.1. Introduction to Molecular Modelling

Although it is general, the Schrodinger equation describing a molecular system is too complex for any practical use, so approximations are made. Since the electrons are several thousand times lighter than the nuclei and therefore move much faster, Born and Oppenheimer [1] proposed the now well known approximation: *the motion of the electrons can be decoupled from that of the nuclei, giving two separate functions.* The first of these functions describes the electronic motion and depends only on the positions of the nuclei and defines an energy E , which is a function of only the coordinates of the nuclei, called the *potential energy surface*; the second function describes the motion of the nuclei on this potential energy surface. The empirical fit to the potential energy surface is the *forcefield* [2, 3].

The forcefield defines the coordinates used, the mathematical form of the equations involving the coordinates, and the parameters adjusted in the empirical fit of the potential energy surface. The forcefields commonly used for describing molecules employ a combination of internal coordinates (bond distances, bond angles and torsions) to describe the bond part of the potential energy surface, and interatomic distances to describe the van der Waals interactions between atoms. The aim of a forcefield is to describe entire classes of molecules with reasonable accuracy.

Together with the actual coordinates of a chosen molecule, the forcefield data allows the creation of an energy expression, or *target function*, for that molecule. This energy expression is the equation which describes the potential energy surface of a particular molecule as a function of its atomic coordinates.

Molecular mechanics is a technique which ignores the time evolution of a system and instead explores the potential energy surface for geometries and their associated energies that are stable points on the surface, or other static properties; this means finding a point in the configuration space where the net force on each atom vanishes. Therefore, by simply minimising the energy, stable conformations can be identified. Minimised structures, in a sense, represent the underlying configurations about which fluctuations occur during dynamics and, as such, provide a meaningful basis for structural analysis [3, 4]

7.2. General Minimisation Strategy

Minimisation of a molecule is done in two steps [5]: first, an equation describing the energy of the system as a function of its coordinates must be defined and evaluated for a given conformation. Target functions may be constructed that include external restraining terms to bias the minimisation, in addition to the energy terms; next, the conformation is adjusted to lower the value of the target function. A minimum may be found after one adjustment or may require many thousands of iterations, depending on the nature of the algorithm, the form of the target function and the size of the molecule. The efficiency of the minimisation therefore depends on both the time

needed to evaluate the target function and the number of structural adjustments needed to converge on the minimum.

The simplest case of a pure quadratic function in two dimensions is presented here. Most minimisation algorithms assume that the energy surface is approximately harmonic. Even for non-harmonic surfaces, the shape of the surface becomes harmonic in the limit of convergence to the minimum. The target function used here is an elliptical surface in two dimensions described by Eqn. 7-1:

$$E(x, y) = x^2 + 5y^2 \quad 7-1$$

Every minimisation begins with some equation analogous to Eqn. 7-1. In addition to an equation defining the energy surface, a starting set of coordinates for (x, y) must be provided.

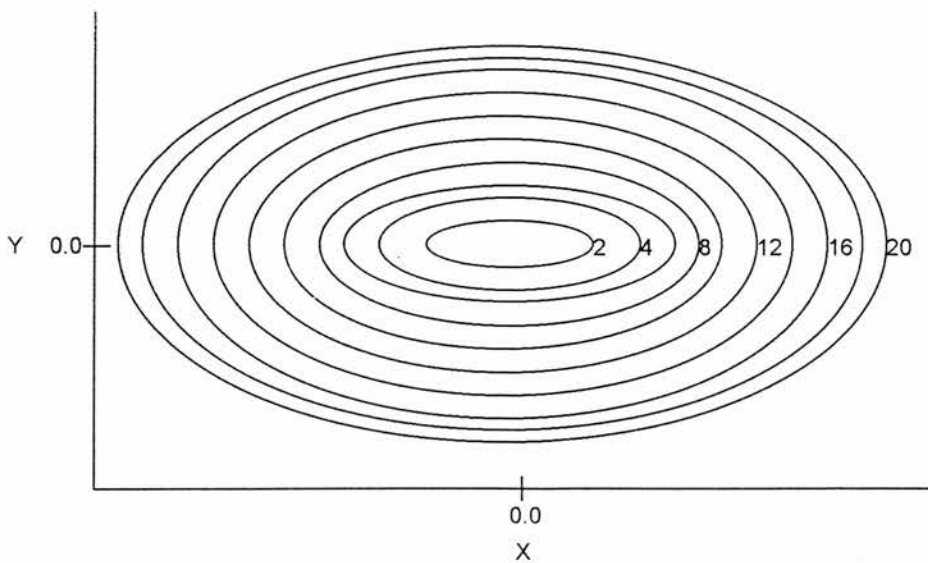


Figure 7-1 Energy contour surface of a simple 2-D function.

Figure 7-1 shows a contour plot of the energy E in the (x, y) plane. Each ellipse is spaced two energy units apart and represents a locus of points having the same energy. The minimum of this simple function is seen to be the origin at $x = 0, y = 0$. Given a target function that defines the energy surface and an initial starting point, a minimiser must determine both the direction towards a minimum and the distance to the minimum in that direction. An initial direction can be taken simply as the slope or derivatives of the function at the current point. There is a direct proportionality of the derivatives with the coordinates, therefore the further the point is from the minimum, the larger the derivatives. A minimisation has converged when the derivatives are equal to zero or nearly equal to zero.

One of the major components of a minimiser is called a *line search*, which changes the coordinates to a new lower energy structure. A line search can be described simply by a one-dimensional minimisation along a given direction. The line to be searched is taken along the direction vector determined at each iteration of the minimisation. The new derivatives are always perpendicular to the previous direction, and therefore produce an efficient path to the minimum for approximately quadratic surfaces.

7.3. Minimisation Algorithms Used [6, 7]

7.3.1. Steepest Descents

In the steepest descents method, the line search direction is simply taken as the current derivative or gradient. After each line search, the old direction is replaced with the gradient at the new point, and the line search is repeated. Figure 7-2 shows the minimisation path followed by a steepest-descent approach on the simple quadratic function.

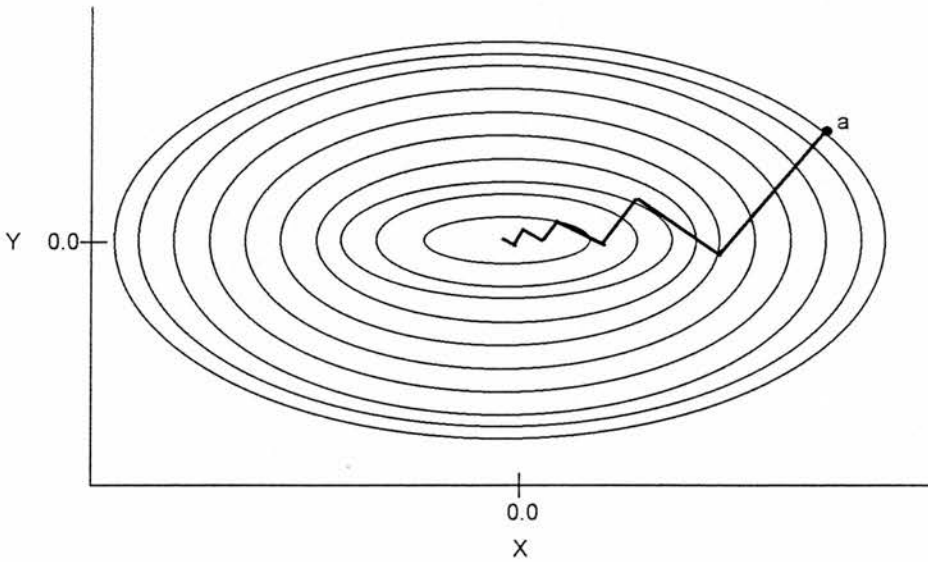


Figure 7-2 Minimisation path followed by a steepest-descents approach.

Each line search produces a new direction that is perpendicular to the previous gradient. However, the directions oscillate on the way to the minimum resulting in an inefficient trajectory. This exclusive reliance on gradients is both the weakness and

strength of steepest descents. Convergence is slow near the minimum because the gradient approaches zero, but the method is very robust. Therefore, the method of steepest-descents is often used initially when configurations are far from the minimum. In fact, more advanced algorithms are often designed to begin with a steepest descents direction as the first step.

7.3.2. *Conjugate Gradients*

The minimisation path followed in steepest descents is inefficient mainly because each segment of the path tends to retrace progress made in an earlier iteration. For example, each line search deviates from the ideal direction to the minimum, and the path continually overcorrects for poor choices of directions in earlier steps.

Each successive step in the conjugate gradients method continually refines the direction toward the minimum. The new direction vector h_{i+1} leading from point $(i+1)$ is computed by adding the gradient g_{i+1} at point $(i+1)$ to the previous direction h_i , scaled by a constant γ_i :

$$h_{i+1} = g_{i+1} + \gamma_i h_i \quad 7-2$$

where γ_i is a scalar defined as :

$$\gamma_i = \frac{g_{i+1} \cdot g_{i+1}}{g_i \cdot g_i} \quad 7-3$$

This direction is then used in place of the gradient in Eqn. 7-2 and a new line search is conducted. The next gradient, g_{i+1} , is orthogonal to all previous gradients, $g_0, g_1, g_2, \dots, g_i$, and the next direction, h_{i+1} , is conjugate to all previous directions, $h_0, h_1, h_2, \dots, h_i$. Thus, the algorithm actually produces a set of mutually *orthogonal gradients* and a set of mutually *conjugate directions*. The minimisation path followed by conjugate gradients on the simple quadratic surface described earlier is shown in Fig. 7-3.

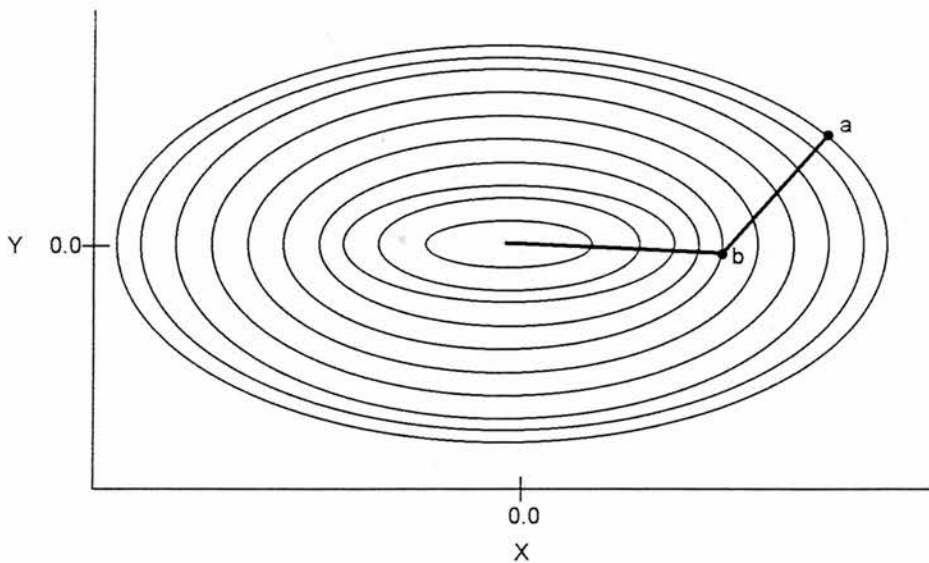


Figure 7-3 Minimisation following a conjugate-gradients path.

7.4. Results and Discussion

Many aspects of lithium electrolyte solutions put forward for rechargeable battery applications are not fully understood. The nature of the free charge carriers in solution, which is an important factor when considering conductivity, remains unclear although advances in available experimental techniques [9-11] provides a large piece of the overall picture. The coordination of lithium cations with anions such as trifluoromethanesulphonate (triflate) in non-aqueous media has been the focus of attention in recent years [12-13]. Despite this, knowledge of ion-ion and ion-solvent interactions, especially in polyether solvents, is slight.

Work is ongoing into the preparation of lithium salts where the anion is designed to reduce the electrostatic association with the Li^+ cation [12]. By adding electron withdrawing groups to a central atom, the single negative charge will be delocalised about a large anion, thus decreasing the charge density. Stable organic anion-based lithium salts have been developed utilising the electron withdrawing SO_2CF_3 group. Conductive properties of lithium methide, $\text{LiC}(\text{SO}_2\text{CF}_3)_3$, and lithium imide, $\text{LiN}(\text{SO}_2\text{CF}_3)_2$ are reported in the literature [12]. The use of modelling techniques allows the user to gain a theoretical view of electrolyte structures.

7.4.1. *Properties of the Anion*

Modified Neglect of Differential Overlap (MNDO) [14] calculations are semiempirical methods based on molecular orbital theory and are particularly useful in the determination of atomic charges and heats of formation. The properties of the

triflate, imide and methide anions were calculated using this method by minimising with MOPAC v6.

The geometrical parameters and interatomic distances for the local minimum structure found for the triflate anion are listed in tables 7-1 and 7-2.

Table 7-1 Geometry parameters (bond lengths and bond angles) for the triflate anion.

Atom (I)	Bond length /Å	Bond angle /°	Twist angle /°			
	N _A :I	N _B :N _A :I	N _C :N _B :N _A :I	N _A	N _B	N _C
S(1)						
O(2)	1.521			1		
O(3)	1.520	114.1		1	2	
O(4)	1.520	114.3	134.0	1	3	2
C(5)	2.004	104.2	113.0	1	3	4
F(6)	1.353	112.4	-62.25	5	1	3
F(7)	1.353	112.3	177.7	5	1	3
F(8)	1.353	112.1	57.75	5	1	3

Ions associate with each other by the attractive interactions of their respective coulombic charges. By treating the atoms as point charges within the anion, an approximate guide to the attractive and repulsive areas to a cation can be seen. Table 7-3(a) lists the calculated charges for each atom in the triflate, imide and methide

anions, respectively. In addition, Table 7-3(b) lists charges calculated for the triflate by the ab-initio technique with a 6-31G* basis set for comparison. The dipole contributions from each anion are shown in Table 7-4

Table 7-2 Interatomic distances for the triflate anion.

	S(1)	O(2)	O(3)	O(4)	O(5)	O(6)	O(6)	O(6)
S(1)	0.000							
O(2)	1.521	0.000						
O(3)	1.520	2.552	0.000					
O(4)	1.520	2.553	2.555	0.000				
C(5)	2.004	2.798	2.796	2.796	0.000			
F(6)	2.813	3.974	3.222	3.183	1.353	0.000		
F(7)	2.812	3.183	3.972	3.220	1.353	2.168	0.000	
F(8)	2.809	3.218	3.178	3.970	1.353	2.169	2.169	0.000

Table 7-3(a) Calculated charges for the atoms of the triflate, imide and methide anions using the MNDO method.

Triflate atom (I)	Charge	Imide atom (I)	Charge	Methide atom (I)	Charge
S(1)	1.6455	S(1)	1.5851	S(1)	1.5539
O(2)	-0.7185	O(2)	-0.6283	O(2)	-0.6107
O(3)	-0.7186	O(3)	-0.6636	O(3)	-0.6233
O(4)	-0.7186	C(4)	0.2977	C(4)	0.3783
C(5)	0.2433	F(5)	-0.2217	F(5)	-0.2017
F(6)	-0.2442	F(6)	-0.2223	F(6)	-0.1953
F(7)	-0.2444	F(7)	-0.2154	F(7)	-0.1856
F(8)	-0.2444	S(8)	1.5621	S(8)	1.5633
		O(9)	-0.6381	O(9)	-0.6447
		O(10)	-0.6599	O(10)	-0.6104
		C(11)	0.3456	C(11)	0.3642
		F(12)	-0.2132	F(12)	-0.1899
		F(13)	-0.2087	F(13)	-0.1969
		F(14)	-0.2213	F(14)	-0.2027
		N(15)	-0.8981	C(15)	-1.3007
				S(16)	1.5610
				O(17)	-0.6043
				O(18)	-0.6178
				C(19)	0.3606
				F(20)	-0.1959
				F(21)	-0.2012
				F(22)	-0.2004

Table 7-3(b) Charges calculated by ab-initio(6-31G*) for the triflate anion.

S(1)	O(2)	O(3)	O(4)	C(5)	F(6)	F(7)	F(8)
1.6455	-0.7185	-0.7186	-0.7186	0.2433	-0.2442	-0.2444	-0.2444

Table 7-4 Dipole contributions to the triflate, imide and methide anions.

Anion	Dipole /D			Total
	X	Y	Z	
Triflate	-0.757	-0.157	-2.72	3.05
Imide	0.0680	-1.22	0.74	1.43
Methide	-0.748	-1.17	-1.44	2.00

A pictorial representation of the minimised geometries and calculated charges listed in the previous tables is shown in Fig. 7-4. The atoms are coloured according to the following specifications: C (green), S (yellow), O (red), F (magenta) and N (blue). Surfaces were created to show the van-der-Waals radii of each atom and are coloured with respect to the charge spectrum shown in the figure. That is, the surface of an atom holding a negative charge is red and of one with a positive charge is blue. Evidently the negative charge does not entirely belong to the oxygens, but a partial negative charge also resides on the fluorines of each anion. On comparing the negative charges of O and F between each anion we can see that their values decreased in the order triflate > imide > methide indicating that the single charge did indeed delocalise as the number of electron withdrawing groups was increased. This effect may then contribute towards the instability of ion-pairs, thus increasing the number of free charge carriers and ultimately leading to an increase in electrolyte conductivity.

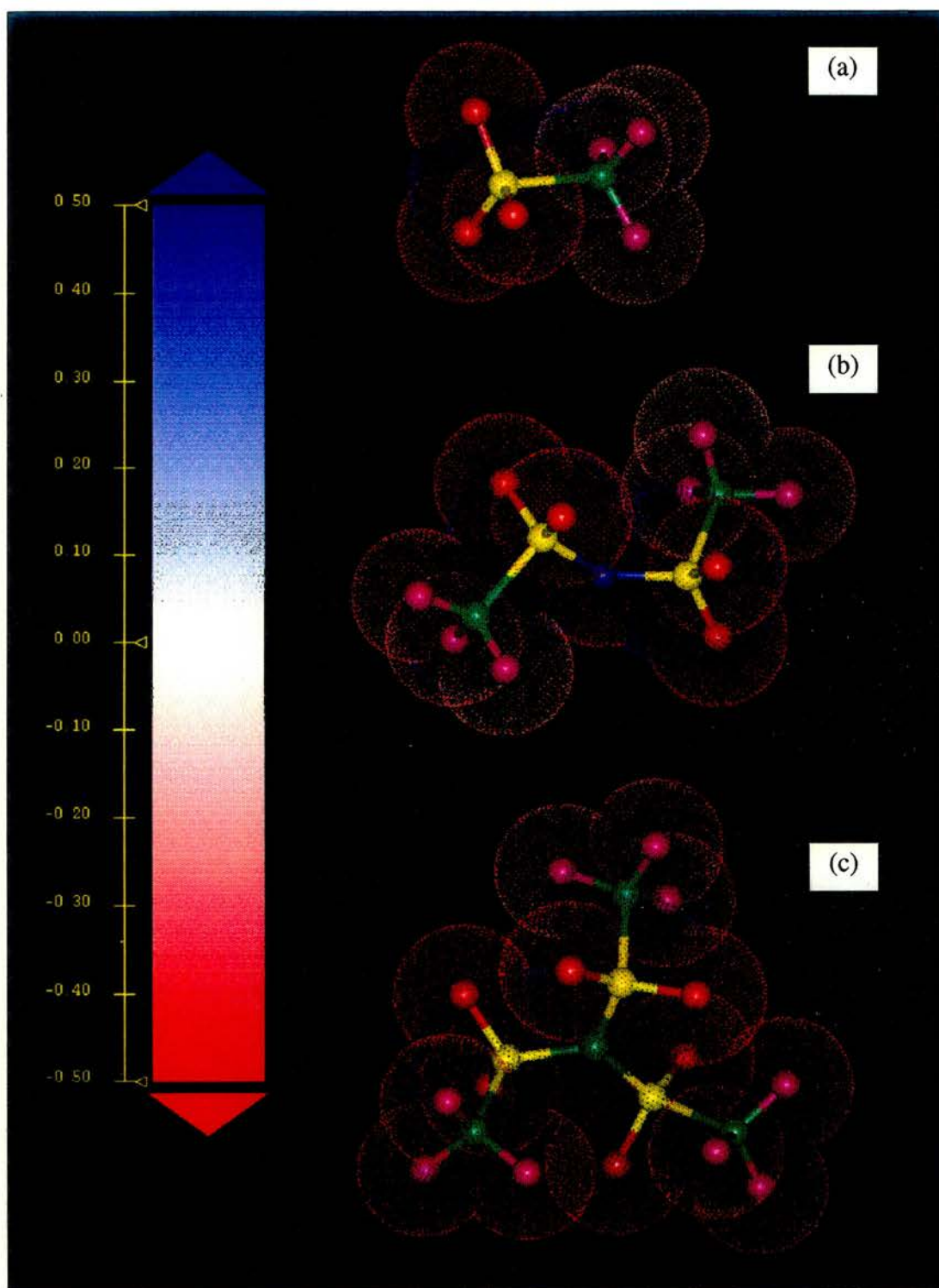


Figure 7-4 Geometries of (a) triflate, (b) imide and (c) methide anions. Surface colours at the van-der-Waals radii show the calculated point charges as indicated on the charge spectrum.

7.4.2. Association to Pairs

The charges around each anion indicate that several configurations are possible, especially as the number of available sites increase in the order triflate < imide < methide. In this chapter, only the simplest of these anions will be considered further, but it will become clear that the results presented here can be extended to the larger imide and methide anions.

Molecular mechanics was used with the CVFF [15] forcefield with a modified non-bond interaction potential of a Li^+ cation from the AMBER [16, 17] forcefield. The steepest descents algorithm was applied for 100 iterations followed by a conjugate gradients algorithm to converge to a deviation of 0.001. Charges were accepted from the MOPAC v6 (MNDO) calculation. Starting models were created by manually changing the location of the Li^+ cation in the vicinity of the triflate anion. Two configurations were found when the starting models were minimised *in vacuo*. Figure 7-5 shows the ion-pairs where the Li^+ is situated at (a) the $-\text{CF}_3$ end and (b) the $-\text{SO}_3$ end. Moving the lithium ion to the side of the anion and minimising results in the preferential coordination of the Li^+ by only two oxygens, as found by Lindgren *at al* [13] in an ab-initio study. The results show that coordination by F is possible in circumstances where only the fluorines are close to the cation. However, in real systems the likelihood of solution conditions allowing this scenario are negligible since many more anions will also be in the vicinity of the cation and the oxygens with their higher charges will coordinate more readily.

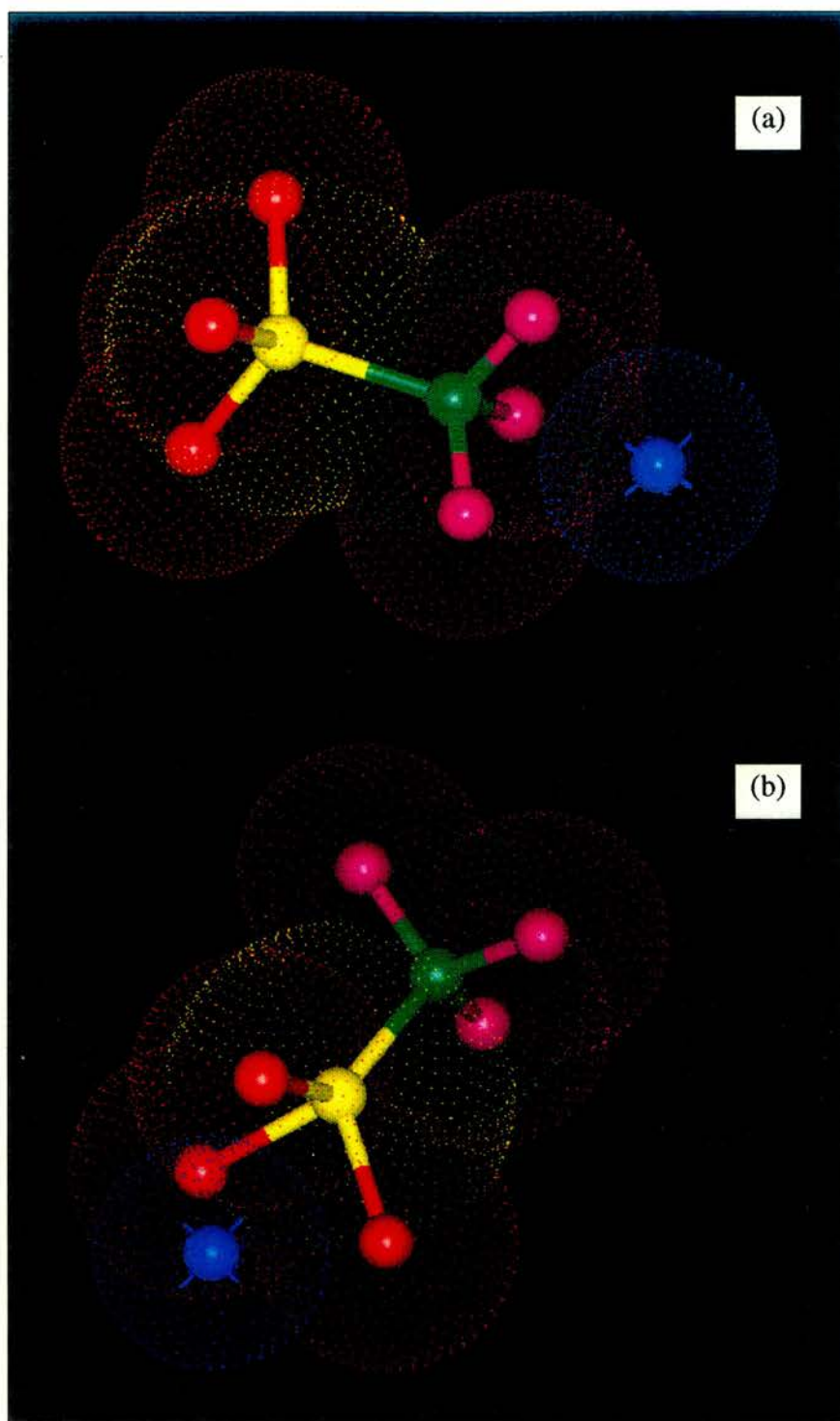


Figure 7-5 Two possible geometries of the $\text{Li}^+\text{CF}_3\text{SO}_3^-$ ion pair, where the lithium is coordinated by (a) the fluorines and (b) the oxygens. The surfaces show the van-der-Waals radii.

The ion-pair was then solvated to view the effect in a theoretical solvent environment. A $\text{Li}^+\text{CF}_3\text{SO}_3^-$ ion-pair was surrounded by a 20\AA sphere of tetraglyme molecules and minimised with no dielectric constant set. The minimum structure calculated is shown in Fig. 7-6. The tetraglyme solvent molecules are coloured dark blue for clarity. The ions have been space-filled to the van-der-Waals radii with atom colourings: C (green), O (red), S (yellow), F (magenta) and Li (blue). The ion-pair remained intact and stable, and the Li cation moved to a position between two oxygens. A similar approach was taken with propylene carbonate. The ion-pair was soaked by a 15\AA sphere of propylene carbonate molecules and again minimised as shown in Fig. 7-7. In this solvent the Li^+ cation became separated from the triflate anion. The MNDO calculations performed on each of these solvents gave dipole contributions of 4.859D and 1.903D for propylene carbonate and tetraglyme, respectively, which contribute to the overall solvent permittivity. It has been shown that for solvents with high permittivities an ion-pair is thermally unstable (Chapter 2) and in solvents of low permittivity at low salt concentrations, molar conductivities decrease due to the association of free ions to pairs. The results shown here correlate well with this idea.

7.4.3. *Higher Aggregates*

In the triple-ion conductance theory, Fuoss and Kraus put forward equilibria [18] describing the formation of ion aggregates higher than pairwise. There were only two postulated triple-ion configurations, both of which were treated as spherical which limits the structural possibilities and greatly simplifies the theoretical problem. The two configurations are shown schematically in Fig. 7-8.

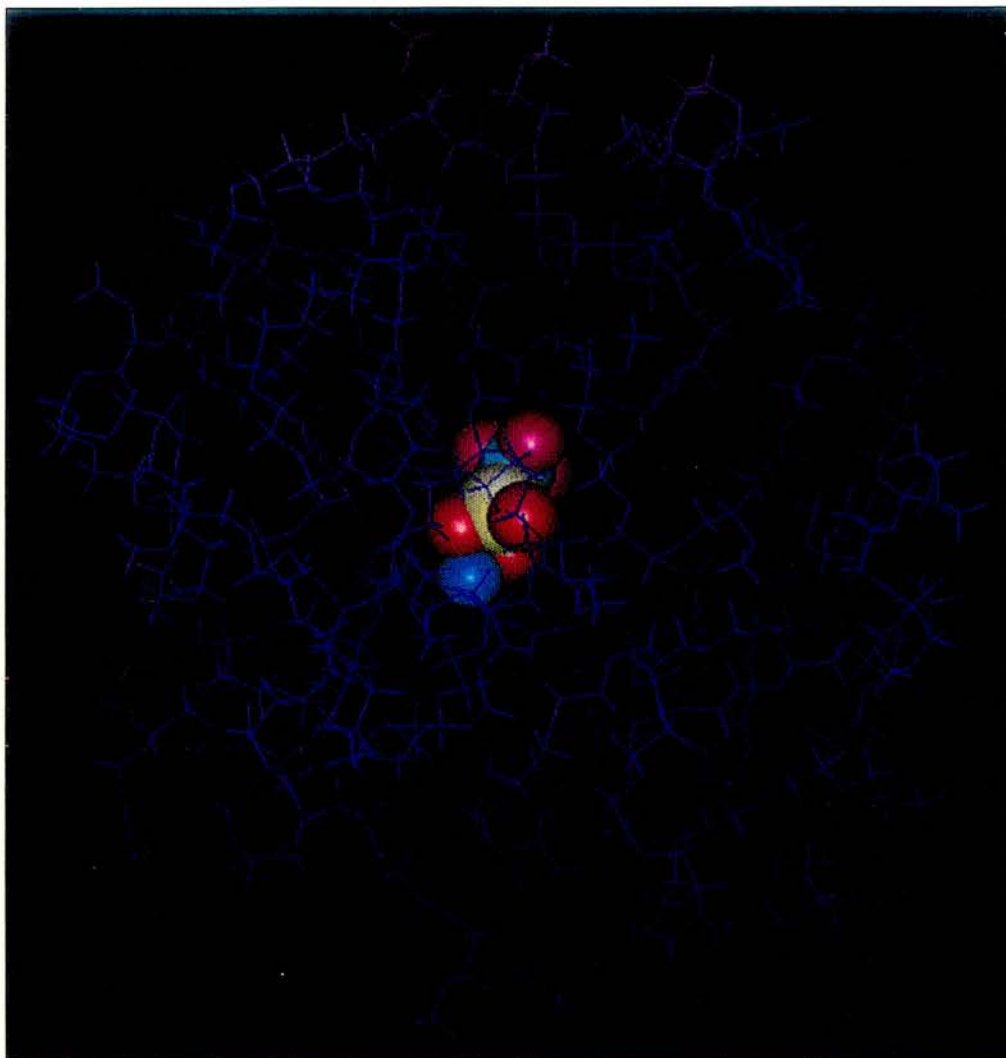


Figure 7-6 Li^+ and CF_3SO_3^- ions surrounded by a 20\AA sphere of tetraglyme solvent molecules. A contact pair has been formed.

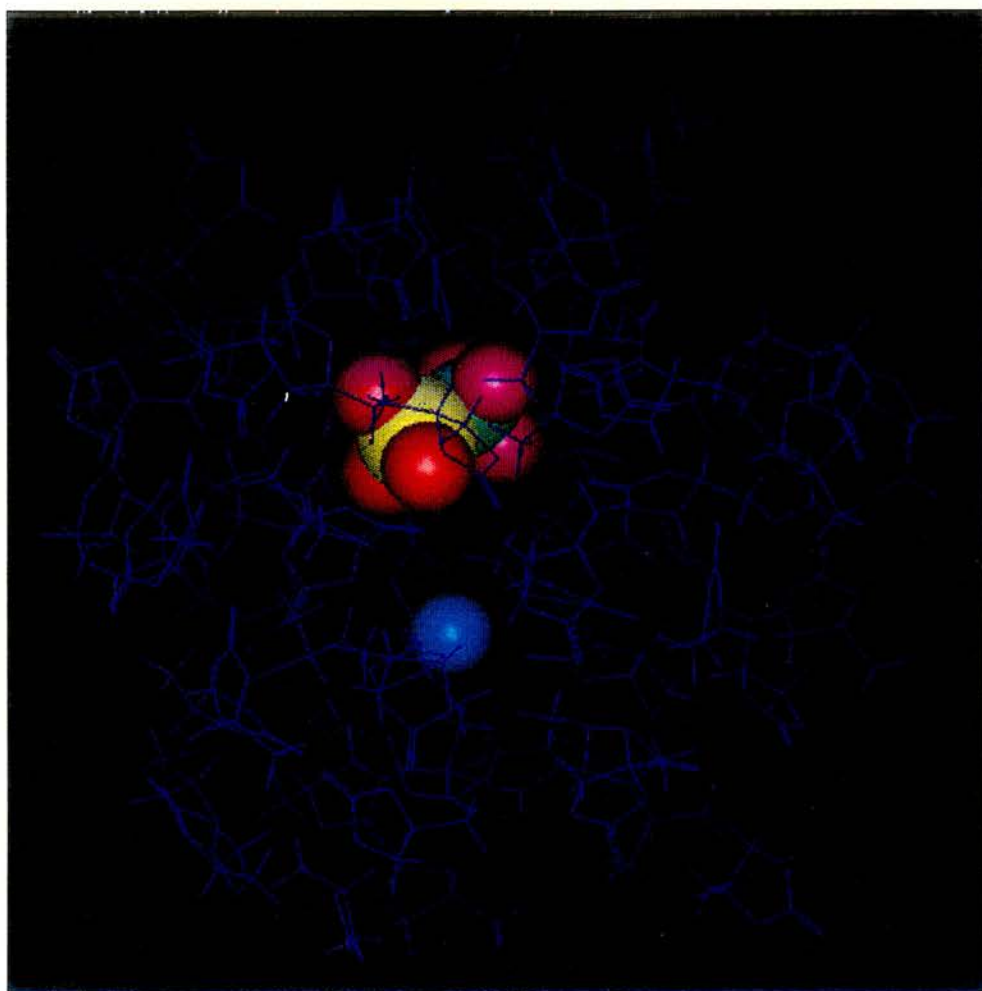


Figure 7-7 Li^+ and CF_3SO_3^- ions surrounded by a 15Å sphere of propylene carbonate solvent molecules. A contact pair has not been formed.

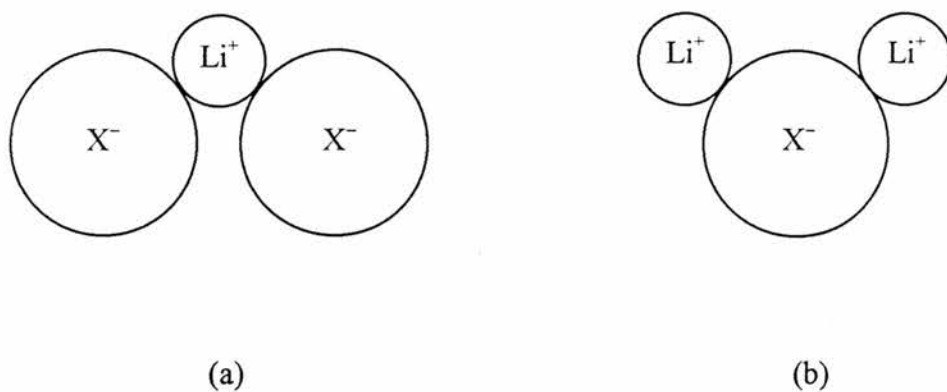


Figure 7-8 Schematic for (a) $M^+X_2^-$ and (b) $M_2^+X^-$ ion-triples as described in the Fuoss-Kraus triple-ion theory.

However, with an anion such as the triflate (and more so with the imide and methide) this is likely to be an oversimplification. The varying charge over the triflate anion surface provides several sites for the cation to sit in, and thus there will exist more than two stable triple-ion configurations. In fact, the ion-pair dipoles calculated from MOPAC were 15.839D and 0.568D for the pairs shown in Fig. 7-5(a) and (b), respectively, implying that a dipole association with a free ion to a triple may be more likely when the lithium is coordinated by the fluorines. Four minima are shown in Figs. 7-9(a)-(d). All of the structures are combinations of one of the ion-pairs shown earlier in Fig. 7-5 and either a lithium cation or triflate anion. The total energies, calculated by MOPAC v6, for each configuration are listed in Table 7-5. There was a large energy difference found between the two general forms, $M_2^+X^-$ and $M^+X_2^-$, with the latter more energetically favourable. Contrary to this, the triple-ion theory makes the assumption that both configurations are equally favourable. The structures in Figs. 7-9(a) and (b) have energies very similar to those of the ion-pairs (-2760.04 eV and -2760.76 eV for pair configurations 7-5(a) and (b), respectively).

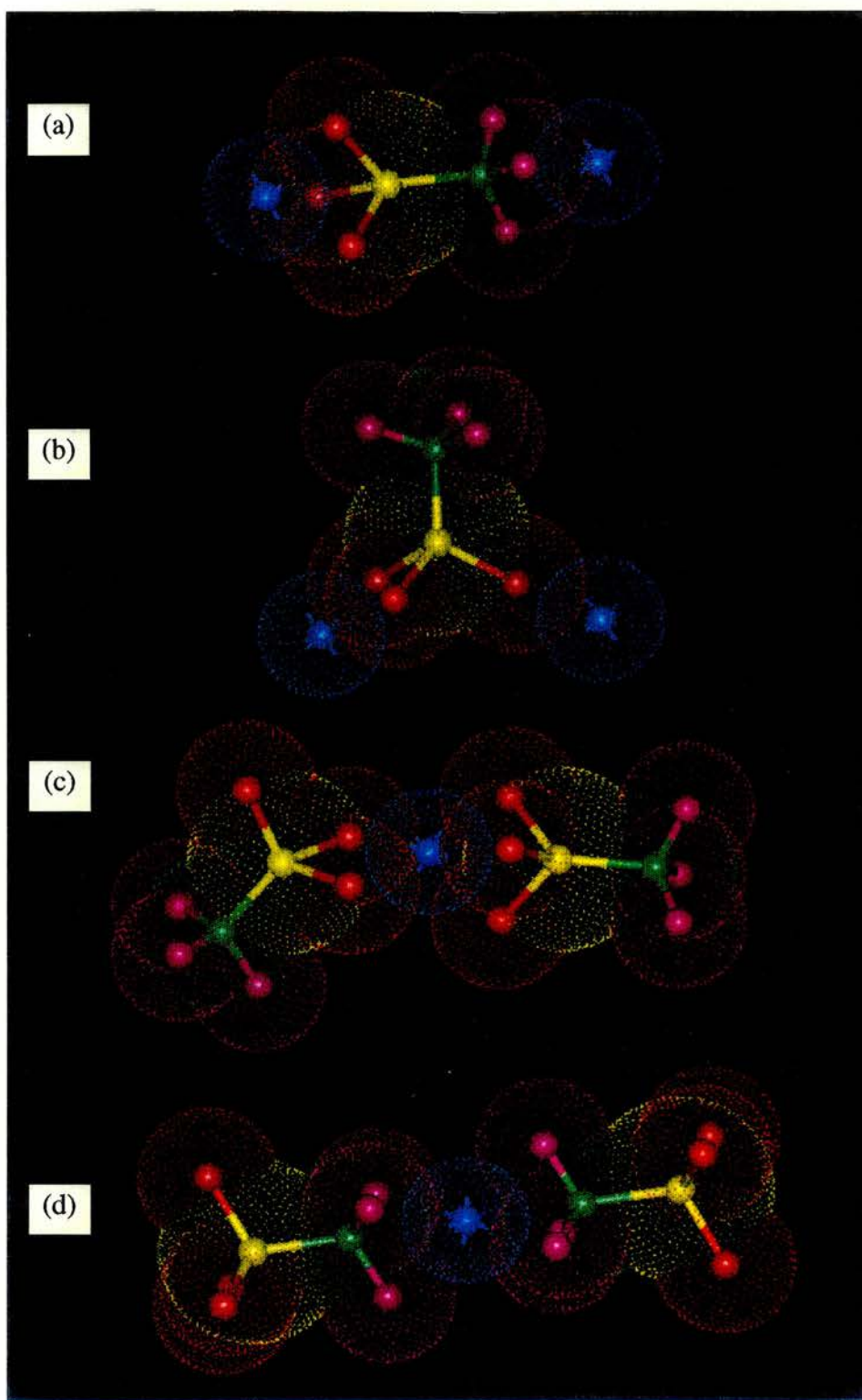


Figure 7-9 Four possible triple-ion configurations of Li^+ and CF_3SO_3^- .

Table 7-5 Total energies and dipoles of the triple-ion configurations.

Triple-ion figure N ^o .	E_{TOT} /eV	Dipole /D
7-9(a)	-2761.32	10.46
7-9(b)	-2761.84	9.680
7-9(c)	-5516.88	5.238
7-9(d)	-5518.99	0.001

In solvents with sufficiently low relative permittivity there is no reason why even higher order clusters, such as quadruples, cannot be formed by similar coulombic and dipolar attractions. It seems likely that two species coupling will have a relatively high probability. Also, the probability of n species docking with each other within the lifetime of a growing cluster will decrease rapidly as n increases. In this work the cluster size was limited to quadruples constructed from combinations of pairs, triples and free ions then minimised using molecular mechanics. Some quadruple minima are shown in Fig. 7-10 and the total energy for each is given in Table 7-6.

Table 7-6 Total energies and dipoles of the quadruple-ion configurations.

Quadruple-ion figure N ^o .	E_{TOT} /eV	Dipole /D
7-10(a)	-5520.75	2.136
7-10(b)	-5519.73	0.000
7-10(c)	-5521.54	20.45
7-10(d)	-5522.01	2.804

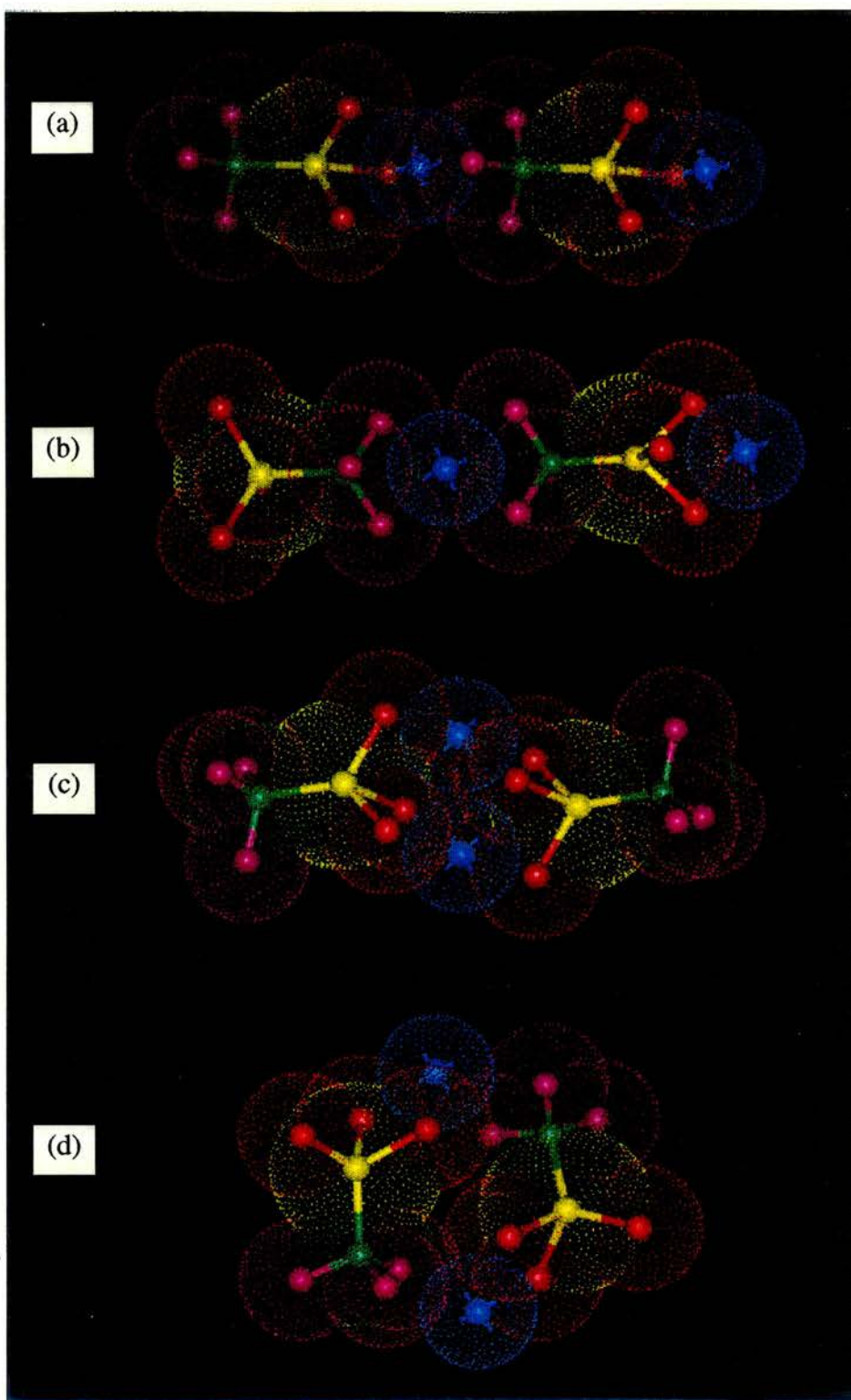


Figure 7-10 Four possible ion quadruple configurations of Li^+ and CF_3SO_3^- .

The listed energies indicate that the quadruple clusters are each as energetically favourable as the most stable triple-ion.

7.5. Conclusions

The results show that semi-empirical methods and molecular mechanics are a powerful tools, providing an insight into electrolyte systems of novel salts. The charge distribution of an anion appears to become more delocalised as the number of electron withdrawing groups around a central atomic site is increased. The likelihood of association to stable pairs of such anions with a univalent cation is therefore lower than association of a smaller anion with a high charge density.

In solvents of low permittivity, clusters greater than pairwise are formed by the interaction of dipoles. When the permittivity is sufficiently low, higher order clusters become more energetically favourable. Aggregates of at least quadruple size are likely to exist and play an important role in electrolyte solution conductivities in low permittivity media. Dipoles also exist with the quadruple species allowing even larger aggregates to form in more concentrated solutions. However, some of the dipoles calculated here are larger than those of the propylene carbonate molecule, suggesting that the solution permittivity would increase as the fraction of such dipolar clusters increased. Experimental evidence for this has been seen previously [10, 11].

REFERENCES

1. M. Born and J.R. Oppenheimer, *Ann. Physik*, 84, 457 (1927).
2. A.T. Hagler in *Conformation in Biology and Drug Design, The Peptides*, (Edited by J. Meienhofer), Academic Press, New York, 7, 213-299 (1985).
3. O. Ermer, *Structure and Bonding*, 27, 161-211 (1976).
4. A.T. Hagler, D.J. Osguthorpe, P. Dauber-Osguthorpe and J.C. Hemple, *Science*, 227, 1309-1315 (1985).
5. R.S. Struthers, J. Rivier and A.T. Hagler in *Conformationally Directed Drug Design: Peptides and Nucleic Acids as Templates or Targets*, (Edited by J.A. Vida and M. Gordon), Am.Chem.Soc., Washington, 239-261 (1984).
6. R. Fletcher, "Subroutines for Minimisation by Quasi-Newton Methods.", AEA, Harwell, Berkshire (1972).
7. R. Fletcher in *Practical Methods of Optimisation*, Vol.1, John Wiley and Sons, New York (1980).
8. W.H. Press, B.P. Flannery, S.A. Teukolsky and W.T. Vetterling in *Numerical Recipes, The Art of Scientific Computing*, Cambridge University Press, Cambridge (1986).
9. S. Schantz, J. Sandahl, L. Borjesson, L.M. Torell and J.R. Stevens, *Solid State Ionics*, 28-30, 1047-1053 (1988).
10. I. Albinsson, B.E. Mellander and J.R. Stevens, *J.Chem.Phys.*, 96(1), 681-690 (1992).
11. I. Albinsson, B.E. Mellander and J.R. Stevens, *Solid State Ionics*, 60, 63-66 (1993).
12. L.A. Dominey, *Electrochimica Acta*, 37, 1551-1554 (1992).

13. S.P. Gejji, K. Hermansson, J. Tegenfeldt and J. Lindgren, *J. Phys. Chem.*, 97, 11402-11407 (1993).
14. *A Handbook of Computational Chemistry* (Edited by T. Clark), Wiley-Interscience, London (1985).
15. Biosym Technologies, San Diego, CA.
16. S.J. Weiner, P.A. Kollman, D.A. Case, U.C. Singh, C. Ghio, G. Alagona, S. Profeta and P. Weiner, *J.Am.Chem.Soc.*, 106, 756-784 (1984).
17. S.J. Weiner, P.A. Kollman, D.T. Nguyen and D.A. Case, *J.Comp.Chem*, 7, 230-252 (1986).
18. R.M. Fuoss and C.A. Kraus, *J. Amer. Chem. Soc.*, 55, 2387-2399 (1933).

CHAPTER EIGHT

Concluding Remarks

8.1. Initial Studies

The addition of suitable ligands during the preparation of lithium salts was proposed as a convenient method for preparing highly pure electrolytes for use in lithium batteries. The added ligand must afford high conductivity of the cation through the solvent medium and allow high efficiencies of lithium plating and stripping when incorporated into a rechargeable cell with a Li negative electrode. An appropriate additive may be thought of as a “*brightener*” which facilitates the formation of a smooth, dendrite free deposit.

A range of Li-salt complexes were prepared with different anions and ligands to identify possible candidates for further studies. Conductivities of the lithium hexafluorophosphate (LiPF_6) salts remained dominant throughout the investigations. A plot of the specific conductivity of propylene carbonate containing $\text{LiPF}_6 \cdot n\text{L}$ complexes is shown in Figure 8-1, where L represents an added ligand. The two ligands which produced a significant increase in the conductivity of LiPF_6 were diglyme (DG) and pentamethyldiethylene triamine (PMDETA).

Although results of lithium salts containing other anions have been presented throughout the thesis, the only systematic studies been performed on LiPF_6 and its complexes with DG and PMDETA.

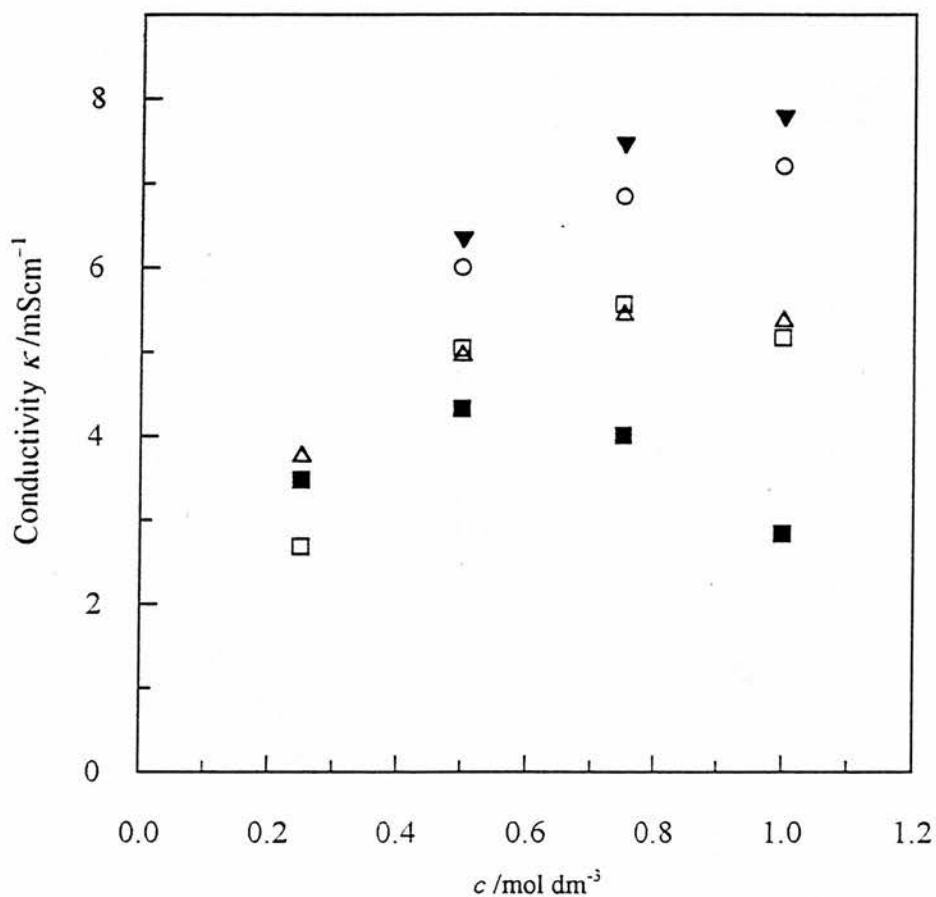


Figure 8-1 Conductivity of propylene carbonate at 20°C containing LiPF_6 in the presence of (Δ) no ligand, (∇) 2DG, (\circ) PMDETA, (\square) 4DMI and (\blacksquare) 4DMPU.

8.2. Electrolytic Conduction

In low permittivity media, the sharp decrease in molar conductivity for each electrolyte at low salt concentrations suggests that association of free Li^+ to non-conducting ion-pairs is dominant. A maximum in the molar conductivity in the moderate to high concentration range, gives an indication of the efficiency of the ligand when protecting the Li cation from association. Evidently, the diglyme (DG) ligand was capable of shielding the Li^+ in a similar way as the tetraglyme solvent molecules, while PMDETA was not. As the molecular weight of the polyether was increased, the performance of the DG complex improved, suggesting that the ligand coordination was different from that of the solvent.

All the ethers have the general formula $\text{CH}_3(\text{OCH}_2\text{CH}_2)_n\text{OCH}_3$, where n is the number of ether oxygens in the chain. The chain lengths of DG ($n = 2$) and TG ($n = 4$) are very similar so both are likely to coordinate to Li^+ in a similar manner. Two DG molecules can wrap around the cation in a pseudo-cyclic structure, offering stable complexation similar to that of a crown-ether. As n increases the complex stability constant will also increase as more oxygens coordinate to the cation, but when $n > 6$ some oxygens will be unable to bind and the stability of the complex will decrease as the unbound oxygens hang "free". As n increases further ($n > 11$), the length of the chain will be sufficient to allow formation of a pseudo-cycle with an arm passing over the face of the cation in a cryptand-like structure. The stability of the complex will once again increase. PEO400 has a value of $n \approx 9$ so the structure of the solvated cation is likely to be different from those of the shorter chain ethers. The results

shown in earlier chapters suggest that the PEO400 does not shield the cation from association as well as DG or TG.

In contrast, the association of ions in high permittivity media for the majority of electrolytes is limited to ion-pairs up to moderate salt concentrations. The overall association constants decrease in the order $\text{LiPF}_6\cdot\text{PMDETA} > \text{LiPF}_6 > \text{LiPF}_6\cdot 2\text{DG}$ in propylene carbonate (PC), suggesting that the PMDETA “cage” is not able to protect the Li cation in a PC environment at low salt concentration. The structural aspect of the ether ligands discussed above can also be used here to suggest possible reasons for the different shielding abilities. Only one PMDETA is capable of coordinating to the Li^+ , allowing association with the anions where the ligand does not protect. It is possible that two anions may even bridge a pair of lithium cations, each with a coordinating PMDETA ligand.

The specific conductivity κ generally passes through a maximum characteristic of the salt and solvent. The maximum κ values of the Li salts and complexes in polyether systems decrease in the order $\text{LiPF}_6\cdot 2\text{DG} > \text{LiPF}_6 > \text{LiPF}_6\cdot\text{PMDETA}$, while in propylene carbonate κ_{max} decreases in the order $\text{LiPF}_6\cdot 2\text{DG} > \text{LiPF}_6\cdot\text{PMDETA} > \text{LiPF}_6$. In all cases, the diglyme complex appeared superior.

8.3. Lithium Plating and Stripping

Cyclic voltammetry (CV) and potential-step experiments at a nickel microelectrode have shown that the kinetics of the Li/Li^+ couple in both high and low permittivity

media is relatively fast, and that the ligands play an important role in the charge transfer process and subsequent deposition of metallic lithium.

The current-transients following a cathodic potential-step show that nucleation and crystal growth occur. The growth mechanisms and rate determining steps for the electrodeposition process that were suggested indicated that in polyether environments, diffusion of the complexed Li^+ to the electrode surface was an important factor. In both the PC and gel environments diffusion control does not appear to be the rate determining step, suggesting that ion mobility is higher. This is clearly an important factor when considering the practical implications.

Galvanostatic and potentiostatic experiments indicate that the LiPF_6 and $\text{LiPF}_6\cdot 2\text{DG}$ in the PMMA(30 wt%) gels have high stripping efficiencies ($> 90\%$). The high macroscopic viscosity of these gels may be sufficient to hinder dendritic growth of Li, normally present in the liquid cell.

8.4. Electrochemical Stability

In a rechargeable Li-ion battery the electrolyte must be stable to beyond +4V vs. Li/Li^+ since high potentials are required by these batteries to satisfy the high energy density requirement. Cyclic voltammetry evidence given here for the stability of propylene carbonate at a Ni microelectrode indicated that the cathodic limit previously seen for this solvent at values positive of 0V vs. Li/Li^+ was due to

reduction of trace water. The anodic limit was shown to start at +4.5V at Ni and +5.5V at Pt.

Other solvents, proposed as ligands, were added in small quantities to pure propylene carbonate (Appendix 1). The only group of solvents which were all stable to oxidation beyond +4V vs. Li/Li⁺ were the ethers, of which DG is a member. Similar results were obtained from propylene carbonate containing the lithium salt complexes of DG and PMDETA, where the latter irreversibly oxidised at +3.3V. This indicates that a suitable ligand with a wide stability window may be identified without the need to prepare the Li-salt complex first.

8.5. General Conclusions

The main aim of each investigation was to determine the electrochemical performance of the lithium salt complexes relative to the “pure” LiPF₆, and to each other. Thermal analysis (Chapter 3) showed that both the DG and PMDETA salt complexes were significantly more stable than the simple salt. In all experiments, the Li salts which were complexed by 2DG maintained their superiority over those complexed by PMDETA, and in some cases over the simple salt also. The anodic limit of the amine ligands excludes them from use in rechargeable Li-ion batteries.

Although much of the work presented here was conducted at microelectrodes, the results suggest that the diglyme complex salts should now be tested in full size practical rechargeable battery systems. The potentials required in a primary battery

system are not as high as those in secondary Li-ion systems, and since the specific conductivity was enhanced by the addition of PMDETA to a PC solution the practical use of this ligand as an electrolyte additive has not necessarily been excluded.

8.6. Future Work

Several aspects of investigation remain unresolved, including a study of the nature of the passivating layer which grows at a freshly deposited lithium surface in contact with the electrolyte. The growth of such an insoluble layer is important when considering the shelf-life of a lithium cell. The use of microscopic techniques, such as atomic force microscopy (AFM), to view the actual Li deposit *in-situ* during its growth at the electrode surface would be of great interest. AFM images could allow actual nuclei to be counted and on comparison of the chronoamperometric fits to the idealised growth models the growth rate constants at specific overpotentials could be calculated.

This work has dealt with the electrochemistry involved at a lithium/electrolyte interface. An alternative to the lithium electrode in practical cells is an insertion material. One direction of further investigation would therefore be a performance study of the LiPF_6 electrolytes with added ligand at selected insertion electrodes. For example, the insertion / extraction processes at $\text{Li}_x\text{Mn}_2\text{O}_4$ (spinel) or carbon can be studied by cyclic voltammetry. Work on this subject may be extended to include the microelectrode behaviour of $\text{Li}_x\text{Mn}_2\text{O}_4$ (spinel).

The host medium itself does not have to be limited to propylene carbonate or ether solvents. As mentioned in Chapter one, optimum performance can be obtained by mixing solvents such as propylene carbonate and ethylene carbonate. The trapping of such an electrolyte solution in a solid host matrix such as PAN, PMMA, or more recently a copolymer blend of poly(vinylidene fluoride) and hexafluoropropylene, known as KYNAR, may offer high liquid-like performance with the macroscopic solid polymer properties. A question arises: *what is the optimum polymer concentration* ? A systematic temperature dependent study using all the techniques seen in this project should be applied to the gel media under investigation at varying polymer concentration. It is likely that as the polymer concentration exceeds ca. 30wt%, the microscopic properties associated with liquid-like behaviour will become more polymer-like.

APPENDIX 1

Solvent Stabilities

For use as an electrolyte additive, the anodic breakdown potentials are required to be as high as possible (>4.5 V vs. Li/Li^+) for battery charging purposes. Table A1-1 summarises the results obtained for cyclic voltammetry sweeps of various ligands in pure propylene carbonate at a $10\ \mu\text{m}$ diameter Pt ultramicroelectrode vs. Li/Li^+ (1M).

Table A1-1 Anodic stability windows for a range of ligands.

LIGAND	ANODIC OXIDATION LIMIT vs. Li/Li^+ /V
TMEDA	+3.4
PMDETA	+3.3
HMTETA	+3.4
DME	$> +5$
DEE	$> +5$
Diglyme	$> +5$
Triglyme	$> +5$
Tetraglyme	$> +5$
Hexaglyme	$> +5$
15-Crown-5	$> +5$
DMI	+4.2
DMPU	+4.6

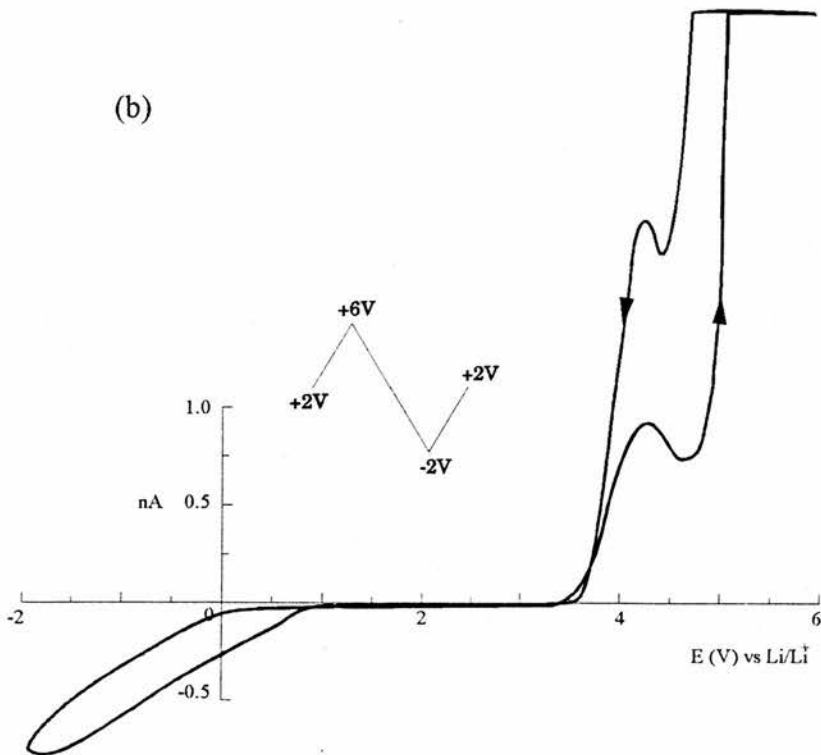
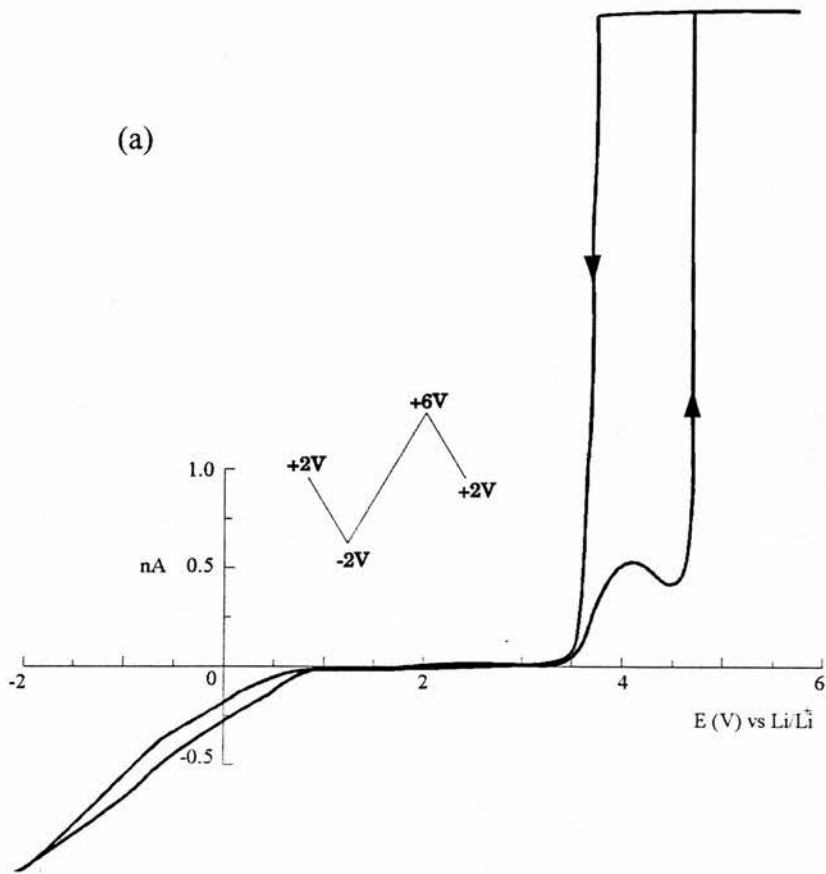


Figure A1-1 TMEDA/PC. Sweep rate = 100 mV/s.

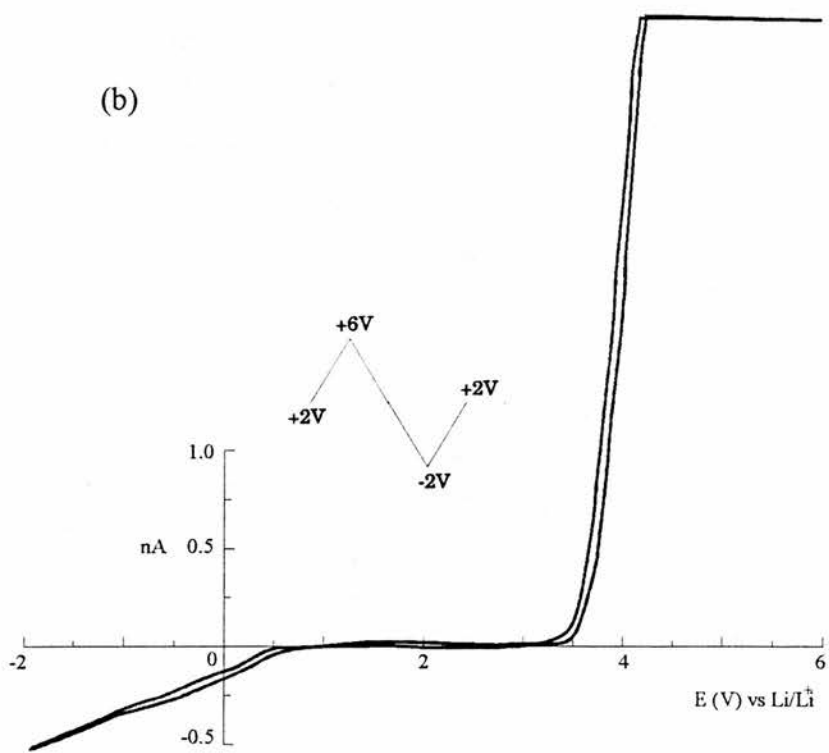
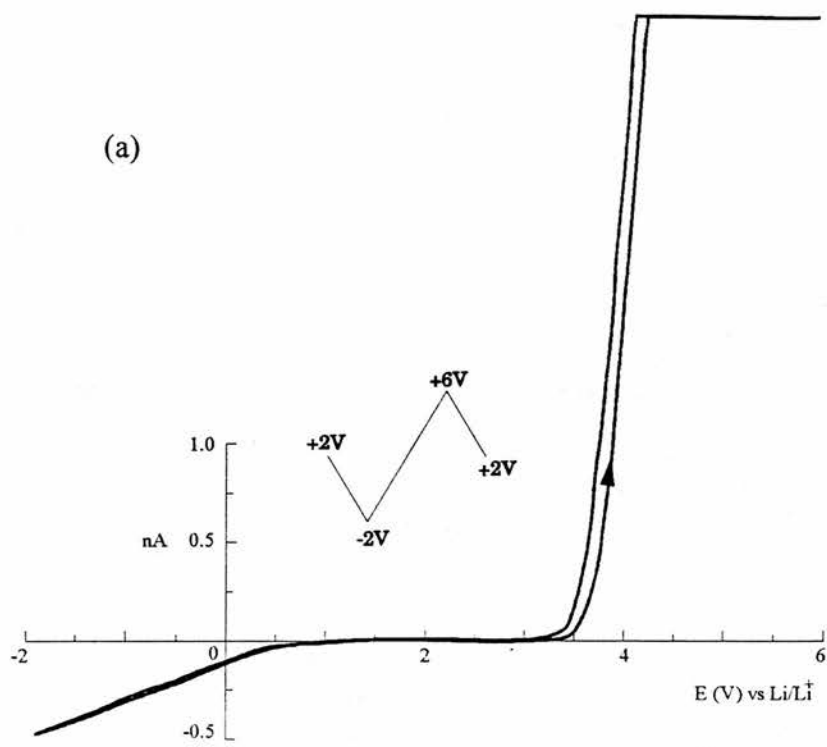


Figure A1-2 HMTETA/PC. Sweep rate = 100 mV/s.

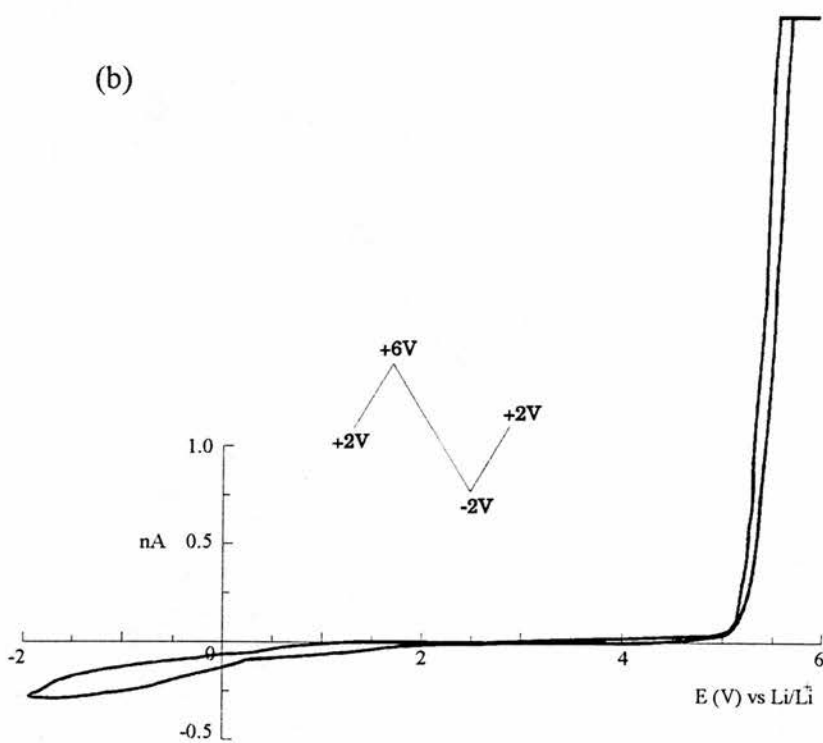
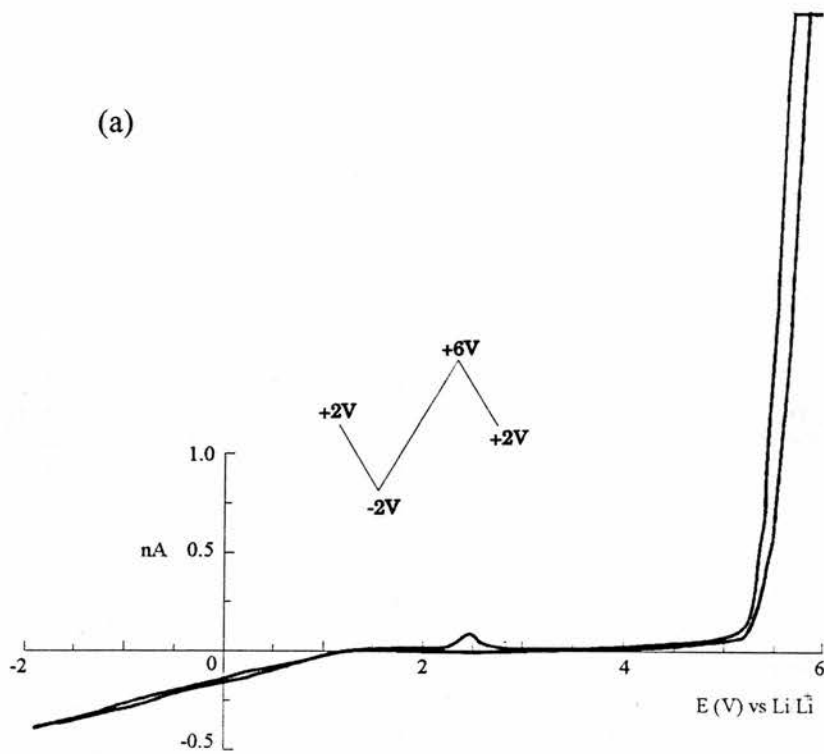


Figure A1-3 DME/PC. Sweep rate = 50 mV/s.

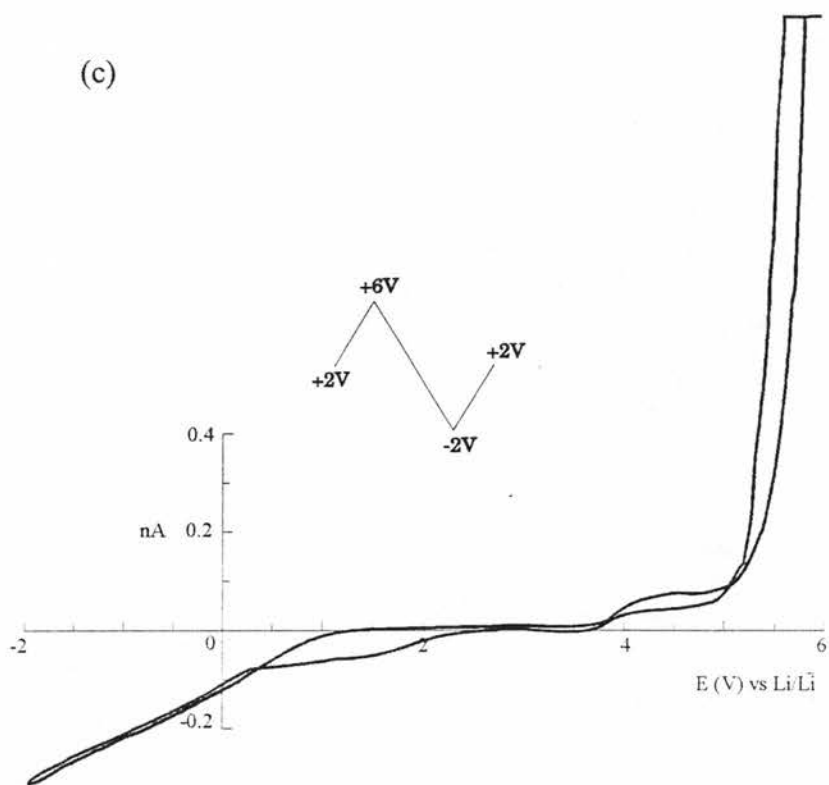


Figure A1-3 (cont.) DME/PC. Sweep rate = 100 mV/s.

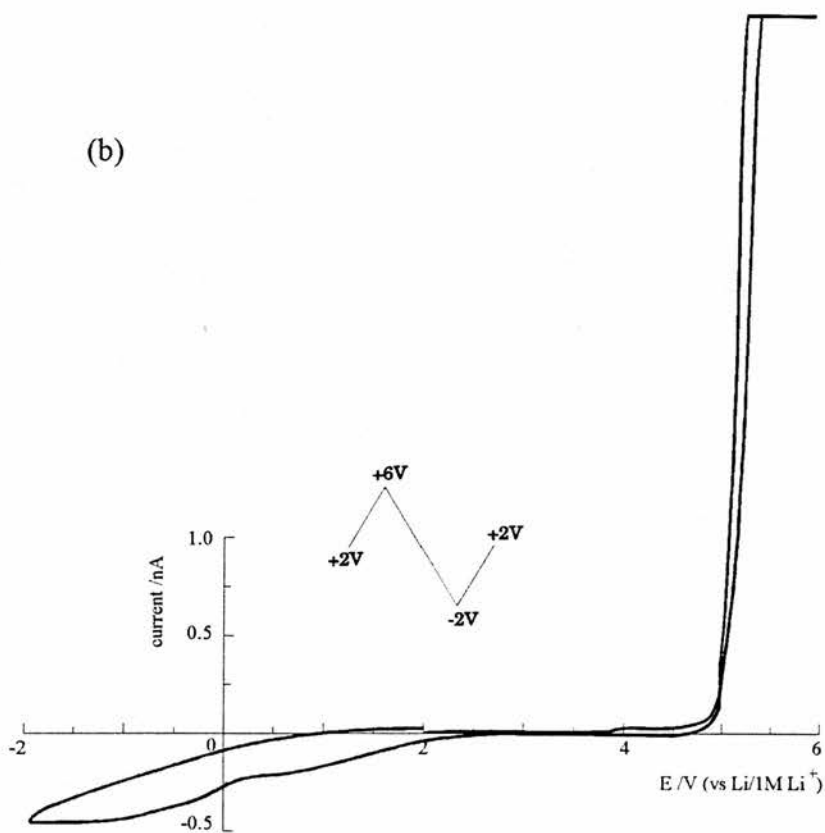
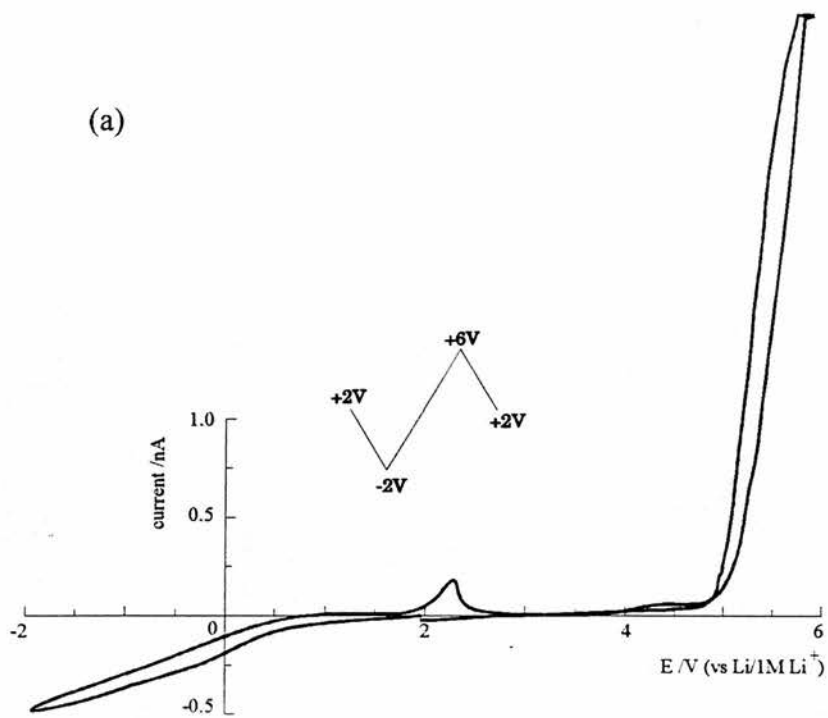


Figure A1-4 DEE/PC. Sweep rate = 100 mV/s.

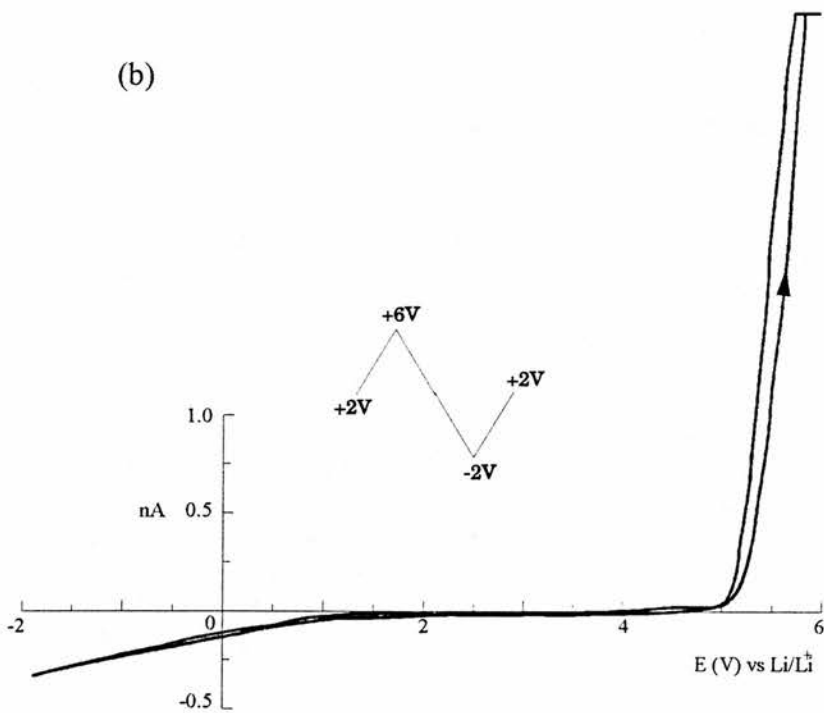
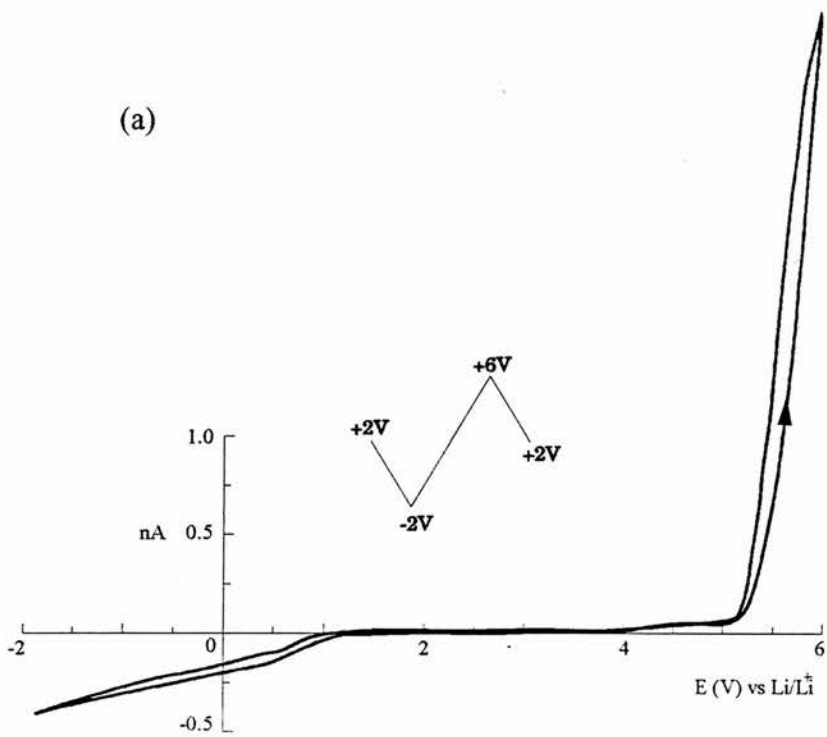


Figure A1-5 Triglyme/PC. Sweep rate = 100 mV/s.

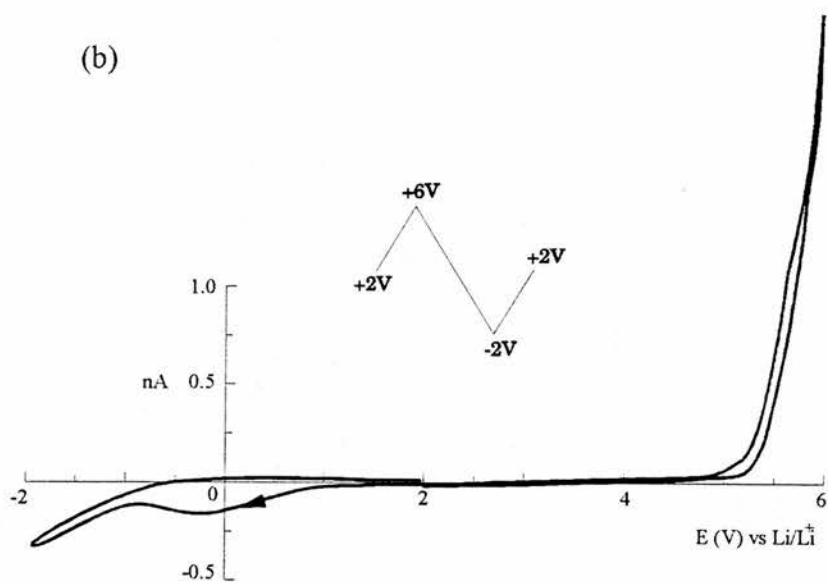
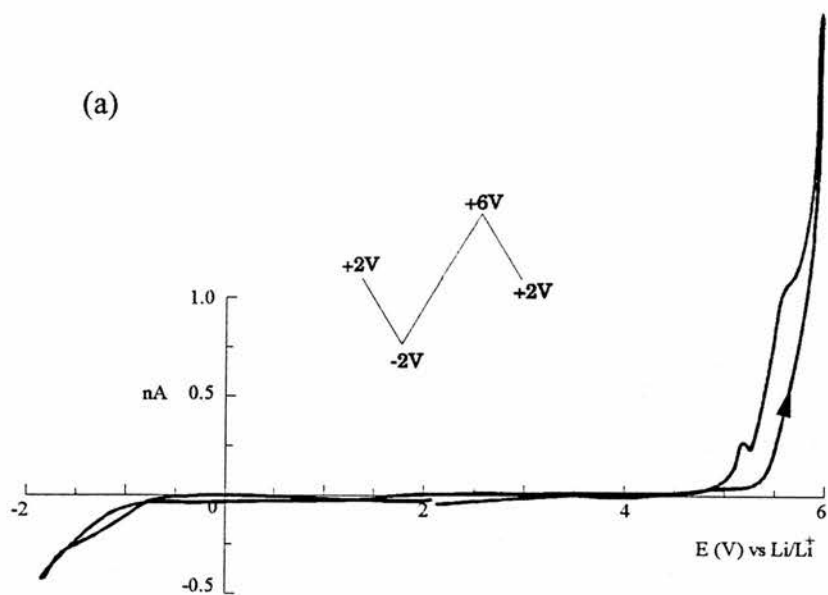


Figure A1-6 Tetraglyme/PC. Sweep rate = 100 mV/s.

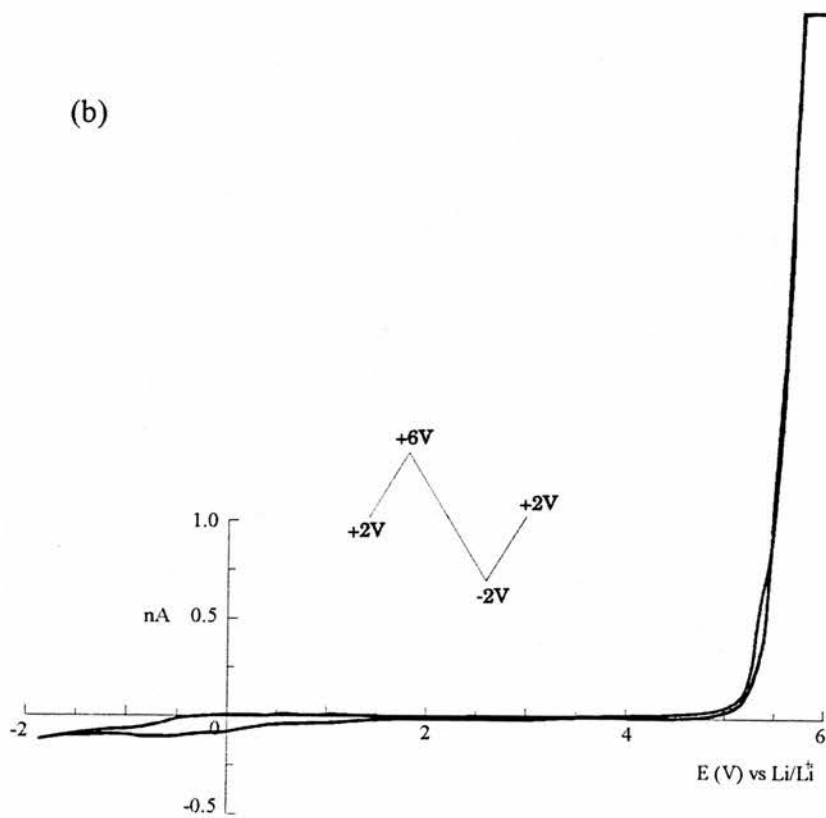
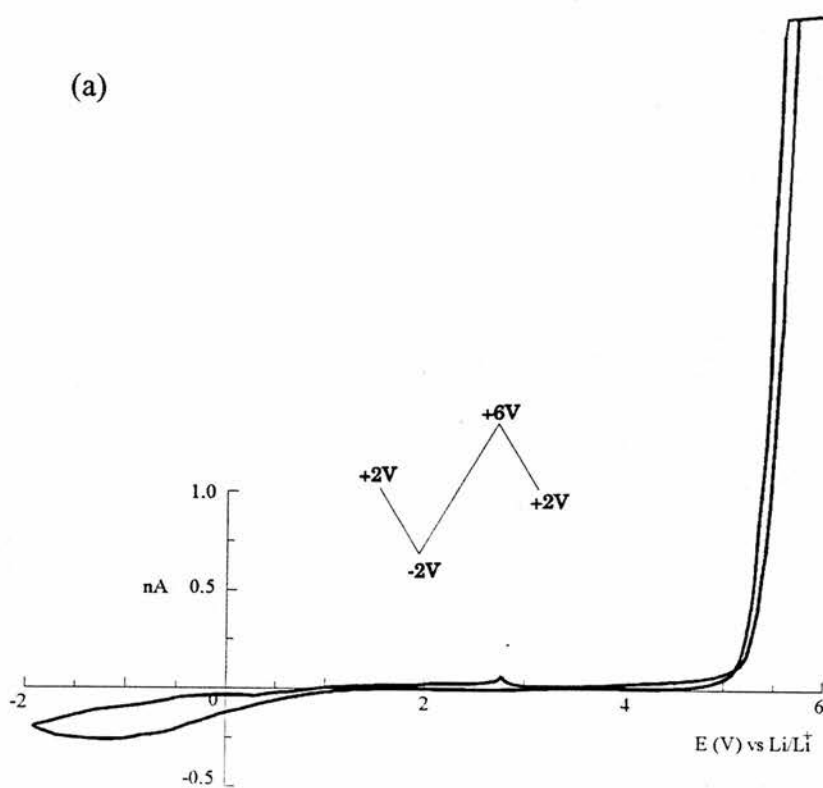


Figure A1-7 Hexaglyme/PC. Sweep rate = 50 mV/s.

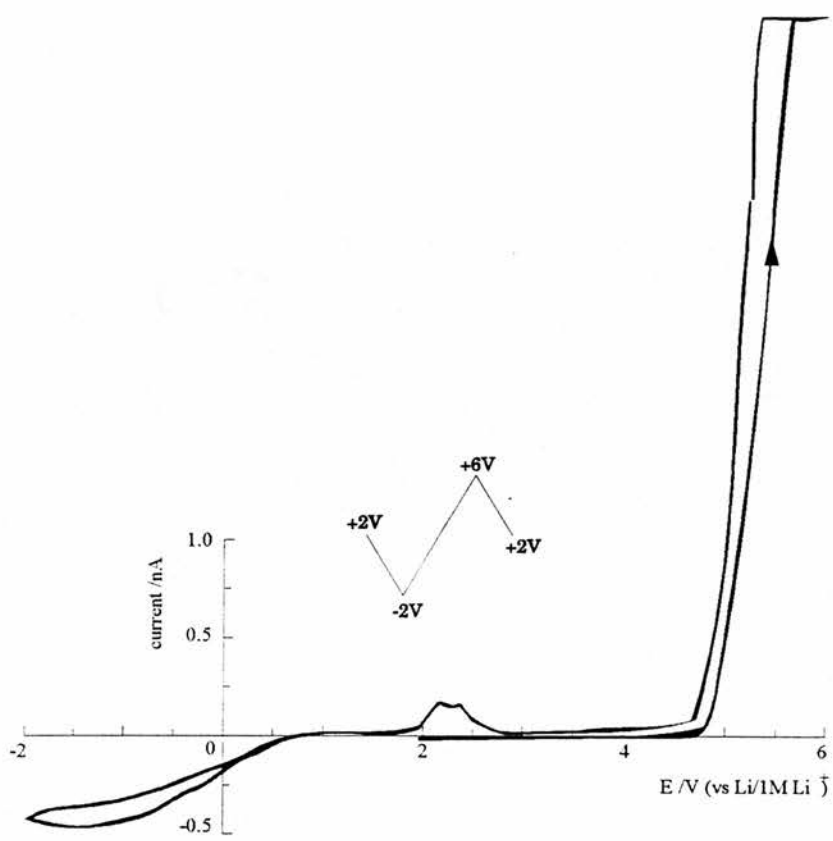


Figure A1-8 15-crown-5/PC. Sweep rate = 50 mV/s.

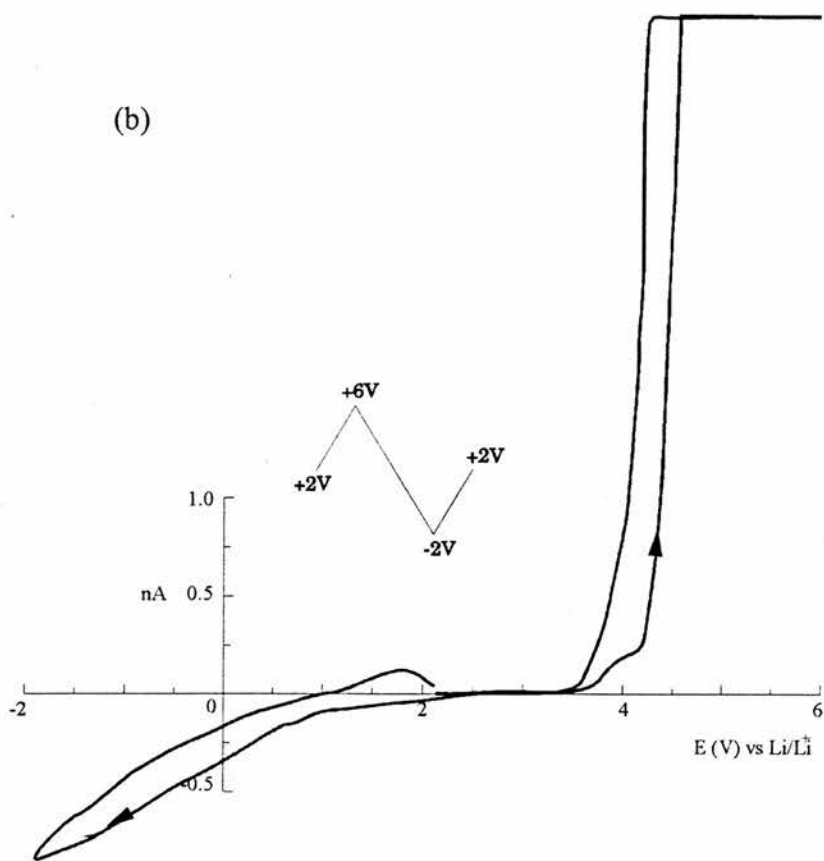
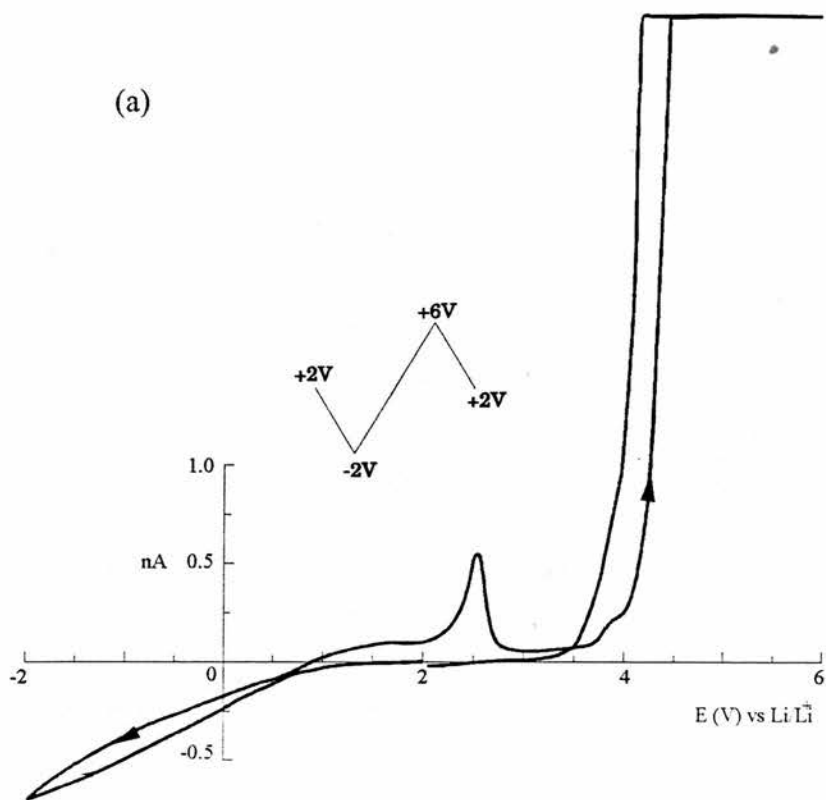


Figure A1-9 DMI/PC. Sweep rate = 100 mV/s.

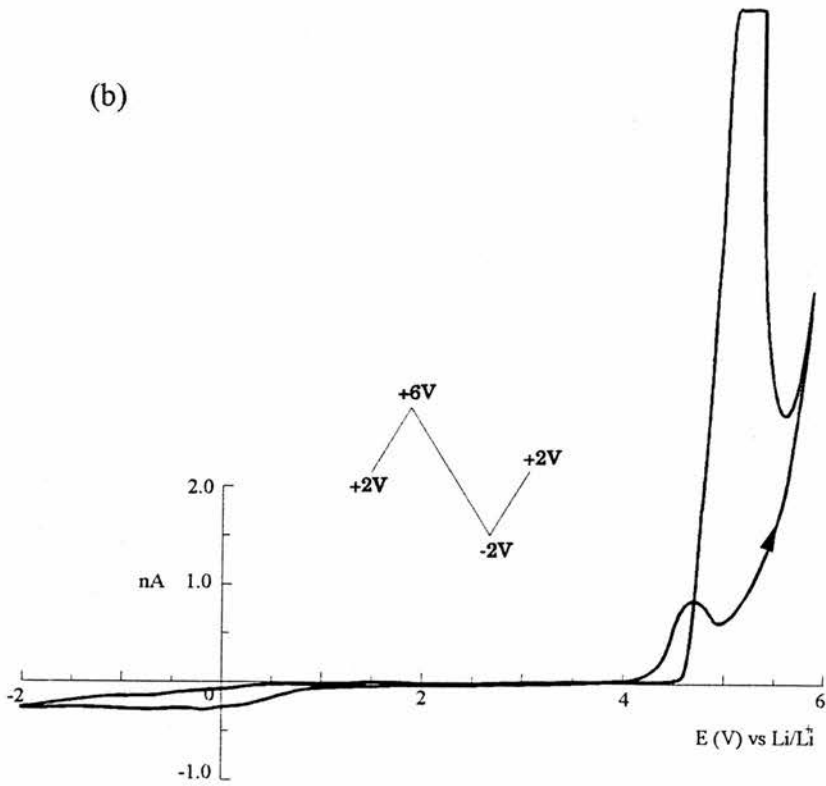
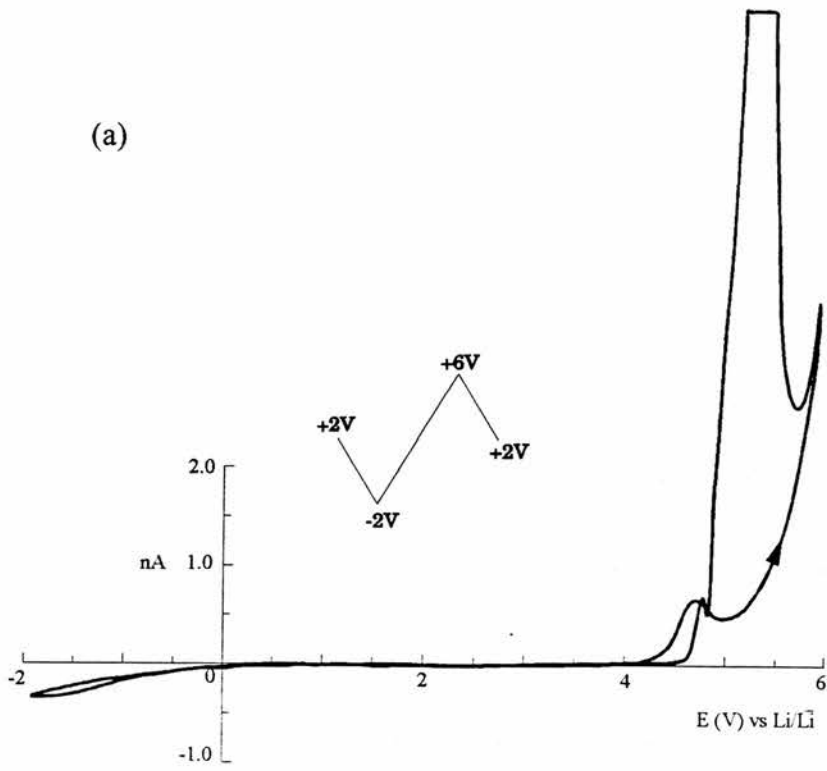


Figure A1-10 DMPU/PC. Sweep rate = 100 mV/s.

APPENDIX 2

Conductivity of PEO₃Lithium Triflate as a Function of Temperature

Although conductivity measurements of LiCF₃SO₃ dissolved in high molar mass PEO (3EO:Li) have been made previously, at temperatures above its phase change, the data have been unable to determine the true nature of the temperature dependence on conductivity. This appendix therefore reports an investigation of the electrolyte system above, independent of the main text of the thesis.

A2.1. Experimental

A2.1.1. Lithium trifluoromethanesulphonate (lithium triflate)



Trifluoromethanesulphonic acid (triflic acid, 0.667 mol dm⁻³) was slowly added to a suspension of lithium carbonate (Li₂CO₃, Aldrich) in distilled water. The solution was stirred for 3 hours, filtered through a fine sinter and the majority of water removed on a rotary evaporator, leaving the hydrated salt. The anhydrous salt was obtained after heating the sample under vacuum for 24 hours at 150°C.

A2.1.2. Preparation of PEO₃Lithium Triflate

A mixture of appropriate amounts of lithium trifluoromethanesulphonate and dry poly(ethylene oxide) was transferred to a stainless-steel tube for cryogrinding. A small sample of the intimate cryoground mixture was pressed to 5 tons for 30 seconds between two stainless-steel discs in a 13mm pellet press. This was heated for at least 3 hours at 200°C under no applied pressure using a band heater. Upon cooling to 100°C, a pressure of 3 tons was applied. The sample was allowed to cool to room temperature overnight under the applied pressure. The film produced was 0.33 mm thick.

A2.1.3. Powder X-Ray Diffraction

A sample of the cryoground powder was sealed into a 0.5 mm glass capillary inside the glove box. Once removed from the box, the sample was heated to 190°C for 6 hours then annealed at 55°C for 4 days. Powder x-ray diffraction data was collected on a Stoe STADI/P high resolution system equipped with a linear position sensitive detector covering $\sim 6\theta$ in 2θ and employing Ge-monochromatised $\text{CuK}_{\alpha 1}$ radiation. After mounting the sample, the data was collected (100 steps, 30 sec/step) in the range $5^\circ < 2\theta < 55^\circ$ at room temperature.

A powder pattern of $\text{PEO}_3\text{LiCF}_3\text{SO}_3$ is shown in Figure A2-3. A good comparison is made with a pattern of the same structure solved previously (P. Lightfoot, M.A. Mehta and P.G. Bruce, *Science*, 262, 883-885 (1993)).

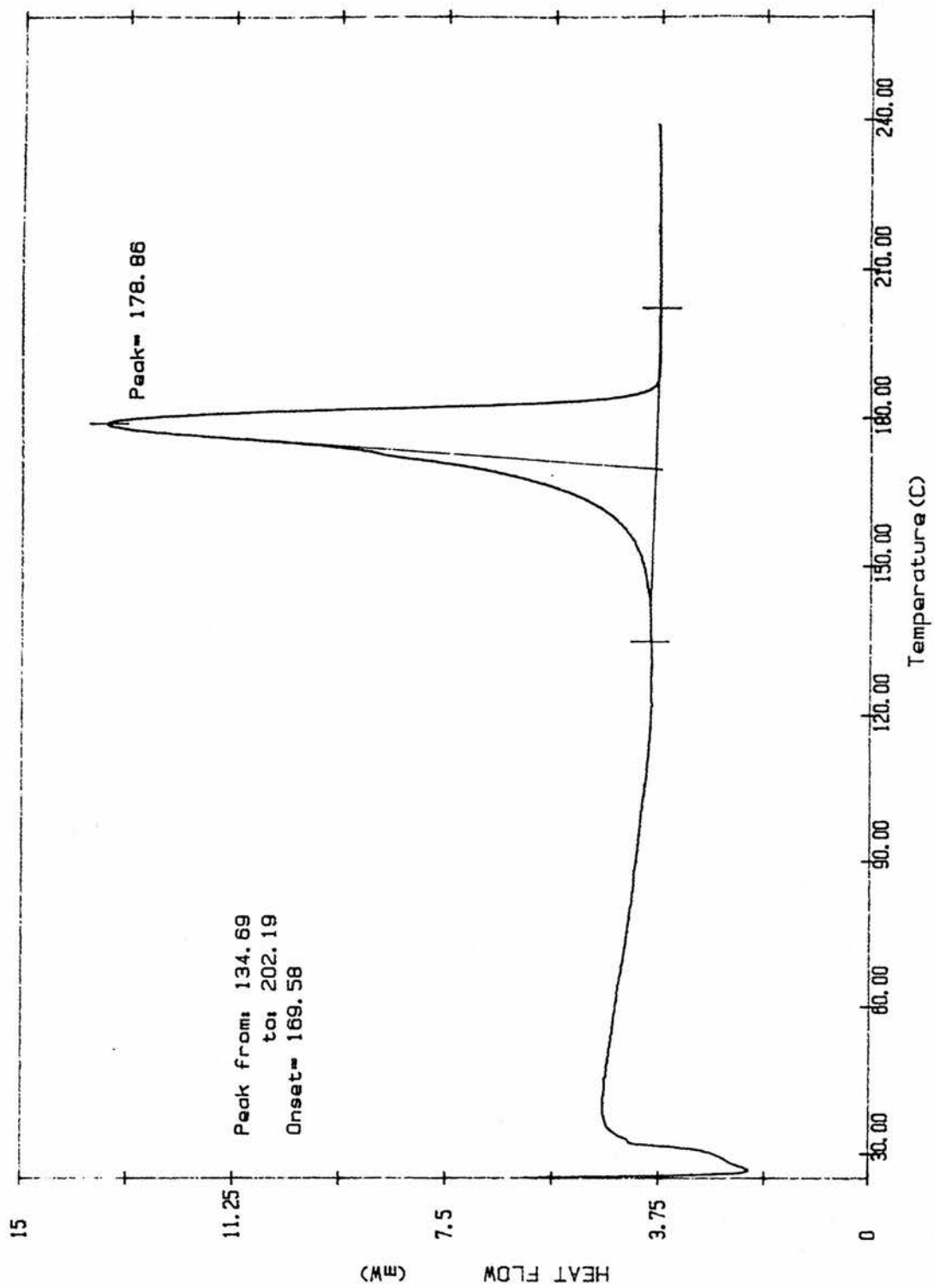


Figure A2-1 DSC heating cycle for PEO₃LiCF₃SO₃.

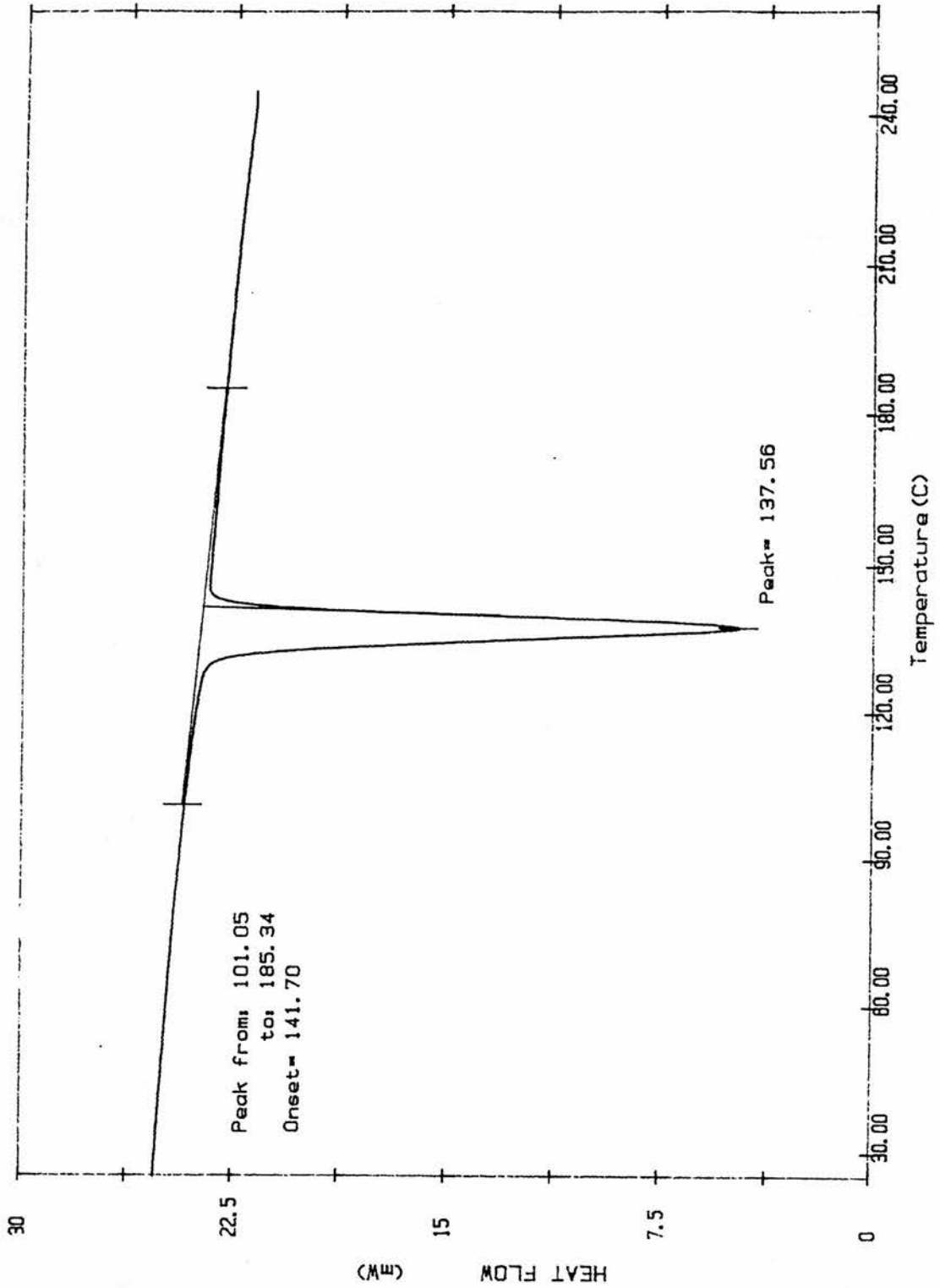


Figure A2-2 DSC cooling cycle for PEO₃LiCF₃SO₃.

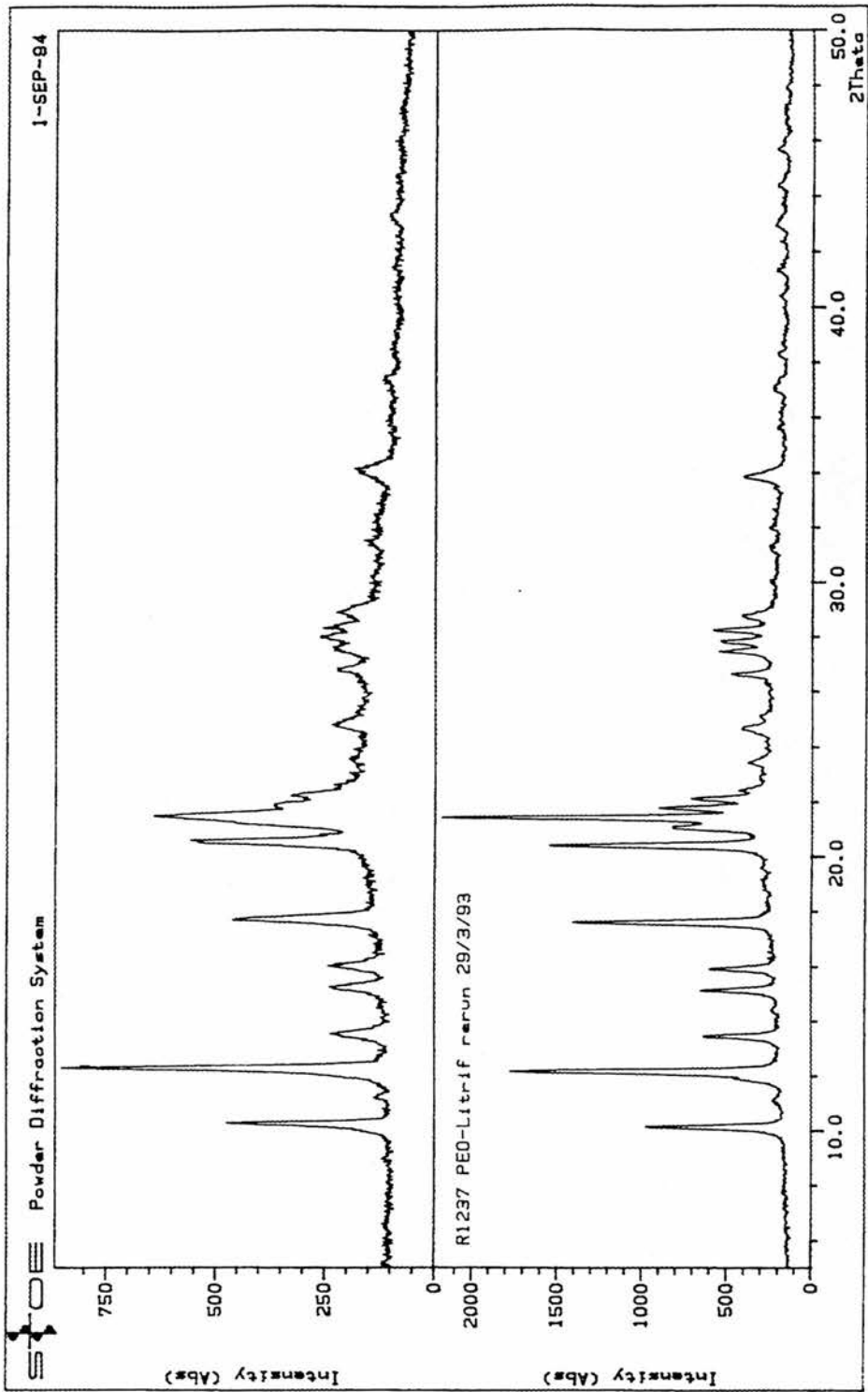


Figure A2-3 Powder x-ray diffraction patterns of $\text{PEO}_3\text{LiCF}_3\text{SO}_3$.

A2.1.4. Conductivity Measurements

AC measurements were performed using a Solartron 1255 frequency response analyser (FRA) coupled to a Solartron 1286 potentiostat, driven by an IBM compatible PC under software control. Measurements were made in the frequency range 100 kHz - 1 Hz.

A two-electrode cell configuration was used as shown in Figure A2-4. The cell body was constructed from ceramic which housed two identical 10mm diameter stainless-steel electrodes. One side had a 0.33 mm deep groove which acted as a compartment for the polymer electrolyte film when the cell was assembled. The cell was placed inside a gas tight, evacuable stainless-steel can (Figure A2-5) which allowed removal from the glove box while maintaining an argon atmosphere. Contact between the cell and the instrumentation was made by BNC electrical breakthroughs at the head of the can. The fully assembled can was placed in a Buchi TO-51 furnace, and the temperature of the cell was monitored by a K-type thermocouple running through the can. Heating the cell to 200°C for 3 hours then cooling overnight ensured good electrical contact between the electrodes and the polymer film. The cell was allowed to thermally equilibrate for at least 1 hour at each temperature before an ac-measurement was made.

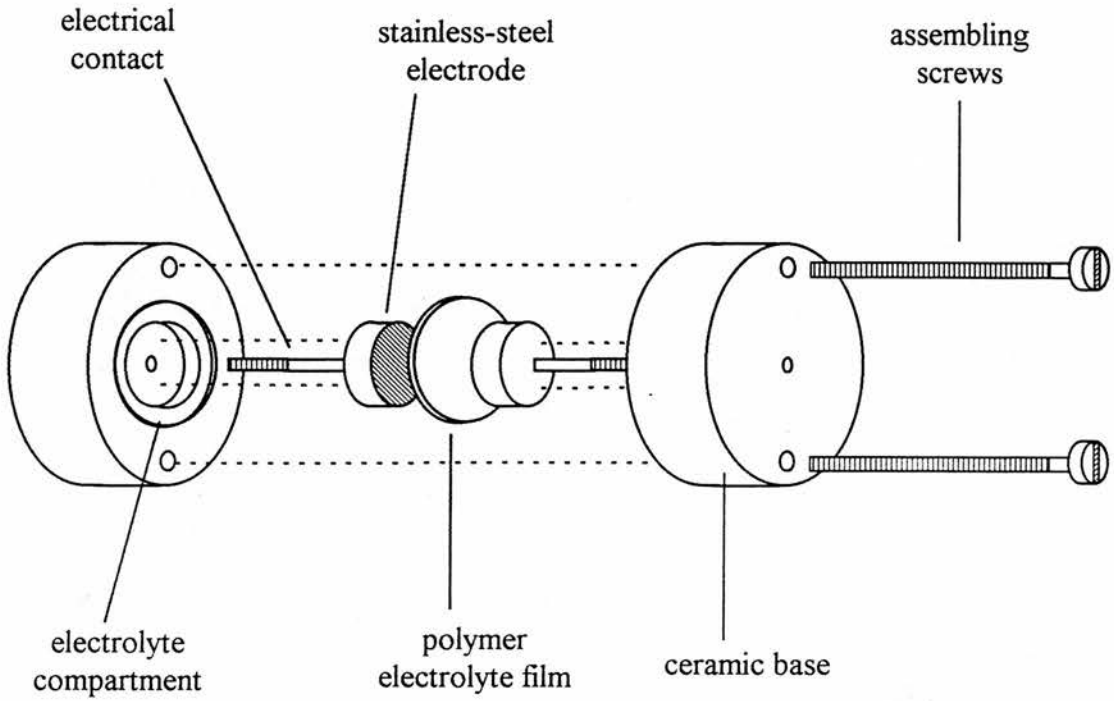


Figure A2-4 Two-electrode cell for measurement of polymer electrolyte conductivities.

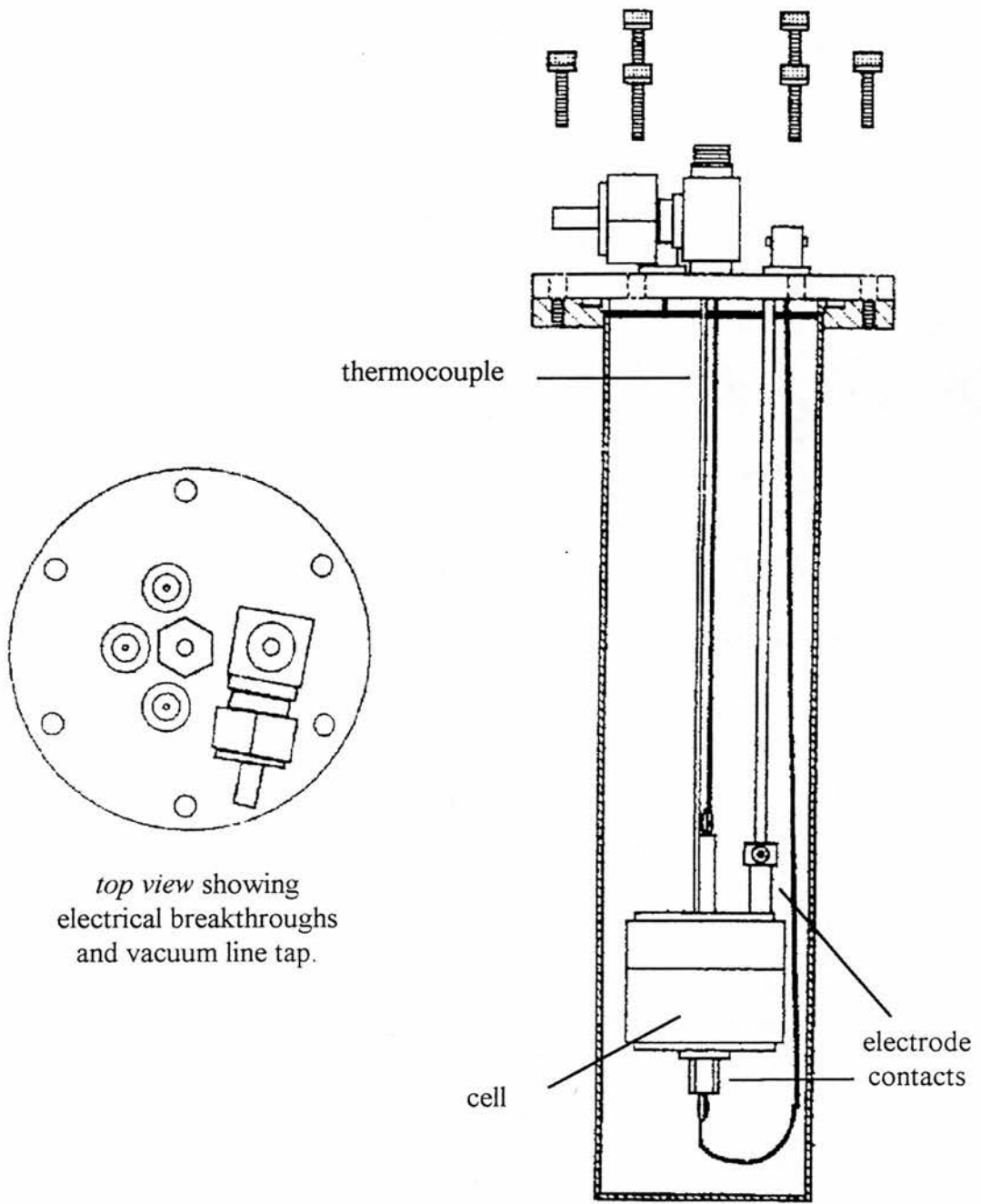


Figure A2-5 The stainless-steel can for removal of the cell from the glove box.

A2.2. Results

Table A2-1 Conductivity data for the heating of $\text{PEO}_3 \text{LiCF}_3\text{SO}_3$.

T (°C)	1000/T (1/K)	R (Ω)	$\ln(\sigma/\text{Scm}^{-1})$
48.40	3.10994	4632900	-18.51878
56.90	3.02984	2312100	-17.82375
67.30	2.93729	1342100	-17.27983
80.50	2.82765	472670.0	-16.23624
93.00	2.73112	188600.0	-15.31747
105.9	2.63817	84199.00	-14.51102
114.7	2.57832	48547.00	-13.96037
123.3	2.52239	27766.00	-13.40165
136.9	2.43873	12439.00	-12.59868
142.7	2.40471	8824.000	-12.25532
158.6	2.31616	3445.900	-11.31503
160.6	2.30548	2917.100	-11.14843
166.3	2.27557	2044.300	-10.79290
168.9	2.26219	1685.100	-10.59967
171.7	2.24795	1325.500	-10.35963
176.4	2.22445	1330.100	-10.36310
179.9	2.20726	540.7400	-9.46302
184.0	2.18747	241.3200	-8.65621
189.5	2.16146	34.62800	-6.71475
197.8	2.12337	26.43700	-6.44485
204.4	2.09402	23.28000	-6.31768
218.2	2.03521	16.14300	-5.95157
226.4	2.00180	13.41100	-5.76616
233.9	1.97219	12.04000	-5.65832
239.4	1.95103	10.63100	-5.53386
252.8	1.90132	8.264700	-5.28208

Table A2-2 Conductivity data for the cooling of $\text{PEO}_3 \text{LiCF}_3\text{SO}_3$.

T ($^{\circ}\text{C}$)	$1000/T$ (1/K)	R (Ω)	$\ln(\sigma/\text{Scm}^{-1})$
227.0	1.99940	15.73200	-5.92578
205.0	2.09139	24.83800	-6.38246
183.3	2.19082	38.89200	-6.83087
161.3	2.30176	2141.500	-10.83935
139.5	2.42336	8462.600	-12.21350
116.8	2.56443	36019.00	-13.66189
93.3	2.72889	218450.0	-15.46440

Figure A2-6 shows a plot of $\ln \sigma$ vs. $1000/T$. The conductivity data reported here compares well with previous literature values. The data were fitted to the Arrhenius equation,

$$\sigma = A \exp\left(\frac{-E}{RT}\right) \quad \text{A2-2}$$

where E is the activation energy and A is a pre-exponential factor. The fitted data in the high temperature region is shown in Figure A2-7. It can be concluded that Arrhenius, rather than VTF, behaviour is followed.

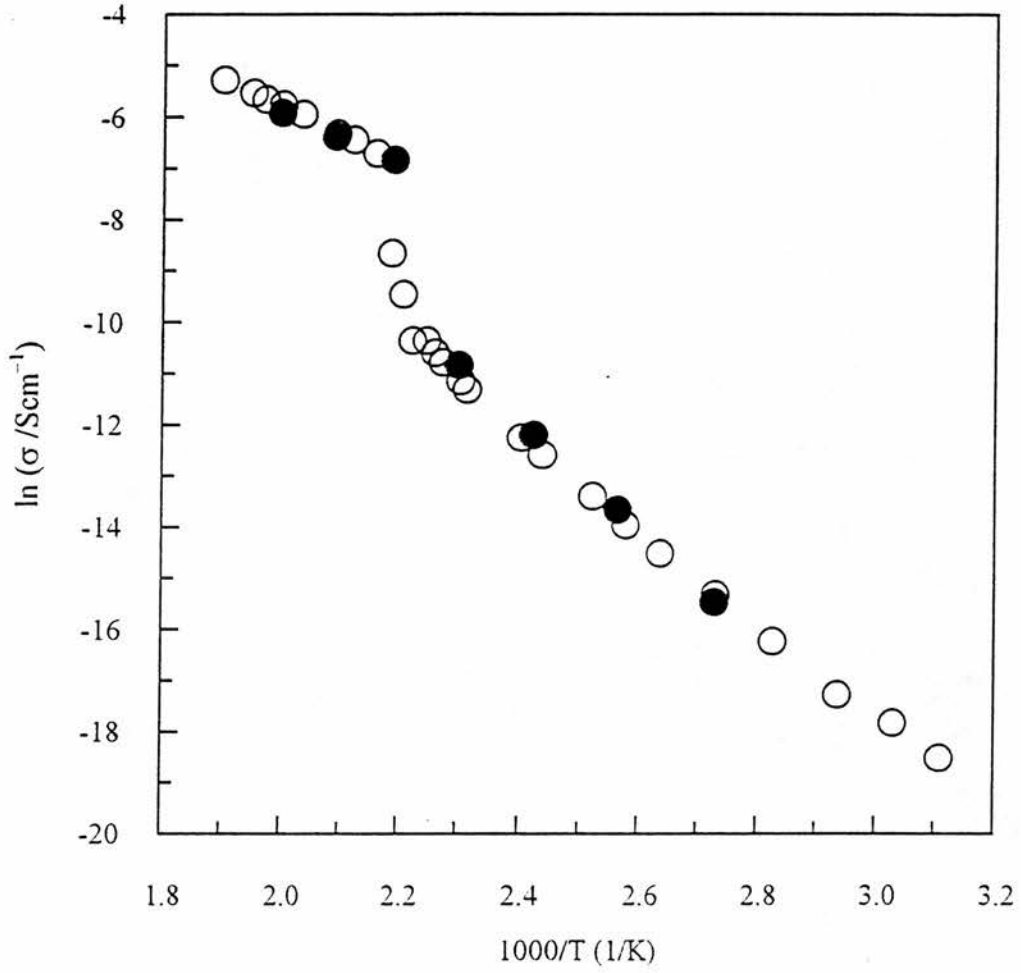


Figure A2-6 Temperature dependence of conductivity for poly(ethylene oxide)₃ LiCF₃SO₃ on (○) heating and (●) cooling.

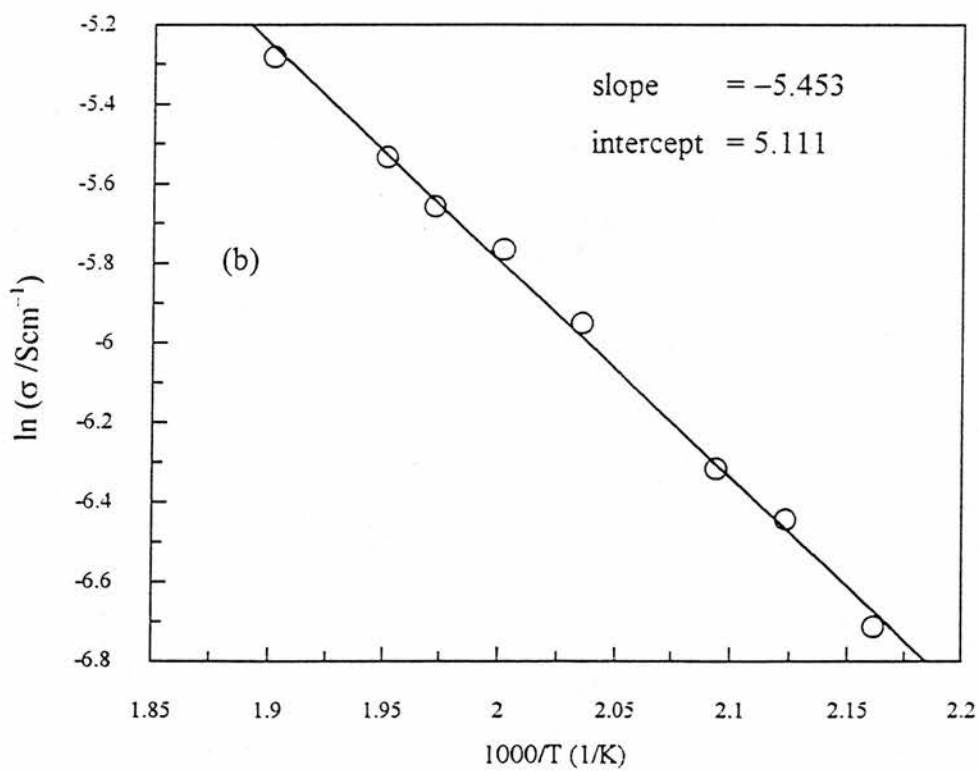
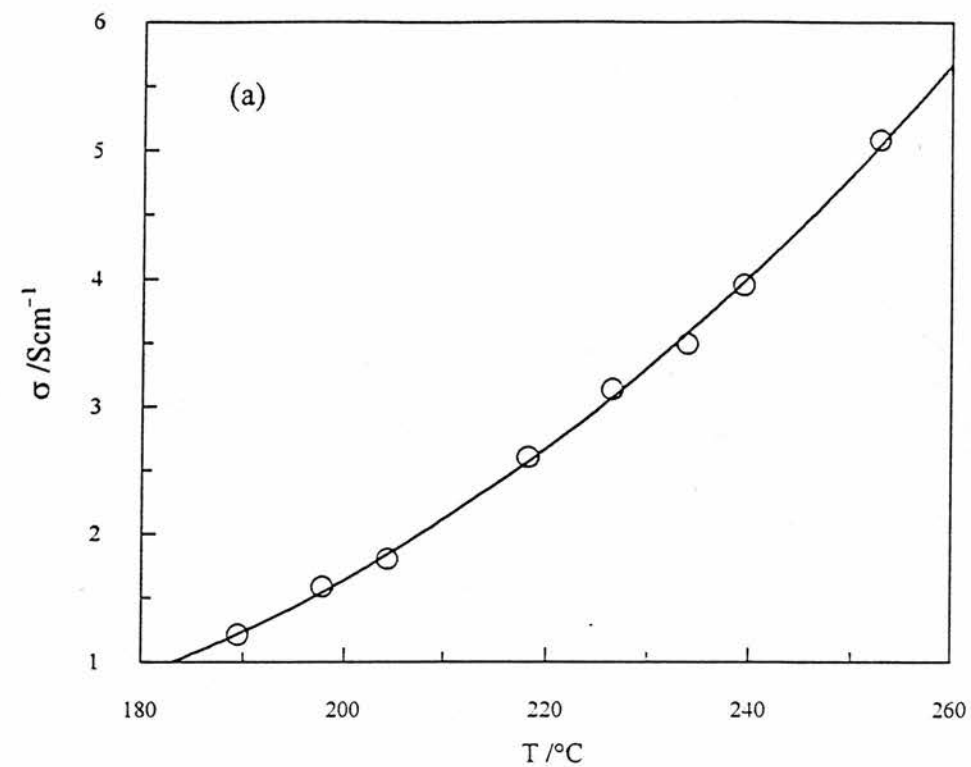


Figure A2-7 Conductivity vs. $1/T$ for $\text{PEO}_3\text{LiCF}_3\text{SO}_3$. The solid lines indicate Arrhenius fits.

APPENDIX 3

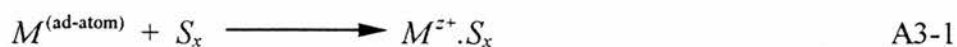
Charge Transfer at a Metal/Ion Electrode

A3.1. Introduction

While the Butler-Volmer equation developed in Chapter two is generally applicable to all systems, it has been discussed in terms of both redox species being soluble and present in solution. A more rigorous treatment (*Electrochemical Kinetics*, K.J. Vetter, Academic Press, London and New York (1967)) of the charge transfer from a solid metal M to its ions M^{z+} in solution, and vice-versa, will now be given.

A3.2. Theory

The partial anodic reaction consists of removal of a metallic ion from the metal surface, accompanied by rupture of the metallic bond and formation of a new bond with the electrolyte. Initially, M^{z+} at the metal surface will be in its ad-atom state located in a preferred site on the surface. The metallic ion M^{z+} must then bond to the solvent molecules in the electrolyte solution to form the solvated ion. The process may be described by:



where S represents the solvent molecules and z the charge valency. The reaction takes place at a rate proportional to c_{ad}^σ and c_S^σ , the surface concentrations of $M^{(ad-atom)}$ and S_x , respectively. The partial anodic current density is therefore given by

$$\vec{I} = \overleftarrow{k}_0 c_{ad}^\sigma c_S^\sigma \exp\left\{\frac{\alpha_A z F}{RT} E\right\} \quad \text{A3-2}$$

The cathodic reaction can be described by



and is proportional to $(M^{z+} \cdot S_x)$ only. The partial cathodic current density is then given by

$$\vec{I} = \overrightarrow{k}_0 c_{MS}^\sigma \exp\left\{\frac{-(1-\alpha_A)zF}{RT} E\right\} \quad \text{A3-4}$$

where c_{MS}^σ is the surface concentration of $(M^{z+} \cdot S_x)$. The total current density is then

$$I = \overleftarrow{k}_0 c_{ad}^\sigma c_S^\sigma \exp\left\{\frac{\alpha_A z F}{RT} E\right\} + \overrightarrow{k}_0 c_{MS}^\sigma \exp\left\{\frac{-(1-\alpha_A)zF}{RT} E\right\} \quad \text{A3-5}$$

where allowance is made for the properties of the metal surface caused by crystal growth and nuclei formation by including c_{ad}^σ . Since the exchange current density is given by

$$\begin{aligned}
 I_0 &= k_0^{\rightarrow} c_{MS}^{\sigma} \exp\left\{\frac{-(1-\alpha_A)zF}{RT} E_e\right\} \\
 &= k_0^{\leftarrow} c_{ad}^{\sigma} c_S^{\sigma} \exp\left\{\frac{\alpha_A zF}{RT} E_e\right\}
 \end{aligned}
 \tag{A3-6}$$

then by substituting eqn. A3-6 into eqn. A3-5 an expression analogous to the usual Butler-Volmer form is obtained:

$$I = I_0 \left\{ \exp\left(\frac{\alpha_A zF}{RT} \eta\right) - \exp\left(\frac{-(1-\alpha_A)zF}{RT} \eta\right) \right\}
 \tag{A3-7}$$